Sílvia Margarida Viana da Silva

Pathophysiology of Hippocampal CA3 Neurons in the APP/PS1 Mouse Model of Alzheimer's Disease

July 2014

· U C ·

Sílvia Margarida Viana da Silva

Pathophysiology of Hippocampal CA3 Neurons in the APP/PS1 Mouse Model of Alzheimer's Disease

Coimbra, Julho 2014

· U C ·

Tese apresentada à Faculdade de Medicina da Universidade de Coimbra para prestação de provas de Doutoramento em Ciências da Saúde, no ramo de Ciências Biomédicas, orientada pelo Dr. Christophe Mulle e pelo Prof. Dr. Rodrigo Cunha
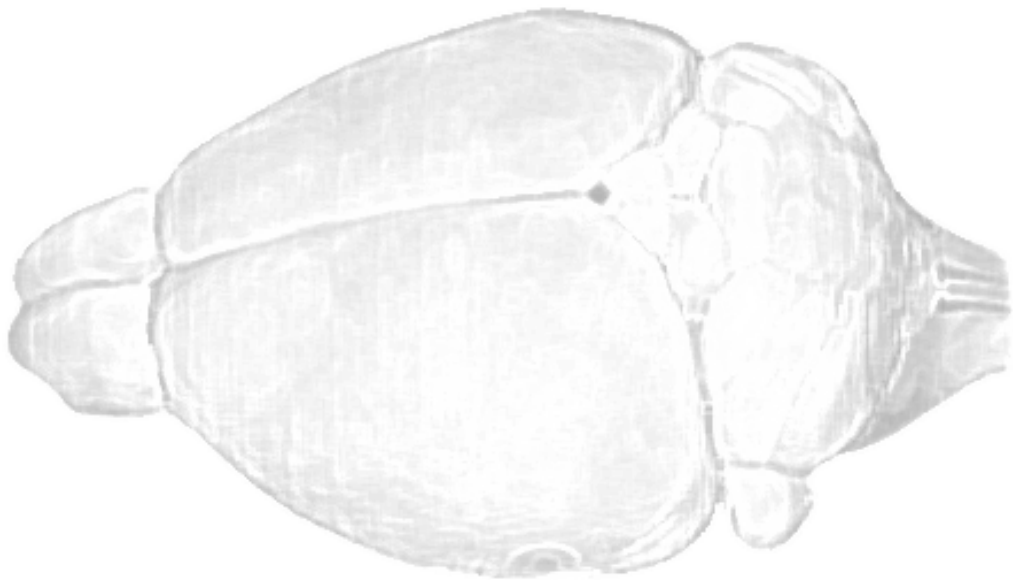
Aos meus avós

Fernando e Eduarda

INDEX

Acknowledgments & Agradecimentos

I would like to specially thank my supervisor Christophe Mulle for these almost five years of science. Thank you for all the patience (you needed a lot!) and freedom to grow and to learn. It has been an honor to work in your lab! You will always be key part of my scientific life. I would like to thank also every single member of the Mulle Lab during these five years for your companionship and help. Thank you Nelson, Mario, Marilena, Stefano and Adam for all the unforgettable good moments and so many scientific discussions. Thank you Nelson and Mario for sharing the *desk* (and every day of this PhD) with me. Thank you Virginie, Julien, Fred, Sri, Vincent, Bernat, Sabine, Gael and Jimmy for all the help, friendship and good moments in the lab. Thank you Christophe Blanchet for all your kindness, help, guidance and statistical notions! Thank you Noelle, Audrey and Melissa for taking very good care of my animals. Finally I would like to thank Fernando, Pato and Andrew, from the neighboring teams, for their scientific advice and contagious laughter!

Agradeço também ao (Professor) Rodrigo por me aceitar como sua aluna e me ter dado a oportunidade de aprender electrofisiologia num laboratório tão estimulante como o do Christophe. Agradeço todo o apoio e todas ideias que tantas vezes partilhou comigo, é inspiradora a sua paixão pela ciência!

I am very grateful to all the scientists I got to know through collaborations, in particular Philipp and Valentin who contributed the valuable STED images to this thesis. Further I would like to think Philippe Legros and the BIC for helping with the confocal microscopy.

Agradeço também ao Nelson e à Joana por tudo o que fizeram por mim em Bordeaux. Agradeço o amor e a paciência. Agradeço a partilha e a dedicação. Agradeço tudo o que me ensinaram no laboratório e na vida. Nunca teria chegado até aqui sem vocês: cada linha desta tese tem um pouquinho de cada um de vós.

I would like to thank very much Andreas and Melanie for their friendship and for making me feel always welcome in their lab. I cannot imagine these five years without all the moments I spent on *your side*. Thank you for all the support and scientific discussions and thank you for sharing your amazing kids with me. Was a pleasure to see them grow!

Life is not only made of science and this PhD allowed me to meet many amazing people that shared with me many important moments. Thank you Elian, Audrey, JC, Maria and Sam for so many good moments. Thank you Filipinha and Elisabetta for your friendship and positive way to see life. You made me a better person! Thank you Elisabetta also for all the music that helped me to write this thesis. Obrigada Inês por meio ano de partilha, que bom foi ter-te em Bordeaux.

Agradeço ao Programa Doutoral BEB e aos meus companheiros do BEB7, espalhados pelo mundo, por tantos momentos inesquecíveis! Obrigada Sofia, Samira, Carolina, Joana, Diana, Pedro, Marco, Beatriz, Ana e Carlos pela amizade e por tantas discussões existenciais! É um prazer assistir ao vosso sucesso científico. Obrigada também ao Professor João Ramalho pelos conselhos e palavras amigas.

Um sentido obrigado aos meus amigos em Portugal, por não se esquecerem de mim, mesmo quando estou longe, e me receberam sempre com tanto amor. Anica, Inês, Joana, Marquinho e Ritito obrigado por tudo e por serem sempre a minha Coimbra! Obrigada Rito pela tua amizade e pelos postais que me enviaste de cada uma das tuas aventuras. Obrigado Sara, Mariana e Raquel pela amizade e carinho de todos estes anos. Obrigado Tiago e Inês Alencoão, João Torres e João Cunha por todas as vezes que me disseram orgulhar-se de mim. Obrigado a todos por terem vindo a Bordeaux ver um pouquinho do meu mundo por aqui.

Agradeço do fundo do coração à Irene Cadime e à Joana Real por toda a ajuda indispensável à entrega e andamento desta tese de doutoramento! Sem vocês também não teria sido possível.

I also whish thank Matthias for being my best friend and the unconditional voice whispering in my ear *Yes, you can do it*! Thank you Matt, for being such a great human being and such an inspiring young scientist. Thank you for all the long nights you have stayed in the lab so I could have one cell before closing the day. Thank you for cleaning my tears every time I could not. Thank you for sharing your passion for science with me, I would have never arrived to the end of this *adventure* without your smile, your extra pair of hands and your love. Thank you for being my companion during this long jorney, nothing gives me more pleasure then to share my days and my science with you!

Agradeço à Teresa e ao Zé por serem meus *fãs* e estarem sempre ao meu lado nos momentos mais importantes! E por nunca me deixarem esquecer de onde venho ou de que sou feita.

Finalmente, agradeço imensamente a toda a minha família pela inspiração e apoio incondicional que sempre me proporcionaram. Não teria embarcado nesta *aventura* sem eles: os meus pais, que são o modelo de ser humano que tento sempre seguir, e o meu irmão que é a minha outra (e melhor) metade. Agradeço aos meus avós pelo exemplo de humanidade, coragem e pelo tanto carinho que têm por mim. Agradeço à Tia Maria por me fazer ter tantas saudades de Portugal. Agradeço à minha mãe por me mostrar, todos os dias, como a doçura, a integridade e a qualidade vivem tão bem juntas na investigação. Agradeço ao meu pai por me fazer acreditar, todos os dias, que tudo é possível e que *tudo vale a pena quando a alma não é pequena*. Agradeço ao meu irmão a sua inspiradora bondade que me enche de orgulho e vaidade todos os dias. Agradeço os abraços apertados a cada volta a casa. Agradeço as cartas com a selecção de recortes de jornal para que eu nunca me sentisse longe de Portugal. Agradeço os livros que me ofereceram para que nunca se perdesse o amor que eu tenho à língua portuguesa. Agradeço a bacalhau e a marmelada escondidos na mala. Agradeço a exímia arte de enxugar lágrimas pelo outro lado do telefone. Agradeço todo o amor com que me deram durante estes últimos cinco anos que nunca me deixou ter medo de falhar. Obrigada! Obrigada também à Kafeca, por fazer parte da família e por me fazer sentir tão em casa apenas com os seus olhos cor de mel e focinho pontiagudo!

Abstract

Alzheimer's Disease (AD) is a progressive neurodegenerative disease characterized clinically by progressive memory loss eventually resulting in dementia. Over the course of AD amyloid-beta (Aβ) deposition forms insoluble amyloid plaques but synapse loss is known be better correlated with the progression of the disease. Although the exact role of Aβ is not fully understood, recent evidence suggests that subtle alterations of synaptic transmission precede neuronal degeneration in the AD progression. Early disturbance of synaptic processes involved in learning and memory have been reported in several transgenic mouse models. In particular, the APP/PS1 transgenic mice display contextual memory impairments at 6 months, before accumulation of amyloid plaques. The Dentate Gyrus (DG) and the CA3 regions of the hippocampus are essential for the rapid encoding of contextual memories. Although this brain structure plays a key role in memory formation it has been poorly studied in AD mouse models. Thus, our project aimed to characterize the structural and functional age-dependent deficits of glutamatergic synaptic transmission in hippocampal CA3 pyramidal region. This region represents also an interesting model to study synaptic physiology and dysfunction since CA3 pyramidal cells receive different types of glutamatergic inputs, from dentate granule cells (mossy fibers), from other CA3 pyramidal cells (associative/commissural fibers), and from the entorhinal cortex (perforant path synapses). These inputs differ in terms of the position along the dendrites where they contact CA3 pyramidal cells, their spine structure, their glutamate receptor composition, their presynaptic properties, and the types of synaptic plasticities expressed (short and long term-synaptic plasticity). Combining patch-clamp electrophysiological recordings in acute hippocampal slices with high-resolution fluorescence microscopy of cells infected with new viral tools to study morphological changes we have characterized synapse specific alterations in APP/PS1 mice with 6 months.

We found that mossy fiber synapses (Mf) are relatively spared in transgenic animals as compared to associative-comisssural (A/C) synapses both functionally and morphologically. The prominent Mf short-term presynaptic plasticities showed not to be affected at 6 months, and their characteristic presynaptic long-term potentiation (LTP) was also normal. Morphology analysis also revealed no alterations in size of the Mf pre and postsynaptic compartments. There was although an alteration in the complexity of

the Mf boutons (presynaptic) that was not matched with a postsynaptic alteration (thorny excrescences, display similar complexity index between genotypes). This result suggests alterations of the filopodia size and/or number, and putative impairments concerning the GABAergic network. In contrast to the lack of presynaptic glutamatergic deficits at Mf synapses, we found a striking loss of NMDA receptor (NMDAR)-dependent long-term plasticity (LTP) at A/C synapses. This loss of LTP was correlated with subtle alterations of the dendritic spine morphology accompanied by a reduced spine density. Importantly, we found that the loss of postsynaptic LTP was not caused by alterations in the amount of synaptic NMDARs, since we found no alteration in NMDAR/AMPAR ratio at A/C synapses. We further exclude alterations in extrasynaptic NMDARs signaling.

At the cellular level processes that result in long-term modifications of synaptic strength such as LTP and LTD are thought to be key mechanisms underlying learning and memory. The results we obtained clearly highlight the importance of addressing the role individual synapses play in AD with the capability of spatially separating inputs and the high temporal resolution that just whole-cell patch-clamp recordings can provide. Our results also point out that, in this model, at an early phase of the disease the main synaptic deficits are post-synaptic, and not presynaptic as some of the previous work suggested. Furthermore, our data points out that the chronic deposition of Aβ disturbed LTP without altering NMDARs conductance (synaptically and extrasynaptically), suggesting that the loss of LTP might be due to alterations in intracellular mechanisms downstream NMDARs. A_{2A} receptors (A_{2A}Rs) and metabotropic glutamate receptors 5 (mGluR5) are known to modulate NMDAR signaling and reported to be important targets for AD treatment. Furthermore, both caffeine (antagonist of A_{2A}R) and MTEP (antagonist of mGluR5) have been reported to rescue behavioural deficits in AD mice models. We found that short application of both these drugs resulted in a partial rescue of the LTP levels in the A/C synapses of APP/PS1 animals. Our study provides novel insight into the mechanisms of early AD, examines the cellular deficits underlying learning and memory impairment and explores promising drugs for their potential to reverse those cellular deficits.

Resumo

A doença de Alzheimer (DA) é uma doença neurodegenerativa que, do ponto de vista clínico, é caracterizada inicialmente pela perda da memória de curto prazo que conduz, irreversivelmente, a perda progressiva de capacidades cognitivas. No curso da DA há acumulação de péptidos β-amilóides (Aβ) que formam depósitos insolúveis denominados placas amilóides. A evidência disponível indica que o início da deterioração da memória observada na DA é devido a alterações na função sináptica e não à acumulação de placas amilóides ou à perda de neurónios. Contudo, o mecanismo de ação pelo qual os péptidos Aβ levam à alteração da transmissão sináptica não é completamente conhecido. Ratinhos transgénicos, que apresentam uma elevada taxa de produção de Aβ, têm sido utilizados como modelos da DA, dado que sofrem uma degradação progressiva da função cognitiva. Em particular, o ratinho transgénico APP/PS1 apresenta uma deterioração da memória de trabalho que tem início antes de formação das placas amilóides. A comunicação entre o giro dentado (GD) e a região CA3 do hipocampo, feita através dos axónios das células granulares do GD, é essencial para este tipo de memória. Também a comunicação sináptica entre os neurónios piramidais de CA3 é fundamental no processamento da informação no hipocampo, em particular no que respeita à implementação de novas memórias. O objetivo principal do trabalho desenvolvido nesta dissertação de doutoramento foi a caracterização das alterações estruturais e funcionais das sinapses glutamatérgicas na região CA3 de ratinhos transgénicos APP/PS1. Esta região do hipocampo, apesar do seu papel na formação de traços mnemónicos, tem sido muito pouco estudada em modelos animais da DA. Além disso, os circuitos neuronais de CA3 são modelos interessantes no estudo da transmissão e plasticidade sináptica pois os neurónios de CA3 recebem vários tipos de aferentes glutamatérgicos: das fibras musgosas (Mf) provenientes do GD; das fibras associativas/comissurais (A/C) provenientes de outros neurónios de CA3; das fibras da via perfurante (PP) diretamente do córtex entorrinal. Estes três aferentes apresentam diferenças importantes em termos de localização dos seus terminais nervosos ao longo da árvore dendrítica, mas também em termos de morfologia da espinha dendrítica, da composição de recetores de glutamato e das propriedades de plasticidade sináptica de curto e longo termo prazo. Através de estudos de electrofisiologia e de imagiologia confocal de *super-resolução*,

procedeu-se à caracterização de alterações de vários destes parâmetros nos ratinhos APP/PS1 que modelam a DA.

Este estudo permitiu identificar que, em ratinhos APP/PS1 com 6 meses de idade, as sinapses das Mf estão relativamente preservadas em termos de alterações fisiológicas e morfológicas, em comparação com as sinapses A/C. Diferentes protocolos de estimulação pré-sináptica mostraram que a plasticidade sináptica característica das Mf não sofreu alterações. Em linha com estes resultados não se registaram também alterações no volume ou na área dos terminais pré-sinápticos ou componentes pós-sinápticos. Contudo, observou-se uma alteração no índice de complexidade dos terminais pré-sinápticos, sem alterações pós-sinápticas, que pode ser indicativa de alterações no número ou tamanho dos contactos (*filopodia*) com interneurónios GABAérgicos. Em contaste com a ausência de défices na comunicação glutamatérgica nas Mf, observou-se uma total perda da capacidade de potenciação de longa duração (LTP) nas sinapses A/C. Esta alteração electrofisiológica foi acompanhada por uma subtil alteração da densidade sináptica, mas sem modificações morfológicas de relevo. Surpreendentemente, concluiu-se que esta perda de LTP não é devida a alterações no número ou nas características dos recetores de glutamato presentes na membrana, uma vez que os rácios de recetores AMPA e NMDA na sinapse não se encontravam alterados. Também o número e/ou condutância dos recetores NMDA extrasinápticos, importantes para a plasticidade sináptica, não estava alterado neste modelo de AD.

As modificações da plasticidade sináptica como LTP e LTD (depressão de longa duração) são considerados os principais mecanismos neurofisiológicos que estão na base da aprendizagem e memória. Os resultados obtidos neste estudo ilustram o potencial e a importância que a investigação de sinapses individuais, através de técnicas de *patch-clamp*, oferece para compreender os mecanismos da DA, com vista a melhorar as terapêuticas disponíveis. Por exemplo, no modelo de DA utilizado neste estudo, a produção anormal de péptidos Aβ causou défices sinápticos que foram maioritariamente pós-sinápticos, sendo estas alterações independentes do número ou da composição molecular dos recetores NMDA. Estes dados sugerem que a perda de LTP se deve à alteração de mecanismos intracelulares de controlo dos recetores NMDA e não a defeitos na sua ativação. Os receptores de adenosina A_{2A} e os receptores metabotrópicos de glutamato do tipo 5 (mGluR5) tem a capacidade de

modular processos de plasticidade sináptica dependentes de recetores NMDA. Estes recetores A_{2A} e mGluR5 estão presentes na membrana pós-sináptica de várias sinapses do hipocampo, sendo ambos alvo de fármacos (cafeína, antagonista de recetores A_{2A} e MTEP, antagonista de mGluR5) responsáveis pela atenuação de sintomas da DA em diversos modelos animais da DA. Conformemente, observou-se que uma curta incubação de fatias de cérebro de ratinhos APP/PS1 com um antagonista de recetores A_{2A} ou de recetores mGluR5 foi suficiente para recuperar parcialmente os níveis de LTP registados nas sinapses A/C. Em conclusão, ao analisar as células de CA3, este estudo permitiu detalhar alterações sinápticas que estão subjacentes à aprendizagem e memória, bem como documentar efeitos sinápticos de fármacos capazes de reverter os sintomas da DA.

List of Publications

Published:

Annexe 1

Carta, M.*, Lanore, F.*, Rebola, N.*, Szabo, Z., Da Silva, SV., Lourenço, J., Verraes, A., Nadler, A, Schultz, C., Blanchet, C., Mulle, C. Membrane lipids tune synaptic transmission by direct modulation of presynaptic potassium channels.
Neuron. 2014 Feb 19; 81(4):787-99.
doi: 10.1016/j.neuron.2013.12.028. Epub 2014 Jan 30.

Annexe 2

Haberl, M.*, **Viana da Silva, S.***, Guest, M., Ghanem, A., Ginger, M., Mulle, C., Oberlaender, M., Conzelmann, K.K., Frick, A. *An anterograde rabies virus vector for high-resolution large-scale reconstruction of 3D neuron morphology.* ***equal contribution.***
Brain Struct Funct. 2014 Apr 11.
doi: 10.1007/s00429-014-0730-z. [Epub ahead of print]

Annexe 3

Pascual, M., **Viana da Silva, S.**, Di Scala, M., Garcia-Barroso, C., González-Aseguinolaza, G., Mulle, C., Alberini, C., Cuadrado-Tejedor, M., Garcia-Osta, A. *Insulin-like growth factor 2 reverses the pathogenic and synaptic phenotype in APP transgenic mice.*
EMBO Mol Med. 2014 Aug 6. pii: e201404228.
doi: 10.15252/emmm.201404228. [Epub ahead of print]

In Preparation:

Viana da Silva, S., Haberl, M., Bethge, P., Frick, A., Nagerl, V., Cunha, R., Mulle, C. *Rescue of LTP Deficits in the Associative Network of a Chronic Mouse Model of Alzheimer's Disease.* In Preparation

Viana da Silva, S., Labrousse, V., Haberl, M., Frick, A., Mulle, C. *Morphofunctional Characteristics of the Hippocampal Mossy Fiber in the Early Phase of a Chronic Mouse Model of Alzheimer's Disease.* In Preparation

González-González, I., Petrovic, M., **Viana da Silva, S**., Mulle, C., Henley J. *Postsynaptic kainate receptor-dependent hippocampal LTP.* Nature Neuroscience, In revision

Opazo, P., **Viana da Silva, S**., Carta, M., Petersen, J., Coussen F., Mulle C., Choquet D. *Aβ disrupts the surface dynamics of AMPA Receptors.* In Preparation

List of Abbreviations

3D	Three dimensional
[Ca^{2+}]i	Intracellular calcium concentration
A/C	Associative/commissural
A$_1$R	Adenosine type 1 receptor
A$_{2A}$R	Adenosine type 2A receptor
A$_{2B}$R	Adenosine type 2B receptor
A$_3$R	Adenosine type 3 receptor
AAV	Adeno-associated virus
AC	Adenylate cyclase
aCSF	Artificial cerebrospinal fluid
AD	Alzheimer's disease
ADAM	A disintegrin and metalloprotease
ADP	Adenosine 5′-diphosphate
AMPA	α-Amino-3-hydroxy-5-methyl-4-isoxazolepropionic acid
AMPAR	α-Amino-3-hydroxy-5-methyl-4-isoxazolepropionic acid receptor
AP	Action potential
APH-1	Anterior pharynx-defective
ApoE	Apolipoprotein E
APP	Amyloid precursor protein
APPsα	α-secretase-derived secreted APP
APPsβ	β-secretase-derived secreted APP
ATD	Amino-terminal domain
ATP	Adenosine 5′-triphosphate
Aβ	Amyloid β
BACE	β-site APP cleaving enzyme
BDNF	Brain-derived neurotrophic factor
Bicuculline	[R-(R*,S*)]-6-(5,6,7,8-Tetrahydro-6-methyl-1,3-dioxolo[4,5g] isoquinolin-5-yl)furo[3,4-e]-1,3-benzodioxol-8(6H)-one
CA	Cornu ammonis field
CaMK II	Ca^{2+}/calmodulin-dependent protein kinase II
cAMP	Cyclic adenosine monophosphate
CB1R	Endocannabinoid receptor 1

CFC	Contextual fear conditioning
CGP-55845	(2S)-3-[[(1S)-1-(3,4-Dichlorophenyl)ethyl]amino-2-hydroxypropyl] (phenylmethyl)phosphinic acid hydrochloride
CNIH	Cornichon homologs protein
CNS	Central nervous system
CTD	Carboxyl-terminal domain
D-APV	D-(-)-2-Amino-5-phosphonopentanoic acid
DG	Dentate gyrus
DIC	Differential interference contrast
DMSO	Dimethyl sulfoxide
EC	Entorhinal cortex
eCB	Endocannabinoids
eGFP	Enhanced green fluorescent protein
EGTA	Ethylene glycol-bis(2-aminoethylether)-N,N,N′,N′-tetraacetic acid
EM	Electron microscopy
EPSC	Excitatory postsynaptic current
EPSP	Excitatory postsynaptic potential
ER	Endoplasmatic reticulum
ERK	Extracellular signal-regulated kinases
FAD	Familial Alzheimer's disease
FF	Frequency Facilitation
FWHM	Full width at half maximum
GABA	γ-aminobutyric acid
GABA$_A$R	GABA receptor type A
GABA$_B$R	GABA receptor type B
GABAR	γ-aminobutyric acid receptor
GPCR	G-protein-coupled receptor
GTP	Guanosine-5'-triphosphate
GWAS	Genome-wide association studies
HEK	Human embryonic kidney
HEPES	4-(2-hydroxyethyl)-1-piperazineethanesulfonic acid
HFS	High-frequency stimulus
IEI	Inter event interval
iGluRs	Ionotropic glutamate receptors

IP_3	Inostiol-3-phosphate
IP_3R	Inostiol-3-phosphate receptor
IPSP	Inhibitory postsynaptic potential
ISI	Inter stimulus interval
KARs	Kainate receptors
KS test	Kolmogorov–Smirnov test
L-CCG-I	(2S,1'S,2'S)-2-(Carboxycyclopropyl) glycine
LBD	Ligand-binding domain
LRP1	Low-density-lipoprotein-related protein 1
LTD	Long-term depression
LTP	Long-term potentiation
LV	Lentivirus
MAGUKs	Membrane associated guanylate kinase proteins
MAPK	Mitogen-activated protein kinase
MCI	Mild cognitive impairment
mEPSC	Miniature excitatory postsynaptic potential
Mf	Mossy fiber
MfB	Mossy fiber bouton
mGluR	Metabotropic glutamate receptor
min	Minute
MPEP	3-((2-Methyl-1,3-thiazol-4-yl)ethynyl)pyridine hydrochloride
MWM	Morris water maze
N.A.	Numerical Aperture
nAChR	Nicotinic acetilcoline receptor
NBQX	2,3-dihydroxy-6-nitro-7-sulfamoyl-benzo[f]quinoxaline-2,3-dione
NETO	Neuropilin tolloid-like protein
NFT	Neurofibrilary tangles
NMDA	N-methyl-D-aspartate
NMDAR	N-methyl-D-aspartate receptor
NRP	Non-recyclable pool (also called reserve pool)
NT	Neurotransmitter
PBS	Phosphate buffered saline
PEN-2	Presenilin enhancer 2

PFA	Paraformaldehyde
PIP$_2$	Phosphatidylinositol-4,5-bisphosphate
PKA	Protein kinase A
PLC	Phospholipase C
PMT	Photomultiplier tube
PP	Perforant path
PP1	Protein phosphatase 1
PPF	Paired pulse facilitation
Pr	Probability of release
PrP	Prion protein
PrPR	Prion Protein Receptor
PS1	Presenilin 1
PS2	Presenilin 2
PSD	Post synaptic density
PTP	Post-tetanic potentiation
RAWM	Radial arm water maze
Ro 25-6981	[R-(R*,S*)]-α-(4-Hydroxyphenyl)-β-methyl-4-(phenylmethyl)-1-piperidinepropanol maleate
RP	Recyclable pool
RRP	Ready-releasable pool
RV	Rabies virus
S/C	Schaffer collateral
SCH-58261	2-(2-Furanyl)-7-(2-phenylethyl)-7H-pyrazolo[4,3-e] [1,2,4]triazolo[1,5c] pyrimidin-5-amine
SEM	Standard error of the mean
STDP	spike-timing dependent plasticity
STED	Stimulated emission depletion
STP	Short-term plasticity
TARPs	Transmembrane AMPA receptor regulatory proteins
ThE	Thorny excrescences
TM	Transmembranar
TMD	Transmembrane domain
TTX	Tetrodotoxin
TX	Triton X

VGCC	Voltage-activated calcium channel
VGLUT	Vesicular glutamate transporters
Wt	Wild-type

Chapter 1

GENERAL INTRODUCTION

1.1 Alzheimer's Disease

1.1.1 Background

Alzheimer's disease (AD) is the most common form of dementia and also the most prevalent neurodegenerative disease in the elderly population, affecting close to 40 million people worldwide. AD progression has been associated with a gradual damage of the hippocampus and neocortex, the vulnerable brain areas involved in memory and cognition (Selkoe, Mandelkow, & Holtzman, 2012). The Bavarian psychiatrist Alois Alzheimer was the first to clinically describe this disease characterized by a progressive impairment of memory (particularly short-term memory at early stages) and loss of very important functions such as reasoning, abstraction, and language. Alzheimer established the characteristics of a neuropathological phenotype that enabled diagnostic specificity, although only at the end of the patient's life. The microscopic lesions that he described are considered the hallmarks of the disease (Figure 1.1); **amyloid plaques**, which are extracellular deposits consisting largely of aggregated amyloid beta (Aβ) peptide and **neurofibrillary tangles** (NFTs), which are composed of intracellular filamentous aggregates of hyperphosphorylated tau, a microtubule-binding protein [reviewed in (Selkoe, 2011)].

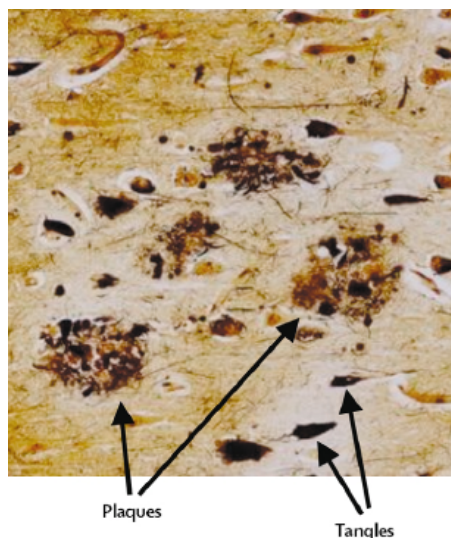**Figure 1.1 Plaques and tangles in the cerebral cortex in AD**

Plaques are extracellular deposits of Aβ surrounded by dystrophic neurites, reactive astrocytes and microglia, whereas NFTs are intracellular aggregates composed of a hyperphosphorylated form of the protein tau. Figure adapted from (Blennow, de Leon, & Zetterberg, 2006)**.**

The best correlation between the progression of dementia and histopathological changes is observed with NFTs, whereas the relationship between the density of amyloid plaques and loss of cognition is weaker (H. Braak & Braak, 1990; Nagy et al., 1995). In addition to amyloid plaques and NFTs, many AD cases exhibit also widespread Lewy body pathology. Lewy bodies are intracellular inclusion bodies containing aggregates of alpha-synuclein and other proteins. It is important to note that there is a considerable overlap between AD, frontotemporal dementia, Lewy body dementia and vascular disease, particularly in very old patients (above 80 years), whereas pure AD occurs quite rarely (Fotuhi, Hachinski, & Whitehouse, 2009). Furthermore amyloid plaques can be found in a minority of non-demented elderly patients who may represent a "presymptomatic" AD population.

Neurodegeneration in Alzheimer's disease is estimated to start 20–30 years before clinical onset. During this preclinical phase, plaque and tangle load increase and the first symptoms appear after a certain threshold. This clinical phase is often designated mild cognitive impairment (MCI) and defined on the basis of subjective reports of memory loss (Petersen, 2004). MCI is an aetiologically heterogeneous entity because many patients have MCI as part of the normal ageing process or due to other disorders (Gauthier et al., 2006). The memory-predominant subtype amnestic MCI has been suggested to constitute a transitional stage between normal ageing and Alzheimer's disease (Petersen, 2004). Age is the most important risk factor, with the prevalence of AD rising exponentially after 65 years (Blennow et al., 2006). Some environmental factors might increase the risk of sporadic AD although it also has a significant genetic background (Gatz et al., 2006). The apolipoprotein E (ApoE) gene (*APOE*) is the most important genetic susceptibility factor for AD (Poirier, 1994; Raber, Huang, & Ashford, 2004), with the relatively common ApoE4 allele (16% prevalence in the population) increasing the risk for AD three to fourfold in heterozygous dose (Corder et al., 1993; J. Kim et al., 2009). ApoE4 might have different effects that include competing with Aβ for clearance through the low-density-lipoprotein-related protein 1 (LRP1) receptor and enhancing aggregation and fibrillogenesis of extracellular Aβ. In addition, because of the role of ApoE in lipid metabolism and repair mechanisms, it is plausible that, when compared with other ApoE isoforms (such as ApoE2 and 3), the ApoE4 allele might have a less effective activity in response to various noxious stimuli (Cramer et al., 2012). In the last years several other genetic risk factors have been identified by genome-wide association studies (GWAS). Many of

these genes implicated in AD's pathogenesis are involved in multiple cellular pathways, showing that the sporadic form of AD might not be a homogeneous disease entity but that several susceptibility genes act in concert, each one conferring only a minor increase in risk (Cruchaga et al., 2014; Lambert et al., 2013). *PICALM*, *CLU*, *CR1* are some of the genes identified to be associated with sporadic AD (Eisenstein, 2011).

Besides sporadic AD there is another form of the disease, the familial AD (FAD), which is an autosomal dominant disorder with an onset before the age of 65 years. The first mutation causing the familial form of the disease was identified in the amyloid precursor protein (APP) gene on chromosome 21 (Goate et al., 1991). Several additional APP mutations were found afterwards in other families with AD. However, APP mutations explain only a few familial cases. In contrast, mutations in the presenilin 1 (*PSEN1*, located in chromosome 14) and presenilin 2 (*PSEN2*, located in chromosome 1) genes account for the vast majority of cases of the familial disease (Levy-Lahad et al., 1995; Sherrington et al., 1995). Mutations in PSEN1 gene account for more then 90% of the FAD cases, but familial forms of the disease are considered rare, having a prevalence in the population below 1% (Harvey, Skelton-Robinson, & Rossor, 2003).

Aβ peptide is produced constitutively during normal cell metabolism by sequential cleavage of APP carried out by two enzymatic complexes known as β- and γ-secretases (Figure 1.2) (Haass et al., 1992). Extracellular cleavage of APP by an integral membrane aspartyl protease called β-site APP-cleaving enzyme 1 (BACE 1) creates a soluble extracellular fragment and a fragment bound to the cellular membrane referred to as β-stub (Vassar et al., 1999). Cleavage of the β-stub within its transmembrane domain (TM) by γ-secretase releases the intracellular domain of APP (sAPPβ) and produces Aβ. γ-secretase is an intramembranous protease complex composed of four proteins: presenilin, nicastrin, presenilin enhancer 2 (PEN-2) and anterior pharynx-defective (APH-1). Presenilin, an aspartyl protease, is the catalytic subunit of the protein complex [reviewed in (De Strooper, Iwatsubo, & Wolfe, 2012)]. Under normal conditions, cerebral Aβ is degraded by the peptidases insulin-degrading enzyme, neprilysin, and by the endothelin-converting enzyme (Carson & Turner, 2002).

APP can also undergo a non-amyloidogenic pathway (Figure 1.2) in which enzymes called α-secretases cleave within the TM region. This cleavage occurs closer to the cell membrane in comparison to BACE induced cleavage, precluding the formation of the AD-associated Aβ peptide. α-secretases are a family of proteolytic

enzymes, such as the ADAM (a disintegrin and metalloprotease domain) family, which are expressed and anchored on cell surfaces. Upon cleavage by α-secretases, APP releases its extracellular domain designated as α-secretase-derived secreted APP (APPsα) and a membrane bound fragment called α-stub.
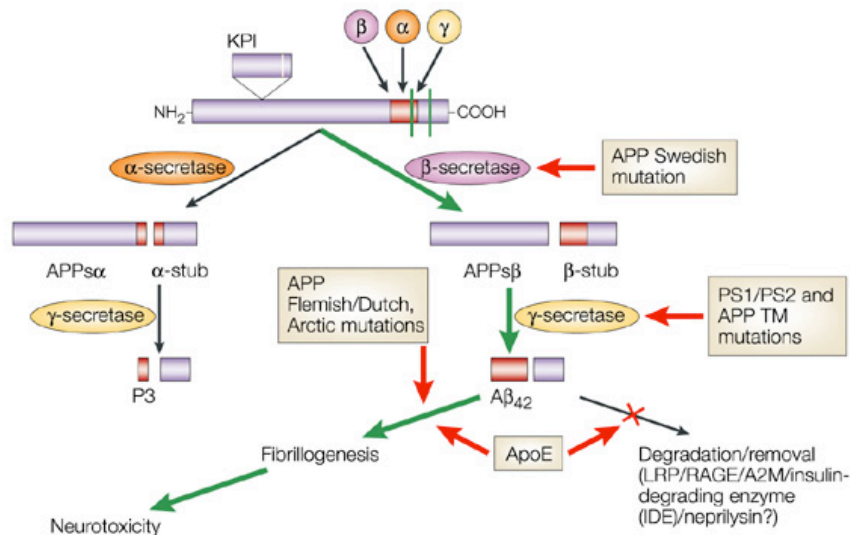
Nature Reviews | Neuroscience

Figure 1.2 Scheme of the proteolytic events, respective cleavage products generated during the processing of APP and main familiar risks

The Wt form of APP is predominantly processed by the α-secretase pathway, giving rise to a soluble form of APP (sAPPα) and to the α-stub. The Swedish mutation of APP makes it a more favored substrate for β-secretase cleavage, thereby increasing the flux of APP down the β-secretase–γ-secretase cleavage pathway that generates Aβ. The mutations in presenilin 1 (PS1) and PS2 alter γ-secretase cleavage and promote the overproduction of Aβ42 fragment, more prone to fibrillogenesis. Similarly, mutations within the TM domain of APP (shown in red) make it an improved substrate for γ-secretase, leading to the overproduction of Aβ42. The APP Flemish/Dutch and Arctic mutations seem to alter the propensity of Aβ fibril formation. ApoE4 actions on extracellular Aβ for clearance or aggregation also increase the risk for AD. Figure from (Sisodia & St George-Hyslop, 2002)**.**

In all FAD yet examined, mutations in the *APP* gene or in the presenilin coding genes increase the production and/or aggregation of Aβ in the brain (Hardy & Selkoe, 2002). This feature of AD has been reproduced in numerous transgenic models (McGowan, Eriksen, & Hutton, 2006). In contrast, none of the known mutations in the gene encoding BACE causes early-onset, familial Alzheimer's disease.

1.1.2 Transgenic Animal Models of Alzheimer's Disease

The finding that all the familial forms of AD are result of mutations in genes that encode either APP or proteins involved in the metabolism of APP, suggested a causal role for these proteins and led to the generation of transgenic animal models [reviewed in (Blennow et al., 2006; Holtzman, Morris, & Goate, 2011)]. Mice expressing mutant APP reproduce the accumulation of Aβ peptides in the brain and some of the characteristic memory impairments described in patients. For this reason, transgenic mice have become a widely used tool to study AD-related pathologic mechanisms *in vivo*. However, it is still under debate whether Aβ species represent the main toxic entity in AD, whether amyloid plaques are harmful or finally whether both act synergistically. It has been proposed that senile plaques could act as "reservoirs" that release soluble oligomers, explaining why synapse loss seems to be maximal very close to plaques (Koffie et al., 2009; Spires-Jones et al., 2007) even though amyloid plaques do not correlate with the disease progression in AD patients. Behavioral tests are therefore essential to functionally validate AD models and assess treatments (Puzzo, Lee, Palmeri, Calabrese, & Arancio, 2014). Some routine methods to evaluate hippocampus-dependent memory functions are shown in Figure 1.3 (Götz & Ittner, 2008).

The behavioral tasks that are most often used to test cognitive changes in AD mice can be divided in three categories. 1) **Spatial memory tasks** such as the Morris water maze (MWM) (Figure 1.3 A) and the radial arm maze (RAM) (Figure 1.3 C). More recently the radial arm water maze (RAWM) task has been designed to combine the positive aspects of the above-mentioned tasks. RAWM is slightly more difficult than the classic MWM (an open swim field) as it forces the animal to use special cues and working memory to find one of the several arms (6-8) in the water bath (Arendash et al., 2001; Morgan et al., 2000). 2) **Working memory tests** include the T-maze (Deacon & Rawlins, 2006) and the Y-maze (Figure 1.3 B). The Y-maze is similar to the T-maze, but it has three identical arms. The animal starts at the end of one arm and then chooses one of the other two. The Y-maze is a little easier than the T-maze because gradual turns decrease the learning time. This category also includes the novel object recognition task (Figure 1.3 D). Finally 3) **Contextual memory tasks** such as contextual fear conditioning (CFC) and passive-avoidance learning have been used to access hippocampus-dependent deficits in AD. Importantly context learning

has been shown to require input from the hippocampus, especially from the CA3 region (Ramamoorthi et al., 2011). CFC is a one trial associative learning paradigm that assesses the memory formed by association between an aversive stimulus, such as a mild foot shock, and a salient environmental cue. In CFC the context combines multisensorial environmental cues. Freezing behavior (defined as a complete absence of movement) is a characteristic fear response in rodents and is used, in CFC, as readout of memory. Animals that show good memory freeze upon re-presentation of the context (Phillips & LeDoux, 1992).
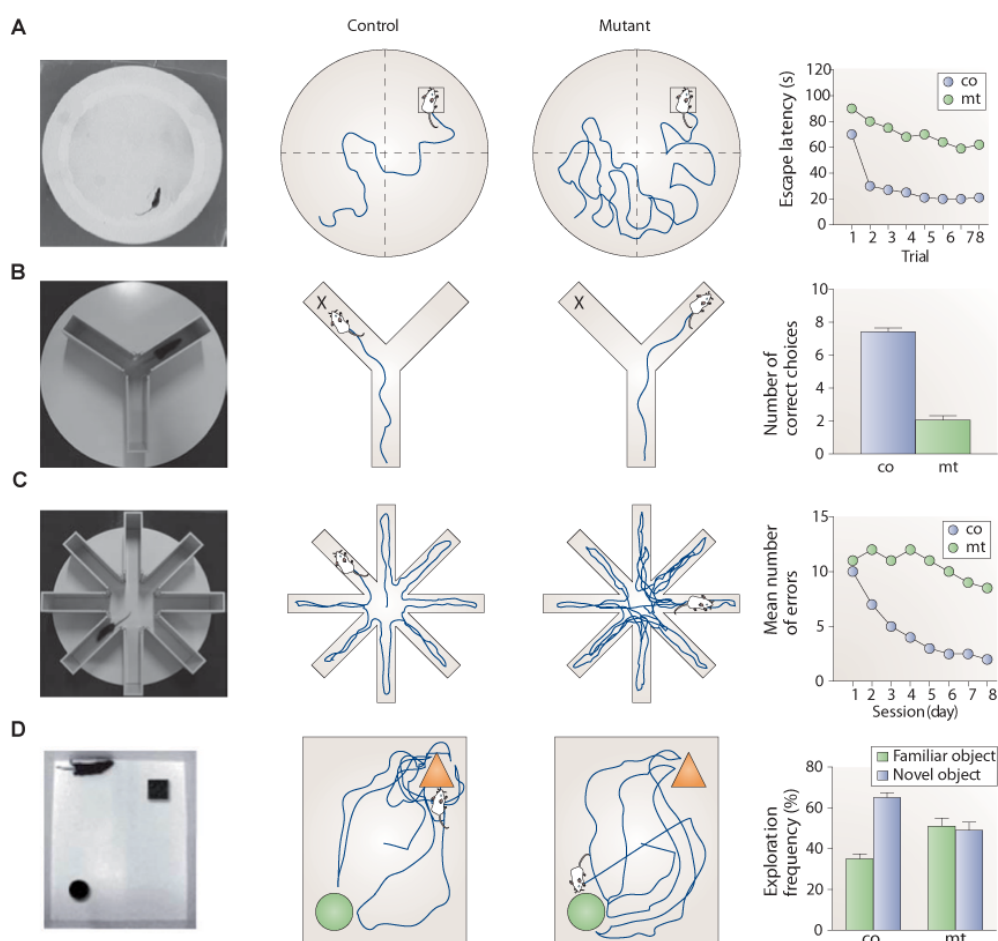
Figure 1.3 Behavioral tests used to assess memory functions in AD mouse models

A. The **Morris water maze** measures spatial reference memory. Mice are trained in a circular pool filled with an opaque liquid. Distant visual cues are provided for navigation around the pool. A platform is hidden just below the water surface. Mice swim until they find the platform. There are different ways to perform the test and also many parameters to assess memory, including path length and time to find the platform (escape latency). The test can be divided into two phases, an acquisition phase followed by a reversal phase during which the platform is moved to the opposite

corner. **B.** The **Y-maze** measures spatial working memory. One arm is blocked off while the mouse explores the other two arms for about 15 minutes. After several hours, the blocked arm is uncovered and the mouse is allowed to explore the maze. Memory is judged to be better when the mouse does not enter the arm it has entered before but explores the 'novel' arm. **C.** The **radial arm maze** measures short-term working memory. During training, a food pellet is placed at the end of each arm. In the test phase, which is without pellets, the mouse must go down each arm only once to successfully complete the maze, using short-term memory and spatial cues to remember which arms have already been visited. **D.** In the **novel object recognition** test the mouse is placed in an enclosure where it is exposed to two objects for a defined time. The mouse is removed and later re-tested in the same environment, in which one of the two previously used objects has been replaced with a novel object. The time spent on exploring the new object is recorded and reflects ability to remember what is new and what is old.

Legend: co, control; mt, mutant. Figure from (Götz & Ittner, 2008)

No single animal model fully replicates the pathogenesis of AD, but each model mimics different aspects of the disease. Obviously, no mouse model can completely recapitulate the complex cognitive deficits observed in human AD. The anatomical makeup and cognitive ability of mice make it difficult to model all of the intricacies of higher-order cognitive function exclusive to humans. Nevertheless, each mouse model allows to gain insights into different aspects of cognition related to AD [reviewed in (Webster, Bachstetter, Nelson, Schmitt, & Van Eldik, 2014)]. For our research work we chose a mouse model of AD with well characterized cognitive deficits: the double transgenic APPswe/PS1DE9 (APP/PS1) mouse, that was first described in 2001 (Jankowsky et al., 2001). The APP/PS1 mice show normal behavior in the first months of age (Gimbel et al., 2010) and then progressively develop deficits, observed in water based spatial working memory tasks such as MWM (Cao, Lu, Lewis, & Li, 2007; Ding et al., 2008; Park et al., 2006) and radial arm water maze (RAWM) (Lalonde, Kim, Maxwell, & Fukuchi, 2005; Um et al., 2013). Other reports also found deficits in CFC starting at 6 months of age (Bonardi, de Pulford, Jennings, & Pardon, 2011; Kilgore et al., 2010; Um et al., 2013).

1.2 The Hippocampal Formation

Hidden within the medial temporal lobe of the human brain lies a large structure composed of millions of neurons that form a unique circuitry unlike any other in the entire nervous system. This paired structure consists of two mirror-image halves, one in either hemisphere of the brain and was named by Giulio Aranzi as *Hippocampus* because of its resemblance with the seahorse. This structure was also called "Cornu Ammonis" due to its resemblance to ram's horn (the Egyptian god Ammon had ram's horns). The hippocampus is one of the most extensively studied areas of the mammalian central nervous system (CNS) because of two main reasons. Firstly, the hippocampus displays a beautifully laminated structure in which both neuronal cell bodies and zones of connectivity are arranged in organized layers. Secondly, the hippocampus plays a central role in learning and memory processes (Kandel, 2001). In a landmark paper Scoville *et al.* reported a *permanent loss of the ability to encode new information into long-term memory* in a patient (H.M.) who underwent bilateral hippocampal removal as a treatment for pharmacological resistant epilepsy (SCOVILLE & MILNER, 1957) . We know today that this structure plays a pivotal role in humans and other species for the ability to store long-term memory traces (Burgess, Maguire, & O'Keefe, 2002; J. J. Kim & Baxter, 2001). In rodents, the hippocampus plays a crucial role in spatial information processing, where specific cells, named *place cells*, exhibit an increased firing frequency when the animal moves across a specific location. The place field describes the specific environmental location in which a place cell fires (O'Keefe, 1992).

1.2.1 Hippocampal Neuroanatomy

The hippocampal formation is comprised of the hippocampus proper and the surrounding regions of the dentate gyrus (DG), subiculum and enthorhinal cortex (EC). It appears as an elongated, banana-shaped structure with its long axis extending in a C-shaped appearance. The long axis of the hippocampus is designated as the septotemporal axis, and the orthogonal axis is referred to as the transverse axis. It is interesting to note that the shape of the hippocampus is conserved across a wide range of mammalian species. The study of hippocampal neuroanatomy benefited from the pioneering work from scientists such as Camillo Golgi and Karl Schaffer. But the

drawings of Santiago Rámon y Cajal were the first to illustrate the detailed stratification of the various afferent systems (Figure 1.4).
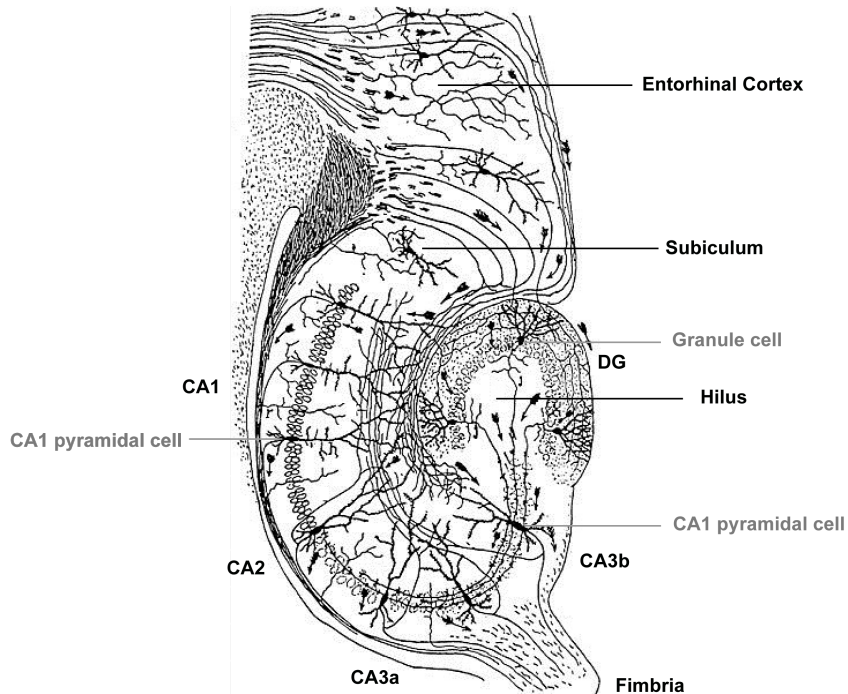
Figure 1.4 The hippocampal formation

Classical drawing of the hippocampal formation by Ramón y Cajal. Different regions and principal cells (grey) are identified. Figure adapted from (Andersen, 2007).

The **DG** is a cortical region composed of granule cells arranged in a characteristic V or U shape. The portion of the granule cell layer that is located between the CA3 and CA1 fields is called suprapyramidal blade and the portion opposite of this is the infrapyramidal blade. Granule cells do not have pyramidal morphology; they rather comprise a small ovoid cell body with a single, conical shape, dendritic tree. DG granule cells receive input from several sources; mainly from layer II of the EC via the perforant path (into the more distal parts of the dendritic tree), but also from the axons of mossy cells. Ramon y Cajal termed the axons of granule cells as mossy fibers (Mf). Each granule cell gives rise to a single unmyelinated axonal fiber with a total length of about 3 mm (Acsády, Kamondi, Sík, Freund, & Buzsáki, 1998; Claiborne, Amaral, & Cowan, 1986). These axons form several collaterals throughout the hilus, innervating numerous cell types (mainly interneurons) present in the hilar subregion, before projecting to the apical dendrites of CA3 pyramidal neurons. One particularly interesting class of cells present in the hilus are the glutamatergic

interneurons designated as mossy cells. The axons of mossy cells leave the DG of one side of the brain to innervate the DG of the contralateral hemisphere. After leaving the hilus the Mf axons do not contain further branch points, projecting along the first 100 *µ*m of CA3 pyramidal cells' apical dendrites. The hippocampal subregion composed by the Mf terminals is called *stratum lucidum,* as the lack of myelin on the Mf makes this region appear lighter in fresh tissue. Three basic types of Mf terminals exist along the entire length of the axon: large Mf terminals (4 to 10 *µ*m), filopodial extensions that project from the Mf boutons (MfB) and small *en passant* varicosities (0.5-2 *µ*m) (Amaral, 1979; Claiborne et al., 1986; Frotscher, 1991). The number of large Mf terminals along a single axon is around 10 in the hilar region and 11 to 18 in the *stratum lucidum*. Furthermore, Mf projections to CA3 also provide a robust innervation (40 to 50 synapses per axon) of all types of interneurons that have dendrites in the *stratum lucidum* (40-50 synapses per Mf axon) (Acsády et al., 1998). Large MfBs contain thousands of small vesicles and many large, dense-core, vesicles (Amaral & Dent, 1981). In addition to the vesicles these structures also have smooth endoplasmic reticulum (ER) and several mitochondria [reviewed in (Henze, Urban, & Barrionuevo, 1999)].

The hippocampus proper has three subdivisions: CA3, CA2 and CA1 (CA derives from *cornu ammonis*) identified by the neuroanatomist Rafael Lorent de Nó in 1934. The CA4 region is more commonly designated as hilus and corresponds to the initial part of the CA3 region. The hippocampus is a four-layered structure comprising the *stratum oriens*, the *stratum pyramidale*, *stratum radiatum* and *stratum lacunosum-moleculare*. The somata of excitatory neurons (pyramidal cells) are arranged in a layer that forms the *stratum pyramidale*. All these neurons have apical dendrites arborizing in the *stratum radiatum* and *lacunosum-moleculare*. In contrast to pyramidal neurons inhibitory GABAergic interneurons are widely distributed in all hippocampal layers. However different types of interneurons can be restricted to specific layers.

In 1934 Lorente de Nó already subdivided the **CA3** region into a CA3a, b, and c subareas (X. G. Li, Somogyi, Ylinen, & Buzsáki, 1994) where CA3a is closer to CA2 and CA3c closer to DG. Ishizuka and colleagues have shown that there is great heterogeneity within the dendritic trees of CA3 pyramidal cells. They describe a graded difference between the pyramidal neurons along the CA3 region with the cells within the DG limbs (CA3c) having smaller cell bodies and no dendrites extending into *stratum lacunosum-moleculare* (Ishizuka, Weber, & Amaral, 1990). In contrast, those

cells located distally in CA3 have about the same percentage of their dendritic tree in *stratum lacunosum-moleculare* as in *stratum radiatum* (Ishizuka, Cowan, & Amaral, 1995). This difference implies that CA3 pyramidal cells closer to the DG are under much greater influence from the granule cells. Additionally all CA3 pyramidal cells also have a great diversity in their spine morphologies along the dendrite, with a characteristic spine class called *thorny excrescences* (ThEs). ThEs constitute the postsynaptic targets of Mf synapses from DG granule cells. Each CA3 neuron has about 40 of these specialized spine clusters (Amaral & Witter, 1989). ThEs are mainly located in the apical dendrites, relatively close to the soma in the stratum lucidum. Albeit, in the proximal regions of CA3, closer to the DG, they can be found also in the basal dendrites (Gonzales, DeLeon Galvan, Rangel, & Claiborne, 2001) receiving input from the Mf in the infrapyramidal blade. In general on the postsynaptic side a ThE has 1 to 16 heads that emerge from a single dendritic origin (neck). These complex spines have subcellular organelles like mitochondria or microtubles that are normally absent in other spines like mitochondria or microtubles. Usually each ThE is surrounded by one individual MfB, which can synapse onto multiple spine heads (Figure 1.5). The remaining segments of both apical and basal dendrites have spines that are similar in shape and distribution to other hippocampal pyramidal cells (Jonas, Major, & Sakmann, 1993). Each CA3 pyramidal neuron projects with a single axon bilaterally to the CA1, CA2 and CA3 areas and to the lateral septal nucleus (Amaral & Witter, 1989; Ishizuka et al., 1990). These axons are thin and myelinated and under the microscope show abundant en passant varicosities (Shepherd & Harris, 1998).

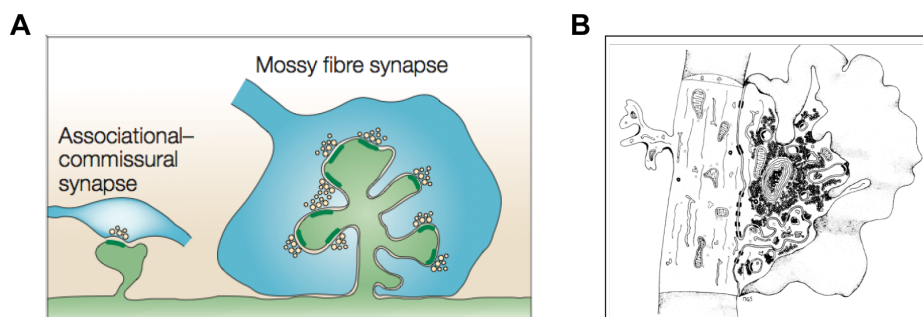**Figure 1.5 The Mf and AC synapses at CA3 pyramidal cells of the hippocampus**

A. Comparison of the large Mf synapse terminal with the A/C synapse terminal, which are in close proximity on the dendrites of CA3 pyramidal cells. Figure adapted from (Nicoll & Schmitz, 2005) **B.** Detailed drawing of a Mf synaptic complex observed at the electronmicroscopic level. Figure adapted from (Amaral & Dent, 1981).

In contrast with the diversity of CA3 principal cells, **CA1** pyramidal cells are quite homogenous along their dendritic tree (Pyapali, Sík, Penttonen, Buzsáki, & Turner, 1998). They have distinctly smaller cell bodies compared to CA2 or CA3 neurons (Ishizuka et al., 1995). From each CA1 pyramidal cell a single axon emerges, which projects through *stratum oriens* into the *alveus*. The axons form many branches projecting onto several targets within and beyond the hippocampal formation. Another difference between CA3 and CA1 neurons is that the latter do not connect among themselves. The most significant intrahippocampal connection of CA1 neurons is to pyramidal neurons in the subiculum (Amaral & Dent, 1981). Despite the apparent homogeneity of CA1 cells their axons branch extensively in the subiculum in a defined topological manner (Tamamaki & Nojyo, 1990). The extrahippocampal projections of pyramidal CA1 cells, via the fimbria, also depend on their position along the septo-temporal axis.

1.2.2 Hippocampal Circuitry

The main inputs to the hippocampus come from the EC, the septum and the contralateral hippocampus. A major input is provided by axons of the ***perforant path*** (PP), which convey multisensory information, like the one coming from touch, auditory, olfactory and visual pathways, from neurons in layer II of the EC. These axons project onto the neurons in the DG establishing a glutamatergic connection. The granule cells of DG, in their turn, send the **Mf** axons to the proximal apical dendrites of CA3 pyramidal cells. The information is therefore transferred by CA3 axons that project to ipsilateral CA1 pyramidal cells through ***Schaffer collaterals*** (SC) and to contra-lateral CA3 and CA1 pyramidal cells through commissural connections. The denominated ***trisynaptic circuit*** *(PP→Mf→SC)* allows the signal entering the hippocampus to return to the cortical areas from which it originated (Figure 1.6). The computation taking place during this process are believed to be essential for information storage (Bliss & Collingridge, 1993).

The CA2 region remained for a long time understudied. Recently, this small hippocampal region has gained much attention with the discovery of a ***disynaptic circuit*** between EC→CA2→CA1 neurons (Chevaleyre & Siegelbaum, 2010; M. W. Jones & McHugh, 2011; Kohara et al., 2014) which plays a role in certain memory

functions (Hitti & Siegelbaum, 2014; Wintzer, Boehringer, Polygalov, & McHugh, 2014). In addition to these sequential circuits CA3 pyramidal cells also form a dense **associative network,** interconnecting from the same or from the contralateral hippocampus, via the *fimbria*. CA3 pyramidal cells further receive a direct input from the EC onto the distal part of their apical dendrites. The distal apical dendrites of CA1 pyramidal neurons also receive a direct input from layer III cells of the EC.
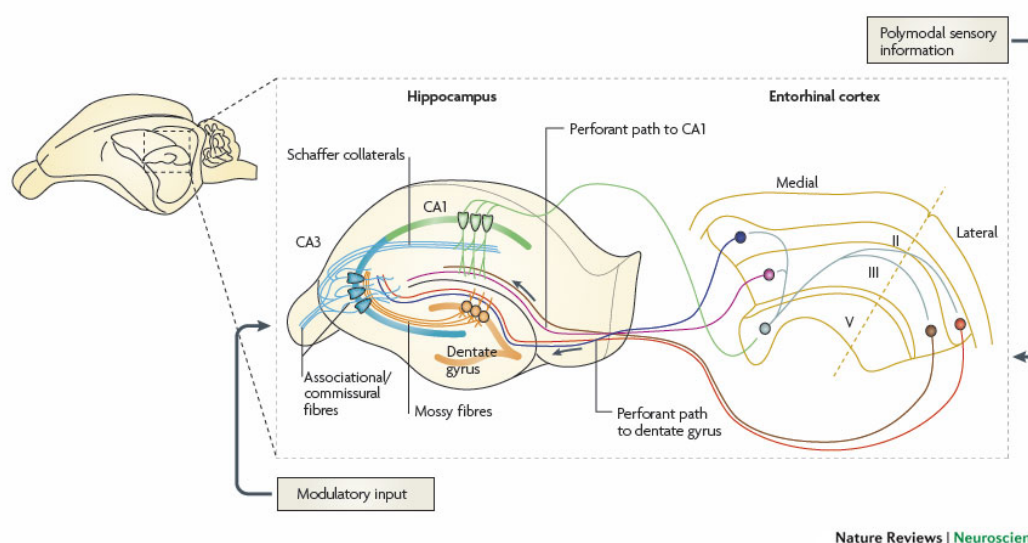
Figure 1.6 The wiring diagram of the hippocampus

The EC receives sensory information that afterwards sent to the hippocampus trough several pathways. The lateral/medial layers II of the EC project directly to DG via the perforant path. This pathway (although is not clear if the same exact fibers) can also directly innervate the distal regions of CA3 pyramidal cells. Medial/lateral layers III of the EC project to the distal regions of CA1 apical dendrites. DG granule cells send their Mf axons to the proximal regions of CA3 pyramidal cell's dendrites, defining a region called stratum lucidum. Moreover, CA3 pyramidal cells form a highly interconnected network by sending their axons to other CA3 cells in both hippocampi. Besides the A/C fibers, CA3 pyramidal cells project also send fibers to the proximal regions of CA1 pyramidal cell's dendrite. These projections can be to the ipsilateral CA1 pyramidal cells by the Schaffer collaterals or to contralateral CA1 cells by the commissural fibers. Finally CA1 works as the main output region of the hippocampus, sending fibers to the deeper layers of EC. There is also substantial modulatory input to hippocampal neurons brought by fibers from other important areas such as the septum. Figure modified from (Neves, Cooke, & Bliss, 2008)

Besides the glutamatergic circuit established by the pyramidal cells, the hippocampus is endowed by a large variety of inhibitory GABAergic interneurons.

These neurons, by releasing GABA onto principal cells and other interneurons, exert an important control on the network excitability that was shown to be essential for information processing in the brain [reviewed in (Klausberger, 2009) and (Chevaleyre & Piskorowski, 2014)].

1.2.3 Role of the Hippocampal CA3 region

One of the most intriguing features of the hippocampal formation is the high-recurrent connectivity between specific sets of principal cells. As previously described, in the rodent brain, CA3 pyramidal cells receive direct input from up to 4% of all CA3 cells within the same hippocampus (~2% if we consider the two hippocampi) (Amaral, Ishizuka, & Claiborne, 1990). Such high degree of connectivity aroused several theories about how information was encoded by the hippocampal network. In 1994, Edmund Rolls and Alessandro Treves suggested that: *the CA3 stage acts as an autoassociation memory that enables episodic memories to be formed and stored for an intermediate term in the CA3 network, and that subsequently the extensive recurrent collateral connectivity allows for the retrieval of a whole representation to be initiated by the activation of some small part of the same representation (the cue)* (Rolls & Treves, 1994). This would suggest that the CA3 network is crucial for the storage of associative memory. CA3 neurons do this by mediating the convergence of multiple representations of upstream cortical areas into a single memory trace. CA3 principal cells also play an important role in retrieval of short-term memory information based on a spatial pattern, in a process called *pattern completion* [reviewed in (Kesner, 2013; Papp, Witter, & Treves, 2007)].

In recent years both in vivo and in vitro studies have allowed to better understand functional properties of the CA3 auto-associative network and its role in information processing. CA3 region is essential for the formation of one-trial memory [reviewed in (Kesner, 2007)]. Experiments in which infusion of NMDARs antagonists or neurotoxic lesions were performed in specific regions of the hippocampal formation provided the first clues that the CA3 hippocampal region, and in particularly NMDARs of CA3 cells, are essential for the acquisition of spatial 'working memory' in a novel environment (Hasselmo, 2005; I. Lee & Kesner, 2002). Genetically engineered mice allowed to bypass the limitations of drug diffusion and target the knock down of NMDARs activity to specific subregions of the hippocampal formation (Nakazawa et al., 2002). Data collected from behavior analysis of CA3-GluN1-KO mice, which have the

NR1gene deleted only from CA3 pyramidal cells, further proved that CA3 NMDARs are crucial for rapid hippocampal encoding of novel information, which is necessary for rapid learning of one-time experience (Nakazawa et al., 2002; Nakazawa, McHugh, Wilson, & Tonegawa, 2004; Rajji, Chapman, Eichenbaum, & Greene, 2006).

It is difficult to distinguish the role of each input to the CA3 region, but it has been widely proposed that behavioral tasks that analyze episodic memory, like CFC, need the connections between DG and CA3 cells, while the CA3 recurrent network alone can encode spatial information that requires paired associations, supporting retrieval of short-term memory information based on a spatial pattern completion process (Daumas, Halley, Francés, & Lassalle, 2005; P. E. Gilbert & Brushfield, 2009; J. K. Leutgeb, Leutgeb, Moser, & Moser, 2007; S. Leutgeb & Leutgeb, 2007; Rajji et al., 2006). Nevertheless the synaptic mechanisms responsible for these processes have not been addressed yet.

New data from genetically engineered mice show that the CA3 region might be dispensable for slow, incremental spatial learning, but the full trisynaptic (DG→CA3→CA1) is necessary for rapid one-trial CFC and pattern completion-based memory recall (Liu et al., 2012; Nakashiba, Buhl, McHugh, & Tonegawa, 2009). Further evidence for the involvement of CA3 in memory formation has come from the observation of fast structural changes in Mf synapses (Ruediger et al., 2011) and activation of major transcriptional factors in the CA3 region after rapid contextual learning (Ramamoorthi et al., 2011).

1.3 Synaptic Transmission

1.3.1 The Synapses

The CNS is composed of many billions of cells that communicate between them allowing the transmission and processing of information. In the nineteenth century Ramon y Cajal proposed that neurons work as individual entities and Charles Sherrington coined the term synapses for specialized junctions in between them, which would make communication possible between the individual nerve cells. Since the beginnings of the *Neuron Doctrine*, cells from the nervous system were divided into two very broad categories: nerve cells – **neurons** – and supporting cells – **glia**. Generally, neurons are cells specialized in the transmission of electrical signals; in contrast, glial cell are not capable of electrical signaling. Nevertheless these cells have several important functions in the nervous system. The basic cellular organization of neurons resembles that of other cells, but they have specialized morphology and intracellular organization for transmitting electrical signals. One of the more obvious signs of specialization is their extensive branching. Every neuron has a cell body or **soma**, containing the cell nucleus and other machinery essential for cell function. From the cell body arise the **dendrites**, which are elaborated branched processes that work as primary target for electrical signals coming from other neurons. The axon on the other hand is a projection specialized in transmitting the electrical impulses away from the cell body, forming contacts that allow communication with other cells.

Neuronal communication relies on a process called synaptic transmission. Two different types of synapses can be distinguished based on their mechanism of transmission. (i) At **electrical synapses**, current flows thought specialized membrane channels, the gap junctions. Although electrical synapses are a minority, they are present in every major region of the brain and were shown to be very important during maturation, allowing direct, passive flow of electrical current from one neuron to another (Connors & Long, 2004; Pereda, 2014). In contrast, (ii) **chemical synapses** enable cell-to-cell communication via secretion of neurotransmitters (NTs). The chemical agents released by the presynaptic neuron produce a secondary current flow in the postsynaptic neuron, through the activation of specific receptor molecules (neurotransmitter receptors). The two components of the synapse (pre and post-

synaptic compartments) are very close, yet physically separated by an interval of extracellular space called the **synaptic cleft**.

One essential element of all chemical synapses is the presence of small, membrane-bounded organelles called synaptic vesicles within the presynaptic terminal. These vesicles are filled with NT. Signal transmission in these synapses is initiated when an action potential (AP) travels into the terminal of the presynaptic compartment. The change in membrane potential – depolarization – caused by the arrival of the AP leads to an opening of voltage-gated calcium channels (VGCCs) present at the presynaptic membrane. The opening of these channels causes a rapid increase of the intracellular calcium concentration ($[Ca^{2+}]i$), which triggers a fusion of synaptic vesicles with the plasma membrane of the presynaptic neuron and consequently a release of their content into the extracellular space. Following this exocytosis, NTs diffuse across the synaptic cleft, binding to specific receptors located on the membrane of the postsynaptic neuron. Finally, synaptic vesicles are retrieved via endocytosis in order to recover the releasable pool of vesicles [reviewed in (Littleton, 2006; Schweizer & Ryan, 2006)]. In the postsynaptic side, NTs evoke electrical responses that can cause excitatory or inhibitory postsynaptic potentials (EPSPs or IPSPs, respectively). Whether the postsynaptic actions of a specific NT are excitatory or inhibitory is defined (i) by the ionic permeability of the ion channel the NT affects and (ii) by the present difference between concentration of the permeant ions inside and outside the cell. The summation of EPSPs and IPSPs by a postsynaptic neuron allows a neuron to integrate the electrical information provided by all active synapses at a given time. Whether the summation of the active synaptic inputs leads to the production of an AP in the postsynaptic neuron depends on the balance between excitation and inhibition: if enough depolarization is produced to raise the membrane potential above a threshold, then the postsynaptic cell will produce an AP, otherwise the cell will remain silent [reviewed by (Lisman, Raghavachari, & Tsien, 2007)].

There are two major classes of receptors: (i) those in which the receptor complex is also an ion channel – **ionotropic receptors** (iGluRs) – and (ii) those in which the receptor and the ion channel are separated molecules – **metabotropic receptors** (mGluRs). These two families of receptors influence the postsynaptic potential with very different time courses, producing postsynaptic responses that range from less then a millisecond (for iGluRs) to minutes or hours (in the case of mGluRs). Importantly, a given NT may activate both ionotropic and metabotropic receptors and

produce both fast and slow changes at the same synapse. The action of the NT on postsynaptic receptors is terminated by its enzymatic degradation in the synaptic cleft, by uptake of the NT back into the cell or by diffusion out of the synaptic cleft (where the NT can, for example, be taken up by astrocytes).

1.3.2 The Glutamatergic System
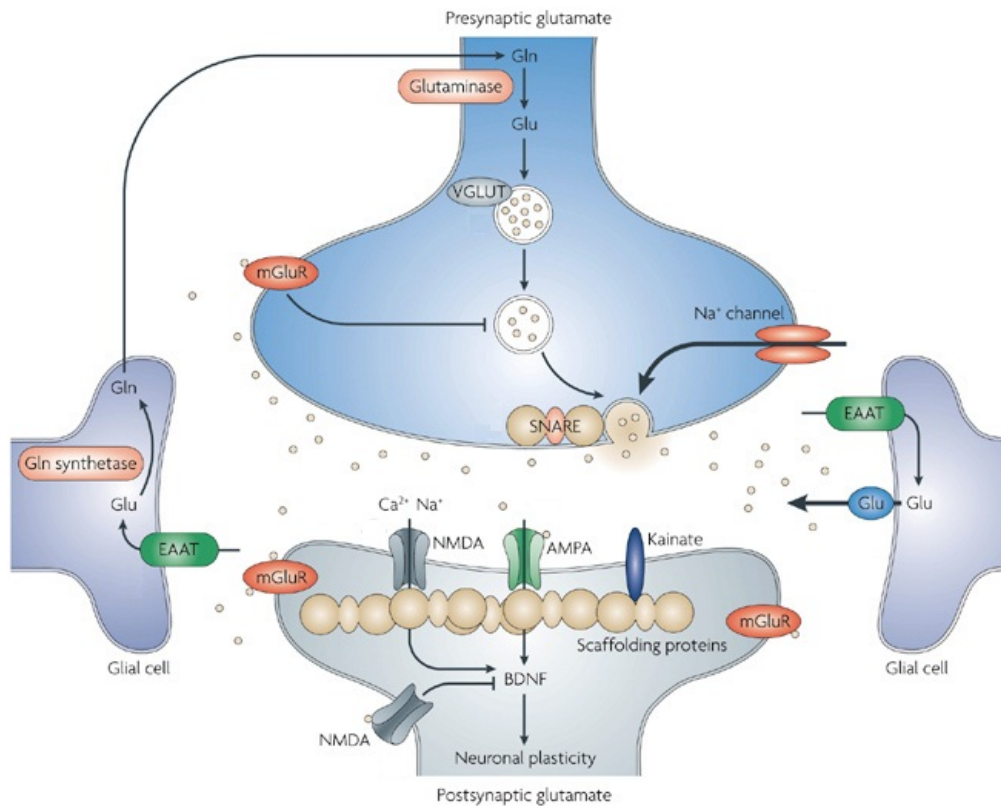
Nature Reviews | Drug Discovery

Figure 1.7. Glutamatergic neurotransmission

Glutamate is packaged into presynaptic vesicles by the VGLUTs and released from the neuron in an activity-dependent manner through interactions with soluble N-ethylmaleimide-sensitive factor attachment receptor (SNARE) proteins. Various glutamate receptors are present on presynaptic and postsynaptic neurons as well as on glial cells. These include both iGluRs (NMDAR, AMPAR and KARs) and mGluRs. The effect of Glu is determined by the receptor subtype, localization and interactions with various scaffolding and signaling proteins in the postsynaptic density (PSD). NMDARs can also exist in extrasynaptic locations. Activation of glutamate receptors results not only in rapid ionotropic effects, but also in long-term synaptic plasticity. mGluRs can be located pre or postsynaptically. Legend: Gln, glutamine; Glu, glutamate; BDNF, brain-derived neurotrophic factor. Figure modified from (Sanacora, Zarate, Krystal, & Manji, 2008)

Glutamate is the most important excitatory NT in the vertebrate central nervous system. This non-essential aminoacid does not cross the blood-brain barrier and therefore needs to be synthesized in the brain. Glutamate is produced from local precursors by neurons. The most prevalent precursor of glutamate is glutamine, which is released by glial cells. Once glutamate is produced in the presynaptic terminal it is packaged into synaptic vesicles by transporters called VGLUT. When it is released into the synaptic cleft, glutamate can be removed by high-affinity glutamate transporters (EAATs) localized in glial cells or at the presynaptic terminals (Divito & Underhill, 2014). Figure 1.7 shows the classical organization of a glutamatergic synapse.

The **iGluRs** are non-selective cation channels abundantly expressed in the postsynaptic density (PSD) at the large majority of excitatory synapses. iGluRs can be divided in three main categories: NMDA receptors (NMDARs), AMPA receptors (AMPARs) and kainate receptors (KARs). These receptors are named after their agonist, respectively, NMDA (N-methyl-D-aspartic acid), AMPA (α-Amino-3-hydroxy-5-methyl-4-isoxazolepropionic acid) and kainic acid. All three types of receptors are integral membrane proteins composed of four large subunits with a central ion channel pore (Mayer & Armstrong, 2004; Smart & Paoletti, 2012). The tetramers are composed of a combination of different subunits: AMPARs are formed by coassembly of GluA1–4 subunits, KARs by coassembly of GluK1–5, and NMDARs by coassembly of GluN1 with GluN2A–D and GluN3A–B. iGluR subunits are modular structures that contain four discrete semiautonomous domains: the extracellular amino-terminal domain (ATD), the extracellular ligand-binding domain (LBD), the transmembrane domain (TMD), and an intracellular carboxyl-terminal domain (CTD) (Traynelis et al., 2010).

In the synapse, iGluRs interact with several auxiliary proteins that regulate their trafficking, turnover, subcellular localization, synaptic stabilization and kinetics. Diverse families of auxiliary subunits, capable of fine-tuning receptor function have been identified for each receptor subtype. For example, the transmembrane AMPA receptor regulatory proteins (TARPs) and the cornichon homologs-2 and 3 (CNIH-2 and CNIH-3) modulate AMPARs. In addition, the proteins neuropilin tolloid-like 1 and 2 (NETO1 and NETO2) modulate the activity of KARs [reviewed in (Kumar & Mayer, 2013)]. NETO 1 was recently shown to also regulate the activity of NMDARs (Straub & Tomita, 2012; Wyeth et al., 2014). The auxiliary subunits can affect multiple aspects of receptor pharmacology, function as well as regulate intracellular trafficking and synaptic localization of iGluRs via direct interactions with the post-synaptic density (PSD)

scaffolding proteins such as the family of membrane-associated guanylate kinases proteins (MAGUKs) (Copits & Swanson, 2012). This family, that includes proteins like PSD-95, SAP102, SAP97, PSD-93, CASK and MAGIs, affects the clustering of glutamate receptors and other receptors with implications to regulating the strength of synaptic transmission (Gardoni, Marcello, & Di Luca, 2009).
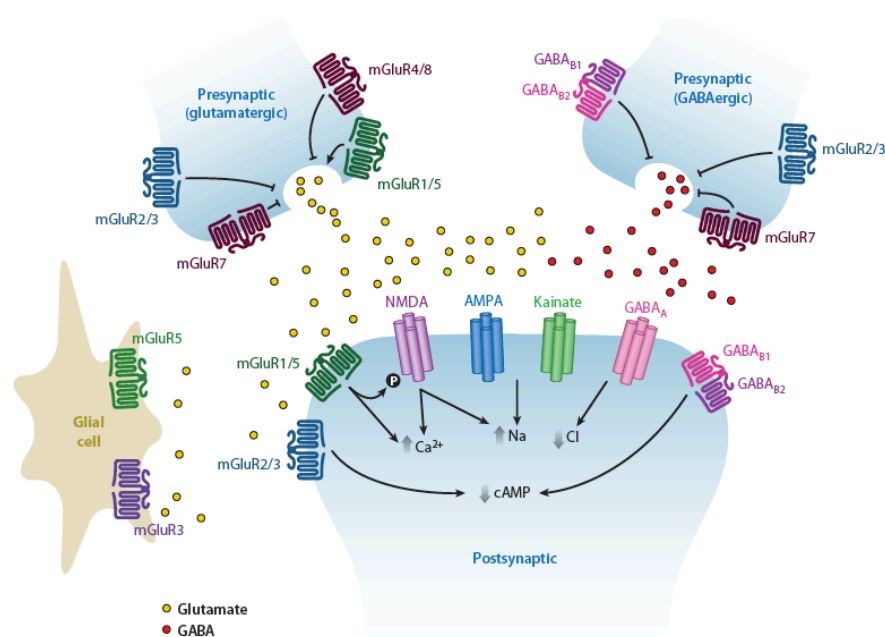
Figure 1.8 Schematic representation of mGluRs and their localization at the synapse

Group I mGluRs (in green) are localized mainly postsynaptically, and group II (blue) and III (red) receptors are localized in presynaptic locations, although exceptions occur. In presynaptic locations, mGluRs 2, 3, 4, and 8 are generally found in extrasynaptic locations, and mGluR7 is highly localized to the active zone. Group II and III receptors inhibit release of glutamate (left, yellow circles) or GABA (right, red circles), whereas group I receptors promote release when present. At the postsynaptic terminal, AMPARs and KARs respond to glutamate with an increase in intracellular sodium or calcium, promoting cell excitability. Group I mGluRs signaling via G_s proteins to increase intracellular calcium; additionally, mGluR5 and NMDA receptors are closely linked signaling partners reciprocally regulated by phosphorylation. Postsynaptic mGluR2/3 and $GABA_{B1/2}$ receptors couple to cAMP inhibition. $GABA_A$ chloride channels (pink) modulate intracellular chloride. Expression of mGluR3 and mGluR5 on glia is now emerging as another key site for mGluR regulation of synaptic activity.

Figure from (Niswender & Conn, 2010).

The eight types of **mGluRs** described are members of the G-protein-coupled receptor family (GPCR) and they can be organized into three subgroups based on the signaling transduction pathways they activate. Figure 1.8 describes the localization of

several subtypes of mGluRs at synapses and their principal actions upon activation. Group I includes mGluRs 1 and 5. These receptors are predominantly postsynaptic and act primarily through activation of phospholipase C (PLC). This classical pathway leads to calcium mobilization and activation of protein kinase C (PKC). In contrast with group I, group II and III mGluRs are coupled predominantly to $G_{i/o}$ proteins that classically lead to adenylate cyclase (AC) inhibition and/or direct regulation of ion channels (activation of K^+ channels and inhibition of Ca^{2+} channels) via liberation of $G_{\beta\gamma}$ subunits. Group II, which includes mGluRs 2 and 3, can be pre- or postsynaptic. Finally the group III includes mGluRs 4, 7 and 8, which are localized mainly presynaptically [reviewed in (Niswender & Conn, 2010)]. Although single mGluRs can bind G proteins, a dimeric organization of mGluRs is required for signaling induced by agonists (Moustaine et al., 2012).

1.3.3 Focus on NMDA Receptors

NMDARs are thought to underlie higher cognitive functions as many NMDAR dysfunctions are reported to be involved in various neurological and psychiatric disorders, such as AD (Fan, Jin, & Wang, 2014; Paoletti, Bellone, & Zhou, 2013). Furthermore, NMDARs exhibit remarkable properties that distinguish them from other types of ligand-gated ionotropic receptors and designate them as essential mediators of brain activity. An important feature of NMDARs is the voltage-dependent Mg^{2+} block of their ion channel, which means that the postsynaptic neuron has to be already depolarized to open NMDARs following activation by glutamate binding (Karakas & Furukawa, 2014). Another important feature is that, besides being permeable to monovalent cations, like Na^+ and K^+, these receptors are also permeable to Ca^{2+}. Moreover NMDAR activation requires the presence not only of glutamate but also of a co-agonist, glycine or d-serine (Traynelis et al., 2010). In addition, NMDARs display an unusually slow activation and deactivation kinetics (due to slow glutamate unbinding), when compared for example to AMPARs. Finally NMDARs have also several allosteric modulatory sites, which give them great sensitivity to the extracellular milieu (for example, to zinc and protons). In summary, NMDARs function as detectors and integrator of coincident activity at the synapse, which makes them capable of converting specific patterns of neuronal activity into long-term changes in synapse structure and function [reviewed in (Paoletti et al., 2013)].

NMDARs exist as heterotetrameric assemblies that typically associate GluN1 subunits with GluN2 subunits or a mixture of GluN2 and GluN3 subunits. The properties vary depending on the exact receptor composition, with each type of subunit affecting the receptor's biophysical, pharmacological and signaling attributes (Figure 1.9) (Paoletti et al., 2013). More importantly, there is evidence that, even at fully mature synapses, NMDARs subunit content might change depending on neuronal activity (Paoletti et al., 2013). The four GluN2 subunits, which are major determinants of the receptor's functional heterogeneity, show strikingly different spatiotemporal expression patterns. Four different genes encode each of the GluN2 subunits: GluN2A, GluN2B, GluN2C and GluN2D. In the adult CNS, particularly in higher brain structures, such as the hippocampus and cortex, GluN2A and GluN2B are the predominant subunits, indicating that they have central roles in synaptic function and plasticity [reviewed in (Paoletti & Neyton, 2007; Traynelis et al., 2010)].
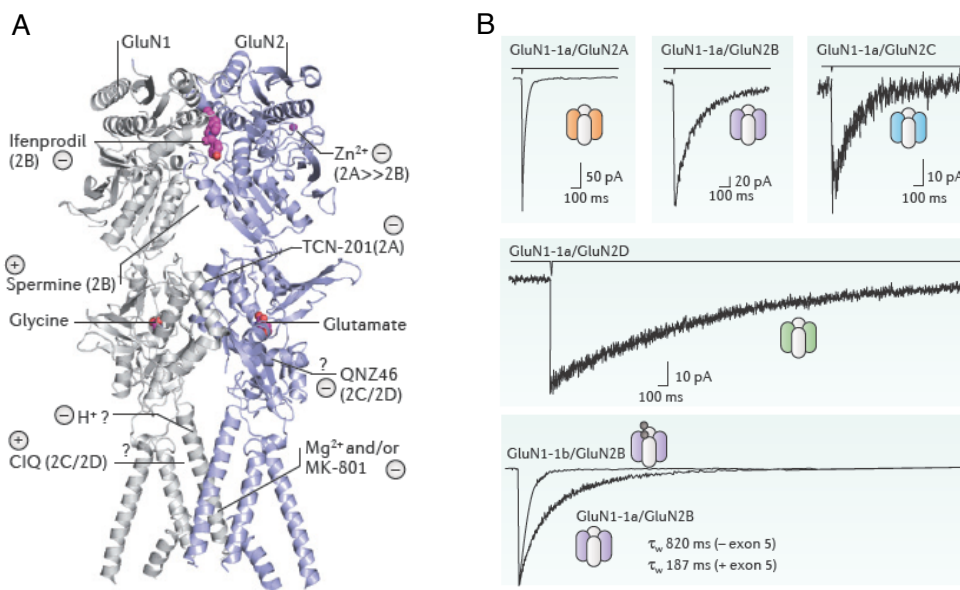
Figure 1.9 Subunit composition determines NMDARs properties

A. NMDARs harbor multiple binding sites for extracellular small-molecule ligands acting as subunit-selective allosteric modulators. A model of a GluN1/GluN2 heterodimer is shown with the + and − signs indicating positive and negative allosteric modulators, respectively. (?) indicate uncertainty about the exact location of the binding site. **B.** Influence of the GluN2 subunit composition on the glutamate deactivation kinetics. NMDAR-mediated currents recorded from transfected human embryonic kidney (HEK) cells were induced by a brief (<5 ms) application of saturating glutamate (1 mM). GluN2A-containing receptors deactivate much faster than all other receptor subtypes. **C.** In the GluN1 subunit the presence of the extracellular N1 cassette (GluN1-1b splice variant) accelerates glutamate deactivation kinetics. Figure adapted from (Paoletti et al., 2013).

1.3.4 Synaptic Input on CA3 Pyramidal Cells

The CA3 pyramidal cells receive glutamatergic inputs from three distinct regions within the hippocampal formation. Information from the EC arrives directly from the PP or indirectly via the Mfs, the axons of granule cells. In addition, other CA3 cells also send axons that contact CA3 pyramidal cells on their apical and basal dendrites. The synapses performed by each of these inputs display differences in terms of position along the dendrites, spine morphology and content of synaptic receptors. These differences are, followed by different synaptic physiology. Synaptic transmission depends not only on the composition of pre- and postsynaptic receptors, but also the structural arrangement of the release machinery.

Large **Mf** terminals exhibit several unique properties that shape neurotransmission at these synapses. EM reconstructions have shown that MfB have multiple release sites (Chicurel & Harris, 1992; Rollenhagen & Lübke, 2010)). According to these reconstructions the number of release sites varies between 18 to 45 with a mean surface area of 0.1 μm^2 and a small distance (around 0.45 μm) between individual sites (Rollenhagen et al., 2007). This short distance between release sites indicates a possible crosstalk occurring either presynaptically via Ca^{2+} diffusion or postsynaptically via glutamate spillover from neighboring release sites. Another feature of the Mf is the very large number of vesicles present at their terminals. The number of vesicles at individual release sites is extensive, which might be important to sustain reliable neurotransmission during high-frequency activity. Although Mf synapses exhibit a very low release probability (p=0.02-0.2), because of their large number of release sites, the EPSCs can reach unusually high amplitude, such as 1nA (Kitzing, Jonas, & Sakmann, 1994) (Bischofberger, Engel, Frotscher, & Jonas, 2006; Lanore et al., 2010). Glutamate released from MfBs mediates fast ionotropic responses at the postsynaptic membrane mainly by activating **AMPARs** (Jonas et al., 1993; Nakagawa, Cheng, Ramm, Sheng, & Walz, 2005). Moreover, postsynaptic **KARs** mediate a slow postsynaptic current at Mf synapses (Castillo, Malenka, & Nicoll, 1997b; Mulle et al., 1998; P. S. Pinheiro et al., 2013). Comparing to other hippocampal synapses, the ThEs of CA3 pyramidal cells present a smaller density of **NMDARs** (Jonas et al., 1993; Rebola, Carta, Lanore, Blanchet, & Mulle, 2011; Rebola, Luján, Cunha, & Mulle, 2008). Glutamate can also act on group I **mGluRs** at the postsynaptic membrane of ThE,

where it leads to the activation of mGluR5 capable to regulate PLC activity via G_q proteins. Activation of PLC results in the hydrolysis of phosphatidylinositol-4,5-bisphosphate (PIP_2) which releases the second messengers 1,2-Diacylglycerol (DAG) and inositol 1,4,5-trisphosphate (IP3). DAG is the physiological activator of protein kinase C (PKC), which in turn activates various intracellular signaling cascades. For example, IP_3 can bind to intracellular IP_3 receptors (IP_3R) on the membrane of endoplasmic reticulum (ER) initiating Ca^{2+} release from the ER lumen into the cytoplasm, promoting the generating complex Ca^{2+} concentration-dependent signals (Piers et al., 2012).

Furthermore, group II mGluRs (mGluR2) are also present in presynaptic terminal compartments (Kamiya, Shinozaki, & Yamamoto, 1996). This raises the question how this receptor might be activated physiologically; if mGluR2 acts as an autoreceptor, the synaptically released glutamate must travel some distance to reach these receptors (Kamiya et al., 1996). Both pre and postsynaptic mGluRs have important roles in Mf synaptic plasticities (Rebola et al., 2008; Yokoi et al., 1996). Endogenous glutamate can also activate presynaptic KARs (Contractor, Swanson, & Heinemann, 2001), leading to the enhancement of AP evoked calcium influx in the terminal, and therefore increased facilitation (P. S. Pinheiro & Mulle, 2008; P. S. Pinheiro et al., 2007; Schmitz, Mellor, Breustedt, & Nicoll, 2003).

In addition to glutamate and some neuropeptides, MfBs contain and release several other neuromodulators such as ATP/Adenosine and zinc (Vergnano et al., 2014). At the presynaptic compartment, Mf synapses display Adenosine A1 receptors (**A1R**). A1Rs are GPCRs, linked to G_o proteins that, when activated, cause inhibition of AC and stimulation of PLC. Postsynaptically, CA3 pyramidal cells express adenosine A2 receptors (**A_{2A}Rs**) (Rebola et al., 2008). A_{2A}Rs are also GPCRs but are normally linked to G_s proteins that are involved in the activation of AC, elevation of cAMP and consequent activation of PKC. The A_{2A}Rs can also sustain a G protein independent signaling pathway by interactions of the C-terminus with accessory proteins (Gsandtner & Freissmuth, 2006; Zezula & Freissmuth, 2008).

Finally, there are several reports that the Mf pathway contains and releases GABA (Sandler & Smith, 1991; Sloviter et al., 1996). Ionotropic $GABA_A$ receptors ($GABA_A$Rs), permeable to Cl^- are found in both pre and postsynaptic membranes of Mf synapses (Bergersen, Ruiz, Bjaalie, Kullmann, & Gundersen, 2003; Ruiz et al., 2003). **$GABA_A$Rs** seem to have a dual role in modulating transmission and LTP at Mf

synapses. In addition, there are metabotropic GABA$_B$ receptors (**GABA$_B$Rs**) at perisynaptic regions of MfBs. Presynaptically, these receptors mediate heterosynaptic depression of Mf transmission when activated by GABA. This activation normally occurs during strong activity and spillover of GABA from adjacent synapses (Vogt & Nicoll, 1999). Like other metabotropic receptors, GABA$_B$Rs also exist as functional dimers (Gaiarsa & Porcher, 2013). Presynaptic GABA$_B$Rs are considered inhibitory as they can trigger the opening of K$^+$ channels, preventing the opening of VGCCs and NT release (Guetg et al., 2009).

1.3.5 Adenosine Neuromodulation

The purine nucleotide adenosine is a component of nucleic acids and plays an important role in cell metabolism. Besides the metabolic role, adenosine can also act as neuromodulator and/or as a homeostatic regulator (Gomes, Kaster, Tomé, Agostinho, & Cunha, 2011) capable of controlling NT release, neuronal excitability and information flow through neuronal circuits. In the CNS extracellular adenosine can either be released through specific channels responsible for equilibrating the levels of adenosine in and out of the cell; or produced extracellularly from ATP by enzymes that can sequentially hydrolyze ATP in ADP (ecto-ATPase), ADP in AMP (ecto-apyrase) and AMP in adenosine (ecto-5'-nucleotidase). Each of these metabolites can activate a specific type of receptor: ATP and ADP are agonists of P2 receptors while adenosine binds P1 receptors [Reviewed in (Fredholm, Chen, Cunha, Svenningsson, & Vaugeois, 2005)] (Figure1.10). Extracellular ATP can have different sources, being released by neurons or glial cells through multiple mechanisms (Chen, Eltzschig, & Fredholm, 2013). Hippocampal neurons can co-release ATP present in synaptic vesicles together with other NTs. There are four types of adenosine receptors (P1 receptors): A$_1$R, A$_{2A}$R, A$_{2B}$R and A$_3$R, but the density of A$_1$R and A$_{2A}$R in the brain is much higher then the remaining ones, suggesting that the impact of adenosine in the CNS might depend mostly on these subtypes of receptors (Fredholm et al., 2005).

As mentioned before, A$_1$Rs activation causes mainly inhibition of the excitatory synaptic transmission via receptors present in the presynaptic terminal (Dunwiddie & Haas, 1985; Dunwiddie & Masino, 2001). This presynaptic effect relies on the inhibition of N-type Ca^{2+} channels (L. G. Wu & Saggau, 1994) but also on the ability of presynaptic A$_1$R to down-regulate the sensitivity of the release machinery (Scanziani,

Capogna, Gähwiler, & Thompson, 1992; Scholz & Miller, 1992). Moreover, these receptors can also be present postsynaptically (controlling NMDARs activation for example) and nonsynaptically (controlling K^+ channels and leading to neuronal hyperpolarization) (de Mendonca, Sebastião, & Ribeiro, 1995; Rebola, Pinheiro, Oliveira, Malva, & Cunha, 2003). A_1R can further be localized in glial cells, both microglia and astrocytes [reviewed in (Chen et al., 2013; Gomes et al., 2011)].

Nature Reviews | Cancer
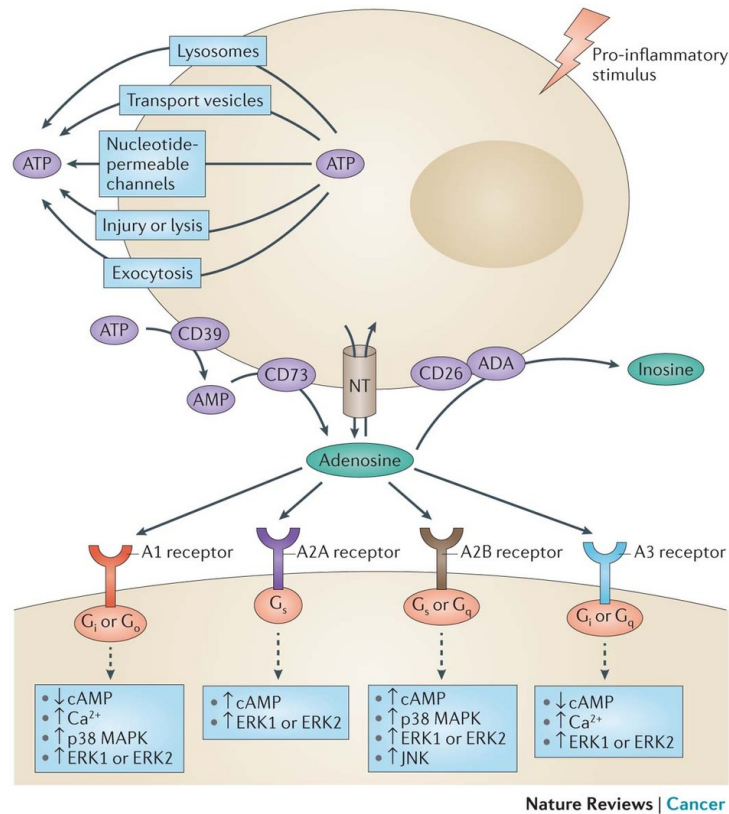
Figure 1.10 Adenosine and Adenosine Receptors

Schematic diagram illustrating the biosynthesis and catabolism of adenosine and the second messenger pathways that are coupled to adenosine receptor subtypes. The occurrence of pathological events can promote an extracellular accumulation of ATP, which is followed by its sequential degradation to AMP by the cell surface enzymes. Extracellular adenosine can bind to four different GPCRs. The stimulation of A1 and A3 receptors can also stimulate the release of calcium ions from intracellular stores. Moreover, all adenosine receptors are coupled to MAPK pathways, including extracellular signal-regulated kinase 1 (ERK1), ERK2 and p38 MAPK. In the extracellular space, adenosine concentrations are controlled by adenosine deaminase (ADA; which catalyses the conversion of adenosine into inosine) and by the activity of nucleoside transporters (NTs). Legend: JNK, JUN N-terminal kinase. Figure from (Antonioli, Blandizzi, Pacher, & Haskó, 2013)

$A_{2A}R$ are preferentially located at synapses (Rebola, Canas, Oliveira, & Cunha, 2005) and, upon activation, these receptors are linked to an activation of AC and PKC. Presynaptically $A_{2A}R$ have been described to counteract the A_1R-mediated inhibition of synaptic transmission. Importantly, $A_{2A}R$ are also present in the postsynaptic compartment were they seem to have an important role in hippocampal synaptic plasticity (Rebola et al., 2008), without altering basal transmission. $A_{2A}Rs$ have also been reported to activate the mitogen-activated protein kinase (MAPK) pathway (Fredholm et al., 2005). It has been shown in several conditions of brain injury that in particular $A_{2A}R$ can undergo increased expression in both neurons and glia (Cunha, 2005; Matos et al., 2012).

1.4 Synaptic Plasticity

Many synapses in the CNS show activity-dependent changes in synaptic strength and therefore modify neural circuit function. At pre-existing synapses, there can be increases or decreases in synaptic efficacy, in response to specific patterns of activation. Modifications can occur both pre- and postsynaptically and can endure for short (milliseconds) but also long (hours or days) periods of time. **Synaptic plasticity** describes all these kinds of alterations and has been proposed to assume a key role in the incorporation of an experience into memory. In line with this, many groups have dedicated efforts to study synaptic plasticity in animals that model neuropsychiatric and neurodegenerative diseases.

Excitatory synapses can express several forms of plasticity simultaneously. Furthermore, different synapses might display very different forms of plasticities. In CA3 pyramidal cells, different glutamatergic inputs display different types of short- and long-term plasticities [reviewed in (Nicoll & Schmitz, 2005)].

1.4.1 Short-Term Plasticity

Diverse forms of short-term modifications have been described in hippocampal synapses (reviewed in (Citri & Malenka, 2008; Regehr, 2012)). Short-term plasticities (STPs) are thought to underlie short-term adaptations to sensory inputs, playing an important role in transient changes of behavioral states and short-lasting forms of memory. Most forms of STPs are triggered by short bursts of activity and they can be mediated by accumulation of Ca^{2+} in the presynaptic terminal (Figure 1.11 B), but also by the type of vesicles present at the presynaptic compartment (Figure 1.11 A). Additionally, postsynaptic mechanisms can also mediate forms of STPs. For instance, Figure 1.11 represents a situation where the number of receptors present at the postsynaptic membrane limits the size of the EPSCs due to saturation of postsynaptic receptors (Foster, Kreitzer, & Regehr, 2002). Furthermore, STP can also depend on the gating properties of postsynaptic receptors, if these receptors desensitize (Figure 1.11 A), they will no longer be available for subsequent activation (Fioravante & Regehr, 2011).

The amount of Ca^{2+} that reaches the multiple low-affinity sites on synaptotagmin and triggers vesicle fusion and NT release depends of several factors [reviewed in (Schneggenburger & Neher, 2005; Südhof & Rothman, 2009)]. One of

these factors is the nature of Ca^{2+}-binding proteins present at the presynaptic bouton: Ca^{2+}-binding proteins with rapid kinetics are particular effective at intercepting Ca^{2+} before it reaches the release sensors, consequently reducing the probability of release [reviewed in (Amici et al., 2009)] . The remaining free Ca^{2+} (residual Ca^{2+}) will be slowly extruded from the terminal being able to affect STPs within few seconds [reviewed in (Fioravante & Regehr, 2011)].
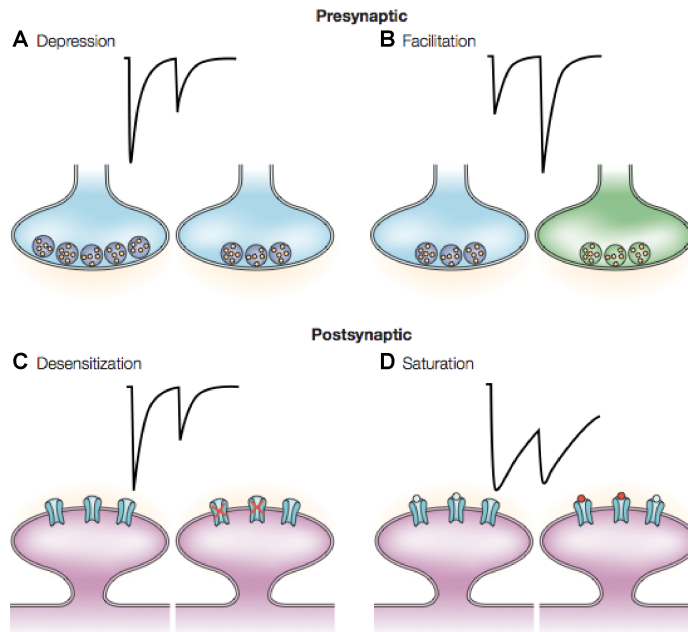

Figure 1.11 Pre and postsynaptic mechanisms of short-term plasticity

Schematized voltage-clamp traces illustrate the influence of two presynaptic mechanisms (A and B) and two postsynaptic mechanisms (C an D) of plasticity on a pair of excitatory postsynaptic currents (EPSCs). Cartoons of presynaptic boutons illustrate possible explanations for presynaptic depression and facilitation and cartoons of postsynaptic spines illustrate desensitization and saturation. **A.** Presynaptic **depression** results in a smaller second EPSC. Fewer vesicles are available for release on the second stimulus than on the first. **B. Facilitation** results in a larger second EPSC. The residual elevation in intracellular calcium (green shading), combined with the influx of calcium in response to the second stimulus, results in enhanced release. **C.** Similar to depression, **desensitization** results in a smaller second EPSC. Under prolonged exposure to transmitter, some receptors can enter a non-responsive state (red crosses, right) and be unable to respond to transmitter released during a second stimulus. **D.** Channels with slow kinetics (such as NMDARs) that experience **saturation** can produce a large amount of current following a second stimulus, despite the smaller incremental amplitude of the second EPSC, owing to summation with the previous EPSC. As displayed in the cartoon, for receptors with high affinity for the transmitter, a population of receptors can remain bound with transmitter (red circles) and therefore be unavailable to respond to the transmitter released in response to a second stimulus. Figure modified from (Blitz, Foster, & Regehr, 2004).

Besides Ca^{2+} dynamics, also the nature and properties of the vesicles present at the different synaptic terminals will influence the forms STPs displayed by those terminals. Rizzoli and Betz 2005 classify synaptic vesicles at the active zone into 3 categories: the reserve pool (or non recyclable pool, NRP), the recycling pool (RP) and the ready releasable pool (RRP). The NRP makes up ~80–90% of the total pool of vesicles and is very difficult to trigger their release. The RP is significantly smaller (~10–15%) and can be released with sustained high-frequency stimulation. The readily releasable pool (RRP) consists of few vesicles (~1%) that seem to be docked and primed for release (Rizzoli & Betz, 2005). The number of vesicles released by a single AP will be highly correlated with size of the RRP; if an AP releases a large fraction of the RRP, a subsequent stimulus delivered before replenishment will lead to the fusion of fewer vesicles.

The delivery of two stimuli within a short interval (20-100ms) can cause that the second EPSC is bigger (paired pulse facilitation) or smaller in size (paired pulse depression) when compared with the EPSC evoked by the fist stimulus. Both A/C and Mf synapses display **paired pulse facilitation** (PPF), but Mf synapses, display greater degree of PPF (Salin, Scanziani, Malenka, & Nicoll, 1996). PPF is though to be caused by residual Ca^{2+} left over from the invasion of the terminal by the first AP. This residual Ca^{2+} contributes to additional release during the second stimulus. The magnitude of this potentiation is inversely related to the initial probability of release (Pr) of the synapse under study and, as previously described, Mf synapses have very low Pr (reviewed in (Evstratova & Tóth, 2014). A synaptic failure occurs when a presynaptic action potential does not lead to an EPSC. When compared with A/C, Mf synapses have a higher **failure rate**, which is related to the low Pr at these synapses. Although the mechanisms responsible for such a low Pr at Mf synapses are not completely known. It has been recently suggested that these synapses work in a loose coupling regime between Ca^{2+} entry and release sensors and, in addition, possess significant amounts of an endogenous Ca^{2+} buffer with fast Ca^{2+} binding kinetics (Vyleta & Jonas, 2014). Both these factors would contribute in part to the reduced initial release probability.

Another very characteristic feature of Mf synapses is their capacity to perform **frequency facilitation**, another form of short-term plasticity. FF describes the increase in synaptic strength caused by modest increases in stimulus frequencies. For example, while stimulating one particular Mf axon, when switching the stimulus frequency from

low (0.1Hz) to intermediate (1Hz), the amplitude of the EPSCs recorded increases strongly up to 7-fold, by a mechanism which is not well understood. The same experiment performed at A/C synapses leads to a facilitation not higher then 1.25fold (Salin et al., 1996). The large extent of STP at Mf synapses is associated with a low initial release probability and supported by a large ready releasable pool (RRP) that provides a reliable support of vesicles during high frequency stimulus (Gundlfinger, Breustedt, Sullivan, & Schmitz, 2010). During high frequency trains of stimulation (> 20Hz), there is an activity-dependent broadening of the APs recorded from MfB (Geiger & Jonas, 2000) that increases the total Ca^{2+} influx.

Another type of short-term plasticity that is very prominent at Mf synapses is **post-tetanic potentiation** (PTP). PTP inducing protocols differ from synapse to synapse. Furthermore the time course of PTP at Mf synapses is different from A/C synapses, lasting over 3 minutes and less than one minute, respectively (Zalutsky & Nicoll, 1990). At Mfs, the induction of PTP is associated with a decrease of PPF, which suggests an increase in Pr (Regehr & Tank, 1991). Residual Ca^{2+} plays an important role in PTP, but might not explain the whole phenomena, as Ca^{2+} levels return to baseline at MfB before Mf EPSCs do (Regehr, Delaney, & Tank, 1994). Alterations of the RRP or PKC activity have been some of the proposed mechanisms [reviewed in (Henze et al., 1999; Regehr, 2012)].

At Mf synapses the diverse forms of STPs can also be mediated by synaptically released glutamate acting on presynaptic glutamate receptors. For example presynaptic KARs that facilitate transmitter release (Lauri et al., 2001; Schmitz, Mellor, & Nicoll, 2001), can enhance the AP evoked Ca^{2+} influx in the terminal during short high frequency trains (Dargan & Amici, 2009; Scott, Lalic, Kullmann, Capogna, & Rusakov, 2008). On the other hand, mGluRs present at presynaptic regions depress transmitter release, most likely via inhibition of VGCCs (Pelkey, Topolnik, Lacaille, & McBain, 2006; Toth, Suares, Lawrence, Philips-Tansey, & McBain, 2000). There is a controversy about the net effect of these two types of glutamate autoreceptors for the unique robust Mf synapses short-term plasticities with research groups reporting KARs effects essential (Lauri et al., 2001; P. S. Pinheiro et al., 2007) and others describing that presynaptic mGluRs are main effectors of auto regulation at this synapse (Kwon & Castillo, 2008a; Scanziani, Salin, Vogt, Malenka, & Nicoll, 1997), especially at lower frequencies. Very recently our lab described that arachidonic acid (AA) released in an activity-dependent manner from the postsynaptic hippocampal CA3 neuron can act as

retrograde messenger. At the presynaptic terminal it induces a robust facilitation of Mf EPSCs over several minutes (Carta et al., 2014). We further show that AA acts by broadening presynaptic APs through the direct modulation of voltage-gated K^+ channels (Kv), which are involved in the repolarization of the terminal after the AP (Carta et al., 2014).

The different forms of STPs present at one synapse both depend and can modulate the Pr. This fact has important consequences in terms of information processing at distinct synapses, because it enables them to act as filters with a broad range of properties. Synapses that have a low initial Pr, such as Mfs, will act as high-pass filters as they will facilitate during high-frequency AP bursts. On the other hand, a burst of activity with low frequency will not be transmitted with the same efficacy. In contrast with low Pr synapses, synapses with an initially higher Pr will depress during high-frequency bursts but reliably relay low-frequency activity, working as low-pass filters (Abbott & Regehr, 2004).

1.4.2 Long-Term Plasticity

More than 50 years ago Donald Hebb proposed that associative memories are formed in the brain by a process of synaptic modification that is capable of strengthening connections between neurons. Synaptic strengthening would depend on the coincidence of pre- and postsynaptic cell activities. Shortly after Bliss and Lomo reported that the repetitive activation, at high frequencies, of excitatory synapses in the hippocampus caused potentiation of synaptic strength that could last for several hours, even days [reviewed in (Mayford, Siegelbaum, & Kandel, 2012)]. Partially because this **long-term portentiation** (LTP) was first described at hippocampal synapses, there was an early assumption that this type of synaptic plasticity could represent a mechanism for memory acquisition. Nowadays it is widely believed that an experience modifies a subsequent behavior at least in part through activity-dependent, long-lasting modifications of synaptic strength (Citri & Malenka, 2008; Pastalkova et al., 2006; Whitlock, Heynen, Shuler, & Bear, 2006). Furthermore is also clear that synaptic strength at excitatory synapses is bidirectionally modifiable by different patterns of activity, meaning most hippocampal synapses that express LTP also display **long term-depression** (LTD) (Malenka & Bear, 2004).
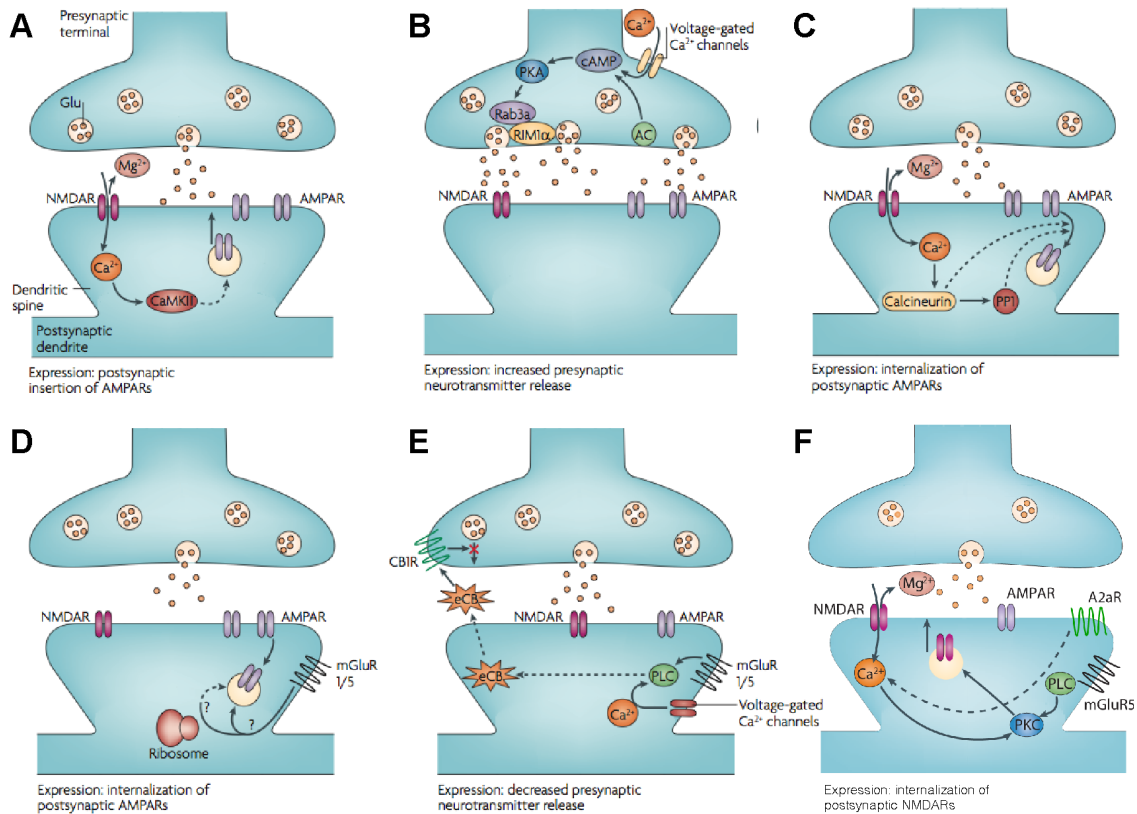
Figure 1.12 Major forms of LTP and LTD at hippocampal synapses.

Well-described forms of LTP and LTD. Highly simplified diagrams of the induction and expression of synaptic plasticity observed in the rodent brain. **A.** NMDAR-dependent LTP has been observed in many different brain regions and is dependent on postsynaptic NMDAR activation and CaMKII for its initiation. The voltage-dependent relief of the magnesium block of the NMDAR channel allows the synapse to detect coincident presynaptic release of glutamate and postsynaptic depolarization. AMPAR insertion into the postsynaptic membrane is a major mechanism underlying LTP expression. **B.** Presynaptic LTP has been best characterized at Mf-CA3 hippocampal synapses. Repetitive synaptic activity leads to the entry of presynaptic Ca^{2+}, which activates a Ca^{2+}-sensitive AC leading to a rise in cAMP and the activation of PKA. This in turn modifies the functions of Rab3a and RIM1α leading to a long-lasting increase in glutamate release. **C.** NMDAR-dependent LTD is triggered by Ca^{2+} entry through postsynaptic NMDAR channels, leading to increases in the activity of the protein phosphatases calcineurin and protein phosphatase 1 (PP1). The primary expression mechanism involves internalization of postsynaptic AMPARs and a downregulation of NMDARs by an unknown mechanism. **D.** mGluR-dependent LTD has been best characterized at hippocampal synapses. Activation of postsynaptic mGluR1/5 triggers the internalization of postsynaptic AMPARs, a process that under some conditions appears to require protein synthesis. **E.** Endocannabinoid-LTD is the most recently discovered form of LTD, and has been observed in many brain regions. Either mGluR1/5 activation, leading to activation of PLC or an increase of intracellular Ca^{2+} (or both), in the postsynaptic neuron initiates the synthesis of an endocannabinoid (eCB). The eCB is subsequently released from the postsynaptic neuron, travels retrogradely to bind to presynaptic cannabinoid 1 receptors (CB1R) and this prolonged activation of CB1Rs depresses neurotransmitter release via unknown mechanisms. **F.** NMDARs-dependent LTP at Mf is induced and expressed

postsynaptically. The activation of CA2+ permeable NMDARs leads to the influx of Ca2+ at the postsynaptic site. mGluRs and A2ARs act synergistically to rise Ca2+ via activation of PLC and consequent activation of PKC. This intracellular cascade will induce insertion of NMDARs at the synapse. Figure adapted from (Kauer & Malenka, 2007)

Figure 1.12 summarizes in a simplistic way the molecular actions involved in several distinct forms of long-term synaptic plasticity that can occur in different regions of the hippocampal formation. Besides LTP and LTD additional two other forms of synaptic plasticity have been identified that provide long-term modifications: homeostatic plasticity and metaplasticity. *Synaptic scaling* is the major form of **homeostatic plasticity,** refers to the capacity of neurons to regulate their own excitability relative to network activity. This means that prolonged decreases in overall activity cause a net up scaling of the total synaptic strengths. In contrast prolonged increases in activity will cause scaling down of the synaptic strengths (Abraham & Bear, 1996; Heynen, Abraham, & Bear, 1996; Hulme, Jones, & Abraham, 2013). The time scale of this plasticity is much slower then the one of the LTP and LTD described in figure X. **Metaplasticity**, described as the plasticity of synaptic plasticity, it refers to the effects that prior activity can have on the capacity of synapses to express long-term plasticity [reviewed in (Turrigiano & Nelson, 2004)]. LTD is beyond the scope of this thesis, we will mainly focus on the study of forms of LTP present at synapses of CA3 pyramidal neurons.

The three glutamatergic inputs arriving to hippocampal CA3 neurons display different forms of long-term synaptic plasticity. A/C synapses display a classical form of LTP, dependent of NMDARs activation. Experimentally this LTP can be achieved by application of a high-frequency tetanic (HFS) stimulation to the synapses or using a pairing protocol, where the postsynaptic cell is directly depolarized (allowing the Mg^{2+} blockage of NMDARs to be released) while low-frequency synaptic activation is sustained. A third method to achieve long-term plasticities at S/C and A/C synapses is to induce afferent stimulation within a discrete window prior or after firing of the postsynaptic cell (Dan & Poo, 2006; Kobayashi & Poo, 2004). This protocol is called spike-timing dependent plasticity (STDP) and LTP is normally induced when stimulation of presynaptic fiber(s) happen before the postsynaptic cell fires [for review see (Caporale & Dan, 2008; Feldman, 2012)]. LTP at A/C synapses (Figure 1.12 A) cells has been shown to be associative, meaning that both pre- and postsynaptic cells

are necessary (Chattarji, Stanton, & Sejnowski, 1989; Hunt, Puente, Grandes, & Castillo, 2013; C. O. Martinez, Do, Martinez, & Derrick, 2002). The NT release from the presynaptic terminal is coupled with depolarization of the postsynaptic neuron and activation of NMDARs (Zalutsky & Nicoll, 1990). Moreover, the large NMDAR-dependent increase in dendritic spine Ca^{2+} leads to activation of intracellular signaling cascades involving a number of protein kinases, most notably CaMKII (Hell, 2014; Lisman, Yasuda, & Raghavachari, 2012). Activation of kinases leads to an increase in the single-channel conductance of synaptic AMPARs and more importantly, promotes the incorporation of additional AMPARs into the membrane. The new synaptic AMPARs are readily associated to auxiliary proteins, which interact with PDZ domain-containing proteins such as PSD-95 promoting a stabilization of these complexes at the synapse. At the same time, structural changes within the synapse occur, such as increase of size of the PSD. For example, at S/C synapses alterations of the size of PSD are accompanied with alterations of the morphology of dendritic spines (Kasai, Fukuda, Watanabe, Hayashi-Takagi, & Noguchi, 2010; Matsuzaki, Honkura, Ellis-Davies, & Kasai, 2004; Tønnesen, Katona, Rózsa, & Nägerl, 2014). Alterations in the postsynaptic compartment are believed to drive an increase in the size of the presynaptic active zone, such that the potentiated synapses can be 'permanently' enlarged [reviewed in (Citri & Malenka, 2008)]. Experimentally many protocols can trigger LTP that can last for several hours. The maintenance of these changes depends on *de novo* transcription and local dendritic protein synthesis in order to supply the proteins necessary for maintaining synaptic strength (Sutton & Schuman, 2006).

In contrast with both A/C synapses on CA3 neurons and S/C on CA1 neurons, Mf synapses display a form of LTP that has been shown to be non associative, non-cooperative and non-Hebbian (Nicoll & Schmitz, 2005; Zalutsky & Nicoll, 1990). Figure 1.12 B schematically represents this form of LTP that does not depend on NMDARs which, as described above, are responsible for coincident detection of pre- and postsynaptic activity that triggers subsequent changes in synaptic strength (E. W. Harris & Cotman, 1986). Nevertheless, NMDARs are present at Mf synapses (Weisskopf & Nicoll, 1995). At MfB, the repetitive synaptic activity leads to the entry of presynaptic Ca^{2+} via VGCC, which activates a calcium-sensitive AC producing cAMP (Weisskopf, Castillo, Zalutsky, & Nicoll, 1994). The rise in the levels of cAMP will lead to activation of PKA that in turn modifies Rab3a and RIM1 functions, leading to a long-lasting increase in glutamate release (Castillo et al., 1997a), [for review see (Nicoll &

Schmitz, 2005)]. This type of LTP is triggered and expressed presynaptically and is preceded by a characteristic PTP lasting around 5 minutes after the induction protocol (Reid, Dixon, Takahashi, Bliss, & Fine, 2004). Both KARs activation in the presynaptic membrane, and Ca^{2+} released from internal stores are thought to play a role in Mf presynaptic LTP (Bortolotto, Lauri, Isaac, & Collingridge, 2003; Contractor et al., 2001; Lauri et al., 2001; P. S. Pinheiro et al., 2007).

Our lab and others have observed that a robust LTP of NMDA-EPSCs but not of AMPA-EPSCs can be induced with short bursts of presynaptic stimulation at Mf-CA3 synapses (Kwon & Castillo, 2008b; Rebola et al., 2008) (Figure 1.12 E). This selective LTP of NMDA-EPSCs, induced with physiologically relevant patterns of stimulation, provides clear evidence that synaptic NMDARs can undergo activity-dependent long-term modifications with mechanisms different from the ones responsible for LTP of AMPARs. The Mf NMDARs LTP induction depends on the Ca^{2+} influx through NMDARs, but it requires the activation of both postsynaptic adenosine $A_{2A}R$ and mGluR5 (Rebola et al., 2008). The molecular mechanism by which $A_{2A}R$ may be essential to this form of LTP is not fully understood. $A_{2A}R$ might play an important role in the amplification of Ca^{2+} accumulation (Tebano et al., 2005). Activation of postsynaptic mGluR5 leads to activation of G_s proteins and PLC with consequent PKC-dependent recruitment of NMDARs to the plasma membrane at the synapse (Kwon & Castillo, 2008b; Rebola et al., 2008).

Considering the importance of NMDARs for hippocampal function (Kishimoto, Nakazawa, Tonegawa, Kirino, & Kano, 2006; Nakazawa et al., 2002; Rajji et al., 2006) it is relevant to also study this form of plasticity in our disease model. It is not completely clear what role Mf LTP plays in the behaving animal, as much of the work has been done in slices. Some reports have described associative plasticity between Mf and A/C synapses *in vivo* (Derrick & Martinez, 1994) and *in vitro* (Hunt et al., 2013; Kobayashi & Poo, 2004; Sachidhanandam, Blanchet, Jeantet, Cho, & Mulle, 2009) with the induction of LTP in A/C synapses being boosted by trains to a single Mf input. Furthermore, this form of NMDARs LTP at Mf is responsible for a metaplastic switch that makes Mf synapses competent to generate NMDARs-dependent form of LTP of AMPA EPSCs similar to the one of A/C and S/C synapses (Rebola et al., 2011). Rebola *et al.,* also showed an increase in information processing that is beyond the plasticity *per se,* as the metaplastic switch allows a strong reinforcement of Mf synapses that undergo recurrent activation in an NMDARs-dependent manner (Rebola

et al., 2011). More recently a mechanism of heterosynaptic metaplasticity between Mf and A/C synapses has been described (Hunt et al., 2013), broadening the degree of flexibility in the information processing at CA3 pyramidal cells. NMDARs metaplasticities described at the Mf synapse might tune the involvement of the DG in learning process. In line with this, also the ahead described short-lived DPE at Mf synapses can change the threshold for induction of the presynaptic form of LTP observed at these synapses (Carta et al., 2014).

1.5 Synaptic Dysfunction in Alzheimer's Disease

1.5.1 Alzheimer's Disease as a Synapse Failure

The most recent version of the **amyloid hypothesis (**or Aβ hypothesis) suggests that AD dysfunction arises from synaptic toxicity mediated by soluble microaggregates (oligomers) of Aβ, leading to synaptic dysfunction and synapse loss (Cleary et al., 2005; Haass & Selkoe, 2007; Klyubin, Cullen, Hu, & Rowan, 2012; Lesné et al., 2006; Selkoe, 2002; Shankar et al., 2007; Tanzi, 2005). The main difference of the new theory in relation to the early versions is that previously the adverse effects were attributed to the Aβ plaques surrounding dendrites, axons and glia (Hardy & Higgins, 1992; Selkoe, 1991). Over the last decade many publication have shown that Aβ peptides exert several neurotoxic actions in rodents by two different significantly different experimental paradigms:

1) **acute application of microaggregates of Aβ peptides** to Wt neurons. There have been different variations concerning the nature of the Aβ peptides as well as on the type of neuronal preparation. Peptides can be synthetic, isolated from human brain or naturally secreted by specific cell lines. In addition, the available literature shows Wt neurons exposed to different Aβ species in neuronal preparations that range from dissociated cultures to acute brain slices or even in-vivo preparations (infusions of peptides).

2) **chronic Aβ production in transgenic mice** that express FAD mutations of APP and/or PS1 or 2 over long periods of time.

Both experimental paradigms increase Aβ concentrations, but the resulting pathological effects of this increase are substantially different between the two cases [for review see (Selkoe, 2011; Sheng, Sabatini, & Sudhof, 2012)]. For the work of this thesis we used a chronic model of Aβ exposition, the APP/PS1 animal. Nevertheless we will introduce the main insights obtained by acute Aβ peptide applications [reviewed in (Haass & Selkoe, 2007)]. The origin and concentration of toxic forms of Aβ used on AD research is extremely diverse [reviewed and discussed in (S. Li, Shankar, & Selkoe, 2010a; Mucke & Selkoe, 2012)]. Regardless of that, many species of Aβ oligomers have the ability to impair LTP (Cleary et al., 2005; Cullen, Wu, Anwyl, & Rowan, 1996; Jo et al., 2011; Klein, 2002; Townsend, Shankar, Mehta, Walsh, & Selkoe, 2006; Q. Wang, Rowan, & Anwyl, 2004) while they leave LTD unaffected or, in some reports,

enhanced (Hsieh et al., 2006; Shankar et al., 2007; 2008; H.-W. Wang et al., 2002). When applied *in vivo* Aβ peptides can also impair rodent spatial memory (Haass & Selkoe, 2007; Walsh et al., 2002). In line with the effects on LTP and LTD, oligomers also lead to a structural loss of synapses (Hsieh et al., 2006; Lacor et al., 2007; Shankar et al., 2007; 2008; Wei et al., 2010), that seems to be mediated by activation of caspases (D'Amelio et al., 2011; Jo et al., 2011; Z. Li et al., 2010b; Talantova et al., 2013). Synapse loss, which is the anatomical feature that best correlates with cognitive deficits in human AD (Terry et al., 1991), is likely a morphological consequence of the synaptic dysfunction that begins early in the disease.

The deleterious effects observed at the synapses after application of Aβ to Wt neurons assumes the existence of an Aβ synaptic or extrasynaptic receptor. Indeed, many of the synaptic receptors have been proposed as candidates, for example, NMDARs (De Felice et al., 2008; Wei et al., 2010), VGLUT (S. Li et al., 2009), mGluR5 (Renner et al., 2010; Snyder et al., 2001), α7-nicotinic acetylocoline receptors (nAchR) (H. Y. Wang et al., 2000) and cellular PrP (Laurén, Gimbel, Nygaard, Gilbert, & Strittmatter, 2009). This last one, the PrP receptor (PrPR), has gained a lot of interest since it was observed that Aβ pathology can spread during the time course of months in mouse brain, after infusion of Alzheimer's brain extracts (Eisele et al., 2010; Kane et al., 2000). These experiments suggested a "prion-like" mechanism for AD, in which Aβ conformation is capable of nucleating conformational changes of endogenous normal Aβ, but the role of PrP and PrPR in synaptic transmission remains very controversial (Cissé et al., 2011; Kessels, Nguyen, Nabavi, & Malinow, 2010; Laurén et al., 2009; Um et al., 2013).

Several types of **transgenic AD models** allow the study synaptic physiology during the process of chronic deposition of Aβ into amyloid plaques. Given the acute toxic effects of exogenous Aβ application it is surprising that almost no animal model displays neuronal cell death, even at advanced age/accumulation of senile plaques. Nevertheless, animal models overexpressing APP or both APP and PS show a reduction in spine density, particularly close to the senile plaques (Perez-Cruz et al., 2011; Spires & Hyman, 2005). We will focus in particular on transgenic animals that model the amyloidosis aspect of AD.

Recently Marchetti and Marie have compiled a comprehensive review about the synaptic alterations (short- and long-term plasticities) described in the various models of AD at the different hippocampal subfields: DG, CA3 and CA1 (Marchetti & Marie,

2011). Overall, many reports found that AD transgenic animals display abnormal synaptic transmission, and impairments in LTP and LTD, even before plaque deposition (P. F. Chapman et al., 1999; Hsia et al., 1999). This review pools together several contradictory results within different or the same region of the hippocampus analyzed and discusses possible explanations for that. Importantly the authors point out that *some crucial aspects of hippocampal synaptic function, such as CA3 transmission and plasticity have been almost, if not completely, ignored* (Marchetti & Marie, 2011). Reports about alterations in the basal synaptic transmission at CA1 synapses provide diverse findings. Some publications report no alterations of input/output curves (I/O) (P. F. Chapman et al., 1999; Trinchese et al., 2004), while others do (D'Amelio et al., 2011; Fitzjohn et al., 2001). The same occurred in the case of AMPAR/NMDARs ratios with reports showing a reduction of NMDARs component ((Cissé et al., 2010; D'Amelio et al., 2011; Hsia et al., 1999) in contrast to the results from Saganich *et al.* (Saganich et al., 2006). Regarding the LTP at S/C fibers several papers described deficits, but without agreement about the age of onset of these LTP impairments [for review see (Marchetti & Marie, 2011; Sheng et al., 2012)]. Focusing on results obtained from our APP/PS1 animal model, there have been reports of LTP deficits in PP synapses into the DG (Yoshiike et al., 2008) as well as in CA1 S/C synapses (Fitzjohn et al., 2010; Gureviciene et al., 2004; Um et al., 2013). At the beginning of my doctoral work, there were no reports on putative alterations of synapses in the CA3 region. In 2010, Witton *et al.* showed that Mf synapses of CA3 pyramidal cells display short-term and long-term plasticity deficits at the late stage of 24 months (Witton, Brown, Jones, & Randall, 2010).

1.6 Objectives

Although CA3 and DG are both unaffected by the formation of plaques, tangles and neuronal loss until a very late stage of AD in humans [reviewed in (Ohm, 2007)] it has been found that the region corresponding to DG and CA3 displays reduced volumes in humans with MCI compared to age-matched healthy controls (Hanseeuw et al., 2011; Yassa et al., 2010). Furthermore, deficits in pattern separation (described as capacity to recognize differences between very similar events) have been portrayed as one of the first symptoms of amnesic MCI and can be correlated with hyperexcitability of DG/CA3 (Yassa et al., 2010). Both, the DG-CA3 and CA3-CA3 synaptic connections are known to be essential for this process (Bakker, Kirwan, Miller, & Stark, 2008; J. K. Leutgeb et al., 2007; S. Leutgeb & Leutgeb, 2007). In mice it has further been shown that the CA3 region plays an important role in terms of rapid acquisition of episodic memory and associative retrieval of spatial information [reviewed in (Nakazawa et al., 2004)].

The contradictory indications of a lack of deposits (in CA3 and DG) but an impaired function of DG/CA3 could be explained by recent findings suggesting that alterations of synaptic transmission precede neuronal degeneration in the progression of AD. Therefore our aim was to study synaptic transmission, between these two hippocampal regions (DG-CA3) and the recurrent CA3-CA3 connections, in the early form of a chronic mouse model of AD. Hippocampal CA3 pyramidal cells additionally constitute a unique model to assess pre and postsynaptic effects of chronic amyloid deposition, as they receive inputs with very distinctive synaptic characteristics. Our project aimed to characterize the initial structural and functional deficits of glutamatergic synaptic transmission in hippocampal CA3 pyramidal cells of APP/PS1 mouse model of AD. Using APP/PS1 animals at 6 months of age, when the impairments in episodic memory (Bonardi et al., 2011; Kilgore et al., 2010; Um et al., 2013) occur without apparent amyloid deposition in the hippocampus, we specifically aimed to:

- correlate the behavioral deficits that APP/PS1 mice which have been described at 6 months of age with alterations in short- and long-term plasticities at both Mf and A/C synapses;

- provide insight and mechanistic understanding about the deregulation of synaptic function and alterations of dendritic spine morphology of two different types of synapses present on the same CA3 pyramidal cells;
- unravel if chronic deposition of Aβ peptides can alter the content of specific glutamate receptors or subunits at CA3 pyramidal cells in the AD mouse model and explain the deficits in NMDAR-dependent plasticities;
- understand if pharmacological approaches known to rescue behavioral deficits in AD mice models could modulate the deficits in synaptic plasticities.

Chapter 2

MATERIALS AND METHODS
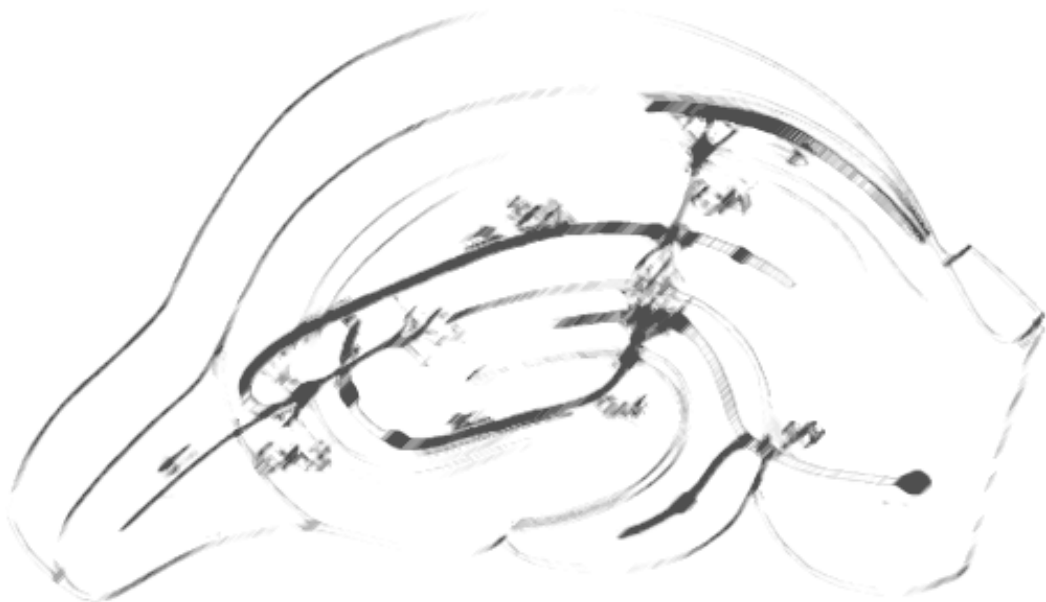
2.1 Animals

The APP/PS1 mouse line was obtained from Jacksons Lab and used in all of the experiments described. The breeding and all experiments were performed in agreement with ethically approved standard procedures of the European and French directives 2010/63/EU. The colony was maintained as a hemizygote by crossing transgenic female mice to B6C3F1/J male mice. Throughout all their life littermate male mice were housed in groups ranging from 4 to 10 per cage with free access to water and food. The large, transparent Plexiglas cages were kept in a temperature-regulated room on a 12 hours light/dark cycle, and protected from the exterior pathogens by a filter. All experiments were performed in the light phase of the circadian cycle and all animals were 6 months of age.

A full description of the generation of the APP/PS1 mouse model for Alzheimer's disease can be found at *The Jackson Laboratory* website (http://jaxmice.jax.org/strain/005864). Briefly, the APP/PS1 double transgenic mice express a chimeric mouse/human amyloid precursor protein (Mo/HuAPP695swe) and a mutant human presenilin 1 (PS1-dE9) both directed to CNS neurons (Jankowsky et al., 2001). The two expression plasmids (Mo/HuAPP695swe and PS1-dE9) were designed to each be controlled by independent mouse prion protein (PrP) promoter elements, directing the transgene expression predominantly to CNS neurons. Both transgenes were inserted in a single locus. The Mo/HuAPP695swe transgene expresses a "humanized" mouse APP gene modified at three amino acids to reflect the human residues and further modified to contain the K595N/M596L mutations linked to familial Alzheimer's. The PS1-dE9 transgene expresses a mutant human presenilin 1 carrying the exon-9-deleted variant (PSEN1dE9) associated with familial Alzheimer's disease. The transgenic mutant human presenilin protein (PS1-dE9) in high levels displaces detectable endogenous mouse protein (Jankowsky et al., 2004).

2.2 Drugs

Unless stated differently all chemicals and salts were purchased from Sigma-Aldrich. The drugs used during the electrophysiology experiments are listed in Table 1.1. All compounds were bought in the water-soluble form, in case it was not possible they were dissolved in dimethyl sulfoxide (DMSO) at the maximum concentration.

2.3 Electrophysiology Recordings

2.3.1 General Principles of the Patch-Clamp Technique

In 1991 Bernd Sakmann and Erwin Neher received the Nobel Prize in Physiology and Medicine for their development of the patch-clamp technique. Their work made possible to record currents of single ions channels proving their involvement in fundamental cell processes such as action potential conduction. Especially in neuroscience, the physiology of ion channels has always been a major topic of interest. This method can be applied to study the current flowing through individual ion channels but also across the whole plasma membrane of excitable cells, in particular, neurons.

Generally patch-clamp techniques use a glass micropipette that has an open tip diameter of about one micrometer. The interior of the pipette is filled with a solution matching either the ionic composition of the bath solution, as in the case of cell-attached recordings, or the cytoplasm for whole-cell recordings. A chloride-coated silver wire is placed inside the micropipette contacting with this solution. Currents fluxing through the channels can flow into the micropipette and hence be recorded by the electrode that is connected to a highly sensitive differential amplifier. The micropipette is pressed against a cell membrane of a living neuron and gentle suction is applied to assist in the formation of a high resistance seal between the glass and the cell membrane (Gigaseal). The high resistance of this seal allows to electronically isolate the currents measured across the membrane patch with little competing noise and it provides some mechanical stability to the recording. The neuron can be kept in this configuration, named "cell-attached", or the membrane under the micropipette tip can be ruptured by application of additional brief suction pulses. The new configuration, where the interior of the micropipette becomes continuous with the cytoplasm, is called "whole cell" (Figure 2.1). Although a hole is created in the membrane the high resistance seal between the membrane and the micropipette is maintained. The whole-cell configuration can be used to measure currents flowing across the membrane (voltage-clamp mode) or to follow the membrane potential (current-clamp mode) under different conditions. Although the whole-cell patch clamp configuration allows the control of the intracellular environment, it is important to note that it also leads to a disadvantageous washout of putatively important cytosolic factors.
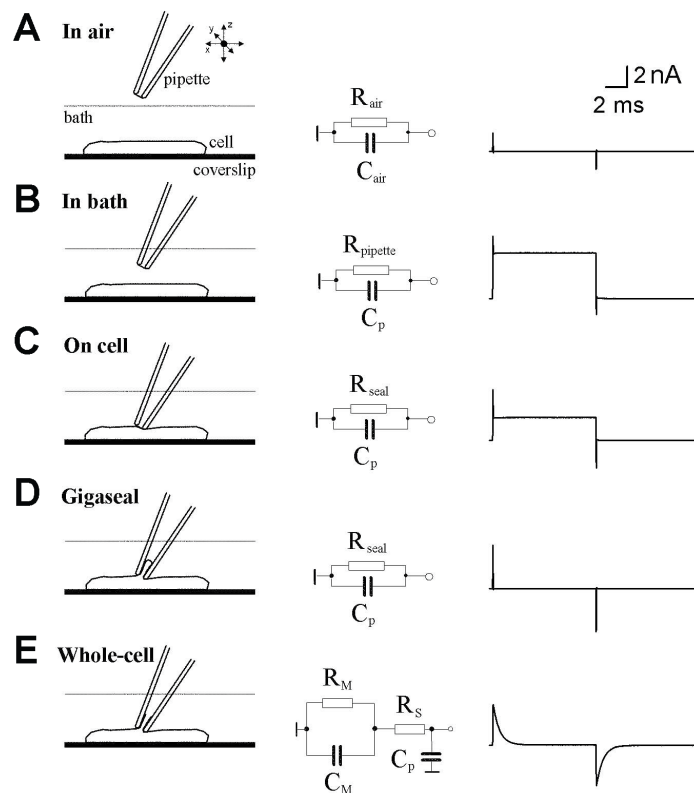
Figure 2.1.   Illustration of the several steps needed for establishing the whole-cell recording configuration

The procedure of preparing the whole-cell configuration is decomposed into 5 states: **A.** *In air*, **B.** *In bath*, **C.** *On cell*, **D.** *Gigaseal* and finally **E.** *Whole-cell*. The left column illustrates position of the patch-pipette with respect to the cell and the bath solution in a given state. Mutual arrangement of the pipette, cell membrane and the bath results in equivalent electrical circuits is shown in the middle column. The right column displays typical current responses to the square wave voltage stimulation. The equivalent circuits consist of two elements with the resistive element describing the resistance in the air (R_{air}), the resistance of the patch-pipette ($R_{pipette}$) or the resistance of the seal between the membrane and the pipette (R_{seal}) and the capacitive element describing the capacitance over the air (C_{air}) or the capacitance of immersed part of the pipette (C_P). In the "Whole-cell" configuration the number of elements in the equivalent circuit increases to four with the membrane resistance (R_M), the membrane capacitance (C_M), the series resistance (R_S) and the parasite capacitance (C_P). Figure adapted from (Novák & Zahradník, 2005).

Voltage-clamp allows the experimenter to "clamp" the membrane at a defined potential (the holding potential) by an electronic feedback circuit. In this condition, when the membrane voltage is different from the command potential, the amplifier injects current into the neuron to maintain the holding potential. The currents recorded will therefore be an accurate representation of the ionic current flowing across the

membrane under study in response to any voltage step. Many patch clamp amplifiers do not use true voltage clamp circuitry but instead are differential amplifiers that use the bath electrode to set the zero current level.

In contrast, in the current-clamp configuration the membrane potential is not fixed (there is no voltage clamp) and the experimenter can study how the cell membrane potential responds to different current injections. This configuration resembles a nearly physiological condition and is very suitable to study cell/circuit excitability and the properties of spikes. However, a detailed study of synaptic conductance is difficult in current-clamp, because a change in the membrane potential can in return alter the function of some ion channels. For example, voltage dependent ion channels have gating mechanisms that respond to membrane potential variations. Furthermore some synaptic channels have the ion flow restricted by cytosolic factors at certain membrane potentials (NMDAR, for example). All electrophysiology experiments described in this thesis were therefore performed in whole-cell voltage-clamp configuration.

2.3.2 Acute Brain Slice Preparation from Adult Animals

Mice were anesthetized with a ketamine (75mg/Kg; Kétamine 500, Virbac) and xylazine (10mg/Kg; Rompum 2%, Bayer Healthcare) mix. After verifying absence of pain reflexes, mice were intracardiacaly perfused with ice-cold oxygenated "cutting" solution composed of 200mM of sucrose, 20mM glucose, 0.4mM $CaCl_2$, 8mM $MgCl_2$, 2mM KCl, 1.3mM NaH_2PO4, 26mM $NaHCO_3$, 1.3mM ascorbate, 0.4mM pyruvate and 3mM kynurenic acid (pH 7.3). When the solution coming out of the heart was free of blood (30 sec to 1min after starting the perfusion) the mice were decapitated and the head immersed in ice-cold cutting buffer. The brain was quickly dissected and slices of 350 μm were cut using a Leica vibratome (Leica VT 1200S) in the same solution. The slices were kept for 20min, in an oxygenated "resting" artificial cerebrospinal fluid (aCSF) containing 110mM NaCl, 2.5mM KCl, 0.8mM $CaCl_2$, 8mM $MgCl_2$, 1.25mM NaH_2PO_4, 26mM $NaHCO_3$, 0.4mM ascorbate, 3mM pyruvate and 14mM glucose (pH 7.3) at 33°C in the presence of kynurenic acid (2mM). This drug blocks all glutamatergic inputs to minimize the cell depolarization and excitotoxicity during the cutting and initial resting procedure. After this period of incubation the slices were

transferred into another "resting" aCSF, now without kynurenic acid and left at room temperature (24-26ºC) for a maximum of 6 hours after cutting.

The quality of the slices was found to be crucial for a positive outcome of our experiments. We optimized the composition our cutting and resting solutions in order to achieve best possible cell health and recording stability. As in many other laboratories, we used sucrose to substitute NaCl in the cutting solution. This replacement is shown to decrease neurotoxic effects of passive chloride influx, swelling and lysis of neurons that occur during slicing procedure. Our solutions were also supplemented with an antioxidant (ascorbic acid 0.4mM) to reduce oxidative cellular injury, such as mitochondrial damage and membrane lipid peroxidation (Keller et al., 1998). To offset the rapid depletion of ATP that occurs right after decapitation and during all slicing procedure pyruvate (3mM) was also added to our solutions.

2.3.3 Patch-Clamp recording from CA3 pyramidal cells

To perform patch-clamp recordings from hippocampal CA3 cells, brain slices were transferred to a recording chamber in which they were continuously superfused with oxygenated (95% O_2 and 5% CO_2) aCSF composed by 125mM NaCl, 2.5mM KCl, 2.3mM $CaCl_2$, 1.3mM $MgCl_2$, 1.25mM NaH_2PO_4, 26mM $NaHCO_3$ and 14mM glucose (pH 7.4). Before starting the recording the slices were washed for 10min to remove the excess of Mg^{2+} of the resting solution. All recordings were performed at room temperature from visually identified CA3 pyramidal cells (Figure 2.2) at the deepest layers below the surface of the slices to ensure recordings of good quality from healthy cells. Cells were identified by differential interference contrast (DIC) microscopy using an Olympus fixed stage upright microscope (BX51WI) equipped with a 40x magnification immersion objective. This optical microscopy illumination technique is very important to enhance the contrast of otherwise transparent samples, such as neurons and brain tissue. All recordings were performed with patch pipettes pulled from borosilicate glass capillaries (Harvard Instruments, GC150F-10) using a P-97 Micropipette Puller (Sutter Instruments) to have a resistance of 3 to 4 MΩ when filled with the intracellular solution. The majority of the recordings was acquired in low EGTA levels, and unless differently stated, were performed with a cesium methanesulfonate based solution containing $CsMSO_3$ 140mM, $MgCl_2$ 2mM, NaCl 4mM, EGTA 0.2mM, P-creatine 5mM, $ATPNa_2$ 3mM, GTP 0.4mM, HEPES 10mM (pH 7.2). For particular

experiments such as the AMPAR/NMDAR ratios the quantity of EGTA was elevated to 10mM, and the intracellular solution composition was the following: $CsMSO_3$ 120mM, $MgCl_2$ 2mM, $CaCl_2$ 3.75mM, NaOH 6mM, EGTA 10mM, P-creatine 5mM, $ATPNa_2$ 3mM, GTP 0.4mM, HEPES 10mM (pH 7.2). The access resistance of the recordings was always inferior 20 MΩ and recordings were discarded from analysis if the resistance changed by >20% over the course of the experiment. Recordings were made using an EPC 10.0 amplifier (HEKA Elektronik) and were filtered at 0.5–1 kHz, digitized at 1–5 kHz. Data was stored on a personal computer for additional analysis using IGOR PRO 6.2 (Wavemetrics) and Neuromatic V2.6 softwares.

Figure 2.2 Visualized Patch in the CA3 region

Infrared-DIC image of the CA3 pyramidal cell layer in a hippocampal brain slice from an APP/PS1 animal with 6 months. The patch pipette is positioned on one pyramidal cell in the CA3b region.

All neurons were voltage-clamped at -70mV during the first 5 minutes after rupture of the membrane. In certain cases the cells were held at positive potentials (+30 or +40mV) to allow recordings of NMDAR. EPSCs were evoked using a patch pipette filled with a HEPES-based extracellular solution. All stimulation protocols were only recorded 10 minutes after establishment of whole-cell configuration. Bicuculline (10μM) was always present in the extracellular solution and Table 2.1 lists all other drugs used in the experiments described in this thesis.

Compound	Supplier	Activity	Concentration
Bicuculline	Tocris/R&D	Competitive $GABA_AR$ antagonist	10μM
CGP 55845	Tocris/R&D	Competitive $GABA_BR$ antagonist	3μM
NBQX	Abcam	Competitive AMPAR/KaR antagonist	20μM
D-APV	Abcam	Competitive NMDA antagonist	50μM
L-CCG-I	Tocris/R&D	Potent group II mGluR agonist	10μM
TTX citrate	Tocris/R&D	Na^+ channel blocker	1μM
Ro 25-6981	Abcam	Blocker of NR2B containing NMDAR	1μM
SCH58261	Tocris/R&D	Competitive $A2_AR$ antagonist	50nM
MPEP	Abcam	Non-competitive mGluR5 antagonist	10μM

Table 2.1. List of compounds and corresponding concentration used in all electrophysiology experiments

2.4 Stereotaxic Injection of Rabies Virus

Prior to the surgery the mice were anaesthetized by inhalation of isoflurane (Iso-Vet, Piramal Healthcare) in a small Plexiglas chamber (induction chamber) connected to tubing that delivered a mix of air and isoflurane at 4% concentration. Once the animals were immobile they were placed on a heating pad (at 36ºC) while they continued to receive anesthesia via a small mask. At this point the concentration of isolflorane was decreased to 2%. After briefly shaving the head fur with an electrical razor, a small (20μL) subcutaneous injection of lidocaine (Lurocaïne, Vétoquinol) was performed just bellow the scalp in order to provide local anesthesia/analgesia. Mice were then transferred to the stereotaxic frame (David Kopf Instruments) under anesthesia. The mouse nose had to be positioned in a mask that delivered the mix of isoflurane (1.5% - 2%) and air. The incisor teeth were "fitted" in the hole of the nose clamp and both the air flow rate and the concentration of anesthetic were adjusted during the surgery in order to maintain the animals with a slow but constant breathing and absence of toe-pinch reflex. The tongue of the animal was gently pulled out and aside, with a small blunt forceps, to prevent breathing problems.

The mouse head was fixed to the stereotaxic frame using ear bars and once the head was correctly positioned the ear bars were tightened and an ophthalmic cream (Lacrigel, Europhta) was applied to prevent drying of the eyes during the surgical procedure. During all the surgery the animal was placed on a heating pad with a body temperature kept at 36ºC (controlled by a rectal probe). A small scalpel was used to make an incision along the medial axis of the scalp, to expose the scull. The skin was held open using 4 small clamps (FST Inc.). Once the skull bone was exposed and cleaned a binocular microscope was used to identify the two main coordinates of the skull: **bregma** (the point of intersection of the sagittal suture with the curve of best fit along the coronal suture) and the **lambda** (midpoint of the curve of best fit along the lambdoid suture, Figure 2.3) (Cetin, Komai, Eliava, Seeburg, & Osten, 2006; Zhang et al., 2010). The tip of the injection needle was used to align the bregma and the lambda to the same dorsal–ventral (or Z) coordinate by adjusting the height of the nose clamp on the stereotactic frame. From this moment on the head of the animal was leveled and the nose piece clamp was tighten. By measuring X and Y coordinates of bregma and lambda we could verify that the animal's head is straight along the anterior/posterior axis.
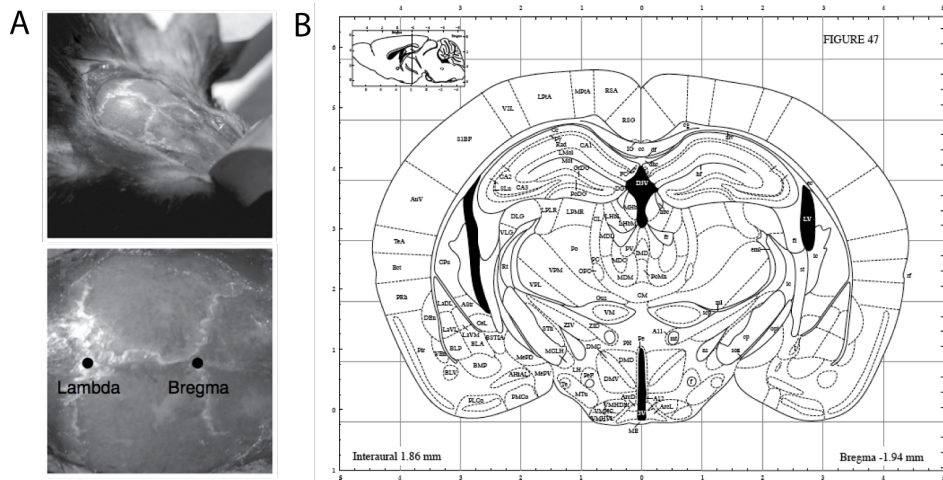
Figure 2.3 Brain Coordinates

A. Stereotaxic landmarks on the skull. Rodent skull surface diagram includes the sagittal, coronal and lambdoid sutures defining the stereotaxic landmarks bregma and lambda. Figure adapted from (Zhang et al., 2010) **B.** Stereotaxic coordinates used for the injections. Figure adapted from (Paxinos & Franklin, 2008)

Using the mouse brain atlas (Paxinos & Franklin, 2008) (Figure 2.3) we identified the coordinates for the different hippocampus subregions (Table 2.2) and moved the needle to the targeted area. Using a fine micro drill (FST Inc.) a small craniotomy was performed, producing a hole in the bone. To minimize damage to the brain, we avoided drilling through the dura and instead used a fine forceps to remove this membrane.

Virus injections were performed always using a 10μL Nanofill syringe (WPI) with a 35 or 34 gauge beveled needle (WPI). The microsyringe was driven by an electronic micro pump system – UltraMicroPump (WPI) – connected to a microprocessor operator – Micro4 – allowing to precisely control both the amount of virus infused and the velocity of this injection. Table 2.2 shows detailed parameters used for all the viral injections performed. After penetrating the dura the needle was slowly lowered to the desired Z coordinate and the viral tracer infused in the brain with a rate ranging from 30 to 50nL per minute. The needle was left in place for ten additional minutes to allow the virus to diffuse in the brain and then pulled very slowly to avoid backflow of the virus to the surface. After completely withdrawing the needle we check if it was not clogged by pumping out a small droplet (0.1 μL) and repeated the same procedure to inject the contralateral hippocampus. Finally the two

craniotomies were covered with bone silicone (Kwik-Sil, WPI), and the skin sutured (Ethilon 5-0, FS-3 Needle). The head skin was treated with Betadine (10%, MedaPharma) for local disinfection and better cicatrization. The mice were then let rest on a heating pad until they were awake. A small intracutaneous injection (~50μL) of buprenorphine (0.03mg/mL; Buprecare, Axience SAS) was given for post-operative analgesia.

Targeted Region	Injection Site Coordinates	Viral Vector Insert	Velocity (nL/min)	Volume Infused (nL)
DG	AP: -1.92 Lat: ±1.15 Z: -2.00	SADΔG-myrTom(VSV^{RtmC}) **RV Anterograde** Membrane bound TdTomato	50	500
CA3	AP: -1.92 Lat: ±1.50 Z: -1.35	SADΔG-eGFP(SAD G) **RV Retrograde** Soluble eGFP	40	300

Table 2.2. Viral Injections Details

Legend: RV= Rabies Virus. AP= antero posterior; Lat=Lateral; Z=depth

The rabies virus was injected always bilaterally, and the cellular morphology analyzed from both hippocampi. For labeling CA3 cells we used the glycoprotein deleted rabies virus variant coated with the native glycoprotein (Wickersham, Finke, Conzelmann, & Callaway, 2007). This virus leads to a retrograde infection of cells projecting to the injection site. Here we injected into the CA1 area to achieve labeling of CA3 cells.

To achieve infection of DG cells we could not use the same retrograde rabies virus as both CA3 and DG cells project to the CA3 region. We therefore tried to label DG cells and their projections with anterograde tracers. These enter the cells locally, label them and fill their axonal projections anterogradely. Lentivirus (LV) and adeno-associated virus (AAV) are two commonly used anterograde viral tracers. We therefore tested to infect DG cells in the APP/PS1 animals at 6 months with these viral vectors but the number of infected cells with LV was very low and the fluorescence level achieved with AAV was weak, making reconstructions very difficult and inaccurate. To overpass this difficulty, we worked together in collaboration with the Frick Lab (INSERM, U862) to develop and employ a new anterograde variant of the glycoprotein

deleted rabies virus (Haberl et al., 2014). The viral expression lead to a complete and intense labeling of the granule cells processes, including their axons and boutons projecting to *stratum lucidum*. Using these two rabies virus variants the site of injection and the region of image acquisition were at physically separate locations in both experimental settings, which also reduces the risk of artifacts due to neuroinflamation. The retrograde rabies virus was injected in CA1 *stratum radiatum* and the anterograde rabies virus in the hilus of the DG.

2.5 Sample Preparation for Fluorescence Microscopy

2.5.1 Preparation of Fixed Brain Slices

After 6 days, the animals were anesthetized with a intraperitoneal injection (~0.2mL) of Pentobarbital (54.7mg/mL, Pentobarbital Sodique, Ceva Santé Animale) and transcardiacally perfused with cold (4°C) ringer buffer (135mM NaCl, 5.4mM KCl, 1.8mM $CaCl_2$, 1mM $MgCl_2$, 5mM HEPES with pH 7.2 adjusted with NaOH) to remove all the blood from the animal and afterwards the perfusion was switched to a phosphate-buffered saline solution (PBS) with 4% paraformaldehyde (PFA). Following a perfusion of at least 100mL of PFA, the mice were decapitated and the brain removed and post-fixed overnight in 10mL of 4% PFA. Fixed brains were stored in PBS at 4°C until further manipulation.

The cerebellum of the fixed brains was cut off and the brains gently glued with the resulting surface onto a platform of a leica vibratome (Leica VT 1000S). Coronal sections with 70μm were obtained from the entire longitudinal length of the hippocampus. The slices for confocal microscopy were later mounted on glass slides, embedded in Vectashield (Vector Laboratories) mounting medium and covered by individual round glass coverslips of 18mm diameter (0.17mm±0.01mm thickness). Those brain sections used for stimulated emission depletion or STED microscopy were immunohistochemistically processed before mounting.

2.5.2 Immunohistochemistry

For the STED microscopy we performed immunohistochemistry to further increase the signal to background ratio of our fluorescent samples. Importantly the fluorochromes used to enhance the signal also exhibit more stability towards photobleaching (destruction of fluorophores by light) then fluorescent proteins. To permit better access of the antibody to its antigen Triton X-100 (TX) is added at several steps to the solutions. TX is a commonly used detergent for immunohistochemical stainings that permeabilizes the slices by dissolving cellular membranes without disturbing protein-protein interactions.

After initially washing the brain slices three time with 0.5% TX in 1x PBS (20min each) they were preincubated one hour in a serum solution, isotypic to the secondary antibody (goat serum 10% + 0.5% TX in 1xPBS), in order to reduce the non-

specific binding of the antibodies used later. The slices were washed three times with 1x PBS and then they were emerged in the primary antibody solution (A11122, Invitrogen^{TM}) (rabbit anti-GFP antibody 1/1000 + TX 0.5% in 1x PBS) for 24 hours at 4°C on a shaker. The TX facilitates the antibody diffusion into the tissue and cells and thereby its binding to the antigen (here GFP). After washing four times with 1x PBS, the slices were incubated in the solution with the secondary antibody (1/1000 diluted in 1x PBS TX 0.5%), which is directed against the primary antibody (goat anti-rabbit antibody) for 2 hours at room temperature. The secondary antibody used was coupled with an Alexa Fluor® 488 fluorochrome (A11008, Invitrogen^{TM}) and therefore enhanced the fluorescent signal of the GFP. For these experiments the brain slices were mounted in ProLong Gold Antifade mounting medium (Invitrogen/Molecular Probes), which is optimized to minimize bleaching and to permit long-term storage of the samples and covered by individual round glass coverslips of 18mm diameter (0.17mm±0.01mm thickness).

Immunolabelings for visualization of Amyloid Plaques were performed in the same manner as described above, using a primary antibody raised against Human Aβ peptides (polyclonal rabbit antibody, 1/500; ABCAM ab2539) and goat anti-rabbit secondary antibody coupled with Alexa Fluor® 488.

2.6 Imaging and Analysis of Fluorescence Labeled Structures

To analyze the pre and postsynaptic compartments of Mf synapses we used confocal imaging (SP5, Leica Microsystems) equipped with an Argon 488 Laser, to acquire Z stacks at randomly chosen positions in the *Stratum Lucidum* of CA3b. Images were obtained with a 63x objective (numerical aperture, N.A. 1.4) and regular photomultipliers (PMTs), which digitize the emitted signal. The Z stacks were then analyzed with IMARIS software (Bitplane) performing 3D volume reconstructions of the MfBs and ThEs and obtain, in a semiautomatic way the values of volume and surface area for each structure.

Further calculations were performed to estimate the surface complexity of the MfBs, which provides an indirect assessment of the number of filopodia, since those structures add a lot of surface but only little volume. For the calculation of the complexity we therefore calculate the maximum volume (V_{Max}) the bouton could span given the measured surface, which would be a sphere and divide it by the real measured bouton volume (V_{Bouton}) (Bednarek & Caroni, 2011).

$$Complexity = \frac{V_{Max}}{V_{Bouton}}$$

To calculate V_{Max} from the surface we use a spherical shape, which has a defined relationship between surface area (A) and volume, which therefore defines our maximum volume from the measured surface as follows:

Equation 1: $\quad V = \frac{4}{3} \pi r^3$ $\qquad$ Equation 2: $\quad A = 4 \pi r^2$

From Equation 2: $\quad r = \sqrt{\frac{A}{4\pi}}$

Inserted in Equation 1 : $\quad V_{Max} = \frac{4}{3} \pi \left(\sqrt{\frac{A}{4\pi}} \right)^3$

Although the large Mf synapses are large enough to be accurately revealed and reconstructed with our approach, the study of CA3 A/C spines was more difficult and would be less precise using confocal microscopy as these structures are much smaller in their size and in many cases around the diffraction limit (Wilke et al., 2014). With the objective to perform an accurate study of the morphology and density of A/C spines we have established a collaboration with the lab of Valentin Nagerl (IINS, Bordeaux) and performed stimulated emission depletion microscopy (STED) (Hell & Wichmann, 1994; Klar, Jakobs, Dyba, Egner, & Hell, 2000).

2.6.1 Working Principle of STED Microscopy

Fluorescent microscopy is an indispensable technique for life sciences, which is widely used for visualization of cell structures and processes. Unfortunately the theoretical resolution (Δr) of conventional fluorescence or laser scanning microscopy like confocal microscopy is limited by the diffraction of light in the optical system, which can be calculated with the Abbe's law ($\Delta r = 0.5\ \lambda/NA$; λ: wavelength of the light; NA: limiting numerical aperture of the objective or condenser).

The term *fluorescence* describes the capacity of a molecule – fluorophore – to absorb photons (light) and produce the emission of other photons of lower energy (light with longer wavelength). In its excited state the fluorophore can be de-excited by arriving photons that match the energy difference between the excited state and the ground state. When this happens, the molecule returns to the ground state before spontaneous fluorescence emission can occur. This process called stimulated emission gives rise to photons that are slightly less energetic, red shifted and can thus be separated from those photons emitted spontaneously. STED microscopy is an imaging technique that takes advantage of these two non-linear properties of fluorophores (Hell & Wichmann, 1994). With STED microscopy the resolution can be improved beyond the diffraction limit due to a doughnut-shaped depletion laser beam quenching the fluorescence. Therefore the recorded, spontaneous fluorescence emission occurs restricted at the small central point, which is spared by the doughnut-shaped beam.

2.6.2 STED Images

Superresolution images were obtained by our collaboration with a custom-built STED microscope assembled around a standard commercial inverted microscope (DMI 6000 CS Trino, Leica, Mannheim, Germany), which was custom fitted with a pulsed-laser diode (PDL 800-D, Picoquant, Berlin, Germany) to deliver excitation pulses with a 485 nm wavelength and of 90 ps duration. The pulses for the STED beam were delivered by a Ti:Sapphire laser (Coherent Chameleon; Santa Clara, California, USA) operating at 80 MHz and emitting at $\lambda=836$ nm which was used to pump an optical parametric oscillator (APE, Berlin, Germany) to produces pulses of $\lambda=595$ nm. The pulses of originally 200 fs duration were stretched to ~300 ps by dispersion in two 25-cm-long glass rods (SF6) and then in a 100-m-long polarization-preserving fiber (Schäfter & Kirchhoff, Hamburg, Germany). To create the STED focal doughnut, a polymeric phase plate (RPC Photonics, Rochester, NY) was introduced into the path of the expanded STED beam, imprinting a helical phase ramp onto the wavefront. The STED and excitation pulses were synchronized via external triggering of the laser diode, and the delay was adjusted with an in-house-built electronic delay generator. Both beams were overlapped with a dichroic mirror (AHF Analysentechnik, Tübingen, Germany), and focused into the 1.47 NA objective lens (HCX PL APO 100x Oil; Leica, Wetzlar, Germany) (Tønnesen, Nadrigny, Willig, Wedlich-Söldner, & Nägerl, 2011; Urban, Willig, Hell, & Nägerl, 2011). The z-position of the objective was controlled via a piezo actuator (P-721 PIFOC, PI Physik Instrumente, Karlsruhe, Germany). The fluorescence was collected by the same lens, separated by another dichroic mirror, filtered with a 525/50 band-pass, and imaged onto a multimode optical fiber connected to an avalanche photodiode (SPCM-AQR-13-FC, PerkinElmer, Waltham, MA). A telecentric beam scanner (Yanus IV, TILL Photonics, Gräfelfing, Germany) in combination with scan and tube lenses from the microscope manufacturer was used to scan the laser beams across the sample. Images were acquired using ImSpector software (http://www.max-planck-innovation.de/de/industrie/technologieangebote/software/).

All images were acquired in *stratum radiatum* above the CA3b region as stacks of ten z-planes with a step size of 192 nm and a pixel size of 40 nm x 40 nm. All morphological parameters were measured on raw images of entire stacks using the image analysis software ImageJ (NIH). Spine lengths were measured from the base of the dendrite to the central end of the head, following the curvature of the spine neck in

x, y and z. The maximum diameter of each head was measured orthogonal to the axis of the spine neck. The width of each spine neck was determined by measuring the full width half-maximum (FWHM) of a Gaussian fit applied to an intensity profile plot of a line crossing the neck perpendicular to its axis.

2.7 Statistical Analysis

All statistical analysis were performed with Prism6 software, from GraphPad Software, Inc. Values are presented as mean ± SEM (standard error of the mean) of n experiments. For all the experiments the normality of the distribution of results was tested using the D'Agostino & Pearson omnibus normality test. If data was normally distributed a student T-test (to compare two groups of neurons) or one-way ANOVA (to compare more then two independent groups of neurons) was performed. When the data did not pass the normality test, a Mann–Whitney test was applied. Distributions were analyzed using the Kolmogorov–Smirnov (KS) test that compares using the data from Wt animals as reference.

Chapter 3

RESULTS
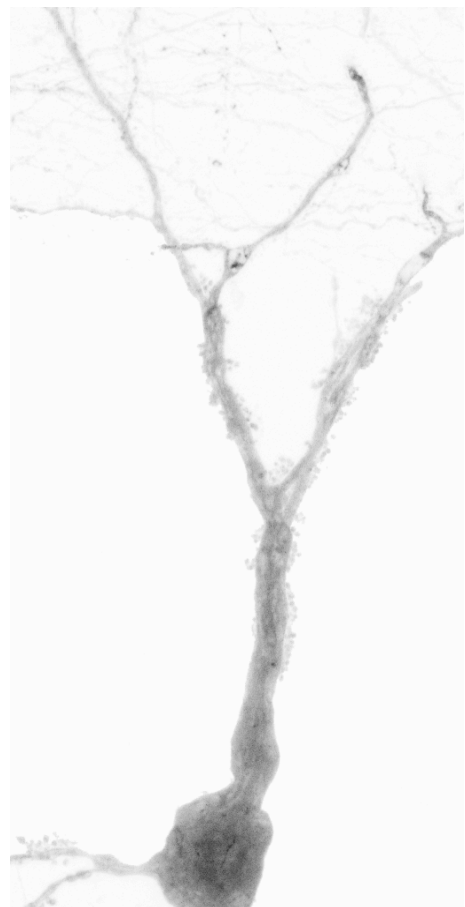
3.1 Study of the CA3 region in APP/PS1 Mice

3.1.1 Absence of Amyloid Deposition in the CA3 Region in APP/PS1 Mice

The deposition of insoluble amyloid plaques begins in APP/PS1 mice at 6 months of age (Jankowsky et al., 2001). To test the progression of amyloid deposition in the CA3 region of the hippocampus we sacrificed mice at 4, 6, 12 months of age and performed immunohistochemistry, against the Aβ peptide, in sections of APP/PS1 and Wt littermates (3-4 mice at each time-point per condition) (Figure 3.1).
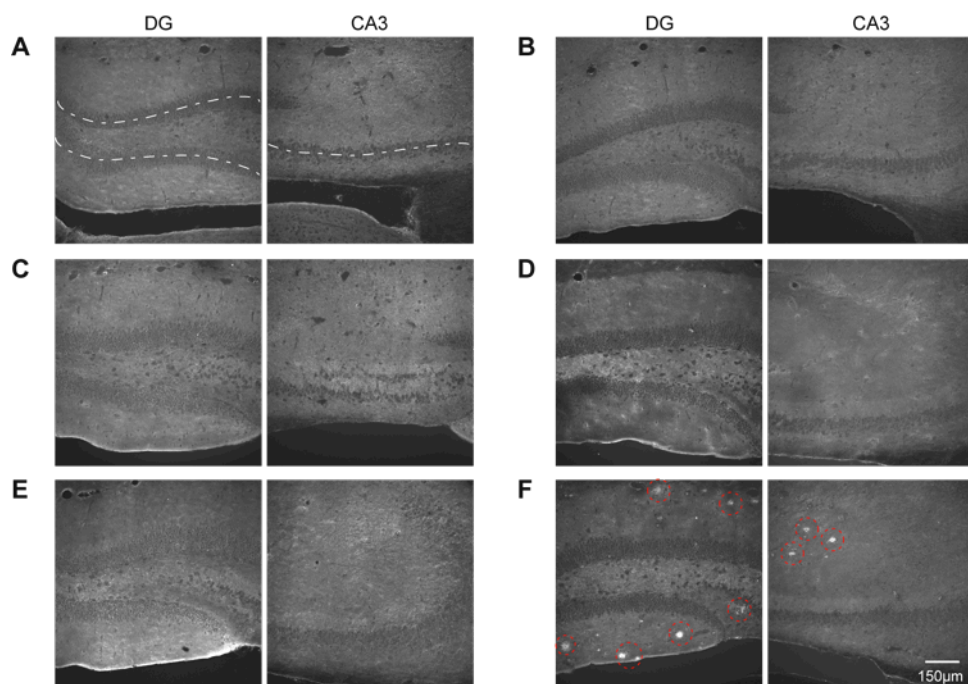

Figure 3.1 Hippocampal CA3 region of APP/PS1 mice is spared of amyloid plaque deposition until 12 months of age

Plaque deposition in the hippocampus of APP/PS1 mice and control littermates at 4, 6 and 12 months of age. **A.** Images taken from a Wt animal at 4 months of age. Dashed white lines highlights the cell body layers of the DG and CA3 areas, respectively. **B.** Images acquired from an APP/PS1 animal at 4 months, show no plaque deposition in the hippocampus. **C.** Pictures acquired in the hippocampus of a Wt animal at 6 months. **D.** Images acquired in the hippocampus of a 6 months old APP/PS1 animal. No deposits are found in the CA3 area and also the DG seems largely unaffected. **E.** Hippocampal pictures from a Wt control animal at 12 months. **F.** Images acquired from an APP/PS1 animal at 12 months. The red circles indicate strong plaque deposits, which are mainly found around the DG area. The scale bar length of 150µm is representative for all images.

No Aβ plaque was found in the CA3 region (*stratum lucidum* and *radiatum*), or in the hilar region inside the DG, at any of the time points examined. In fact, in the 4 APP/PS1 mice analyzed at 6 months of age, no amyloid depositions were observed elsewhere in the hippocampus (Figure 3.1 D). At this age plaques were only present in the cortex. In addition, during all slice recording experiments described in this thesis, performed in 6 months old mice, amyloid plaques (visible under the DIC microscope) were never observed in the CA3 region (hilus, *statum lucidum* or *stratum radiatum*). At 12 months, a strong amyloid plaque deposition was registered in the proximity of DG, particularly in the molecular layer (Figure 3.1 F). 1

3.1.2 Altered Glutamatergic Inputs into CA3 Pyramidal Cells

The fusion and release of NT vesicles from the presynaptic terminal is probabilistic and can happen even without stimulation of the presynaptic cell. Stochastically a single vesicle can be released into the synapse, generating miniature EPSPs (mEPSPs). The synaptic response to the release of NT from a single vesicle is defined as quantal size, and quantal content is the number of effective vesicles released in response to an action potential. To determine whether excitatory synapse number and strength was altered in the APP/PS1 mice, we recorded miniEPSCs from the soma of pyramidal neurons visually identified in the CA3b region of the hippocampus in the presence of 1 μM TTX to block action potentials. Cells were held at -70 mV and left to stabilize for 8 minutes after whole-cell configuration was established. Synaptic activity was registered for 15 minutes in the presence of the GABA$_A$ receptors blocker, bicuculline (10 μM), in order to isolate the glutamatergic inputs.

The mean amplitude of all events occurring during 15 minutes was significantly decreased in APP/PS1 compared to Wt mice (Wt: 24.9 pA ± 1.1 pA, n=15, 8 mice; APP/PS1: 20.2 pA ± 0.6 pA, n=15, 9 mice, t-test p=0.0009). (Figure 3.2 B and C). Moreover, the distribution of the amplitudes from the first 100 events recorded from APP/PS1 mice also was significantly different when compared with the one from Wt mice (Wt 26.7 ms ± 0.7 ms, n=1500 events; APP/PS1 22.5 ms ± 0.6 ms, n=1500; KS test p<0.0001, bin size of 2; Figure 3.3 A). Observing the cumulative probability distributions we found that APP/PS1 mice have an increased number of smaller events compared to Wt littermates at 6 months. Further, the probability plot suggests that the

distribution of the amplitudes is more altered in the range of smaller amplitudes (<45pA).
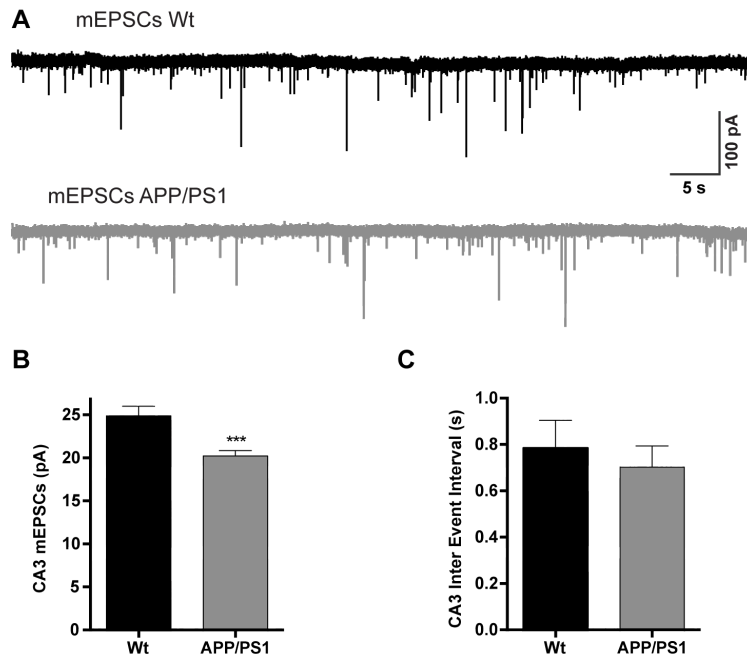

Figure 3.2 The amplitude of CA3 miniature EPSCs is reduced in APP/PS1 mice
A. Representative recording of mEPSCs (1 mM TTX) during one minute, illustrating the difference of amplitude registered between CA3 cells from Wt and APP/PS1 mice. **B.** Summary plot of the mean mEPSCs amplitude registered during 15 minutes showing a decrease in mEPSCs amplitude from the APP/PS1 cells. Black bar represents Wt cells (n=15, 8 mice), grey bar represents cells from APP/PS1 mice (n=15, 9 mice), t-test p=0.0009. **C.** Summary graph showing no difference between genotypes of the mEPSCs mean inter event intervals registered during a 15 minutes period. Black bar represents Wt cells (n=15, 8 mice) and grey bar represents cells from APP/PS1 mice (n=15, 9 mice), t-test p=0.5863. Data represented as mean ± SEM, *** represents p<0.001.

The mean values of all mEPSCs inter event intervals (IEI), indicating the overall frequency of mEPSCs, was not statistically different between Wt and APP/PS1 mice (Wt: 0.8 ms ± 0.1 ms, n=15; APP/PS1: 0.70 ms ± 0.09 ms, n=15; p=0.5863; Figure 3.2.C), primarily due to the large variation in the mEPSCs frequency between recordings. However, when evaluating the cumulative probability of IEI of the first 100 events (Figure 3.3 B) we observed a statistical difference in their distribution in the Wt compared to the APP/PS1 mice (Wt 0.70 s ± 0.03 s, n=1500; APP/PS1 0.70 s ± 0.02 s, n=1500; KS test p=0.0025, bin size 0.02).
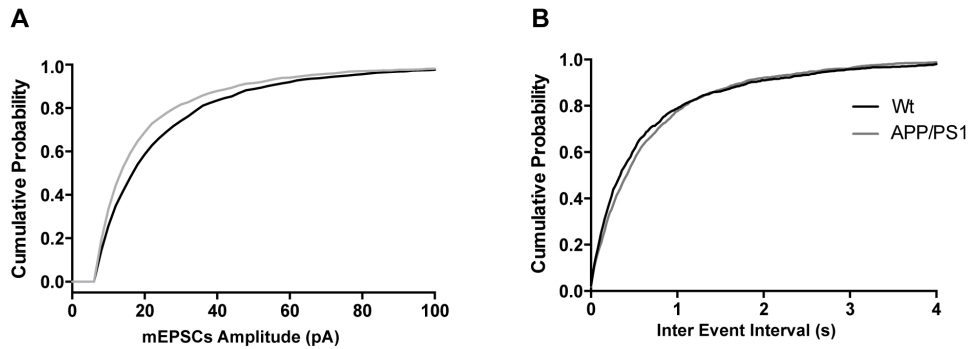
Figure 3.3 Distribution of mEPSCs amplitude and frequency is altered in APP/PS1 mice

A. Cumulative probability distribution of the amplitudes from the first 100 mEPSCs registered from each cell. Black line represents the amplitude distribution of 1500 events from 15 CA3 cells successfully patched in Wt slices (n=8 mice); Mean values: Wt 26.7 pA ± 0.7 pA; APP/PS1 22.5 pA ± 0.6 pA; KS test p<0.0001, bin size of 2. **B.** Cumulative probability distribution histogram of the IEI values between the first 100 mEPSCs registered from each cell. Black line represents the distribution of the intervals between 1500 events from 15 CA3 cells successfully patched in APP/PS1 slices (n=9 mice); Mean values: Wt 0.7 s ± 0.03 s; APP/PS1 0.7 s ± 0.02 s; KS test p=0.0025, bin size 0.02. Note that all histograms in this figure are truncated for presentation purposes.

Elimination of DG cells by γ-irradiation showed that 95% of the mEPSCs recorded from CA3 neurons, with an amplitude above 45 pA derive from Mf synapses (Henze, Card, Barrionuevo, & Ben-Ari, 1997; Henze, McMahon, Harris, & Barrionuevo, 2002a). Events smaller than 45 pA have an equal probability of being from any of the three inputs contacting CA3 pyramidal cells as schematically shown in the Figure 3.4 A. The percentage of mEPSCs larger than 45 pA was not significantly different in the APP/PS1 CA3 cells in comparison with Wt cells (Wt 11.9 pA ± 1.5 pA, n=15; APP/PS1 8.5 pA ± 0.8 pA, n=15; Mann-Whitney test p=0.0718) although a tendency for a decrease can be observed Figure 3.4 B. Furthermore, when analyzing the distribution of peak amplitudes smaller than 45 pA, we observe a significant alteration in the cumulative probability between Wt and APP/PS1 mice. In the APP/PS1 mice the mean amplitude of mEPSCs was decreased as compared to cells from Wt mice (Wt 17.76 pA ± 0.06 pA; n=22375; APP/PS1 16.23 pA ± 0.06 pA, n=22912; KS test p<0.001, bin size 2) Figure 3.4 C. This difference was not significant for the distribution of mEPSC amplitudes for Mf synapses (amplitudes above 45 pA) as shown in Figure 3.4 D (Wt 76.8 pA ± 0.6 pA; n=3861; APP/PS1 78.4 pA ± 1.2 pA; n=1949; KS test p>0.999, bin size 2). It can thus be concluded that CA3 cells in APP/PS1 mice display a larger number of small events in comparison to Wt littermates.
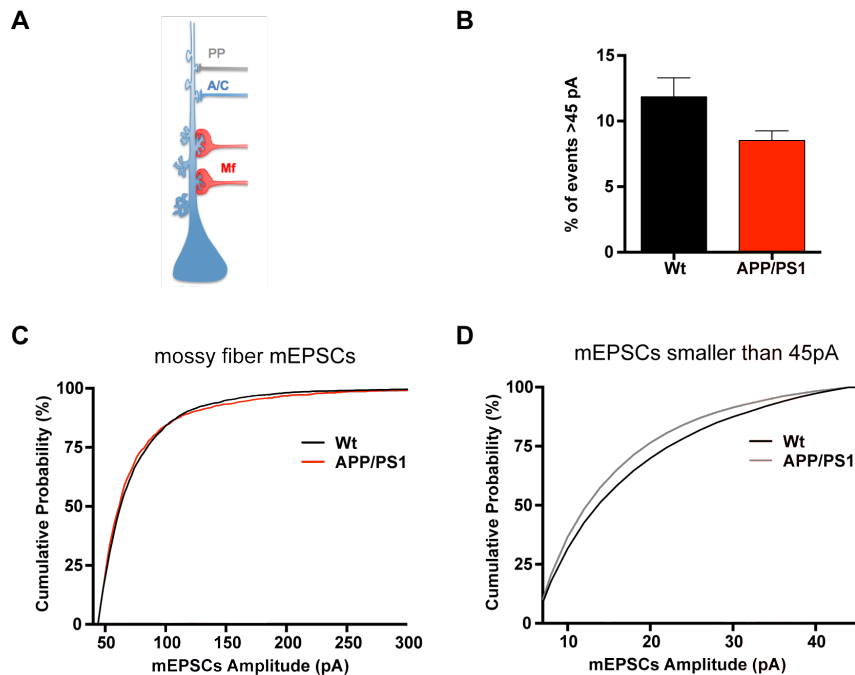
Figure 3.4 Mossy fiber input is not selectively affected in APP/PS1 mice with 6 months

A. Schematic representation of the three types of fibers contacting CA3 pyramidal cells. In red are Mf axons, in blue the recurrent A/C contacts and in green the PP fibers contacting the more distal portion of the CA3 cells dendrites. **B.** Bar graphs representing the percentage of the putative Mf events (with an amplitude larger than 45 pA) for each of the 15 cells recorded, during a period of 15 minutes. A tendency was found towards a reduced number of Mf-generated events, which is not statistically significant (Mann-Whitney test p=0.0718). Black bar, Wt cells (n=15, 8 mice). Grey bar, APP/PS1 mice (n=15, 9 mice). Data represented as mean ± SEM. **C.** Cumulative distribution of the amplitudes of events with high probability of being from Mf synapses is not different between Wt and APP/PS1 mice. Plot used all the events larger than 45 pA obtained over a period of 10 minutes per cell (150 minutes in total per genotype). Mean values are 76.8 pA for Wt and 78.4 pA for APP/PS1; KS test p>0.999, bin size 2. **D.** Cumulative distribution of the amplitudes of events smaller than 45 pA showing a difference between Wt and APP/PS1 mice. Plot used all the events under 45 pA obtained over a period of 10 minutes per cell (150 minutes in total per genotype). Mean values are 17.7 pA for Wt and 16.2 pA for APP/PS1; KS test p<0.001, bin size 2.

These experiments suggest that the Mf synaptic component is not specifically affected, but the extent to which different inputs to CA3 cells are altered cannot be directly assessed with mEPSC recordings. Therefore we conducted further experiments evoking separately each input pathway to understand whether our animal model of AD shows synapse specific alterations into CA3 pyramidal neurons.

3.2 Mossy Fiber Synapses in APP/PS1

3.2.1 Mossy Fiber Presynaptic Parameters in APP/PS1 Mice Display Minor Alterations

Mf synapses are known to display particular properties compared to other synapses. They undergo prominent pre-synaptic short-term plasticity such as PPF, FF and PTP (Henze, Urban, & Barrionuevo, 1999). To evaluate basal properties of Mf synaptic inputs in APP/PS1 mouse model of AD, CA3 cells were patched and the membrane potential was held at -70mV.
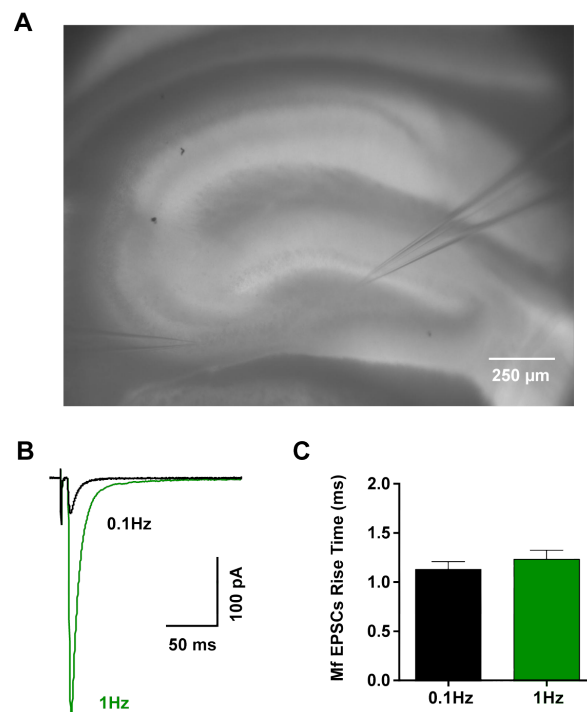

Figure 3.5 Frequency Facilitation used as selection method to distinguish Mf synapses from other inputs

A. Example image of our recording conditions: a mouse brain slice under the microscope with the patch-pipette recording a CA3 cell and the stimulating pipette inside the DG, positioned between the hilus and the starting CA3a region. **B.** Representative traces of Mf-EPSCs evoked in our experimental conditions (room temperature). A facilitation of 5- to 7-fold in EPSCs amplitude is characteristic for Mf synaptic inputs, when the stimulation frequency is switched from 0.1Hz (black trace) to 1Hz (green trace) - frequency facilitation. **C.** Average of rise time (20-80%) of Mf-EPSCs recorded for both genotypes was always shorter than 1.5ms (0.1Hz 1.13 ms ± 0.080 ms, n=34; and 1Hz 1.23ms ± 0.094ms, n=34). Data represented as mean ± SEM.

All recordings were made in the presence of bicuculline (10 μM) to isolate glutamatergic synaptic currents. A stimulating electrode was placed inside the DG region, as represented in Figure 3.5 A, in order to selectively evoke Mf EPSCs characterized by a fast rise time, between 1 to 1.5 ms (Figure 3.5 B and C, both genotypes, 0.1Hz 1.13 ms ± 0.080 ms, n=34; 1Hz 1.23 ms ± 0.094 ms, n=34). All Mf EPSCs were recorded with *minimal stimulation* conditions.

Paired pulse facilitation (PPF) is the ability of synapses to increase neurotransmitter release in response to the second of two temporally close afferent stimulations. We first observed that in 6 months-old Wt mice PPF ratio was smaller when compared with PPF ratio values obtained from 3-4 weeks-old Wt mice (Wt 6 months: 2.65 ± 0.19, n=14) (Lanore et al., 2010; Pinheiro et al., 2007). No alteration of this presynaptic feature was seen when comparing Wt with APP/PS1 mice of the same age (Figure 3.6 A and B) (APP/PS1 2.84 ± 0.36, n=17, Mann-Whitney test p=0.732). Low frequency facilitation (FF) represents another presynaptic feature characteristic of Mf synaptic transmission, which can be observed by switching stimulation frequency from 0.1Hz to 1Hz and recording the resulting increase in evoked EPSC amplitudes. The degree of frequency facilitation was significantly decreased in APP/PS1 mice as illustrated in the representative traces in Figure 3.6 C (Wt 6.77 ± 0.47, n=14; APP/PS1 5.57 ± 0.35, n=19; t-test p=0.0446, Figure 3.6 D).

Finally we looked to another basal property of Mf synapses: the failure rate, described as the percentage of times a stimulation of the afferent axon results in no release of synaptic vesicles. Figure 3.6 E shows examples recorded from CA3 pyramidal cells from Wt (black) and APP/PS1 animal (red) while triggering 40 stimuli at 0.1Hz frequency. We found no significant alterations of failure rates in the APP/PS1 mice compared to Wt littermates (Wt 16.5% ± 3.1%, n=14; APP/PS1 12.6% ± 3.3%, n=19; t-test p=0.3097; Figure 3.6 F). In all these experiments the group II mGluR agonist LCCG-I was applied at the end of the stimulating protocols and the EPSCs decreased by more than 80%, confirming that they were Mf-EPSCs. In the rare cases in which this decrease was not observed the cells were discarded. We can conclude that basal presynaptic properties measured from Mf synapses projecting to CA3 cells are mostly unaltered in our model of AD at the age of 6 months.
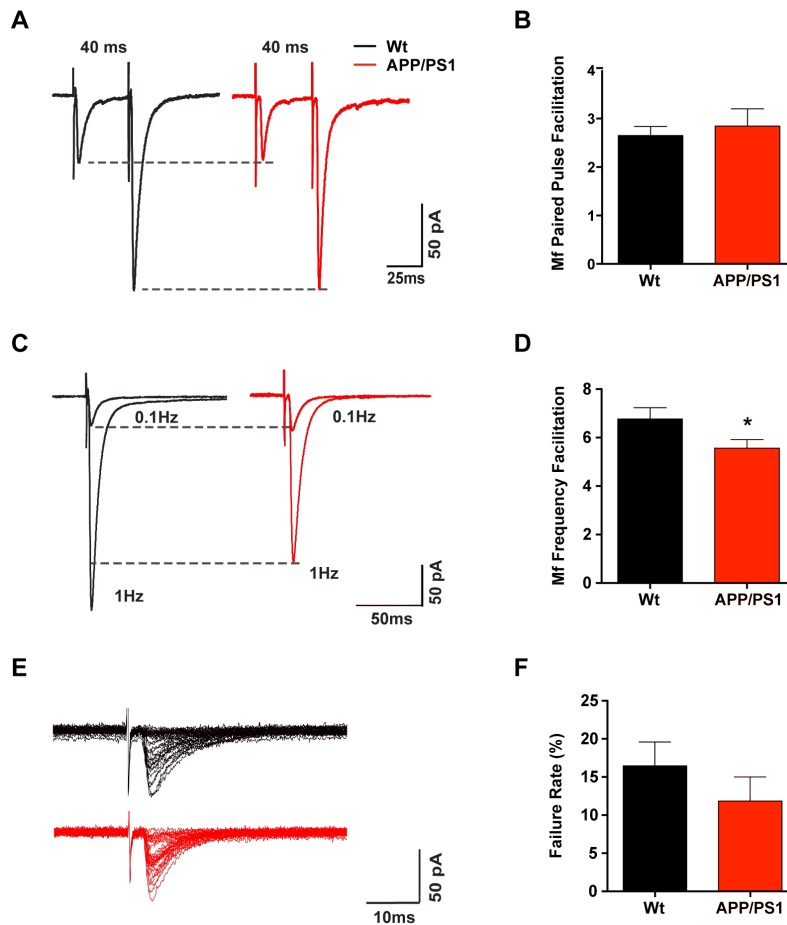
Figure 3.6 Normal synaptic transmission and presynaptic short-term plasticity of Mf synapses at 6months APP/PS1 mice

A. Average of 15 traces illustrating PPF at a inter stimulus interval of 40ms for Wt (black traces) and APP/PS1 (red traces) Mf synapses. **B.** Bar graph representing the ratio between the amplitude of the second over the first EPSCs obtained during PP stimulating protocol. Mann-Whitney test p=0.732 between Wt (n=14) and APP/PS1 (n=17) **C.** Representative average traces of the amplitude increase of Mf-EPSCs with FF. EPSCs obtained at 0.1Hz (40sweeps) and 1Hz (60sweeps) for Wt and APP/PS1 mice. Traces were scaled to similar baseline values for the purpose of a clearer visualization of the decreased facilitation found at 1Hz in APP/PS1 mice. **D.** Bar graph displaying the mean values of FF observed in Wt and APP/PS1 CA3 cells show a significantly smaller FF in the APP/PS1 cells. t-test p=0.0446, n=14 for Wt and n=19 for APP/PS1. **E.** Representative cell for Wt and APP/PS1 mice displaying the typical high variability of the Mf-EPSCs amplitudes obtained at 0.1Hz, with several failures. **F.** Summary bar graph displaying the failure rates shows no significant differences between Wt (n=14) and APP/PS1 (n=19) cells. Values are obtained for each genotype by calculating the percentage of Mf-EPSCs smaller than 5pA obtained at 0.1Hz ISI (inter-stimulus-interval), t-test p=0.3097. Data represented as mean ± SEM. * represents p<0.05.
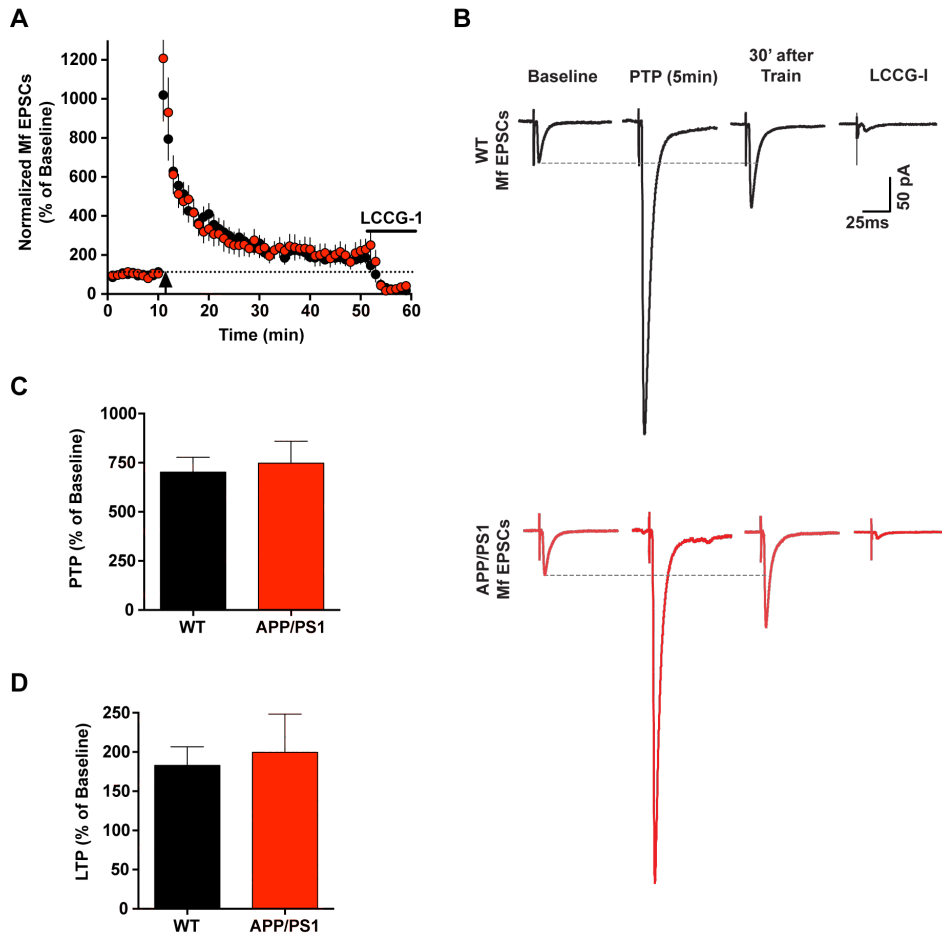
Figure 3.7 Mf presynaptic LTP is not altered in our APP/PS1 model of AD

A. Summary plot of the LTP time course for Wt (black circles, n=12) and APP/PS1 (red circles, n=11) cells. The LTP protocol was applied at the time indicated by the arrow. The LTP protocol (100 pulses at a frequency of 100 Hz repeated 3 times with a 10 s inter train interval) was applied at the time indicated by the arrow. Mf-EPSCs were averaged every minute and normalized to the mean amplitude of the 10 min period preceding the LTP induction protocol. **B.** Traces represent Mf-EPSCs obtained at a stimulus frequency of 0.1 Hz during Baseline (10 min), PTP (5 min), LTP (30-40min after the train) and LCCG (5min after drug application). Black and red traces from representative cells in Wt and APP/PS1 mice, respectively. **C.** Bar graph with average values of PTP recorded 5minutes after the high frequency train was applied shows no difference between the two animal genotypes. Values are expressed as percentage of the baseline amplitude of Mf EPSPs. **D.** Bar graph representing the mean amplitude of Mf-EPSCs recorded between 30 to 40 minutes after LTP induction. Values are expressed as percentage of the baseline Mf-EPSCs amplitude. Data represented as mean ± SEM.

To further analyze the presynaptic function of Mf synapses in APP/PS1 mice we examined the NMDA-independent presynaptic form of LTP. We used a classical high frequency induction protocol consisting of 100 pulses at a frequency of 100Hz repeated 3 times with a 10 s inter train interval, in the presence of bicuculline (10 μM), CGP-55845 (3 μM) and D-AP5 (50 μM) to block GABA$_A$, GABA$_B$ and NMDA receptors, respectively. We compared both the PTP and LTP levels (30 minutes after the train) in Wt and APP/PS1 mice (Figure 3.7 A and B). The group II mGluR agonist LCCG-I (10μM), was again applied at the end of each experiment and only cells that displayed more than 80% of inhibition on their EPSCs were analyzed (representative traces are shown in Figure 3.7 B). Both genotypes displayed similar levels of PTP, measured as the percentage of increase in EPSC amplitudes 5 minutes after the train (Wt 702.5% ± 75.1%, n=12; APP/PS1 747.7% ± 112.5%, n=11; t-test p=0.737; Figure 3.7 B and C), as well as similar levels of LTP measured 30min after the train (Wt 182.9% ± 23.7%, n=12; APP/PS1 199.8%±48.7%, n=11; Mann-Whitney p= 0.723; Figure 3.7 B and D).

3.2.2 Normal NMDAR Transmission at Mossy Fiber Synapses

Although the presynaptic Mf LTP described above is independent of NMDAR activation (E. W. Harris & Cotman, 1986) this does not preclude a contribution of NMDARs to Mf synaptic transmission. NMDARs are present at Mf to CA3 pyramidal neuron synapses and have recently been shown to contribute to Mf synaptic transmission and plasticity (Hunt, Puente, Grandes, & Castillo, 2013; Kwon & Castillo, 2008; Rebola, Carta, Lanore, Blanchet, & Mulle, 2011; Rebola, Luján, Cunha, & Mulle, 2008). At normal resting membrane potentials NMDARs are mostly blocked by extracellular Mg^{2+}, but the large amplitude of unitary EPSPs at Mf-CA3 cell synapses may lead to the release of the Mg^{2+} block, either directly or indirectly by triggering action potentials in CA3 cells (Henze, Wittner, & Buzsáki, 2002b).

After running short-term plasticity protocol at -70 mV (FF and PPF) the holding potential of the cells was increased in steps of 10 mV, until it reached +40 mV. At this membrane potential, evoked EPSCs are mediated by all iGluRs (AMPA, KA and NMDARs). Protocols of FF (0.1 Hz and 1 Hz) were repeated again and NMDA-mediated EPSCs were isolated by blocking AMPA and KARs with 20 μM NBQX. Bicuculline was present (10 μM) throughout all the experiments. Taking advantage of

this experimental procedure we were able to compare the NMDAR/AMPAR ratio by two different ways Figure 3.8:

- **+40mV 40ms/peak:** analyzing the EPSCs obtained at +40 mV in the absence of NBQX (green trace) and comparing the value of the peak (mainly AMPAR mediated) with the amplitude value 40 ms after the peak, where AMPAR/KAR mediated currents should be absent (* mark on the green trace, Figure 3.8);
- **+40/-70mV:** comparing the peak of the NMDAR EPSC obtained at +40 mV in the presence of NBQX (blue trace) with AMPAR EPSC peak recorded initially at -70 mV (black trace);
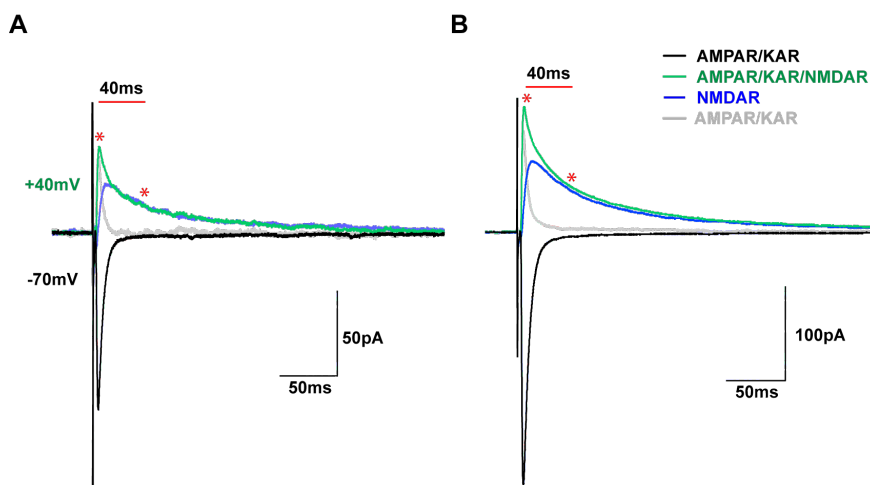

Figure 3.8 Isolation of AMPAR and NMDAR-mediated Mf-EPSCs

A. Average currents recorded with a stimulation frequency of 0.1 Hz and at **B.** 1 Hz. Currents recorded at -70 mV are composed of AMPAR and KAR (black traces). When the holding current is increased to +40 mV currents registered are composed of a mix of EPSCs mediated by AMPAR, KAR and NMDARs (green traces). Pharmacological isolation of NMDAR-mediated currents (blue traces) by application of NBQX (20 μM) allows calculation of a trace representing the AMPAR mediated component at +40 mV (grey traces, obtained by subtraction of blue from the green traces).

We performed these two analyses in Wt and APP/PS1 mice, at both 0.1 Hz and 1 Hz, Figure 3.9 A. The NMDAR/AMPAR ratio obtained with the two methods was similar in both genotypes. At 6 months, at Mf synapses, the NMDAR/AMPAR ratio was about 30% (+40/-70mV method: Wt 28.3% ± 3.3%, n=9; APP/PS1 29.9% ± 3.4%, n=9; t-test p=0.7449; Figure 3.9 B) or 40% (Total +40mV method: Wt 44.5% ± 3.4%, n=8; APP/PS1 49.5% ± 3.4%, n=9; t-test p=0.3206; Figure 3.9 C), without any significant difference observed between the two genotypes.
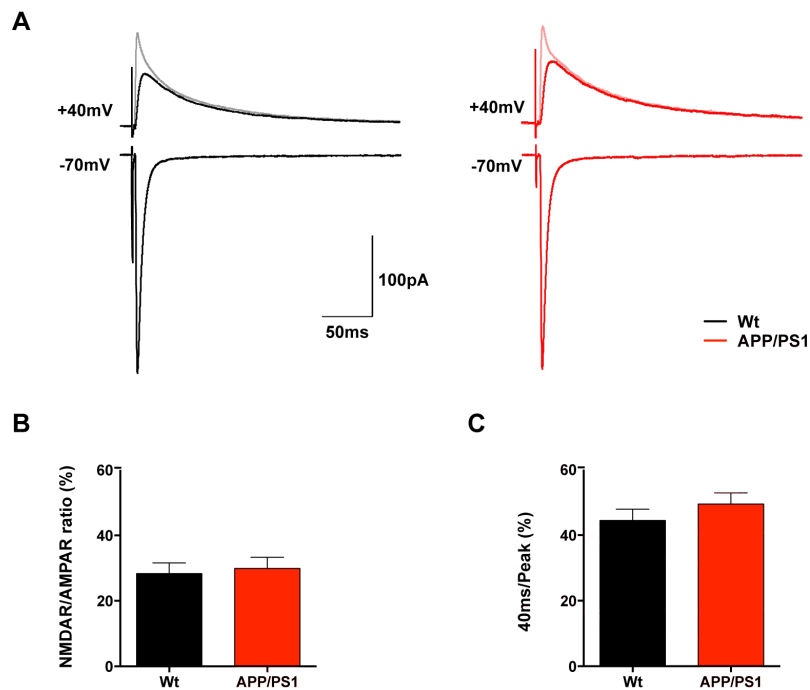
Figure 3.9 Ratio between Mf NMDAR-EPSCs and AMPAR/KAR-EPSCs is maintained in APP/PS1 mice

A. Representative traces of Mf-EPSCs recorded at negative (-70 mV) and positive potentials (+40 mV), with and without NBQX (20 μM) illustrating no major differences between results obtained in the two genotypes. Bicuculline was present throughout all experiments. **B.** Bar graph resuming mean values of NMDAR/AMPAR ratios obtained with isolated currents at -70 mV (AMPAR) and +40 mV (NMDAR with NBQX). Black bar represents results from 9 cells from Wt mice and red bar represents results from 9 APP/PS1 cells. **C.** Bar graph representing mean values obtained for NMDAR/AMPAR ratio performed at +40 mV in the presence of bicuculline. The ratio, calculated as the amplitude 40 ms after the peak divided by the peak amplitude, was not different between the Wt (n=9) and APP/PS1 (n=9) cells analyzed. Data represented as mean ± SEM.

The levels of FF for Mf NMDARs EPSCs frequency facilitation obtained at +40 mV are not different between genotypes (Wt 4.78 ± 0.4, n=29; APP/PS1 4.0 ± 0.2, n=31; Mann-Whitney test p=0.1932; Figure 3.10 A and B), at variance with the observation of decreased FF of AMPA/Kainate receptor-mediated EPSCs described in Figure 3.6 D. In addition, the value of FF (~5fold) mediated by NMDARs is smaller compared to the one performed by AMPAR-mediated currents (~7fold) in adult Wt mice.

As described previously, the subunit composition of NMDARs its determines receptor properties. The identity of the GluN2 subunit impacts on affinity for glutamate,

modulation by glycine, sensitivity to voltage-dependent block by Mg^{2+}, fractional Ca^{2+} current and, consequently, channel kinetics (Cull-Candy & Leszkiewicz, 2004; Paoletti, Bellone, & Zhou, 2013). The NMDAR-EPSC decay time is governed by the channel deactivation kinetics and it can be used as an indicator of the identity of the subunits assembling synaptic NMDARs. Similar decay time of Mf NMDA EPSCs was obtained in Wt and APP/PS1 mice at 6 months. When a stimulation of 0.1 Hz was applied the mean NMDA EPSCs decay time was 103.2 ms ± 12.45 ms (n=27) for the Wt Mf-NMDAR EPSCs and 115.6 ms ± 12.05 ms (n=30) for Mf NMDAR EPSCs from APP/PS1 cells (p=0.4782, t-test, Figure 3.10 C). The results at 1Hz stimulation are slightly faster, with 97.5 ms ± 3.8 ms (n=27) for the Wt mice and 99.0 ms ± 3.605 ms (n=30) for APP/PS1 mice (p=0.7707, t-test; Figure 3.10 D).
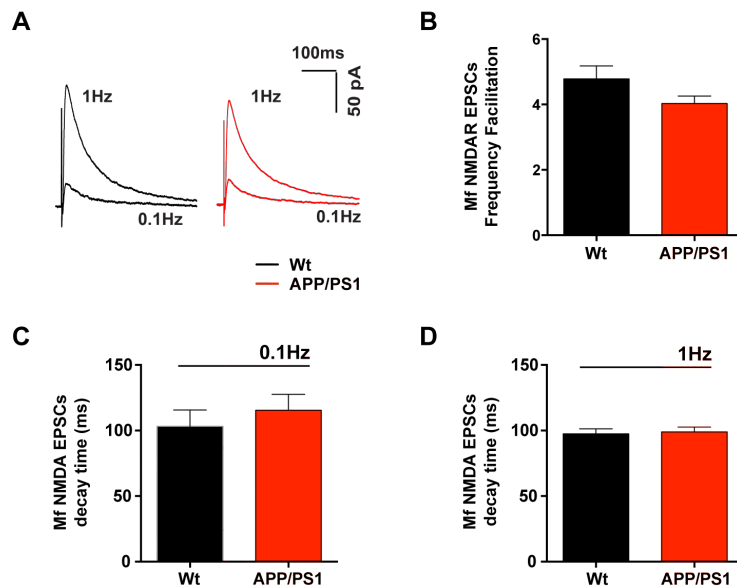
Figure 3.10 Short-term plasticity of NMDAR is normal in 6months old APP/PS1 mice

A. Representative traces of NMDAR-mediated EPSCs recorded at +40 mV, illustrating that both genotypes perform equivalent FF at positive potentials. Black traces illustrate average of 40 traces at 0.1 Hz and 60 at 1 Hz (from 0.1 Hz to 1 Hz) obtained from Wt cells (n=29). Red traces were obtained from APP/PS1 mice (n=31). **B.** Bar graph summarizing mean FF values obtained from NMDAR-EPSCs recorded at positive potentials from Wt and APP/PS1 cells, Mann-Whitney test p=0.1932. **C.** Summary plot of the mean decay time of Mf NMDAR-mediated EPSCs recorded at a frequency of 0.1 Hz. Black and Red bars represent respectively Wt and APP/PS1 values of Mf NMDAR-EPSCs decay time (ms). Average decay times are not statistically different t-test, p=0.4782. **D.** Summary plot of the mean decay time of Mf NMDAR-mediated EPSCs recorded at a 1 Hz frequency. Average decay times are not statistically different (t-test, p=0.7707) between Wt (black bars) and APP/PS1 mice (red bar). Data represented as mean ± SEM.

3.2.3 Loss of Mossy Fiber NMDAR-Dependent LTP in APP/PS1 Mice

Short bursts of stimuli can induce a robust LTP of NMDA-EPSCs but not of AMPA-EPSCs at Mf synapses (Kwon & Castillo, 2008; Rebola et al., 2008). This selective LTP of NMDA-EPSCs, provides clear evidence that synaptic NMDARs can undergo activity-dependent long-term modifications with mechanisms different from the ones responsible for LTP of AMPARs (Rebola et al., 2011). Considering the importance of NMDARs for hippocampal function (Kishimoto, Nakazawa, Tonegawa, Kirino, & Kano, 2006; Nakazawa et al., 2002; Rajji, Chapman, Eichenbaum, & Greene, 2006) it is relevant to study this form of plasticity in our disease model.

CA3 pyramidal cells were patched and the membrane potential clamped at +30 mV. GABAergic input was blocked (10 μM Bicuculline and 3 μM CGP-55845) and NMDAR-EPSCs were isolated from other glutamatergic actions by blocking AMPARs and KARs with 20 μM NBQX. The stimulating pipette was positioned inside the DG and minimal stimulation conditions were used to evoke Mf synaptic currents (as evidenced by FF). After establishment of a stable baseline (10 min) LTP was induced by 6 bursts of 6 stimuli at a frequency of 50 Hz with a 150 s inter burst interval and recorded over a period of 40 min (Figure 3.11 A). Figure 3.11 B and C summarize the time course of the LTP obtained in Wt and APP/PS1 mice. Following PTP of NMDA-EPSCs, we found that Mf LTP was absent in APP/PS1 mice (Wt 135.3% $\pm$ 9.2%, n=10; 98.3% $\pm$ 9.3%, n=10; t-test p=0.0109; Figure 3.11 D).
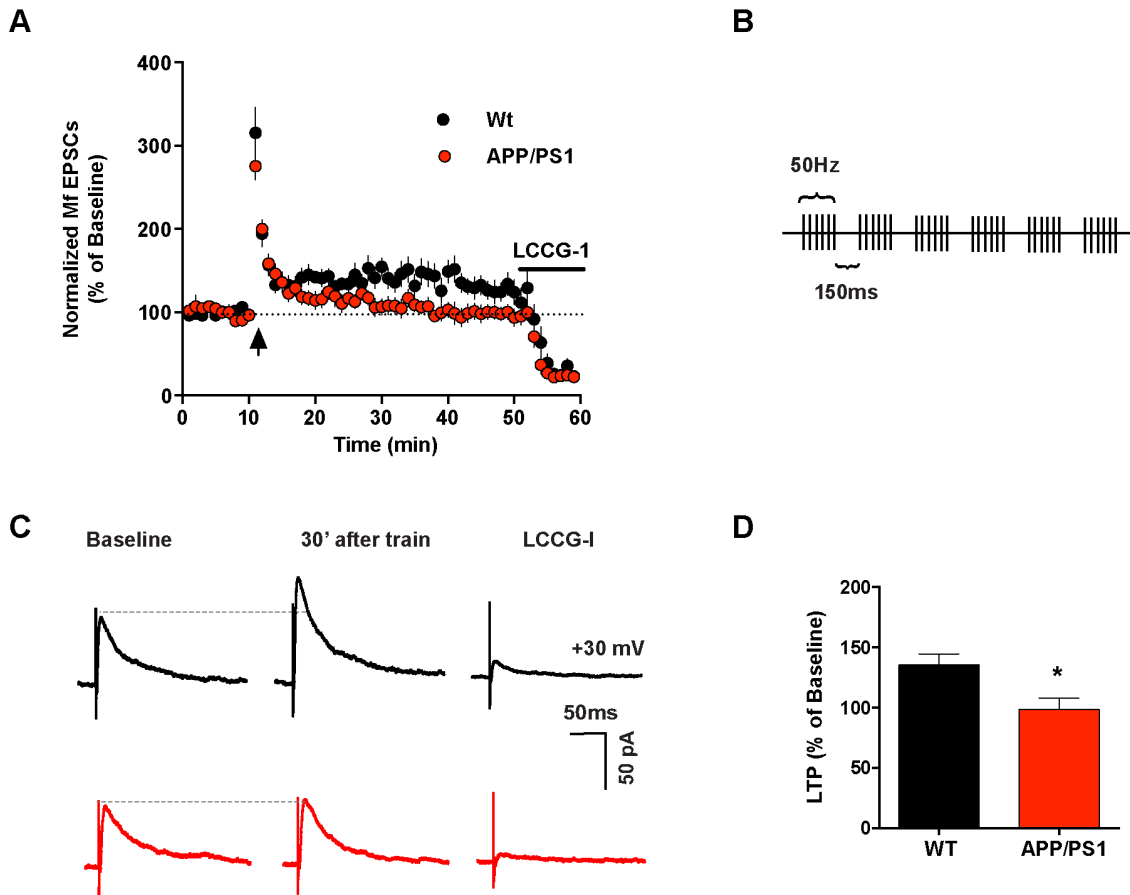
Figure 3.11 Loss of Mf-NMDAR dependent LTP in 6months old APP/PS1 mice

A. Summary plot of Mf NMDAR-LTP time course for Wt (black circles, n=12) and APP/PS1 (red circles, n=11) cells. The LTP protocol was applied at the time indicated by the arrow. Mf NMDAR-mediated EPSCs, evoked every 10 sec (0.1 Hz) were averaged every minute and normalized to the mean amplitude of the 10 min period preceding the LTP induction protocol. **B.** Schematic representation of the train applied to trigger specific NMDAR-dependent LTP at Mf synapses: 6 bursts of 6 stimuli given at a frequency of 50 Hz. The 6 burst were separated by a 150 ms interval. **C.** Traces represent Mf NMDAR-EPSCs obtained at stimulus frequency of 0.1 Hz during Baseline (10min), LTP (between 30 min to 40 min after the train) and LCCG-I application (5 min after drug treatment). Black and red traces from representative cells from Wt and APP/PS1 cells, respectively. **D.** Bar graph representing the mean amplitude of Mf NMDARs EPSCs recorded between 30 to 40 minutes after LTP induction. Values are expressed as percentage of baseline Mf NMDAR-EPSCs amplitude. Data represented as mean ± SEM, * represents $p<0.05$.

3.2.4 Unaltered Morphology of Mossy Fiber-CA3 Pyramidal Cell Synapses

Studies relating structural plasticity to learning and memory have recently led to important observations with processes of specific synapse assembly and synapse loss being unequivocally linked to animal learning and to structural traces of the learning (Caroni, Donato, & Muller, 2012). Based on the close relationship between LTP and

altered spine morphology (Muller, Nikonenko, Jourdain, & Alberi, 2002; Muller, Toni, & Buchs, 2000) we have analyzed whether alterations in the morphology of Mf-CA3 synapses could be observed in APP/PS1 mice, which could be correlated with the loss of NMDAR-LTP described above.
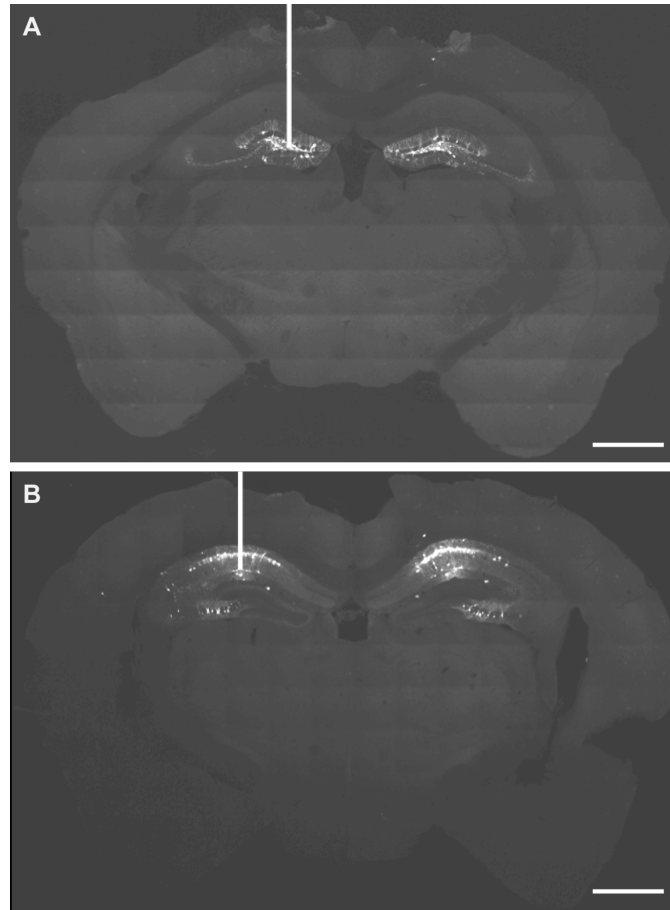
Figure 3.12 Stereotaxic injections of RV in APP/PS1 mice

A. DG granule cells labeled with anterograde RV expressing a membrane-targeted Td-Tomato construct. **B.** Hippocampal CA1 and CA3 regions of the hippocampus infected with a retrograde RV expressing soluble eGFP. Needle trajectories are labeled with a white line. Scale Bars represent 1 mm.

For this study two types of recombinant RV were stereotaxically injected in the brain in order to label DG granule cells and CA3 pyramidal cells Figure 3.12). Local infection was achieved by injecting an anterograde RV expressing a membrane-targeted td-Tomato fluorescent protein (Haberl et al., 2014) in the DG, allowing us to trace DG cells projections as well as presynaptic nerve terminals (MfB) (Figure 3.13 A, for more details see Methods section). MfB from Wt and APP/PS1 mice were

reconstructed from confocal z-stacks obtained from the CA3b region of the hippocampus (the same area in which the electrophysiology experiments were performed). The mean surface area of MfB was not different in the APP/PS1 mice (APP/PS1 67.9 μm^2 ± 1.6 μm^2, n=609, 5 mice) compared to control littermates (Wt 67.1 μm^2 ± 1.8 μm^2, n=898, 5 mice; Mann-Whitney test p=0.6624), as also indicated by cumulative distribution of areas (Figure 3.13 B; KS test p=0.144). In line with this result, the mean volume of MfBs was not different in APP/PS1 and Wt mice (Wt 15.2 μm^3 ± 0.4 μm^3 n=609, 5 mice; APP/PS1 14.6 μm^3 ± 0.4 μm^3, n=898, 5 mice; Mann-Whitney test p=0.1630, Figure 3.13 C). Importantly, Mfs also contact inhibitory interneurons in the hilus and *statum lucidum,* through filopodial protrusions emerging from the MfBs. To get an estimate of the amount of filopodia, we compared the complexity index (calculated as described in the methods section) of the reconstructed MfBs. This index is an indirect method to assess alterations in the intricacy of the structures, such as for example an increase or decrease in size or number of filopodia, since these structures represent a very small volume, but a considerable area of membrane. Our analyses show no significant difference in the average complexity index between both genotypes (Wt 3.0 ± 1.2, n=609, 5 mice; APP/PS1 3.5 ± 1.4, n=898, 5 mice; Mann-Whitney test p=0.3116). However the cumulative distribution analysis showed a strong difference in the complexity index of MfBs between Wt and APP/PS1 mice (KS test p<0.0001; Figure 3.13 D). To further analyse the difference in complexity we divided MfBs in three categories based on their volume: small (< 10 μm^3), medium (10 − 20 μm^3) and large (> 20 μm^3). We observed a tendency for an increased complexity for the large MfBs in the APP/PS1mice. The complexity index for large MfBs is 4.3 ± 0.2 for Wt mice (n=5 mice) and 4.8 ± 0.2 for APP/PS1 mice (n=5 mice; Figure 3.13 E). An increase in the complexity index could indicate an increase in number and/or length of MfB filopodia.
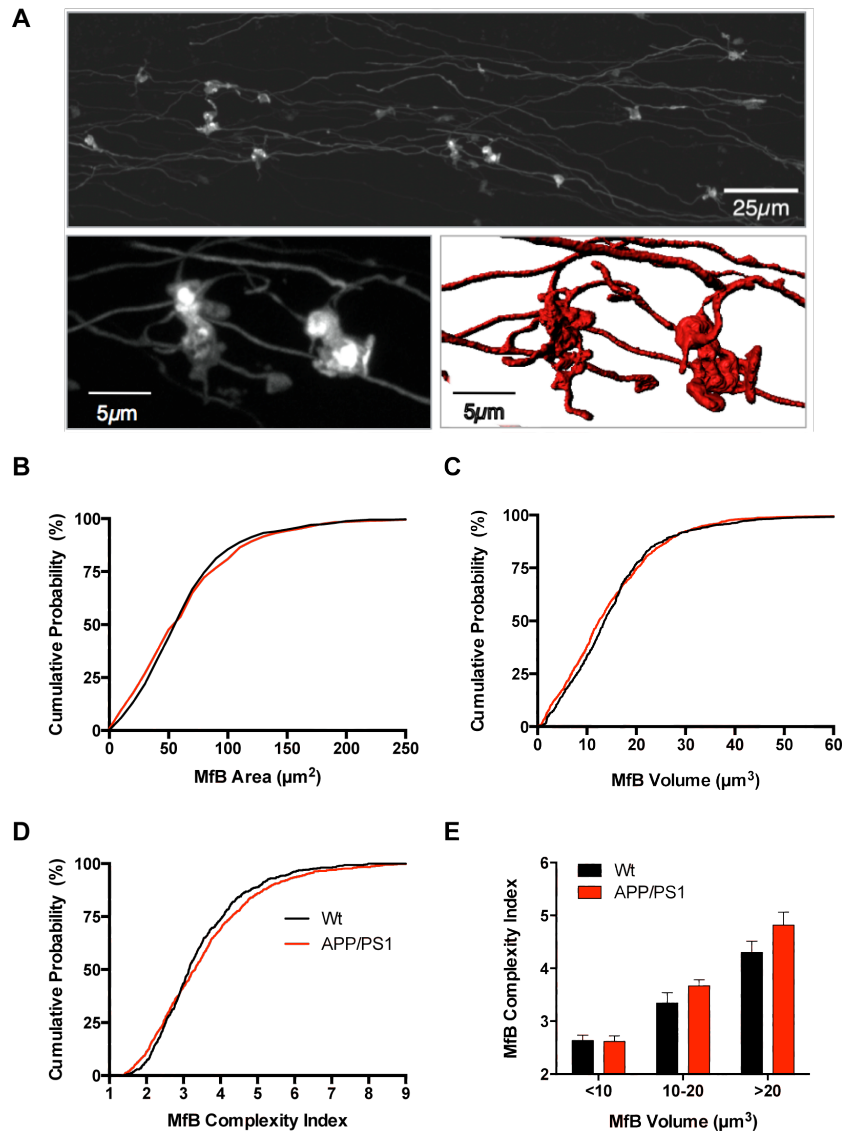
Figure 3.13 MfB morphology is unaltered in APP/PS1 mice at 6 months of age

A. Example image of Mf axons along stratum lucidum acquired with confocal microscopy (upper panel). Zoom in on two examples of MfBs (lower left panel) and a representative reconstruction obtained with IMARIS software (lower right panel). This type of 3D reconstruction allows accurate measurements of surface area and volume. **B.** Cumulative distribution of MfB area from reconstructed MfBs for Wt (black trace) and APP/PS1 mice (red trace), Ks test p=0.144. **C.** Cumulative distribution of volume from reconstructed MfBs from Wt (black trace) and APP/PS1 mice (red trace), Ks test p>0.999. **D.** Cumulative distribution of the complexity index calculated for reconstructed MfBs showing a significant difference between Wt (black trace) and APP/PS1 mice (red trace), Ks test p<0.0001. This index uses both area and volume of each MfB analyzed. **E.** Summary plot representing the complexity index of three classes of MfBs. Smaller MfB have a volume smaller than 10 μm^3, medium MfBs have a volume ranging from 10 to 20 μm^3, and large MfBs have volumes values above 20 μm^3. For Small MfBs the complexity index is 2.6 ± 0.1 for Wt mice and 2.6 ± 0.1 for APP/PS1 mice, displaying no difference between genotypes. Medium sized

MfBs are more complex in both genotypes (Wt 3.3 ± 0.2; APP/PS1 3.7 ± 0.17). Finally for large MfBs with a volume larger than 20 μm^3, the complexity index was, despite the visible tendency, not significantly altered in the APP/PS1 mice (Wt 4.3 ± 0.2; APP/PS1 4.8 ± 0.2, n=5 mice for each genotype). Data represented as mean ± SEM.

ThE, the post-synaptic partners of MfBs, can display alterations in their morphology after different stimuli such as learning and stress conditions (Sandi et al., 2003; Stewart et al., 2005). To study the post-synaptic component of Mf synapses in APP/PS1 mice, a RV with the native envelope was used to infect CA3 cells from their axon terminals. The injection performed in the hippocampal CA1 region resulted in a sparse labeling of CA3 cells ideal for 3D reconstructions (Figure 3.14 A).

Reconstructions were performed for ThEs located in the stratum lucidum. ThEs located on basal dendrites of CA3 pyramidal cells were excluded from the whole study. The number of ThEs per cell was not different between the two genotypes (Wt 58.2 ± 4.0, n=9 complete cells; APP/PS1 51.6 ± 5.8, n=8 complete cells; t-test p=0.3539, Figure 3.14 B). For this analysis only cells with a complete ThE arborization within the 70µm slices were reconstructed and analyzed. Analyzing the surface area of the CA3 thorns reconstructed we found no changes of the mean surface values in the APP/PS1 mice (Wt 16.6μm^2 ± 0.6μm^2, n=1259, 6 mice; APP/PS1 14.2μm^2 ± 0.5μm^2, n=945, 6 mice; Mann-Whitney test p=0.1074). Also the distribution of these surfaces was not altered in the APP/PS1 mice (KS test p=0.99; Figure 3.14 C). In contrast, when plotting the volume of the reconstructed thorns we found no alteration of the thorn mean volume (Wt 2.4μm^3 ± 0.1μm^3, n=1259, 6 mice; APP/PS1 2.0μm^3 ± 0.08μm^3, n=945, 6 mice; Mann-Whitney test p=0.1221) but a significant alteration of the volume distribution (KS test p<0.0001, Figure 3.14 D) in APP/PS1 mice. Summary plot of the area and volume of each ThE reconstructed (Figure 3.14 E) shows that the relationship between these two parameters is not altered by chronic overexpression of Aβ during 6 months (Wt linear regression 5.7 ± 0.04; APP/PS1 linear regression 5.6 ± 0.06).
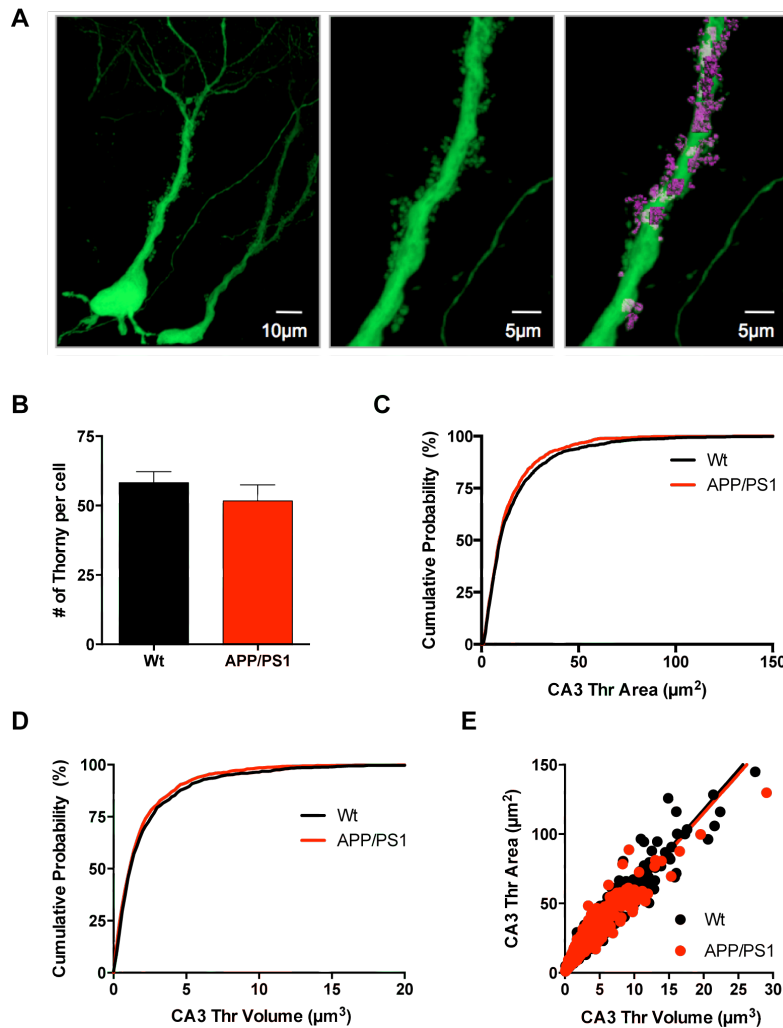
Figure 3.14 Morphology of the postsynaptic thorny excrescences of CA3 cells is normal in the APP/PS1 mice

A. Example image of the proximal dendrite of a CA3 pyramidal cell infected by RABVΔG-eGFP (RG) acquired with confocal microscopy (left panel) and subsequent reconstruction of ThE in *stratum lucidum* obtained by IMARIS software. **B.** Bar graph representing the total number of ThE per pyramidal cell. The number is not different in APP/PS1 and Wt mice. Just ThE on apical dendrites were analyzed and only cells with complete apical dendritic arborization were used (Wt n=9, APP/PS1 n=8, t-test p=0.3539). **C.** Cumulative distribution of the area from reconstructed ThE shows no difference between Wt (black trace) and APP/PS1 mice (red trace), Ks test p=0.99. There is no difference regarding the mean surface area of reconstructed MfBs in the two genotypes (Wt 16.6μm^2 ± 0.6m^2, n=1259, 6 mice; APP/PS1 14.2μm^2 ± 0.5m^2, n=945, 6 mice; Mann-Whitney test p=0.1074). **D.** Cumulative distribution of the volume of reconstructed ThE shows that there is a small difference in the distribution of ThE between Wt (black trace) and APP/PS1 mice (red trace), Ks test p<0.0001. Nevertheless, the mean volume values in the APP/PS1 mice is not different from those in the Wt littermates (Wt 2.4μm^3 ± 0.1μm^3, n=1259, 6 mice; APP/PS1 2.0μm^3 ± 0.08μm^3, n=945, 6 mice; Mann-Whitney test p=0.1221). **E.** Summary plot of the relation between surface area and volume of CA3 thorns in the Wt (black circles) and

After careful morphometric examination of several parameters of Mf synapses, dissecting pre- and post-synaptic compartments, no major alterations were found. The only statistical difference we found was in the volume distribution of thorny excrescences from CA3 pyramidal cells. This could possibly be related to the impairment found in the post-synaptic form of Mf LTP.

3.3 Associative/Commissural Synapses in APP/PS1 Mice

3.3.1 Associative/Commissural LTP is Abolished in APP/PS1 Mice

CA3 pyramidal cells also receive inputs from associative fibers originating from CA3 cells of the ipsilateral hemisphere and from commissural fibers, arising from the contralateral hemisphere (Ishizuka, Weber, & Amaral, 1990). These synapses display a classical form of LTP that is NMDAR-dependent (Debanne, Gähwiler, & Thompson, 1998). The recurrent fibers of the A/C pathway are thought to enable an intense activation of CA3 pyramidal cells that may play a central role in memory formation (Hagena & Manahan-Vaughan, 2011; Kesner & Warthen, 2010; Nakazawa et al., 2002; Treves & Rolls, 1994). To study putative alterations in these connections in APP/PS1 mice, we positioned our stimulating pipette in the *stratum radiatum* as shown in Figure 3.15 A. We used frequency facilitation (when switching the stimulus frequency from 0.1 to 1 Hz) as an exclusion criteria for selecting an A/C inputs against Mf inputs (Figure 3.15 B). A PPF protocol with two consecutive pulses (with 40ms stimulus interval) was applied to test for an alteration of presynaptic properties in APP/PS1 mice. PPF is present at these synapses, although less prominent than the one recorded from Mf synapses. At 6 months, we found no statistical difference in PPF of A/C synapses in APP/PS1 mice (Wt 1.8 ± 0.06, n=21; APP/PS1 1.9 ± 0.07, n=25; t-test p=0.0544; Figure 3.15 D).
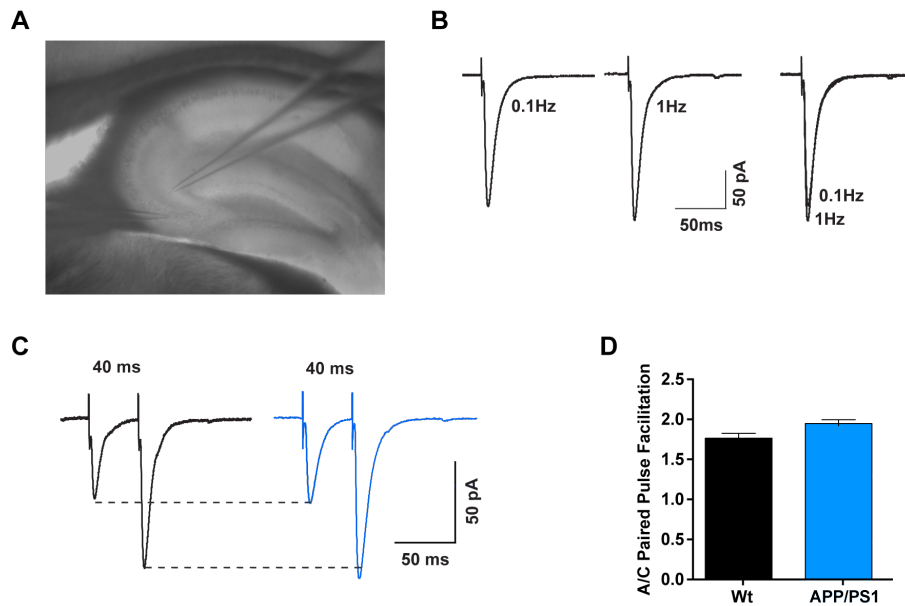
Figure 3.15 A/C synapses of APP/PS1 mice display normal short-term plasticity

A. Example image of our recording conditions: a mouse brain slice under the microscope with a patch pipette recording from a CA3 pyramidal cell and the stimulating pipette positioned in the Stratum Radiatum above the CA3b area. **B.** Representative traces of A/C-EPSCs evoked in our experimental conditions (room temperature). A/C synapses were selected based on the lack of facilitation when the stimulation is switched from 0.1 Hz (left panel) to 1 Hz (middle); the two traces were superimposed in the right panel. **C.** Average of 15 traces illustrating PPF at a inter stimulus interval of 40 ms for Wt (black traces) and APP/PS1 (red traces) A/C synapses. **D.** Bar graph representing the ratio between the amplitude of the second EPSCs over the first EPSCs obtained during the PPF stimulating protocol; t-test p=0.0544 between Wt (black bar, n=21) and APP/PS1 (blue bar, n=27). Data represented as mean ± SEM.

We next investigated if the LTP described at A/C fiber inputs was altered in APP/PS1 mice. We tested a commonly used LTP inducing protocol for triggering NMDAR-dependent plasticity, the depolarization pairing protocol (depo-pairing), where a depolarization from -70 mV to 0 mV of the postsynaptic cell is paired with 100 presynaptic stimuli at 2 Hz (illustrative representation in Figure 3.16 A). The LTP was triggered in the absence of GABAergic input influence (blocked by 10 μM Bicuculline and 3 μM CGP-55845). Surprisingly, at 6 months, no LTP was observed in APP/PS1 mice (Figure 3.16 B). The amplitude of AMPA-EPSCs recorded 30 minutes after the pairing protocol was not different from baseline in APP/PS1 mice (APP/PS1 92.8% ± 11.5%, n=8), whereas a robust potentiation was observed in Wt mice (Wt 218.0% ± 37.5%, n=8; t-test p=0.0066; Figure 3.16 C and D).
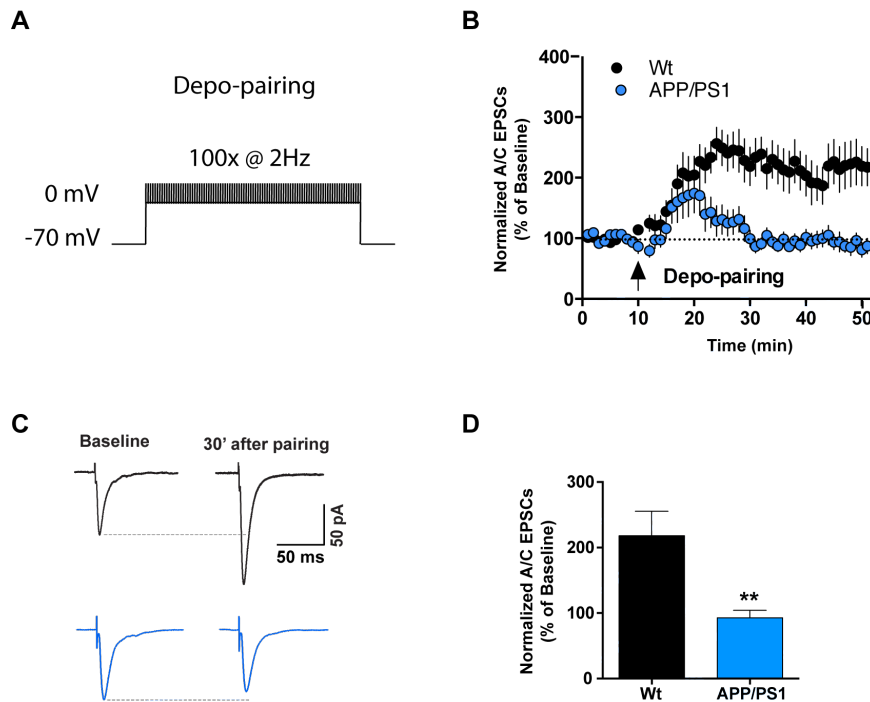
Figure 3.16 Complete loss of NMDAR-dependent LTP at A/C synapses in 6 months APP/PS1 mice

A. Schematic representation of the train applied to trigger NMDAR-dependent LTP at A/C synapses: depolarization from -70 mV to 0 mV of the postsynaptic cell was paired with presynaptic stimulation (100 stimuli at frequency 2 Hz; 50 sec depolarization). **B.** Summary plot of A/C LTP time course for Wt (black circles, n=8) and APP/PS1 (blue circles, n=8) cells. The LTP protocol was applied at the time indicated by the arrow. The LTP protocol was applied at the time indicated by the arrow. Mf AMPAR-mediated EPSCs, obtained every 10 sec (0.1 Hz) were averaged every minute and normalized to the mean amplitude of the 10 min period preceding the LTP induction protocol. **C.** Traces represent A/C EPSCs obtained at -70 mV with a stimulus frequency of 0.1 Hz during Baseline (10 min) and LTP (between 30 min to 40 min after the train). Black traces show an increase of A/C EPSCs, from a representative cell recorded from a Wt animal. Blue traces shown illustrate the lack of LTP of A/C-EPSCs recorded from an APP/PS1 animal. **D.** Bar graph representing the mean amplitude of A/C EPSCs recorded between 30 to 40 minutes after LTP induction. Values are expressed as percentage of baseline A/C EPSCs amplitude. Black bar represents data obtained from Wt mice and blue bar data from APP/PS1 mice, t-test p=0.0066. Data represented as mean ± SEM. ** represent $p<0.01$.

It is well established that there are two requirements for the induction of LTP: glutamate binding to NMDARs and membrane depolarization (Nicoll & Roche, 2013). With the depo-paring protocol, one can precisely control membrane depolarization (facilitated by the use of cesium-based intracellular solution to block most of K^+

channels) during synaptic stimulation. Hence the loss of LTP may be due to a change in NMDARs signaling, but not to insufficient membrane depolarization.

3.3.2 The Associative/Commissural NMDAR/AMPAR Ratio is Not Altered in APP/PS1 Mice

We thus measured the NMDAR/AMPA ratio at A/C synapses, as described above for Mf synapses (Figure 3.9), in both Wt and APP/PS1 mice. After recording the AMPAR component at -70 mV, the cells were held at +40 mV and EPSCs recorded at a frequency of 0.1 Hz with and without NBQX (20 μM) in order to isolate NMDAR-EPSCs. The NMDAR/AMPAR ratio was evaluated using both isolated currents (AMPA-EPSCs at -70 mV and NMDAR-EPSCs at +40 mV in the presence of NBQX) and the two components at +40 mV (AMPA-EPSCs measured as the peak amplitude and NMDAR-EPSCs measured 40 ms after the peak; Figure 3.17 A). While holding the cell at -70 mV, the stimulation strength was tuned to obtain AMPAR-EPSCs of around 200 pA (absolute amplitude values are displayed in Figure 3.17 B) and afterwards kept unchanged until the end of the protocol. At 6 months APP/PS1 mice had a NMDAR/AMPAR ratio of around 40% with no significant difference between genotypes (-70mV/+40mV method: Wt 36.2% ± 4.2%, n=18; APP/PS1 37.1% ± 5.0%, n=16; t-test p=0.8935; Figure 3.17 A and C). Using the values recovered at +40mV the NMDAR/AMPAR ratio was approximately 60%, but again no different was observed between APP/PS1 and Wt mice (Total +40mV method: Wt 53.0% ± 2.1%, n=18; APP/PS1 48.3% ± 3.9%, n=16; t-test p=0.2860 Figure 3.17 D).
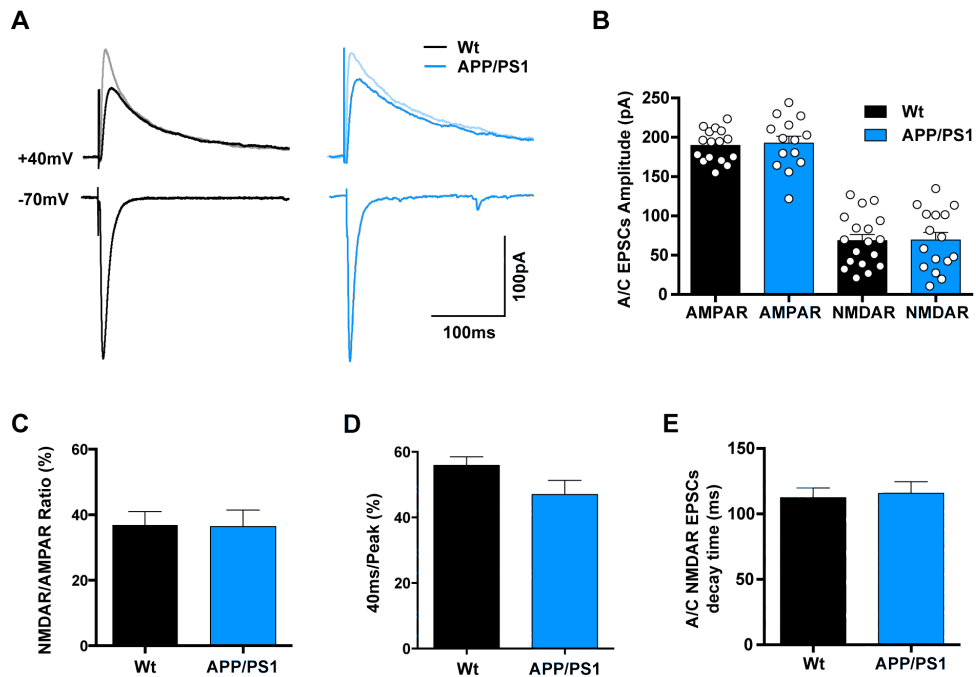
Figure 3.17 The ratio of A/C NMDAR-EPSCs to AMPAR-EPSCs is maintained in APP/PS1 mice with 6months

A. Representative traces of A/C EPSCs recorded at negative (-70 mV) and positive potentials (+40 mV) with and without NBQX (20 μM) illustrating no major differences between the two genotypes (black traces are examples from a Wt cell and blue traces from a APP/PS1 cell). Bicuculline was present throughout all experiments. **B.** Absolute amplitudes of AMPAR-EPSCs obtained at -70 mV (Wt 192.7 pA ± 5.1 pA, n=18; APP/PS1 186.5 pA ± 8.9 pA, n=16) and absolute amplitudes of corresponding NMDAR-EPSCs obtained at +40 mV (Wt 68.4 pA ± 7.8 pA, n=18; APP/PS1 69.3 pA ± 9.6 pA, n=16) in the same cells; black bars from data collected in Wt mice and blue bars from data of APP/PS1 mice. **C.** Bar graph for mean values of NMDAR/AMPAR ratios obtained with isolated currents at -70 mV (AMPAR) and +40 mV (NMDAR with NBQX). Black bar represents Wt mice (n=18 cells) and red bar represents APP/PS1 mice (16 cells). **D.** Bar graph representing mean values obtained for the NMDAR/AMPAR ratio performed at +40 mV in the presence of bicuculline. The ratio, calculated as the amplitude 40 ms after the peak divided by the peak amplitude, was not different between the Wt (black bar, n=18) and APP/PS1 (blue bar, n=16) cells analyzed. **E.** Summary plot of the mean decay time of A/C NMDAR-mediated EPSCs recorded at a frequency of 0.1 Hz and a holding potential of +10 mV. Average decay times are not statistically different (t-test, p=0.9571) between Wt (black bar, n=16) and APP/PS1 mice (blue bar, n=15). Data represented as mean ± SEM.

3.3.3 Morphological Alterations of Associative/Commissural Spines in APP/PS1 Mice

Given the importance of synaptic loss in AD patients and given the alterations of synaptic plasticity we observed in APP/PS1 A/C synapses, it was fundamental to study if these alterations could be correlated with density and/or morphological changes of CA3 dendritic spines situated in the *stratum radiatum*. Bilateral stereotaxic injections of the retrograde RV (Wickersham, Finke, Conzelmann, & Callaway, 2007) was used to infect CA3 cells by their projections onto CA1 (for a more details see Methods section 2.4).

We used superresolution images of STED microscopy to faithfully be able to measure the spines of the A/C which are considerably smaller (see Table 3.1) then the ThEs or MfBs. Similar to previous reports in other hippocampal areas, we found alterations of spine density in 6 months old APP/PS1 mice (Wt 11.5 ± 1.1 spines/10 μm, n=8 branches; APP/PS1 8.7 ± 0.6 spines/10 μm, n=9 branches; unpaired two-tailed t-test p=0.0370; Figure 3.18 B). Despite the decreased A/C spine density, no change in spine size (head diameter, neck diameter of spine length) was found when analyzing spines from distal dendrites of CA3 cells (n=15 branches of 4 Wt mice and n=14 branches of 4 APP/PS1 mice). As illustrated in Figure 3.18 C we noticed no reduction of the spine head diameter in APP/PS1 mice (Data shown in Table 3.1; Mann-Whitney test p=0.2771). Also the distribution of the spine head values obtained was unaltered in the APP/PS1 compared to Wt mice (KS test p=0.287 with n=234 for the Wt and n=155 for APP/PS1; Figure 3.18 D). No alteration of the average spine length was observed in the APP/PS1 mice compared to their Wt littermates (Table 3.1; Mann-Whitney test p=0.1484; Figure 3.18 E). Regarding the spine length distribution we observed an alteration in the cumulative probability plot (Figure 3.18 F; KS test p=0.0437 with n=234 for the Wt and n=155 for APP/PS1 mice). No change was found when examining the spine neck diameter of A/C spines in Wt and APP/PS1 mice (Table 3.1; Mann-Whitney test p=0.6354; Figure 3.18 G). Also the distribution of the spine head neck diameter measurements is unaltered in the APP/PS1 compared to Wt mice (KS test p=0.0844; n=234 spines for the Wt and n=155 spines for APP/PS1 mice; Figure 3.18 H).
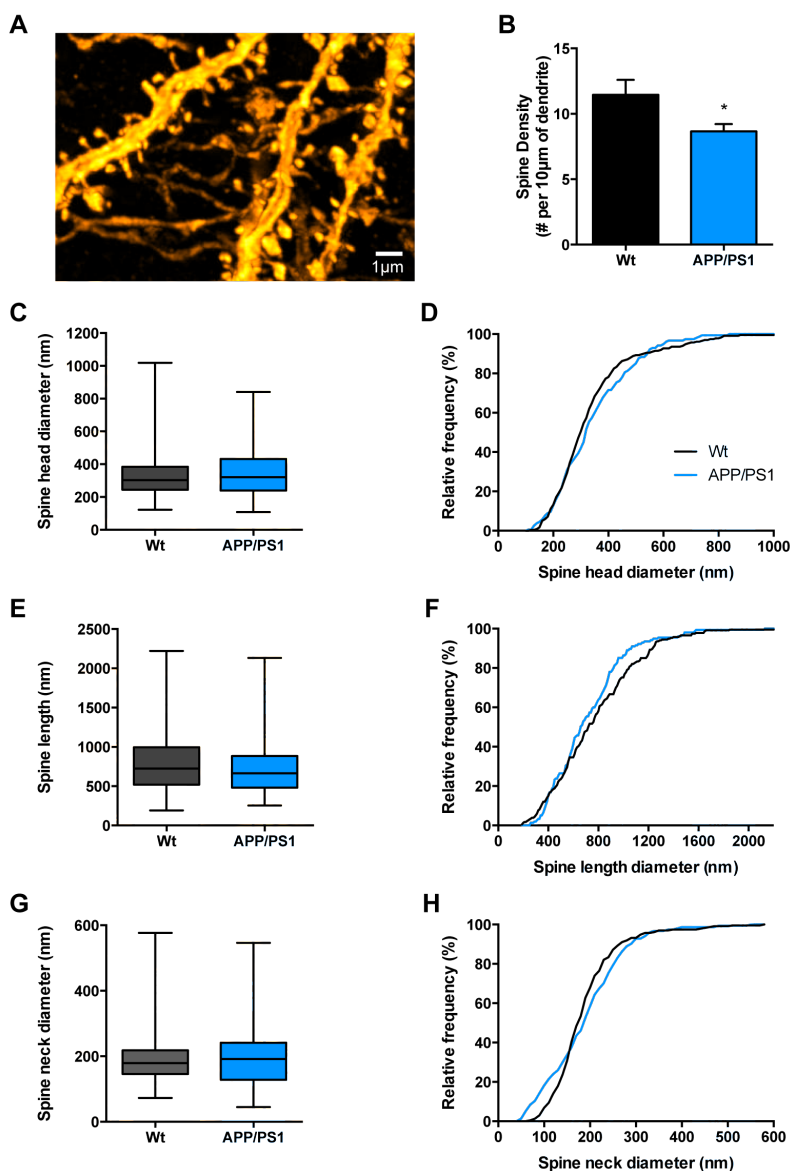
Figure 3.18 CA3 pyramidal cells display a reduction in spine density but no morphological alteration of the dendritic spines in *stratum radiatum*

A. Example STED image of a distal dendrite from a CA3 pyramidal neuron infected with RABV expressing eGFP. Images were acquired in the portion of the dendrite right after the last thorny excrescency. For illustration purposes the image lookup table was changed to a pre-defined Orange LUT using the ImageJ software. **B.** Spine density summary plot shows a significant decrease of the spines density per 10 μm of dendrite found from 11.5 ± 1.1 spines/10 μm in Wt (black bar) to 8.7 ± 0.6 spines/10 μm in APP/PS1 (blue bar, n=9) mice (unpaired two-tailed t-test p=0.0370). For this analysis several branches of distal dendrites from CA3 pyramidal cells were analyzed in Wt (n=8 branches, 4mice) and in APP/PS1 mice (n=9 branches, 4mice). **C.** A combined box and whisker plot displays the average spine head diameter (line in the box) with the SEM (boxes) and the total range from minimal to maximal size values (whiskers). The measurements where performed on all spines found along randomly selected dendritic parts, in Wt (black box) and APP/PS1 (blue box) in 4 mice per condition (n=234, 8 slices for Wt, n=155, 8

slices for APP/PS1, Mann-Whitney test p=0.2771). **D.** Summary histogram of the cumulative probability of the spine head diameter in Wt (black trace) and APP/PS1 mice (blue trace) shows no marked difference between genotypes in the proportion of A/C spines with smaller or larger head, KS test p=0.287 (n=234 for Wt and n=155 for APP/PS1). **E**. A combined box and whisker plot representing the average spine length with the SEM (boxes) and the total range of values (whiskers) shows no difference between Wt (black box) and APP/PS1 (blue box) looking at 4 mice per condition (n=234, 8 slices for Wt, n=155, 8 slices for APP/PS1, Mann-Whitney test p=0.1484). **F**. Summary histogram of the distribution of A/C spine length shows a change in the proportion of longer or shorter spines in the APP/PS1 mice (blue line) compared to Wt mice (black line), KS test p=0.0437 (n=234 for Wt and n=155 for APP/PS1). **G.** A combined box and whisker plot displays the spine neck diameter (line inside the box) with the SEM (boxes) and the extreme values (whiskers). No significant difference between Wt (black box) and APP/PS1 (blue box) mice was found (Mann-Whitney test p=0.6354). **H.** Summary histogram illustrates the proportion of spines with a thin or thick neck diameter revealing the absence of a significant change (KS test, p=0.0844) between Wt (black line) and APP/PS1 (blue line) mice.

Genotype	Values	Spine Head	Spine Neck	Spine Length
Wt	**Range**	122.9 nm – 1018 nm	72,96 nm – 577.1 nm	191 nm – 256.1 nm
	Mean	338.7 nm ± 9.842 nm	191,3 nm ± 4.823 nm	773.6 nm ± 22.76 nm
	Median	303.1 nm	179.1 nm	725.2 nm
	n (slices)	4 animals/ 8 slices/ 234 spines		
APP/PS1	**Range**	108 nm – 841.2 nm	45.1 nm – 546,3 nm	256.1 nm – 2132 nm
	Mean	347.2 nm ± 11.30 nm	192.1 nm ± 6.897 nm	720.3 nm ± 24.41 nm
	Median	320.7 nm	191.7 nm	663.5 nm
	n (slices)	4 animals/ 8 slices/155 spines		

Table 3.1 Summary of the A/C spine size measurements achieved with STED imaging

3.4 Role of CA3 NMDARs in Synaptic Dysfunction

3.4.1 CA3 NMDAR Subunit Composition is Not Altered in Mossy Fiber and Associative/Commissural Synapses

The relative expression of the different GluN2 NMDAR subunits at the synapse strongly modulates long-term plasticity phenomena (ref). We can thus hypothesize that the selective dysfunction of NMDA-dependent long-term synaptic plasticities observed in our APP/PS1 might results from an alteration in the GluN2 NMDAR subunit composition of synaptic NMDARs in CA3 pyramidal cells of our AD model. In addition several works have described GluN2B subunit as the one mediating most of the toxic effects of Aβ oligomers applied in culture neurons and acute slices (Ferreira et al., 2012; Hu, Klyubin, Anwyl, Anwy, & Rowan, 2009; Rönicke et al., 2011). We tested if the chronic accumulation of Aβ peptides in APP/PS1 mice would change the composition of NMDARs at both Mf and A/C synapses.

To unravel putative changes we used a highly selective, activity dependent blocker of GluN2B-containing NMDARs (Ro 25-6981) (Fischer et al., 1997). CA3 pyramidal cells were voltage-clamped at +40 mV and NMDAR-EPSCs were pharmacologically isolated. Mf NMDARs EPSCs were recorded at a frequency of 0.1 Hz for eight minutes. After this short baseline, 20 pulses at 1 Hz were performed in each cell to ensure the identity of the Mf input. Ro 25-6981 (1 μM) was applied after the 1 Hz stimulation and the NMDARs EPSCs registered for 40 minutes at a frequency of 0.1 Hz. The FF was quantified and cells with facilitation smaller than 3-fold were discarded. Figure 3.19 A displays the time course of the Ro 25-6981 action for both Wt and APP/PS1 cells. Our data indicate that GluN2B subunits are present at Mf synapses of both genotypes, as we observed a reduction of both NMDARs EPSCs amplitude and decay time constants after pharmacological inhibition of GluN2B with Ro 25-6981 (Figure 3.19 D). However, there was no difference in the percentage of inhibition between the two genotypes, indicating a similar content in GluN2B. Figure 3.19 B shows quantification of the remaining EPSCs amplitude (Wt 71.8% ± 9.6%, n=11; APP/PS1 66.9% ± 9.2%, n=11; unpaired t-test p=0.8315). In line with this, we found no difference between Wt and APP/PS1 mice in the decay time of NMDARs EPSCs before (Wt$_{control}$ 87.0 ms ± 3.2 ms, n=11; APP/PS1$_{control}$ 90.8 ms ± 5.0 ms, n=11; unpaired t-test p=0.5200) and after the application of Ro 25-6981 (WtRo$_{25-6981}$ 71.2 ms

± 1.9 ms, n=11; APP/PS1$_{Ro25-6981}$ 77.3 ms ± 4.2 ms, n=11; unpaired t-test p=0.1964; Figure 3.19 C and D).

Figure 3.19 Pharmacological inhibition of GluN2B subunits at Mf synapses

A. Summary plot describing the time course of Mf NMDARs-EPSCs inhibition after application of the GluN2B subunit antagonist Ro 25-6981 (1 μM). Recordings from Wt cells are summarized by black circles (n=12) and APP/PS1 cells by red circles (n=11) cells. The antagonist was present from the ninth minute until the end of the recordings. Mf NMDAR-mediated EPSCs, obtained every 10 sec (0.1 Hz) were averaged every minute and normalized to the mean amplitude of the 8 min period preceding the LTP induction protocol. **B.** Bar graph representing the mean amplitude of Mf NMDARs EPSCs recorded between 30 to 40 minutes after drug application. Values are expressed as percentage of baseline Mf NMDAR-EPSCs amplitude. **C.** Traces represent Mf NMDAR-EPSCs obtained at stimulus frequency of 0.1 Hz during Baseline (8 min), and after 30 min of Ro 25-6981 action. Black and red traces from representative cells from Wt and APP/PS1 cells, respectively. **D.** Summary plot of mean decay time of Mf NMDAR-mediated EPSCs recorded at a frequency of 0.1 Hz. Average decay times are not statistically different between Wt (black bars) and APP/PS1 mice (red bars). The mean decay time before and after Ro 25-6981 is different for both genotypes, Wt (paired t-test, p<0.0001) and APP/PS1 (paired t-test p, p=0.0263) mice. Data represented as mean ± SEM, * represents p<0.05, *** represent p<0.0001

We then investigated if the relative content in GluN2B of NMDA-EPSCs at A/C fiber synapses was modified in APP/PS1 mice. The decay time of NMDAR-EPSCs can give an indication about changes in NMDARs subunit composition (Paoletti et al.,

2013). We observed no alteration between the two genotypes at A/C synapses (Wt 114.5 ms ± 6.7 ms, n=16; APP/PS1 115.1 ms ± 8.3 ms, n=15; t-test p= 0.9571; Figure 3.17 E). Pharmacological inhibition of GluN2B subunit containing NMDARs with Ro 25-6981 produced similar effects in both genotypes at these synapses. Figure 3.20 A plots the time course of the drug action on cells of Wt and APP/PS1 mice. In agreement with the literature (Rebola et al., 2011), we found a higher content of GluN2B in the A/C synapses as compared to Mf synapses, leading to the higher decay time values at A/C synapses. A small tendency (not statistically significant) for a decreased content of GluN2B subunits in A/C synapses can be observed in APP/PS1 mice (Wt 59.0% ± 5.9%, n=13; APP/PS1 73.6% ± 7.6%, n=16; unpaired t-test p=0.1551; Figure 3.20 B). In both Wt and APP/PS1 mice the application of Ro 25-6981 (1 μM) resulted in a decrease of the A/C NMDARs decay time (Wt$_{control}$ 119.3 ms ± 11.9 ms; WtRo$_{25\text{-}6981}$ 86.0 ms ± 7.9 ms, n=13, paired t-test p=0.6658; APP/PS1$_{control}$ 127.3 ms ± 13.07 ms; APP/PS1$_{Ro25\text{-}6981}$ 92.70 ms ± 5.388 ms, n=16, paired t-test p=0.4740; Figure 3.20 C and D), confirming the presence of GluN2B containing receptors at these synapses. Nevertheless, and in line with the lack of statistical difference in peak NMDARs amplitudes, we observe no difference in the decay times measure before or after Ro 25-6981 application (Wt$_{Baseline}$ n=13, APP/PS1$_{Baseline}$ n=16; unpaired t-test, p=0.6658; Wt$_{Ro\text{-}256981}$ n=13, APP/PS1$_{Ro\text{-}256981}$ n=16; unpaired t-test p=0.4740; Figure 3.19 D).
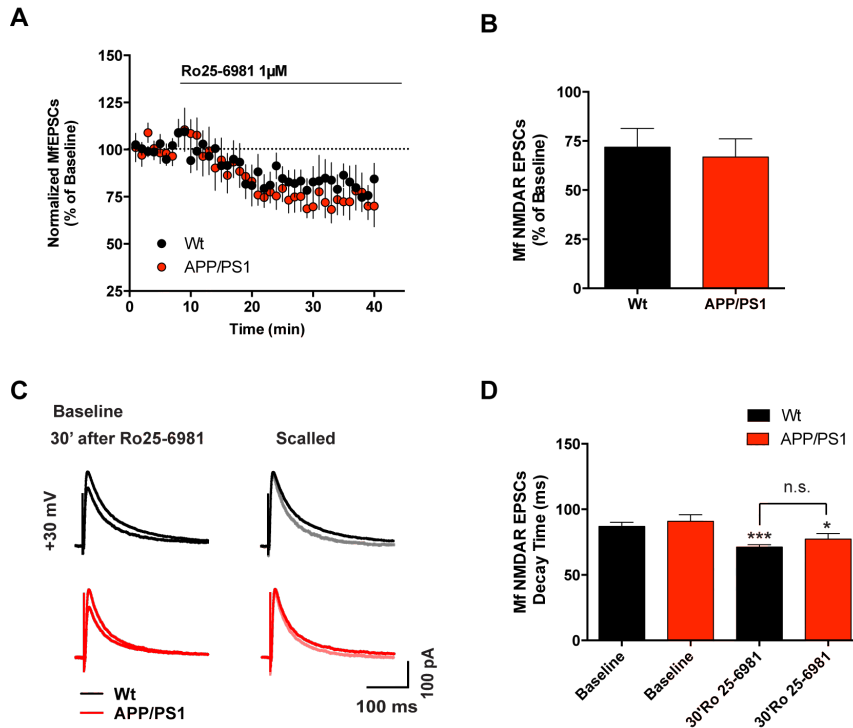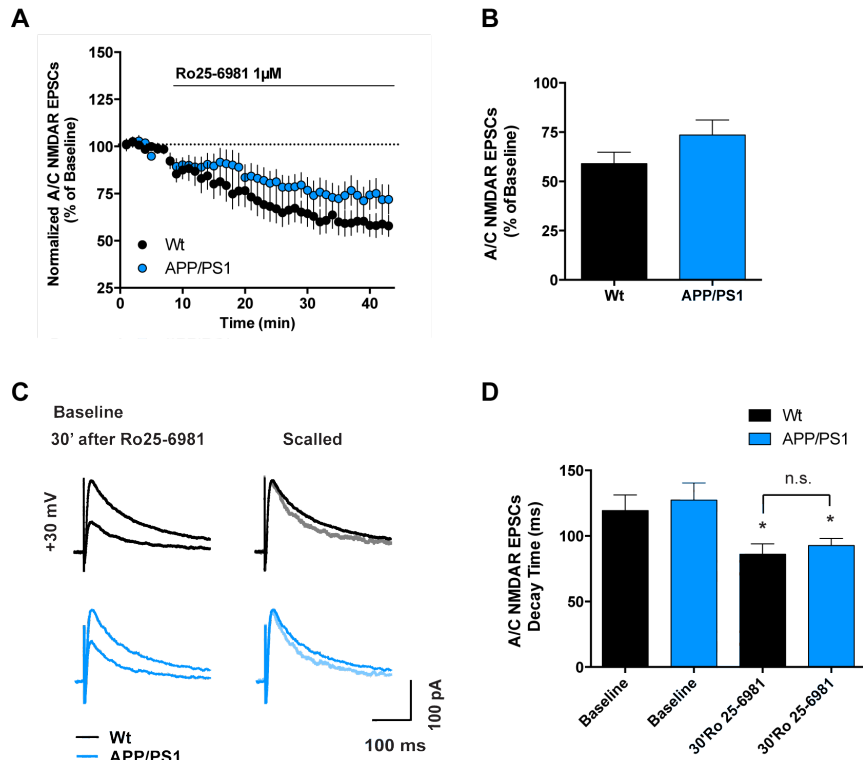
Figure 3.20 Pharmacological inhibition of GluN2B subunits at A/C synapses

A. Summary plot describing the time course of A/C NMDARs-EPSCs inhibition after application of the GluN2B subunit antagonist Ro 25-6981 (1 μM)(Wt cells, black circles n=13; APP/PS1 cells, red circles, n=16). The antagonist was present from the 9th minute until the end of the recordings. A/C NMDAR-mediated EPSCs, obtained every 10 sec (0.1 Hz) were averaged every min and normalized to the mean amplitude of the 8 min period preceding the LTP induction protocol. **B.** Bar graph representing the mean amplitude of A/C NMDARs EPSCs recorded between 30 to 40 minutes after drug application. Values are expressed as percentage of the baseline A/C NMDAR-EPSCs amplitude. Black bar represents data from Wt (n=13) and the blue one from APP/PS1 mice (n=16). **C.** Representative traces of A/C NMDAR-EPSCs obtained at stimulus frequency of 0.1 Hz during Baseline (8 min), and after 30 min of Ro 25-6981 action (10 min). Black and blue traces from representative cells from Wt and APP/PS1 cells, respectively. **D.** Summary plot of the mean decay time of A/C NMDAR-mediated EPSCs recorded at a frequency of 0.1 Hz. Average decay times are statistically different between EPSCs before and after Ro 25-6981 (1 μM) in Wt mice (black bars, n=13; paired t-test p=0.0350) and in APP/PS1 mice (blue bars, n=16; paired t-test p=0.0254). The decay time of NMDARs registered at A/C synapses from Wt and APP/PS1 mice was not different during the 8minutes of baseline (unpaired t-test p=0.6658) of after 30 minutes of Ro25-691 bath application (unpaired t-test p=0.4740). Data represented as mean ± SEM, * represents p<0.05.

3.4.2 Extrasynaptic NMDARs in CA3 Pyramidal Cells

In the adult hippocampus both GluN2A and GluN2B subunit are prevalent. Although there is a tendency for enrichment of GluN2A at synapses versus GluN2B being more abundant at extrasynaptic locations (Groc et al., 2006; Martel, Wyllie, & Hardingham, 2009), there is no description of a clear-cut specific segregation of these subunit. At the synaptic level it is currently accepted that the majority of NMDARs are actually triheteromeric receptors composed of one GluN2A subunit and one GluN2B subunit (Paoletti et al., 2013). With the previous experiments we rule out that the subunit composition of NMDARs is altered as result of chronic overexpression of mutated APP and PS1 genes. Nevertheless, with the experiments in Figure 3.19 and 3.20 we only analyzed the synaptic pool of NMDARs. Synaptic NMDARs are essential for some of the plasticities examined in this thesis, but extrasynaptic NMDARs can also trigger certain types of plasticities, such as LTD (Liu et al., 2004; Massey et al., 2004). In fact it has been reported that the localization of NMDARs receptors (synaptic versus extrasynaptic) leads to the activation of different intracellular signaling pathways (reviewed in (Hardingham & Bading, 2010)). Importantly, extrasynaptic NMDARs were shown to be essential for Aβ mediated toxicity. Li *et al.* show that LTP inhibition by soluble Aβ applied on acute slices depends on activation of GluN2B-containing NMDA receptors (Li et al., 2011).

Taking advantage of our whole-cell patch-clamp approach we further evaluated a possible alteration of extrasynaptic NMDAR content in CA3 pyramidal cells from APP/PS1 mice. Tonic NMDAR-mediated currents were measured as described previously for CA1 pyramidal cells (Le Meur, Galante, Angulo, & Audinat, 2007; Papouin et al., 2012). CA3 neurons were patched and the membrane potential clamped at +40 mV and GABAergic input was blocked with 10 μM Bicuculline and 3 μM CGP-55845. All glutamatergic input through AMPARs and KARs were also blocked with 20 μM NBQX. In these conditions we found that D-AP5 (50 μM) caused a 33.6 pA ± 3.5 pA shift in the baseline current in CA3 neurons of Wt mice (Figure 3.21 A and B). This value corresponds to the tonic activation of extrasynaptic NMDARs in APP/PS1 CA3 neurons (30.3 pA ± 4.5pA; n=14, unpaired t-test p=0.5733). Our experiments rule out differences in tonic NMDAR-mediated currents in APP/PS1 mice. The complete loss of LTP described in this mouse model of AD is thus not correlated to alterations in number or conductance of extrasynaptic NMDARs.
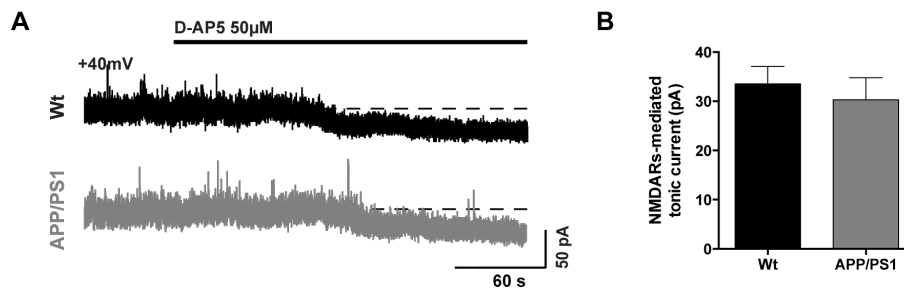
Figure 3.21 Extrasynaptic NMDARs mediate tonic currents at CA3 pyramidal cells
A. Representative examples of the shift in holding current observed at +40 mV in response to D-AP5 (50 μM) revealing the tonic activation of extrasynaptic NMDARs at rest. This shift of similar amplitude in Wt (black trace) and APP/PS1 (green trace). **B.** Summarizing bar graph representing the shift of inward current in Wt (33.6 pA ± 3.5 pA, n=14) and APP/PS1 cells (30.3 pA ± 4.5 pA, n=14, p=0.5733). Data calculated as the difference between baseline (1 minute) and the last of five minutes after drug application. Data represented as mean ± SEM.

3.4.3 D-Serine Does Not Rescue the Impairment of Associative/Commissural LTP

In APP/PS1 mice the average amplitude of mEPSCs recorded in CA3 pyramidal cells is decreased by about 20% (Figure 3.16). This alteration is not accompanied with a change in the NMDAR/AMPAR ratio (Figure 3.2). Based on these experiments we can infer that the NMDAR input to CA3 neurons in APP/PS1 mice should also be reduced. We reasoned that if the loss of LTP at A/C synapses was caused by a reduction in the number of NMDARs, potentiation of synaptic NMDAR-EPSCs by D-serine might rescue the LTP. Conversely if D-serine is without effect on LTP in APP/PS1 mice, the relative decrease in NMDAR amplitude should not be main determinant for the loss of LTP in APP/PS1 mice. Synaptic and extrasynaptic NMDARs are gated by different endogenous coagonists (Papouin et al., 2012), with D-serine acting preferentially on the activity of synaptic NMDARs.
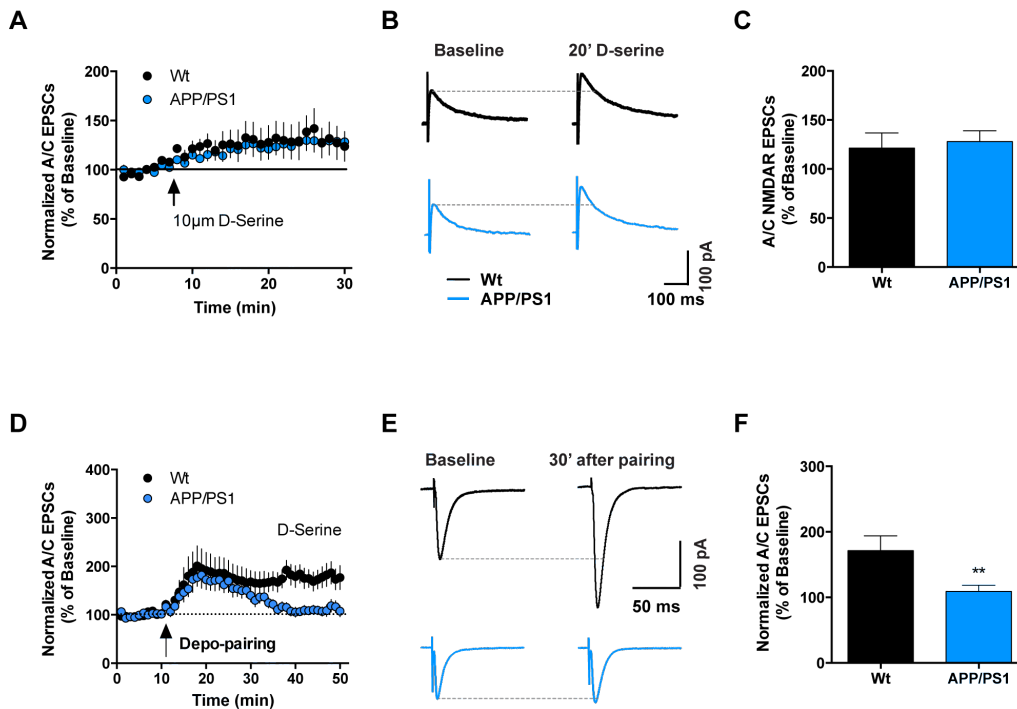
Figure 3.22 D-Serine application increases NMDARs EPSCs at A/C synapses, but does not rescue LTP of A/C inputs

A. Summary plot describing the time course of A/C NMDARs-EPSCs potentiation after bath application of D-serine (10 μM) (Wt cells, black circles, n=8; APP/PS1 cells, red circles, n=8). The co-agonist was applied after 8 minutes baseline recording and present until the end of the recordings (30 min). A/C NMDAR-mediated EPSCs, evoked every 10 sec (0.1 Hz) were averaged every minute and normalized to the mean amplitude of the baseline. **B.** Representative traces of A/C NMDAR-EPSCs obtained at a stimulus frequency of 0.1 Hz during baseline (8 min), and after 20 min of D-serine application (10 min). Black and blue traces from representative cells from Wt and APP/PS1 cells, respectively. **C.** Bar graph representing the mean amplitude of A/C NMDARs EPSCs recorded between 20 to 30 min after drug application. Values are expressed as percentage of the baseline amplitude (Black bar, Wt (n=8); blue bar, APP/PS1 mice, n=8). **D.** Summary plot of A/C LTP time course for Wt (black circles, n=8) and APP/PS1 (blue circles, n=8) cells in the presence of D-serine. The LTP Protocol was applied at the time indicated by the arrow. A/C AMPAR-mediated EPSCs, obtained every 10 sec (0.1 Hz) were averaged every minute and normalized to the mean amplitude of the 10 min period preceding the LTP induction protocol. **E.** Traces of A/C EPSCs obtain at -70 mV with a stimulus frequency of 0.1 Hz during baseline (10 min) and LTP (between 30 min to 40 min after the train) in the presence of D-serine. Black traces show an increase of A/C EPSCs, from a representative cell recorded from a Wt animal. Blue traces shown illustrate the lack of LTP of A/C-EPSCs recorded in APP/PS1 mice. **F.** Bar graph representing the mean amplitude of A/C EPSCs recorded between 30 to 40 minutes after LTP induction. Values are expressed as percentage of baseline A/C EPSCs amplitude. Black bar represents data obtained from Wt mice and blue bar data from APP/PS1 mice, t-test p=0.0076. Data represented as mean ± SEM. ** represents p<0.01.

126

By applying 10 μM of D-serine we could potentiate NMDAR current amplitudes by around 20% (Figure 3.22 A, B). We found no difference between the effect of this coagonist on synapses in Wt or APP/PS1 mice (Wt 121.3 pA ± 15.4 pA, n=8; APP/PS1 127.0 pA ± 11.0 pA, n=8; unpaired t-test p=0.6320; Figure 3.22 C). We next incubated the slices for ~10 minutes before establishing whole-cell configuration and induced the A/C LTP with the depo-paring protocol. No rescue of the A/C LTP was observed in APP/PS1 mice (109.0% ± 9.5%, n=16; unpaired t-test p=0.0076). Surprisingly, we observed a slightly smaller level of LTP at A/C synapses in Wt mice (preincubation with D-serine 171.4% ± 22.6%, n=10; Figure 3.22 C, D and F; control conditions: 218.0% ± 37.5%, Figure 3.16).

3.5 A$_{2A}$R Inhibition Rescues LTP at the Associative/ Commissural-CA3 Pyramidal Cell Synapses

Given the lack of evidence for an impairment of NMDAR signaling, which could be responsible for the loss of A/C LTP in APP/PS1 mice, we focused our attention on signaling by other potentially relevant receptors. The levels of the adenosine A$_{2A}$ receptors in the hippocampus are considered low, but they are potentially relevant in the diseased brain (R. A. Cunha, 2005). In line with this, several A$_{2A}$R antagonists have been shown to prevent memory impairments in different paradigms of AD (Arendash et al., 2006; Canas et al., 2009; G. M. A. Cunha et al., 2008; Espinosa et al., 2013). Furthermore, an up-regulation of A$_{2A}$R (also of A1) was described in brains of AD patients (Albasanz, Perez, Barrachina, Ferrer, & Martín, 2008).

To investigate a possible role of A$_{2A}$Rs in our A/C LTP impairment we incubated the slices for 10 min with SCH 58261 (50 nM), a selective A$_{2A}$R competitive antagonist. After the incubation period, CA3 cells were patched and A/C LTP triggered as described above and the drug was present during all the recording time (SCH 58261, 50nM). We found that blocking A$_{2A}$Rs for 10 min before the triggering of LTP was sufficient to substantially rescue A/C LTP in APP/PS1 mice (APP/PS1$_{control}$ 214.2 ± 33.3%, n=9; APP/PS1$_{SCH58261}$ 154.2 ± 13.9%, n=9; unpaired t-test p=0.0022; Figure 3.22).

A$_{2A}$Rs have been shown to co-localize and act synergistically with mGluR5 in hippocampal neurons (Tebano et al., 2005). At Mf synapses in CA3 pyramidal cells, the two receptors were shown to be essential for LTP of NMDARs (Rebola et al., 2008). Moreover, mGluR5 antagonists have been shown to rescue CFC in APP/PS1 transgenic mice (Um et al., 2013). Based on these evidences we applied a selective antagonist of mGluR5 (10 μM MTEP) for the 10 min prior to the beginning of depo-paring LTP protocol. Experiments done in slices from APP/PS1 animals reveal that 10μM of MTEP can also rescue the LTP levels to values similar to the ones obtained with the A$_{2A}$R antagonist (APP/PS1$_{control}$ 214.2 ± 33.3%, n=9; APP/PS1$_{MTEP}$ 150.8 ± 15.2%, n=8; unpaired t-test p=0.0245; Figure 3.22). The mechanism of action responsible for this striking rescue of LTP is not yet unrevealed, but nevertheless, our data contributes to the idea that both A$_{2A}$Rs and mGluR5s are good targets for AD synaptic deficits (R. A. Cunha, 2005; Um et al., 2013).
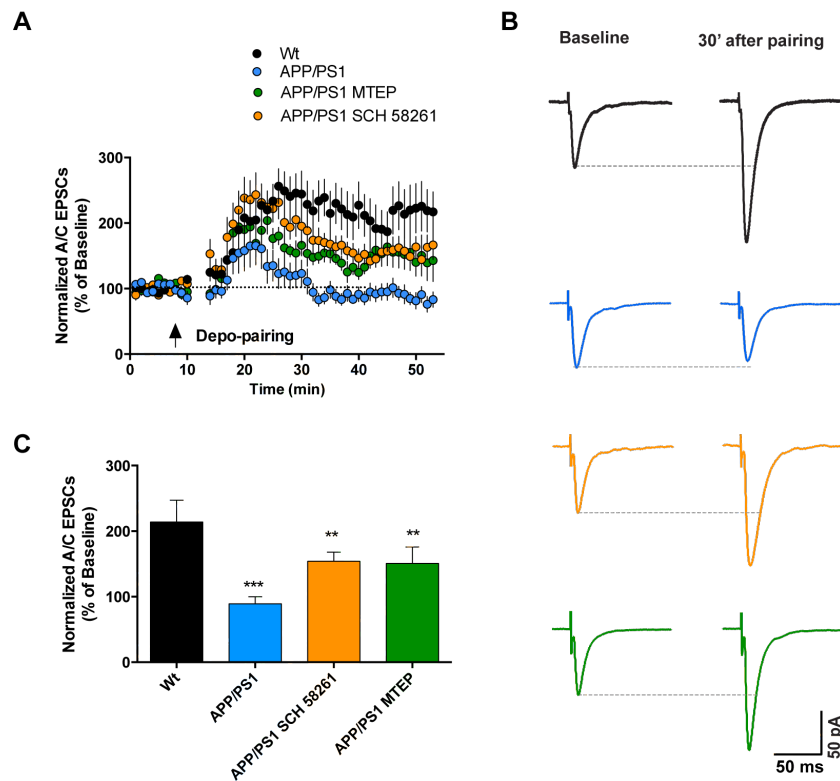
Figure 3.22 A$_{2A}$R and mGluR5 antagonists partially rescue the deficits in A/C LTP

A. Summary plot of A/C LTP time course for Wt (black circles, n=8) and APP/PS1 (blue circles, n=8) mice in the presence of the A$_{2A}$R antagonist (SCH 58261, orange circles) or mGluR5 antagonist (MTEP, green circles). LTP was induced at the time indicated by the arrow. A/C AMPAR-mediated EPSCs, evoked every 10 sec (0.1 Hz) were averaged every minute and normalized to the mean amplitude of the 10 min period preceding the LTP induction protocol. **B.** Traces of A/C EPSCs obtained at -70 mV with a stimulus frequency of 0.1Hz during baseline (10min) and LTP (between 30 min to 40 min after the train) in the presence of SCH58261 and MTEP. Orange and green traces are A/C EPSCs recorded from a representative cell in the presence of SCH58261 or MTEP, respectively. **F.** Bar graph representing the mean amplitude of A/C EPSCs recorded between 30 to 40 minutes after LTP induction. Values are expressed as percentage of baseline A/C EPSCs amplitude (Black bar, Wt mice blue bar APP/PS1 mice). Orange and green bars represent data obtained from APP/PS1 animals in the presence of SCH58261 and MTEP, respectively. One way ANOVA p<0.0001, with Tukey multicomparison test. Data represented as mean ± SEM. ** represents p<0.01, *** represents p<0.001.

Chapter 4

DISCUSSION
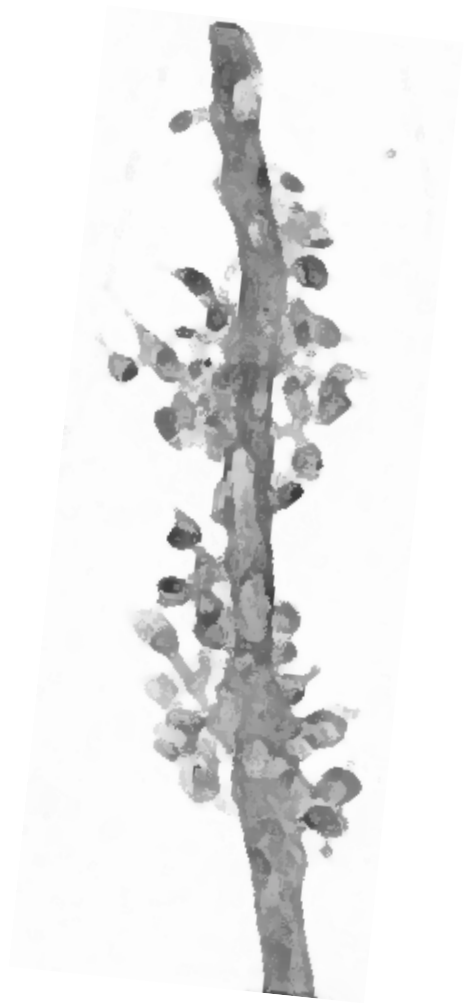
4.1 Physiology of CA3 synapses in Alzheimer's Disease

In the last decade, growing evidence indicates that synaptic loss and dysfunction, accompanied by neural network failure, may be the major cause of cognitive impairments in AD. In this line, amelioration of synaptic function in AD is an important and promising therapeutic approach. The work described in this thesis explores the alterations of the glutamatergic synaptic transmission in the hippocampal CA3 region present in an AD mouse model with early memory deficits. The subsequent paragraphs will discuss the results of this work and address arising questions regarding the implications of the findings. Our work provides new insights concerning the fatal deficits AD causes, clearly discerning the pre versus postsynaptic effects and the apparent synapse specificity of deficits present in CA3 pyramidal cells (Mf vs. A/C synapses). Furthermore, our research examined carefully the contribution of NMDARs to the synaptic failure in a chronic model of AD, offering a potential explanation about the reasons why several drugs, which are currently in clinical trials, show little benefit. Finally we tested the effects of two alternative drug candidates for a rescue, which show in our hands a strong potential restoring the electrophysiological deficits seen on the postsynaptic LTP of A/C-CA3 synapses.

4.1.1 Pre versus Postsynaptic Deficits in Alzheimer's Disease Synapses

As previously described Mf and A/C synapses have different presynaptic properties. The Mf terminals are very particular and constitute an excellent model to evaluate possible effects of chronic Aβ overproduction in presynaptic parameters. After 6 months of overproduction of Aβ peptide and formation of Aβ oligomers we found no differences in the parameters that are correlated with presynaptic function, such as the paired pulse ratio (or PPF) and the failure rate. Furthermore, the characteristic presynaptic form of LTP expressed by MfB is normal in the APP/PS1 mice with 6 months. The HFS applied to induce the Mf LTP caused, simultaneously, a short-term increase in the Mf-EPSCs designated by PTP. Although in our experiments there were no alterations of this parameter neither at 4 (data not shown) or 6 months, there is one report in the literature describing a decrease in Mf PTP in a model of AD (Lee et al., 2012). The work of Lee and colleagues found a decrease in PTP, correlated with altered mitochondrial Ca^{2+} handling, after 2 months of overexpression of Aβ peptides in

an AD mouse model (Tg2576). One possible explanation for this apparent discrepancy is the difference between the two protocols used to trigger this form of short-term plasticity. In the publication of Lee *et al.* the protocol used to induce PTP was milder (25Hz, 5s) and did not trigger presynaptic LTP at Mf synapses. One could hypothesize that the 100 stimuli at 100Hz (repeated 3 times with an interval of 10s (Lanore et al., 2010; Pinheiro et al., 2007) that we used to trigger Mf LTP might have masked subtle alterations on mitochondria Ca^{2+} handling between APP/PS1 and Wt mice and, consequently, no alterations in PTP observed. Several studies support an important role of mitochondrial dysfunction in the early pathology of AD (reviewed in (Moreira, Carvalho, Zhu, Smith, & Perry, 2010)) and the Mf terminals are enriched in mitochondria (Henze, Urban, & Barrionuevo, 1999). Nevertheless a specific presynaptic role of mitochondria in AD related synaptic deficits needs further elucidation.

The APP/PS1 mouse model was recently used in a study looking to alterations on PPF in S/C synapses into CA1 pyramidal cells. This report describes a decrease in PPF at the asymptomatic age of 3 months (Dolev et al., 2013). In contrast with the results from Dolev and colleagues, the great majority of studies performed in AD mouse models overexpressing the APP protein did not find alterations in presynaptic parameters at CA1 S/C synapses over a wide range of ages (Chapman et al., 1999; D'Amelio et al., 2011; Lee et al., 2012; Palop et al., 2007). In agreement, we did not find changes in PPF at 4 (data not shown) or 6 months in both Mf and A/C synapses of CA3 pyramidal cells. Notwithstanding, there is an intriguing reduction of the Mf FF recorded from 6 months APP/PS1 Mf synapses, which is not accompanied by any other presynaptic parameter change at this age. The mechanism responsible for this facilitation is not yet fully understood.

The analysis of the morphology of MfB shows no alterations in APP/PS1 animals with 6 months. These results are in agreement with our electrophysiology data, allowing us to conclude that early behavioral impairments observed in our AD mouse model at 6 months (Kilgore et al., 2010) are not due to a presynaptic failure. It is nevertheless important to mention that data obtained from DG cells suggests that the perforant path synapses arriving from cells in the EC exhibit severe presynaptic deficits (Cissé et al., 2011; Harris et al., 2010; Palop et al., 2007) and it would be interesting to study the PP fibers arriving to the CA3 pyramidal cells in our model.

Despite the lack of volume changes, there is an alteration in the complexity index of MfB. This result can be indicative of alterations in the synaptic contacts between Mfs and GABAergic interneurons. In line with our results, a recent study performed in the CA3 region of a different model of AD reported a significant increase in the number filopodia in the J20 mouse model of AD (a transgenic mouse overexpressing APP with a FAD mutation) (Wilke et al., 2014). Further publications have drawn attention to the involvement of the GABAergic system in the pathophysiology of AD (Jo et al., 2014; Limon, Reyes-Ruiz, & Miledi, 2012; Wu, Guo, Gearing, & Chen, 2014). Although all our experiments have been done in the presence of both $GABA_A$ and $GABA_B$ receptor blockers, we should not exclude the possibility that some alterations of the glutamatergic system that we observe happen in response to an initial GABAergic alteration. Further analysis of the GABAergic signaling in our model is necessary to explore this possibility.

The finding that Mf synapses are apparently spared in the APP/PS1 mouse model at 6 months of age might be explained by the lack of adverse effects of Aβ peptides on presynaptic parameters. This hypothesis is further confirmed by our finding that a form of postsynaptic LTP of NMDARs, described at Mf synapses (Kwon & Castillo, 2008; Rebola, Luján, Cunha, & Mulle, 2008), is impaired in the APP/PS1 transgenic mice. This form of NMDARs LTP is induced and expressed postsynaptically and depends on the coacitvation of $A_{2A}R$ and mGluR5. In the work described in this thesis we analyzed three forms of LTP present at the synapses on CA3 pyramidal cells (Figures 3.7, 3.11 and 3.16) and the two forms of plasticity that are altered in the APP/PS1 model of AD depend on the activation and signaling of NMDARs, raising the question if the lack of LTP depends on the postsynaptic function as a whole, or specifically on alterations in the number/ composition/ conductance of NMDARs.

4.1.2 The Role of NMDARs in the Pathophysiology of Alzheimer's Disease

LTP is generally defined as a long-lasting enhancement of signal transmission between the pre and postsynaptic neuron. The postsynaptic forms of LTP that we studied in the APP/PS1 are characterized by an increase in the number of receptors present in the membrane (Malenka & Bear, 2004; Rebola, Srikumar, & Mulle, 2010). It is also generally agreed that it is the unique properties of NMDARs that make LTP such a compelling model for being the cellular bases of learning and memory.

Nevertheless there are two key aspects of LTP that one needs to evaluate separately: the induction mechanism and the expression mechanism. The NMDAR-dependent forms of LTPs require the existence of glutamate binding to the NMDARs and membrane depolarization. Importantly, there are several aspects that can modulate the efficacy of a particular stimulation protocol to induce membrane depolarization. In our study the A/C LTP was triggered by a depo-paring protocol, where the depolarization of the membrane is achieved in an artificial way (the postsynaptic cell is clamped at 0 mV while the presynaptic fibers are stimulated). With these experiments we are sure that the NMDARs are being activated and that the alterations in LTP expression are due to NMDARs signaling and/or the downstream intracellular cascades activated by them. Regarding the Mf NMDAR LTP, we cannot be sure if the alterations are in the induction or in the expression mechanism, but we found no alterations in NMDARs short-term plasticities or NMDAR/AMPARs ratios that could suggest a problem in induction. Nevertheless this form of LTP depends on the coactivation of both A2ARs and mGluRs. Alterations of the metabotropic signaling of these receptors can explain the loss of Mf NMDARs LTP as will be discussed further ahead.

In contrast with some publications that describe alteration in the ratio between NMDAR/AMPAR in models of AD (Cissé et al., 2011; Roberson et al., 2011), we found no alterations in this ratio in the APP/PS1 mice with 6 months. More importantly we also found that chronic overproduction of AB peptides did not altered the subunit composition of NMDARs present in both Mf and A/C synapses. This suggests that the levels of synaptic GluN2B containing NMDARs cannot explain the loss of NMDARs LTP. This is in apparent contradiction with a large body of evidence from in-vitro experiments that implicate GluN2B-containing NMDAR as particular mediators of neuronal damage in AD (Cui et al., 2013; Ferreira et al., 2012; Hu, Klyubin, Anwyl, Anwy, & Rowan, 2009; Rönicke et al., 2011). Our report also shows for the first time that the chronic overexpression of Aβ peptide does not alter the levels of NMDARs extrasynaptic receptors. Several publications described GluNB receptors as main effectors of the synaptic impairments in AD (Li et al., 2011; Shankar et al., 2007) but our experiments rule out the action of AB oligomers on extrasynaptic NMDARs as the major cause for the synaptic deficits observed in the chronic forms of AD.

Although the composition and conductance of NMDARs is not altered in APP/PS1 mice with 6 months of age, we cannot rule that the internal cascades

activated by NMDARs activation might be altered. In fact other studies reported NMDARs downstream effects such as calcineurin/cofilin, p38 or MAPK pathways activation might be involved in the mechanism of synaptic dysfunction in AD (Li et al., 2009; Shankar et al., 2007; Q. Wang, Rowan, & Anwyl, 2004). Therefore is important to explore other synaptic receptors that might modulate NMDARs signaling.

4.2 Adenosine Receptors as Potential Targets for the Rescue of Associative/Commissural LTP

In the last decade, growing evidence indicates that synaptic loss and dysfunction, accompanied by neural network failure, may be the major cause of AD cognitive impairments. In this line, amelioration of synaptic function in AD is an important and promising therapeutic approach. Adenosine is a molecule that acts as a neuromodulator in the central nervous system and is known to regulate glutamatergic signalling (Cunha, 2005). This neuromodulator controls many brain functions in physiological and pathophysiological conditions via activation of high-affinity A_1R or $A_{2A}R$. Importantly, the genetic manipulation of $A_{2A}Rs$, was shown to modify memory performance in rodents (Giménez-Llort et al., 2007; J. H. Wang, Ma, & van den Buuse, 2006). The Mf NMDARs plasticity, absent in the APP/PS1 animals, has been shown to depend on the activation of $A_{2A}Rs$ (Rebola et al., 2008). $A_{2A}Rs$ are up-regulated in noxious brain conditions, which makes their blockade a potent strategy of brain neuroprotection in adult animals (Cunha, 2005). Because the neuroprotective effect of $A_{2A}R$ antagonists is maintained in chronic noxious brain conditions without observable peripheral effects, an interest in $A_{2A}R$ antagonists as novel strategies to prevent or restrain the development of neurodegenerative diseases, such as Alzheimer's disease, is justified. In accordance with this, $A_{2A}Rs$ antagonists can prevent memory impairment in animal models of Alzheimer's disease (Arendash et al., 2001; Dall'Igna et al., 2007). Our results show that a short incubation with A2AR is sufficient to partially rescue the complete lack of LTP that we found in A/C synapses of APP/PS1 mice.

Chapter 5

BIBLIOGRAPHY
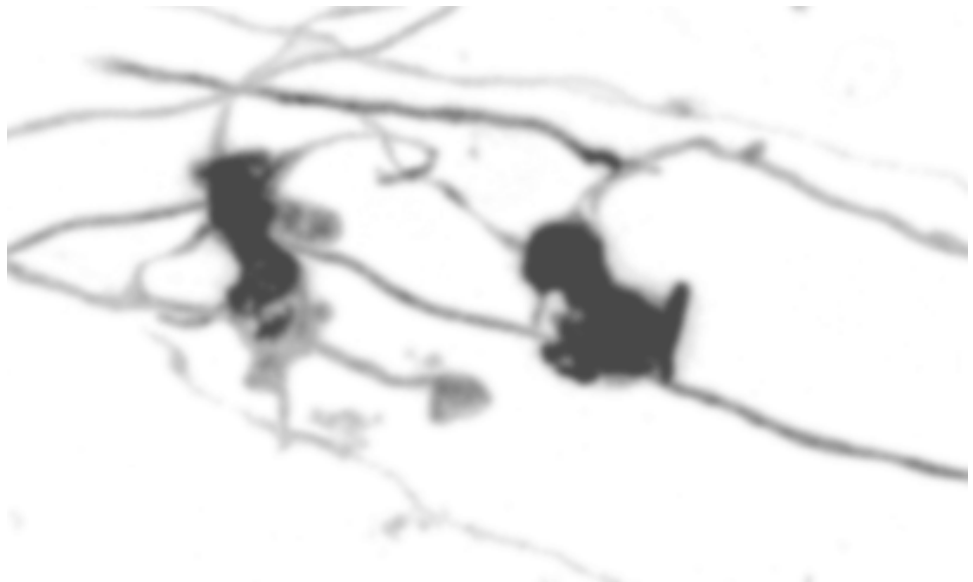
5.1 Books

Andersen, P. (2007). *The Hippocampus Book* (1st ed.). Oxford: Oxford University Press.

Bohlen und Halbach, O., & Dermietzel, R. (2006). *Neurotransmitters and Neuromodulators* (2nd ed.). Weinheim: Wiley-VCH.

Gold, R. S. (2007) *The Axon guide to Electrophysiology and Biophysics Laboratory Techniques.* (3rd ed.), Molecular Devices

Molleman, A. (2003). *Patch clamping* (1st ed.). New York: J. Wiley.

Purves, D. (2008). *Neuroscience* (3rd ed.). Sunderland, Mass.: Sinauer.

Sakmann, B., & Neher, E. (2009). *Single-channel recording* (2nd ed.). New York, NY: Springer.

Walz, W. (2007). *Patch-clamp Analysis* (2nd ed.). Totowa, N.J.: Humana Press.

5.2 List of References

Abbott, L. F., & Regehr, W. G. (2004). Synaptic computation. *Nature*, *431*(7010), 796–803. doi:10.1038/nature03010

Abraham, W. C., & Bear, M. F. (1996). Metaplasticity: the plasticity of synaptic plasticity. *Trends in Neurosciences*, *19*(4), 126–130.

Acsády, L., Kamondi, A., Sík, A., Freund, T., & Buzsáki, G. (1998). GABAergic cells are the major postsynaptic targets of mossy fibers in the rat hippocampus. *The Journal of neuroscience : the official journal of the Society for Neuroscience*, *18*(9), 3386–3403.

Albasanz, J. L., Perez, S., Barrachina, M., Ferrer, I., & Martín, M. (2008). Up-regulation of adenosine receptors in the frontal cortex in Alzheimer's disease. *Brain Pathology*, *18*(2), 211–219. doi:10.1111/j.1750-3639.2007.00112.x

Amaral, D. G. (1979). Synaptic extensions from the mossy fibers of the fascia dentata. *Anatomy and embryology*, *155*(3), 241–251.

Amaral, D. G., & Dent, J. A. (1981). Development of the mossy fibers of the dentate gyrus: I. A light and electron microscopic study of the mossy fibers and their expansions. *The Journal of Comparative Neurology*, *195*(1), 51–86. doi:10.1002/cne.901950106

Amaral, D. G., & Witter, M. P. (1989). The three-dimensional organization of the hippocampal formation: a review of anatomical data. *NSC*, *31*(3), 571–591.

Amaral, D. G., Ishizuka, N., & Claiborne, B. (1990). Neurons, numbers and the hippocampal network. *Progress in brain research*, *83*, 1–11.

Amici, M., Doherty, A., Jo, J., Jane, D., Cho, K., Collingridge, G., & Dargan, S. (2009). Neuronal calcium sensors and synaptic plasticity. *Biochemical Society Transactions*, *37*(Pt 6), 1359–1363. doi:10.1042/BST0371359

Andersen, P. (2007). *The Hippocampus Book*. Oxford University Press.

Antonioli, L., Blandizzi, C., Pacher, P., & Haskó, G. (2013). Immunity, inflammation and cancer: a leading role for adenosine. *Nature Publishing Group*, *13*(12), 842–857. doi:10.1038/nrc3613

Arendash, G. W., Gordon, M. N., Diamond, D. M., Austin, L. A., Hatcher, J. M., Jantzen, P., et al. (2001). Behavioral assessment of Alzheimer's transgenic mice following long-term Abeta vaccination: task specificity and correlations between Abeta deposition and spatial memory. *DNA and cell biology*, *20*(11), 737–744. doi:10.1089/10445490152717604

Arendash, G. W., Schleif, W., Rezai-Zadeh, K., Jackson, E. K., Zacharia, L. C., Cracchiolo, J. R., et al. (2006). Caffeine protects Alzheimer's mice against cognitive impairment and reduces brain beta-amyloid production. *NSC*, *142*(4), 941–952. doi:10.1016/j.neuroscience.2006.07.021

Bakker, A., Kirwan, C. B., Miller, M., & Stark, C. E. L. (2008). Pattern separation in the human hippocampal CA3 and dentate gyrus. *Science*, *319*(5870), 1640–1642. doi:10.1126/science.1152882

Bednarek, E., & Caroni, P. (2011). β-Adducin is required for stable assembly of new synapses and improved memory upon environmental enrichment. *Neuron*, *69*(6), 1132–1146. doi:10.1016/j.neuron.2011.02.034

Bergersen, L., Ruiz, A., Bjaalie, J. G., Kullmann, D. M., & Gundersen, V. (2003). GABA and GABAA receptors at hippocampal mossy fibre synapses. *The European journal of neuroscience*, *18*(4), 931–941.

Bischofberger, J., Engel, D., Frotscher, M., & Jonas, P. (2006). Timing and efficacy of transmitter release at mossy fiber synapses in the hippocampal network. *Pflügers Archiv : European journal of physiology*, *453*(3), 361–372. doi:10.1007/s00424-006-0093-2

Blennow, K., de Leon, M. J., & Zetterberg, H. (2006). Alzheimer's disease. *Lancet*, *368*(9533), 387–403. doi:10.1016/S0140-6736(06)69113-7

Bliss, T. V., & Collingridge, G. L. (1993). A synaptic model of memory: long-term potentiation in the hippocampus. *Nature*, *361*(6407), 31–39. doi:10.1038/361031a0

Blitz, D. M., Foster, K. A., & Regehr, W. G. (2004). Short-term synaptic plasticity: a comparison of two synapses. *Nature Reviews Neuroscience*, *5*(8), 630–640. doi:10.1038/nrn1475

Bonardi, C., de Pulford, F., Jennings, D., & Pardon, M.-C. (2011). A detailed analysis of the early context extinction deficits seen in APPswe/PS1dE9 female mice and their relevance to preclinical Alzheimer's disease. *Behavioural Brain Research*, *222*(1), 89–97. doi:10.1016/j.bbr.2011.03.041

Bortolotto, Z. A., Lauri, S., Isaac, J. T. R., & Collingridge, G. L. (2003). Kainate receptors and the induction of mossy fibre long-term potentiation. *Philosophical transactions of the Royal Society of London. Series B, Biological sciences*, *358*(1432), 657–666. doi:10.1098/rstb.2002.1216

Braak, H., & Braak, E. (1990). Alzheimer's disease: striatal amyloid deposits and neurofibrillary changes. *Journal of neuropathology and experimental neurology*, *49*(3), 215–224.

Burgess, N., Maguire, E. A., & O'Keefe, J. (2002). The human hippocampus and spatial and episodic memory. *Neuron*, *35*(4), 625–641.

Canas, P. M., Porciúncula, L. O., Cunha, G. M. A., Silva, C. G., Machado, N. J., Oliveira, J. M. A., et al. (2009). Adenosine A2A receptor blockade prevents synaptotoxicity and memory dysfunction caused by beta-amyloid peptides via p38 mitogen-activated protein kinase pathway. *Journal of Neuroscience*, *29*(47), 14741–14751. doi:10.1523/JNEUROSCI.3728-09.2009

Cao, D., Lu, H., Lewis, T. L., & Li, L. (2007). Intake of Sucrose-sweetened Water Induces Insulin Resistance and Exacerbates Memory Deficits and Amyloidosis in a Transgenic Mouse Model of Alzheimer Disease. *The Journal of biological chemistry*, *282*(50), 36275–36282. doi:10.1074/jbc.M703561200

Caporale, N., & Dan, Y. (2008). Spike Timing–Dependent Plasticity: A Hebbian Learning Rule. *Annual Review of Neuroscience*, *31*(1), 25–46. doi:10.1146/annurev.neuro.31.060407.125639

Caroni, P., Donato, F., & Muller, D. (2012). Structural plasticity upon learning: regulation and functions. *Nature Reviews Neuroscience*, *13*(7), 478–490. doi:10.1038/nrn3258

Carson, J. A., & Turner, A. J. (2002). Beta-amyloid catabolism: roles for neprilysin (NEP) and other metallopeptidases? *Journal of Neurochemistry*, *81*(1), 1–8.

Carta, M., Lanore, F., Rebola, N., Szabo, Z., Da Silva, S. V., Lourenço, J., et al. (2014). Membrane lipids tune synaptic transmission by direct modulation of presynaptic potassium channels. *Neuron*, *81*(4), 787–799. doi:10.1016/j.neuron.2013.12.028

Castillo, P. E., Janz, R., Sudhof, T. C., Tzounopoulos, T., Malenka, R. C., & Nicoll, R. A. (1997a). Rab3A is essential for mossy fibre long-term potentiation in the hippocampus. *Nature*, *388*(6642), 590–593. doi:10.1038/41574

Castillo, P. E., Malenka, R. C., & Nicoll, R. A. (1997b). Kainate receptors mediate a slow postsynaptic current in hippocampal CA3 neurons. *Nature*, *388*(6638), 182–186. doi:10.1038/40645

Cetin, A., Komai, S., Eliava, M., Seeburg, P. H., & Osten, P. (2006). Stereotaxic gene delivery in the rodent brain. *Nature Protocols*, *1*(6), 3166–3173. doi:10.1038/nprot.2006.450

Chapman, P. F., White, G. L., Jones, M. W., Cooper-Blacketer, D., Marshall, V. J., Irizarry, M., et al. (1999). Impaired synaptic plasticity and learning in aged amyloid precursor protein transgenic mice. *Nature Neuroscience*, *2*(3), 271–276. doi:10.1038/6374

Chattarji, S., Stanton, P. K., & Sejnowski, T. J. (1989). Commissural synapses, but not mossy fiber synapses, in hippocampal field CA3 exhibit associative long-term potentiation and depression. *Brain Research*, *495*(1), 145–150.

Chen, J.-F., Eltzschig, H. K., & Fredholm, B. B. (2013). Adenosine receptors as drug targets--what are the challenges? *Nature Reviews Drug Discovery*, *12*(4), 265–286. doi:10.1038/nrd3955

Chevaleyre, V., & Piskorowski, R. (2014). Modulating excitation through plasticity at inhibitory synapses. *Frontiers in Cellular Neuroscience*, *8*, 93. doi:10.3389/fncel.2014.00093

Chevaleyre, V., & Siegelbaum, S. A. (2010). Strong CA2 pyramidal neuron synapses define a powerful disynaptic cortico-hippocampal loop. *Neuron*, *66*(4), 560–572. doi:10.1016/j.neuron.2010.04.013

Chicurel, M. E., & Harris, K. M. (1992). Three-dimensional analysis of the structure and composition of CA3 branched dendritic spines and their synaptic relationships with mossy fiber boutons in the rat hippocampus. *The Journal of Comparative Neurology*, *325*(2), 169–182. doi:10.1002/cne.903250204

Cissé, M., Halabisky, B., Harris, J., Devidze, N., Dubal, D. B., Sun, B., et al. (2010). Reversing EphB2 depletion rescues cognitive functions in Alzheimer model - Supplementary Info. *Nature*, *469*(7328), 47–52. doi:10.1038/nature09635

Cissé, M., Sanchez, P. E., Kim, D. H., Ho, K., Yu, G.-Q., & Mucke, L. (2011). Ablation of cellular prion protein does not ameliorate abnormal neural network activity or cognitive dysfunction in the J20 line of human amyloid precursor protein transgenic mice. *Journal of Neuroscience*, *31*(29), 10427–10431. doi:10.1523/JNEUROSCI.1459-11.2011

Citri, A., & Malenka, R. C. (2008). Synaptic plasticity: multiple forms, functions, and mechanisms. *Neuropsychopharmacology*, *33*(1), 18–41. doi:10.1038/sj.npp.1301559

Claiborne, B. J., Amaral, D. G., & Cowan, W. M. (1986). A light and electron microscopic analysis of the mossy fibers of the rat dentate gyrus. *The Journal of Comparative Neurology*, *246*(4), 435–458. doi:10.1002/cne.902460403

Cleary, J. P., Walsh, D. M., Hofmeister, J. J., Shankar, G. M., Kuskowski, M. A., Selkoe, D. J., & Ashe, K. H. (2005). Natural oligomers of the amyloid-beta protein specifically disrupt cognitive function. *Nature Neuroscience*, *8*(1), 79–84. doi:10.1038/nn1372

Connors, B. W., & Long, M. A. (2004). Electrical synapses in the mammalian brain. *Annual Review of Neuroscience*, *27*, 393–418. doi:10.1146/annurev.neuro.26.041002.131128

Contractor, A., Swanson, G., & Heinemann, S. F. (2001). Kainate receptors are involved in short- and long-term plasticity at mossy fiber synapses in the hippocampus. *Neuron*, *29*(1), 209–216.

Copits, B. A., & Swanson, G. T. (2012). Dancing partners at the synapse: auxiliary subunits that shape kainate receptor function. *Nature Reviews Neuroscience*, *13*(10), 675–686. doi:10.1038/nrn3335

Corder, E. H., Saunders, A. M., Strittmatter, W. J., Schmechel, D. E., Gaskell, P. C., Small, G. W., et al. (1993). Gene dose of apolipoprotein E type 4 allele and the risk of Alzheimer's disease in late onset families. *Science*, *261*(5123), 921–923.

Cramer, P. E., Cirrito, J. R., Wesson, D. W., Lee, C. Y. D., Karlo, J. C., Zinn, A. E., et al. (2012). ApoE-Directed Therapeutics Rapidly Clear -Amyloid and Reverse Deficits in AD Mouse Models. *Science*, *335*(6075), 1503–1506. doi:10.1126/science.1217697

Cruchaga, C., Karch, C. M., Jin, S. C., Benitez, B. A., Cai, Y., Guerreiro, R., et al. (2014). Rare coding variants in the phospholipase D3 gene confer risk for Alzheimer's disease. *Nature*, *505*(7484), 550–554. doi:10.1038/nature12825

Cui, Z., Feng, R., Jacobs, S., Duan, Y., Wang, H., Cao, X., & Tsien, J. Z. (2013). Increased NR2A:NR2B ratio compresses long-term depression range and constrains long-term memory. *Scientific Reports*, *3*, 1036. doi:10.1038/srep01036

Cull-Candy, S. G., & Leszkiewicz, D. N. (2004). Role of distinct NMDA receptor subtypes at central synapses. *Signal Transduction Knowledge Environment (STKE)*, *2004*(255), re16. doi:10.1126/stke.2552004re16

Cullen, W. K., Wu, J., Anwyl, R., & Rowan, M. J. (1996). beta-Amyloid produces a delayed NMDA receptor-dependent reduction in synaptic transmission in rat hippocampus. *Neuroreport*, *8*(1), 87–92.

Cunha, G. M. A., Canas, P. M., Melo, C. S., Hockemeyer, J., Müller, C. E., Oliveira, C. R., & Cunha, R. A. (2008). Adenosine A2A receptor blockade prevents memory dysfunction caused by beta-amyloid peptides but not by scopolamine or MK-801. *Experimental Neurology*, *210*(2), 776–781. doi:10.1016/j.expneurol.2007.11.013

Cunha, R. A. (2005). Neuroprotection by adenosine in the brain: From A(1) receptor activation to A (2A) receptor blockade. *Purinergic signalling*, *1*(2), 111–134. doi:10.1007/s11302-005-0649-1

D'Amelio, M., Cavallucci, V., Middei, S., Marchetti, C., Pacioni, S., Ferri, A., et al. (2011). Caspase-3 triggers early synaptic dysfunction in a mouse model of Alzheimer's disease. *Nature Neuroscience*, *14*(1), 69–76. doi:10.1038/nn.2709

Dall'Igna, O. P., Fett, P., Gomes, M. W., Souza, D. O., Cunha, R. A., & Lara, D. R. (2007). Caffeine and adenosine A(2a) receptor antagonists prevent beta-amyloid (25-35)-induced cognitive deficits in mice. *Experimental Neurology*, *203*(1), 241–245. doi:10.1016/j.expneurol.2006.08.008

Dan, Y., & Poo, M.-M. (2006). Spike timing-dependent plasticity: from synapse to perception. *Physiological Reviews*, *86*(3), 1033–1048. doi:10.1152/physrev.00030.2005

Dargan, S. L., & Amici, M. (2009). Role of kainate autoreceptors in short-term plasticity at hippocampal mossy fiber synapses. *Journal of Neuroscience*, *29*(18), 5713–5715. doi:10.1523/JNEUROSCI.0549-09.2009

Daumas, S., Halley, H., Francés, B., & Lassalle, J.-M. (2005). Encoding, consolidation, and retrieval of contextual memory: differential involvement of dorsal CA3 and CA1 hippocampal subregions. *Learning & Memory*, *12*(4), 375–382. doi:10.1101/lm.81905

De Felice, F. G., Wu, D., Lambert, M. P., Fernandez, S. J., Velasco, P. T., Lacor, P. N., et al. (2008). Alzheimer's disease-type neuronal tau hyperphosphorylation induced by Aβ oligomers. *Neurobiology of Aging*, *29*(9), 1334–1347. doi:10.1016/j.neurobiolaging.2007.02.029

de Mendonca, A., Sebastião, A. M., & Ribeiro, J. A. (1995). Inhibition of NMDA receptor-mediated currents in isolated rat hippocampal neurones by adenosine A1 receptor activation. *Neuroreport*, *6*(8), 1097–1100.

De Strooper, B., Iwatsubo, T., & Wolfe, M. S. (2012). Presenilins and γ-secretase:

structure, function, and role in Alzheimer Disease. *Cold Spring Harbor perspectives in medicine*, *2*(1), a006304. doi:10.1101/cshperspect.a006304

Deacon, R. M. J., & Rawlins, J. N. P. (2006). T-maze alternation in the rodent. *Nature Protocols*, *1*(1), 7–12. doi:10.1038/nprot.2006.2

Debanne, D., Gähwiler, B. H., & Thompson, S. M. (1998). Long-term synaptic plasticity between pairs of individual CA3 pyramidal cells in rat hippocampal slice cultures. *The Journal of Physiology, 507 (Pt 1)*, 237–247.

Derrick, B. E., & Martinez, J. L. (1994). Frequency-dependent associative long-term potentiation at the hippocampal mossy fiber-CA3 synapse. *PNAS*, *91*(22), 10290–10294.

Ding, Y., Qiao, A., Wang, Z., Goodwin, J. S., Lee, E. S., Block, M. L., et al. (2008). Retinoic Acid Attenuates -Amyloid Deposition and Rescues Memory Deficits in an Alzheimer's Disease Transgenic Mouse Model. *Journal of Neuroscience*, *28*(45), 11622–11634. doi:10.1523/JNEUROSCI.3153-08.2008

Divito, C. B., & Underhill, S. M. (2014). Excitatory amino acid transporters: Roles in glutamatergic neurotransmission. *Neurochemistry International*, *73C*, 172–180. doi:10.1016/j.neuint.2013.12.008

Dolev, I., Fogel, H., Milshtein, H., Berdichevsky, Y., Lipstein, N., Brose, N., et al. (2013). Spike bursts increase amyloid-β 40/42 ratio by inducing a presenilin-1 conformational change. *Nature Neuroscience*, *16*(5), 587–595. doi:10.1038/nn.3376

Dunwiddie, T. V., & Haas, H. L. (1985). Adenosine increases synaptic facilitation in the in vitro rat hippocampus: evidence for a presynaptic site of action. *The Journal of Physiology*, *369*, 365–377.

Dunwiddie, T. V., & Masino, S. A. (2001). The role and regulation of adenosine in the central nervous system. *Annual Review of Neuroscience*, *24*, 31–55. doi:10.1146/annurev.neuro.24.1.31

Eisele, Y. S., Obermüller, U., Heilbronner, G., Baumann, F., Kaeser, S. A., Wolburg, H., et al. (2010). Peripherally applied Abeta-containing inoculates induce cerebral beta-amyloidosis. *Science*, *330*(6006), 980–982. doi:10.1126/science.1194516

Eisenstein, M. (2011). Genetics: finding risk factors. *Nature*, *475*(7355), S20–2. doi:10.1038/475S20a

Espinosa, J., Rocha, A., Nunes, F., Costa, M. S., Schein, V., Kazlauckas, V., et al. (2013). Caffeine consumption prevents memory impairment, neuronal damage, and adenosine A2A receptors upregulation in the hippocampus of a rat model of sporadic dementia. *Journal of Alzheimer's Disease*, *34*(2), 509–518. doi:10.3233/JAD-111982

Evstratova, A., & Tóth, K. (2014). Information processing and synaptic plasticity at hippocampal mossy fiber terminals. *Frontiers in Cellular Neuroscience*, *8*, 28. doi:10.3389/fncel.2014.00028

Fan, X., Jin, W. Y., & Wang, Y. T. (2014). The NMDA receptor complex: a multifunctional machine at the glutamatergic synapse. *Frontiers in Cellular Neuroscience*, *8*, 160. doi:10.3389/fncel.2014.00160

Feldman, D. E. (2012). The spike-timing dependence of plasticity. *Neuron*, *75*(4), 556–

571. doi:10.1016/j.neuron.2012.08.001

Ferreira, I. L., Bajouco, L. M., Mota, S. I., Auberson, Y. P., Oliveira, C. R., & Rego, A. C. (2012). Amyloid beta peptide 1–42 disturbs intracellular calcium homeostasis through activation of GluN2B-containing N-methyl-d-aspartate receptors in cortical cultures. *Cell calcium*, *51*(2), 95–106. doi:10.1016/j.ceca.2011.11.008

Fioravante, D., & Regehr, W. G. (2011). Short-term forms of presynaptic plasticity. *Current Opinion in Neurobiology*, *21*(2), 269–274. doi:10.1016/j.conb.2011.02.003

Fischer, G., Mutel, V., Trube, G., Malherbe, P., Kew, J. N., Mohacsi, E., et al. (1997). Ro 25-6981, a highly potent and selective blocker of N-methyl-D-aspartate receptors containing the NR2B subunit. Characterization in vitro. *The Journal of pharmacology and experimental therapeutics*, *283*(3), 1285–1292.

Fitzjohn, S. M., Kuenzi, F., Morton, R. A., Rosahl, T. W., Lewis, H., Smith, D., et al. (2010). A study of long-term potentiation in transgenic mice over-expressing mutant forms of both amyloid precursor protein and presenilin-1. *Molecular Brain*, *3*(1), 21. doi:10.1186/1756-6606-3-21

Fitzjohn, S. M., Morton, R. A., Kuenzi, F., Rosahl, T. W., Shearman, M., Lewis, H., et al. (2001). Age-related impairment of synaptic transmission but normal long-term potentiation in transgenic mice that overexpress the human APP695SWE mutant form of amyloid precursor protein. *Journal of Neuroscience*, *21*(13), 4691–4698.

Foster, K. A., Kreitzer, A. C., & Regehr, W. G. (2002). Interaction of postsynaptic receptor saturation with presynaptic mechanisms produces a reliable synapse. *Neuron*, *36*(6), 1115–1126.

Fotuhi, M., Hachinski, V., & Whitehouse, P. J. (2009). Changing perspectives regarding late-life dementia. *Nature reviews. Neurology*, *5*(12), 649–658. doi:10.1038/nrneurol.2009.175

Fredholm, B. B., Chen, J.-F., Cunha, R. A., Svenningsson, P., & Vaugeois, J.-M. (2005). Adenosine and brain function. *International review of neurobiology*, *63*, 191–270. doi:10.1016/S0074-7742(05)63007-3

Frotscher, M. (1991). Target cell specificity of synaptic connections in the hippocampus. *Hippocampus*, *1*(2), 123–130. doi:10.1002/hipo.450010202

Gaiarsa, J.-L., & Porcher, C. (2013). Emerging neurotrophic role of GABAB receptors in neuronal circuit development. *Frontiers in Cellular Neuroscience*, *7*, 206. doi:10.3389/fncel.2013.00206

Gardoni, F., Marcello, E., & Di Luca, M. (2009). Postsynaptic density-membrane associated guanylate kinase proteins (PSD-MAGUKs) and their role in CNS disorders. *NSC*, *158*(1), 324–333. doi:10.1016/j.neuroscience.2008.07.068

Gatz, M., Reynolds, C. A., Fratiglioni, L., Johansson, B., Mortimer, J. A., Berg, S., et al. (2006). Role of genes and environments for explaining Alzheimer disease. *Archives of general psychiatry*, *63*(2), 168–174. doi:10.1001/archpsyc.63.2.168

Gauthier, S., Reisberg, B., Zaudig, M., Petersen, R. C., Ritchie, K., Broich, K., et al. (2006). Mild cognitive impairment. *The Lancet*, *367*(9518), 1262–1270. doi:10.1016/S0140-6736(06)68542-5

Geiger, J. R., & Jonas, P. (2000). Dynamic control of presynaptic Ca(2+) inflow by fast-inactivating K(+) channels in hippocampal mossy fiber boutons. *Neuron*, *28*(3),

927–939.

Gilbert, P. E., & Brushfield, A. M. (2009). The role of the CA3 hippocampal subregion in spatial memory: a process oriented behavioral assessment. *Progress in neuro-psychopharmacology & biological psychiatry*, *33*(5), 774–781. doi:10.1016/j.pnpbp.2009.03.037

Gimbel, D. A., Nygaard, H. B., Coffey, E. E., Gunther, E. C., Laurén, J., Gimbel, Z. A., & Strittmatter, S. M. (2010). Memory impairment in transgenic Alzheimer mice requires cellular prion protein. *Journal of Neuroscience*, *30*(18), 6367–6374. doi:10.1523/JNEUROSCI.0395-10.2010

Giménez-Llort, L., Schiffmann, S. N., Shmidt, T., Canela, L., Camón, L., Wassholm, M., et al. (2007). Working memory deficits in transgenic rats overexpressing human adenosine A2A receptors in the brain. *Neurobiology of Learning and Memory*, *87*(1), 42–56. doi:10.1016/j.nlm.2006.05.004

Goate, A., Chartier-Harlin, M. C., Mullan, M., Brown, J., Crawford, F., Fidani, L., et al. (1991). Segregation of a missense mutation in the amyloid precursor protein gene with familial Alzheimer's disease. *Nature*, *349*(6311), 704–706. doi:10.1038/349704a0

Gomes, C. V., Kaster, M. P., Tomé, A. R., Agostinho, P. M., & Cunha, R. A. (2011). Adenosine receptors and brain diseases: neuroprotection and neurodegeneration. *Biochimica et biophysica acta*, *1808*(5), 1380–1399. doi:10.1016/j.bbamem.2010.12.001

Gonzales, R. B., DeLeon Galvan, C. J., Rangel, Y. M., & Claiborne, B. J. (2001). Distribution of thorny excrescences on CA3 pyramidal neurons in the rat hippocampus. *The Journal of Comparative Neurology*, *430*(3), 357–368. doi:10.1002/1096-9861(20010212)430:3<357::AID-CNE1036>3.0.CO;2-K

Götz, J., & Ittner, L. M. (2008). Animal models of Alzheimer's disease and frontotemporal dementia. *Nature Reviews Neuroscience*, *9*(7), 532–544. doi:10.1038/nrn2420

Groc, L., Heine, M., Cousins, S. L., Stephenson, F. A., Lounis, B., Cognet, L., & Choquet, D. (2006). NMDA receptor surface mobility depends on NR2A-2B subunits. *PNAS*, *103*(49), 18769–18774. doi:10.1073/pnas.0605238103

Gsandtner, I., & Freissmuth, M. (2006). A tail of two signals: the C terminus of the A(2A)-adenosine receptor recruits alternative signaling pathways. *Molecular pharmacology*, *70*(2), 447–449. doi:10.1124/mol.106.026757

Guetg, N., Seddik, R., Vigot, R., Turecek, R., Gassmann, M., Vogt, K. E., et al. (2009). The GABAB1a isoform mediates heterosynaptic depression at hippocampal mossy fiber synapses. *Journal of Neuroscience*, *29*(5), 1414–1423. doi:10.1523/JNEUROSCI.3697-08.2009

Gundlfinger, A., Breustedt, J., Sullivan, D., & Schmitz, D. (2010). Natural spike trains trigger short- and long-lasting dynamics at hippocampal mossy fiber synapses in rodents. *PLoS ONE*, *5*(4), e9961. doi:10.1371/journal.pone.0009961

Gureviciene, I., Ikonen, S., Gurevicius, K., Sarkaki, A., van Groen, T., Pussinen, R., et al. (2004). Normal induction but accelerated decay of LTP in APP + PS1 transgenic mice. *Neurobiology of Disease*, *15*(2), 188–195. doi:10.1016/j.nbd.2003.11.011

Haass, C., & Selkoe, D. J. (2007). Soluble protein oligomers in neurodegeneration: lessons from the Alzheimer's amyloid beta-peptide. *Nature reviews. Molecular cell biology*, *8*(2), 101–112. doi:10.1038/nrm2101

Haass, C., Schlossmacher, M. G., Hung, A. Y., Vigo-Pelfrey, C., Mellon, A., Ostaszewski, B. L., et al. (1992). Amyloid beta-peptide is produced by cultured cells during normal metabolism. *Nature, 359*(6393), 322–325. doi:10.1038/359322a0

Haberl, M. G., Viana da Silva, S., Guest, J. M., Ginger, M., Ghanem, A., Mulle, C., et al. (2014). An anterograde rabies virus vector for high-resolution large-scale reconstruction of 3D neuron morphology. *Brain structure & function*. doi:10.1007/s00429-014-0730-z

Hagena, H. H., & Manahan-Vaughan, D. D. (2011). Learning-facilitated synaptic plasticity at CA3 mossy fiber and commissural-associational synapses reveals different roles in information processing. *Cerebral cortex (New York, N.Y. : 1991)*, *21*(11), 2442–2449. doi:10.1093/cercor/bhq271

Hanseeuw, B. J., Van Leemput, K., Kavec, M., Grandin, C., Seron, X., & Ivanoiu, A. (2011). Mild cognitive impairment: differential atrophy in the hippocampal subfields. *AJNR. American journal of neuroradiology*, *32*(9), 1658–1661. doi:10.3174/ajnr.A2589

Hardingham, G. E., & Bading, H. (2010). Synaptic versus extrasynaptic NMDA receptor signalling: implications for neurodegenerative disorders. *Nature Reviews Neuroscience*, *11*(10), 682–696. doi:10.1038/nrn2911

Hardy, J. A., & Higgins, G. A. (1992). Alzheimer's disease: the amyloid cascade hypothesis. *Science, 256*(5054), 184–185.

Hardy, J., & Selkoe, D. J. (2002). The amyloid hypothesis of Alzheimer's disease: progress and problems on the road to therapeutics. *Science, 297*(5580), 353–356. doi:10.1126/science.1072994

Harris, E. W., & Cotman, C. W. (1986). Long-term potentiation of guinea pig mossy fiber responses is not blocked by N-methyl D-aspartate antagonists. *Neuroscience Letters*, *70*(1), 132–137.

Harris, J. A., Devidze, N., Verret, L., Ho, K., Halabisky, B., Thwin, M. T., et al. (2010). Transsynaptic progression of amyloid-β-induced neuronal dysfunction within the entorhinal-hippocampal network. *Neuron, 68*(3), 428–441. doi:10.1016/j.neuron.2010.10.020

Harvey, R. J., Skelton-Robinson, M., & Rossor, M. N. (2003). The prevalence and causes of dementia in people under the age of 65 years. *Journal of neurology, neurosurgery, and psychiatry*, *74*(9), 1206–1209.

Hasselmo, M. E. (2005). The role of hippocampal regions CA3 and CA1 in matching entorhinal input with retrieval of associations between objects and context: theoretical comment on Lee et al. (2005). *Behavioral Neuroscience, 119*(1), 342–345. doi:10.1037/0735-7044.119.1.342

Hell, J. W. (2014). CaMKII: claiming center stage in postsynaptic function and organization. *Neuron, 81*(2), 249–265. doi:10.1016/j.neuron.2013.12.024

Hell, S. W., & Wichmann, J. (1994). Breaking the diffraction resolution limit by

stimulated emission: stimulated-emission-depletion fluorescence microscopy. *Optics letters*, *19*(11), 780–782.

Henze, D. A. D., Urban, N. N. N., & Barrionuevo, G. G. (1999). The multifarious hippocampal mossy fiber pathway: a review. *NSC*, *98*(3), 407–427. doi:10.1016/S0306-4522(00)00146-9

Henze, D. A., Card, J. P., Barrionuevo, G., & Ben-Ari, Y. (1997). Large amplitude miniature excitatory postsynaptic currents in hippocampal CA3 pyramidal neurons are of mossy fiber origin. *Journal of Neurophysiology*, *77*(3), 1075–1086.

Henze, D. A., McMahon, D. B. T., Harris, K. M., & Barrionuevo, G. (2002a). Giant miniature EPSCs at the hippocampal mossy fiber to CA3 pyramidal cell synapse are monoquantal. *Journal of Neurophysiology*, *87*(1), 15–29. doi:10.1152/jn.00394.2001

Henze, D. A., Wittner, L., & Buzsáki, G. (2002b). Single granule cells reliably discharge targets in the hippocampal CA3 network in vivo. *Nature Neuroscience*, *5*(8), 790–795. doi:10.1038/nn887

Heynen, A. J., Abraham, W. C., & Bear, M. F. (1996). Bidirectional modification of CA1 synapses in the adult hippocampus in vivo. *Nature*, *381*(6578), 163–166. doi:10.1038/381163a0

Hitti, F. L., & Siegelbaum, S. A. (2014). The hippocampal CA2 region is essential for social memory. *Nature, 508*(7494), 88–92. doi:10.1038/nature13028

Holtzman, D. M., Morris, J. C., & Goate, A. M. (2011). Alzheimer's disease: the challenge of the second century. *Science translational medicine*, *3*(77), 77sr1. doi:10.1126/scitranslmed.3002369

Hsia, A. Y., Masliah, E., McConlogue, L., Yu, G. Q., Tatsuno, G., Hu, K., et al. (1999). Plaque-independent disruption of neural circuits in Alzheimer's disease mouse models. *PNAS*, *96*(6), 3228–3233. doi:10.2307/47518

Hsieh, H., Boehm, J., Sato, C., Iwatsubo, T., Tomita, T., Sisodia, S., & Malinow, R. (2006). AMPAR removal underlies Abeta-induced synaptic depression and dendritic spine loss. *Neuron*, *52*(5), 831–843. doi:10.1016/j.neuron.2006.10.035

Hu, N.-W., Klyubin, I., Anwyl, R., Anwy, R., & Rowan, M. J. (2009). GluN2B subunit-containing NMDA receptor antagonists prevent Abeta-mediated synaptic plasticity disruption in vivo. *Proceedings of the National Academy of Sciences*, *106*(48), 20504–20509. doi:10.1073/pnas.0908083106

Hulme, S. R., Jones, O. D., & Abraham, W. C. (2013). Emerging roles of metaplasticity in behaviour and disease. *Trends in Neurosciences*, *36*(6), 353–362. doi:10.1016/j.tins.2013.03.007

Hunt, D. L., Puente, N., Grandes, P., & Castillo, P. E. (2013). Bidirectional NMDA receptor plasticity controls CA3 output and heterosynaptic metaplasticity. *Nature Neuroscience*, *16*(8), 1049–1059. doi:10.1038/nn.3461

Ishizuka, N., Cowan, W. M., & Amaral, D. G. (1995). A quantitative analysis of the dendritic organization of pyramidal cells in the rat hippocampus. *The Journal of Comparative Neurology*, *362*(1), 17–45. doi:10.1002/cne.903620103

Ishizuka, N., Weber, J., & Amaral, D. G. (1990). Organization of intrahippocampal projections originating from CA3 pyramidal cells in the rat. *The Journal of*

Comparative Neurology, *295*(4), 580–623. doi:10.1002/cne.902950407

Jankowsky, J. L., Fadale, D. J., Anderson, J., Xu, G. M., Gonzales, V., Jenkins, N. A., et al. (2004). Mutant presenilins specifically elevate the levels of the 42 residue beta-amyloid peptide in vivo: evidence for augmentation of a 42-specific gamma secretase. *Human molecular genetics*, *13*(2), 159–170. doi:10.1093/hmg/ddh019

Jankowsky, J. L., Slunt, H. H., Ratovitski, T., Jenkins, N. A., Copeland, N. G., & Borchelt, D. R. (2001). Co-expression of multiple transgenes in mouse CNS: a comparison of strategies. *Biomolecular engineering*, *17*(6), 157–165. doi:10.1016/S1389-0344(01)00067-3

Jo, J., Whitcomb, D. J., Olsen, K. M., Kerrigan, T. L., Lo, S.-C., Bru-Mercier, G., et al. (2011). Aβ(1-42) inhibition of LTP is mediated by a signaling pathway involving caspase-3, Akt1 and GSK-3β. *Nature Neuroscience*, *14*(5), 545–547. doi:10.1038/nn.2785

Jo, S., Yarishkin, O., Hwang, Y. J., Chun, Y. E., Park, M., Woo, D. H., et al. (2014). GABA from reactive astrocytes impairs memory in mouse models of Alzheimer's disease. *Nature Medicine*. doi:10.1038/nm.3639

Jonas, P., Major, G., & Sakmann, B. (1993). Quantal components of unitary EPSCs at the mossy fibre synapse on CA3 pyramidal cells of rat hippocampus. *The Journal of Physiology*, *472*, 615–663.

Jones, M. W., & McHugh, T. J. (2011). Updating hippocampal representations: CA2 joins the circuit. *Trends in Neurosciences*, *34*(10), 526–535. doi:10.1016/j.tins.2011.07.007

Kamiya, H., Shinozaki, H., & Yamamoto, C. (1996). Activation of metabotropic glutamate receptor type 2/3 suppresses transmission at rat hippocampal mossy fibre synapses. *The Journal of Physiology*, *493 (Pt 2)*, 447–455.

Kandel, E. R. (2001). The molecular biology of memory storage: a dialogue between genes and synapses. *Science*, *294*(5544), 1030–1038. doi:10.1126/science.1067020

Kane, M. D., Lipinski, W. J., Callahan, M. J., Bian, F., Durham, R. A., Schwarz, R. D., et al. (2000). Evidence for seeding of beta -amyloid by intracerebral infusion of Alzheimer brain extracts in beta -amyloid precursor protein-transgenic mice. *Journal of Neuroscience, 20*(10), 3606–3611.

Karakas, E., & Furukawa, H. (2014). Crystal structure of a heterotetrameric NMDA receptor ion channel. *Science*, *344*(6187), 992–997. doi:10.1126/science.1251915

Kasai, H., Fukuda, M., Watanabe, S., Hayashi-Takagi, A., & Noguchi, J. (2010). Structural dynamics of dendritic spines in memory and cognition. *Trends in Neurosciences*, *33*(3), 121–129. doi:10.1016/j.tins.2010.01.001

Kauer, J. A., & Malenka, R. C. (2007). Synaptic plasticity and addiction. *Nature Reviews Neuroscience*, *8*(11), 844–858. doi:10.1038/nrn2234

Keller, J. N., Kindy, M. S., Holtsberg, F. W., St Clair, D. K., Yen, H. C., Germeyer, A., et al. (1998). Mitochondrial manganese superoxide dismutase prevents neural apoptosis and reduces ischemic brain injury: suppression of peroxynitrite production, lipid peroxidation, and mitochondrial dysfunction. *The Journal of neuroscience : the official journal of the Society for Neuroscience*, *18*(2), 687–697.

Kesner, R. P. (2007). Behavioral functions of the CA3 subregion of the hippocampus. *Learning & memory (Cold Spring Harbor, N.Y.), 14*(11), 771–781. doi:10.1101/lm.688207

Kesner, R. P. (2013). A process analysis of the CA3 subregion of the hippocampus. *Frontiers in Cellular Neuroscience, 7*, 78. doi:10.3389/fncel.2013.00078

Kesner, R. P., & Warthen, D. K. (2010). Implications of CA3 NMDA and opiate receptors for spatial pattern completion in rats. *Hippocampus, 20*(4), 550–557. doi:10.1002/hipo.20676

Kessels, H. W., Nguyen, L. N., Nabavi, S., & Malinow, R. (2010). The prion protein as a receptor for amyloid-beta. *Nature, 466*(7308), E3–4– discussion E4–5. doi:10.1038/nature09217

Kilgore, M., Miller, C. A., Fass, D. M., Hennig, K. M., Haggarty, S. J., Sweatt, J. D., & Rumbaugh, G. (2010). Inhibitors of Class 1 Histone Deacetylases Reverse Contextual Memory Deficits in a Mouse Model of Alzheimer's Disease. *Neuropsychopharmacology, 35*(4), 870–880. doi:10.1038/npp.2009.197

Kim, J. J., & Baxter, M. G. (2001). Multiple brain-memory systems: the whole does not equal the sum of its parts. *Trends in Neurosciences, 24*(6), 324–330.

Kim, J., Castellano, J. M., Jiang, H., Basak, J. M., Parsadanian, M., Pham, V., et al. (2009). Overexpression of Low-Density Lipoprotein Receptor in the Brain Markedly Inhibits Amyloid Deposition and Increases Extracellular Aβ Clearance. *Neuron, 64*(5), 632–644. doi:10.1016/j.neuron.2009.11.013

Kishimoto, Y., Nakazawa, K., Tonegawa, S., Kirino, Y., & Kano, M. (2006). Hippocampal CA3 NMDA receptors are crucial for adaptive timing of trace eyeblink conditioned response. *Journal of Neuroscience, 26*(5), 1562–1570. doi:10.1523/JNEUROSCI.4142-05.2006

Kitzing, von, E., Jonas, P., & Sakmann, B. (1994). Quantal analysis of excitatory postsynaptic currents at the hippocampal mossy fiber-CA3 pyramidal cell synapse. *Advances in second messenger and phosphoprotein research, 29*, 235–260.

Klar, T. A., Jakobs, S., Dyba, M., Egner, A., & Hell, S. W. (2000). Fluorescence microscopy with diffraction resolution barrier broken by stimulated emission. *PNAS, 97*(15), 8206–8210.

Klausberger, T. (2009). GABAergic interneurons targeting dendrites of pyramidal cells in the CA1 area of the hippocampus. *The European journal of neuroscience, 30*(6), 947–957. doi:10.1111/j.1460-9568.2009.06913.x

Klein, W. L. (2002). Abeta toxicity in Alzheimer's disease: globular oligomers (ADDLs) as new vaccine and drug targets. *Neurochemistry International, 41*(5), 345–352.

Klyubin, I., Cullen, W. K., Hu, N.-W., & Rowan, M. J. (2012). Alzheimer's disease Aβ assemblies mediating rapid disruption of synaptic plasticity and memory. *Molecular Brain, 5*, 25. doi:10.1186/1756-6606-5-25

Kobayashi, K., & Poo, M.-M. (2004). Spike train timing-dependent associative modification of hippocampal CA3 recurrent synapses by mossy fibers. *Neuron, 41*(3), 445–454.

Koffie, R. M., Meyer-Luehmann, M., Hashimoto, T., Adams, K. W., Mielke, M. L., Garcia-Alloza, M., et al. (2009). Oligomeric amyloid beta associates with

postsynaptic densities and correlates with excitatory synapse loss near senile plaques. *Proceedings of the National Academy of Sciences*, *106*(10), 4012–4017. doi:10.1073/pnas.0811698106

Kohara, K., Pignatelli, M., Rivest, A. J., Jung, H.-Y., Kitamura, T., Suh, J., et al. (2014). Cell type-specific genetic and optogenetic tools reveal hippocampal CA2 circuits. *Nature Neuroscience*, *17*(2), 269–279. doi:10.1038/nn.3614

Kumar, J., & Mayer, M. L. (2013). Functional insights from glutamate receptor ion channel structures. *Annual review of physiology*, *75*, 313–337. doi:10.1146/annurev-physiol-030212-183711

Kwon, H.-B., & Castillo, P. E. (2008a). Long-term potentiation selectively expressed by NMDA receptors at hippocampal mossy fiber synapses. *Neuron*, *57*(1), 108–120. doi:10.1016/j.neuron.2007.11.024

Kwon, H.-B., & Castillo, P. E. (2008b). Role of glutamate autoreceptors at hippocampal mossy fiber synapses. *Neuron*, *60*(6), 1082–1094. doi:10.1016/j.neuron.2008.10.045

Lacor, P. N., Buniel, M. C., Furlow, P. W., Clemente, A. S., Velasco, P. T., Wood, M., et al. (2007). Abeta oligomer-induced aberrations in synapse composition, shape, and density provide a molecular basis for loss of connectivity in Alzheimer's disease. *Journal of Neuroscience*, *27*(4), 796–807. doi:10.1523/JNEUROSCI.3501-06.2007

Lalonde, R., Kim, H. D., Maxwell, J. A., & Fukuchi, K. (2005). Exploratory activity and spatial learning in 12-month-old APP(695)SWE/co+PS1/DeltaE9 mice with amyloid plaques. *Neuroscience Letters*, *390*(2), 87–92. doi:10.1016/j.neulet.2005.08.028

Lambert, J. C., Ibrahim-Verbaas, C. A., Harold, D., Naj, A. C., Sims, R., Bellenguez, C., et al. (2013). Meta-analysis of 74,046 individuals identifies 11 new susceptibility loci for Alzheimer's disease. *Nature Publishing Group*, *45*(12), 1452–1458. doi:10.1038/ng.2802

Lanore, F., Blanchet, C., Fejtova, A., Pinheiro, P., Richter, K., Balschun, D., et al. (2010). Impaired development of hippocampal mossy fibre synapses in mouse mutants for the presynaptic scaffold protein Bassoon. *The Journal of Physiology*, *588*(Pt 12), 2133–2145. doi:10.1113/jphysiol.2009.184929

Laurén, J., Gimbel, D. A., Nygaard, H. B., Gilbert, J. W., & Strittmatter, S. M. (2009). Cellular prion protein mediates impairment of synaptic plasticity by amyloid-beta oligomers. *Nature*, *457*(7233), 1128–1132. doi:10.1038/nature07761

Lauri, S. E., Bortolotto, Z. A., Bleakman, D., Ornstein, P. L., Lodge, D., Isaac, J. T., & Collingridge, G. L. (2001). A critical role of a facilitatory presynaptic kainate receptor in mossy fiber LTP. *Neuron*, *32*(4), 697–709.

Le Meur, K., Galante, M., Angulo, M. C., & Audinat, E. (2007). Tonic activation of NMDA receptors by ambient glutamate of non-synaptic origin in the rat hippocampus. *The Journal of Physiology*, *580*(Pt. 2), 373–383. doi:10.1113/jphysiol.2006.123570

Lee, I., & Kesner, R. P. (2002). Differential contribution of NMDA receptors in hippocampal subregions to spatial working memory. *Nature Neuroscience*, *5*(2), 162–168. doi:10.1038/nn790

Lee, S. H., Kim, K.-R., Ryu, S.-Y., Son, S., Hong, H. S., Mook-Jung, I., et al. (2012).

Impaired short-term plasticity in mossy fiber synapses caused by mitochondrial dysfunction of dentate granule cells is the earliest synaptic deficit in a mouse model of Alzheimer's disease. *Journal of Neuroscience*, *32*(17), 5953–5963. doi:10.1523/JNEUROSCI.0465-12.2012

Lesné, S., Koh, M. T., Kotilinek, L., Kayed, R., Glabe, C. G., Yang, A., et al. (2006). A specific amyloid-beta protein assembly in the brain impairs memory. *Nature*, *440*(7082), 352–357. doi:10.1038/nature04533

Leutgeb, J. K., Leutgeb, S., Moser, M.-B., & Moser, E. I. (2007). Pattern separation in the dentate gyrus and CA3 of the hippocampus. *Science, 315*(5814), 961–966. doi:10.1126/science.1135801

Leutgeb, S., & Leutgeb, J. K. (2007). Pattern separation, pattern completion, and new neuronal codes within a continuous CA3 map. *Learning & memory (Cold Spring Harbor, N.Y.), 14*(11), 745–757. doi:10.1101/lm.703907

Levy-Lahad, E., Wasco, W., Poorkaj, P., Romano, D. M., Oshima, J., Pettingell, W. H., et al. (1995). Candidate gene for the chromosome 1 familial Alzheimer's disease locus. *Science, 269*(5226), 973–977.

Li, S., Hong, S., Shepardson, N. E., Walsh, D. M., Shankar, G. M., & Selkoe, D. (2009). Soluble oligomers of amyloid Beta protein facilitate hippocampal long-term depression by disrupting neuronal glutamate uptake. *Neuron, 62*(6), 788–801. doi:10.1016/j.neuron.2009.05.012

Li, S., Jin, M., Koeglsperger, T., Shepardson, N. E., Shankar, G. M., & Selkoe, D. J. (2011). Soluble Aβ oligomers inhibit long-term potentiation through a mechanism involving excessive activation of extrasynaptic NR2B-containing NMDA receptors. *Journal of Neuroscience, 31*(18), 6627–6638. doi:10.1523/JNEUROSCI.0203-11.2011

Li, S., Shankar, G. M., & Selkoe, D. J. (2010a). How do Soluble Oligomers of Amyloid beta-protein Impair Hippocampal Synaptic Plasticity? *Frontiers in Cellular Neuroscience, 4*, 5. doi:10.3389/fncel.2010.00005

Li, X. G., Somogyi, P., Ylinen, A., & Buzsáki, G. (1994). The hippocampal CA3 network: an in vivo intracellular labeling study. *The Journal of Comparative Neurology, 339*(2), 181–208. doi:10.1002/cne.903390204

Li, Z., Jo, J., Jia, J.-M., Lo, S.-C., Whitcomb, D. J., Jiao, S., et al. (2010b). Caspase-3 activation via mitochondria is required for long-term depression and AMPA receptor internalization. *Cell, 141*(5), 859–871. doi:10.1016/j.cell.2010.03.053

Limon, A., Reyes-Ruiz, J. M., & Miledi, R. (2012). Loss of functional GABA(A) receptors in the Alzheimer diseased brain. *Proceedings of the National Academy of Sciences, 109*(25), 10071–10076. doi:10.1073/pnas.1204606109

Lisman, J. E., Raghavachari, S., & Tsien, R. W. (2007). The sequence of events that underlie quantal transmission at central glutamatergic synapses. *Nature Reviews Neuroscience, 8*(8), 597–609. doi:10.1038/nrn2191

Lisman, J., Yasuda, R., & Raghavachari, S. (2012). Mechanisms of CaMKII action in long-term potentiation. *Nature Reviews Neuroscience, 13*(3), 169–182. doi:10.1038/nrn3192

Littleton, J. T. (2006). Mixing and matching during synaptic vesicle endocytosis.

Neuron, *51*(2), 149–151. doi:10.1016/j.neuron.2006.07.002

Liu, L., Wong, T. P., Pozza, M. F., Lingenhoehl, K., Wang, Y., Sheng, M., et al. (2004). Role of NMDA receptor subtypes in governing the direction of hippocampal synaptic plasticity. *Science*, *304*(5673), 1021–1024. doi:10.1126/science.1096615

Liu, X., Ramirez, S., Pang, P. T., Puryear, C. B., Govindarajan, A., Deisseroth, K., & Tonegawa, S. (2012). Optogenetic stimulation of a hippocampal engram activates fear memory recall. *Nature*, *484*(7394), 381–385. doi:10.1038/nature11028

Malenka, R. C., & Bear, M. F. (2004). LTP and LTD: an embarrassment of riches. *Neuron*, *44*(1), 5–21. doi:10.1016/j.neuron.2004.09.012

Marchetti, C., & Marie, H. (2011). Hippocampal synaptic plasticity in Alzheimer's disease: what have we learned so far from transgenic models? *Reviews in the neurosciences*, *22*(4), 373–402. doi:10.1515/RNS.2011.035

Martel, M. A., Wyllie, D. J. A., & Hardingham, G. E. (2009). In developing hippocampal neurons, NR2B-containing N-methyl-D-aspartate receptors (NMDARs) can mediate signaling to neuronal survival and synaptic potentiation, as well as neuronal death. *NSC*, *158*(1), 334–343. doi:10.1016/j.neuroscience.2008.01.080

Martinez, C. O., Do, V. H., Martinez, J. L., & Derrick, B. E. (2002). Associative long-term potentiation (LTP) among extrinsic afferents of the hippocampal CA3 region in vivo. *Brain Research*, *940*(1-2), 86–94.

Massey, P. V., Johnson, B. E., Moult, P. R., Auberson, Y. P., Brown, M. W., Molnár, E., et al. (2004). Differential roles of NR2A and NR2B-containing NMDA receptors in cortical long-term potentiation and long-term depression. *Journal of Neuroscience*, *24*(36), 7821–7828. doi:10.1523/JNEUROSCI.1697-04.2004

Matos, M., Augusto, E., Santos-Rodrigues, A. D., Schwarzschild, M. A., Chen, J.-F., Cunha, R. A., & Agostinho, P. (2012). Adenosine A2A receptors modulate glutamate uptake in cultured astrocytes and gliosomes. *Glia*, *60*(5), 702–716. doi:10.1002/glia.22290

Matsuzaki, M., Honkura, N., Ellis-Davies, G. C. R., & Kasai, H. (2004). Structural basis of long-term potentiation in single dendritic spines. *Nature*, *429*(6993), 761–766. doi:10.1038/nature02617

Mayer, M. L., & Armstrong, N. (2004). Structure and function of glutamate receptor ion channels. *Annual review of physiology*, *66*, 161–181. doi:10.1146/annurev.physiol.66.050802.084104

Mayford, M., Siegelbaum, S. A., & Kandel, E. R. (2012). Synapses and memory storage. *Cold Spring Harbor Perspectives in Biology*, *4*(6). doi:10.1101/cshperspect.a005751

McGowan, E., Eriksen, J., & Hutton, M. (2006). A decade of modeling Alzheimer's disease in transgenic mice. *Trends in genetics : TIG*, *22*(5), 281–289. doi:10.1016/j.tig.2006.03.007

Morgan, D., Diamond, D. M., Gottschall, P. E., Ugen, K. E., Dickey, C., Hardy, J., et al. (2000). A beta peptide vaccination prevents memory loss in an animal model of Alzheimer's disease. *Nature*, *408*(6815), 982–985. doi:10.1038/35050116

Moustaine, El, D., Granier, S., Doumazane, E., Scholler, P., Rahmeh, R., Bron, P., et al. (2012). Distinct roles of metabotropic glutamate receptor dimerization in agonist

activation and G-protein coupling. *Proceedings of the National Academy of Sciences*, *109*(40), 16342–16347. doi:10.1073/pnas.1205838109

Mucke, L., & Selkoe, D. J. (2012). Neurotoxicity of amyloid β-protein: synaptic and network dysfunction. *Cold Spring Harbor perspectives in medicine*, *2*(7), a006338–a006338. doi:10.1101/cshperspect.a006338

Mulle, C., Sailer, A., Pérez-Otaño, I., Dickinson-Anson, H., Castillo, P. E., Bureau, I., et al. (1998). Altered synaptic physiology and reduced susceptibility to kainate-induced seizures in GluR6-deficient mice. *Nature*, *392*(6676), 601–605. doi:10.1038/33408

Muller, D., Nikonenko, I., Jourdain, P., & Alberi, S. (2002). LTP, memory and structural plasticity. *Current molecular medicine*, *2*(7), 605–611.

Muller, D., Toni, N., & Buchs, P. A. (2000). Spine changes associated with long-term potentiation. *Hippocampus, 10*(5), 596–604. doi:10.1002/1098-1063(2000)10:5<596::AID-HIPO10>3.0.CO;2-Y

Nagy, Z., Esiri, M. M., Jobst, K. A., Morris, J. H., King, E. M., McDonald, B., et al. (1995). Relative roles of plaques and tangles in the dementia of Alzheimer's disease: correlations using three sets of neuropathological criteria. *Dementia (Basel, Switzerland), 6*(1), 21–31.

Nakagawa, T., Cheng, Y., Ramm, E., Sheng, M., & Walz, T. (2005). Structure and different conformational states of native AMPA receptor complexes. *Nature*, *433*(7025), 545–549. doi:10.1038/nature03328

Nakashiba, T., Buhl, D. L., McHugh, T. J., & Tonegawa, S. (2009). Hippocampal CA3 output is crucial for ripple-associated reactivation and consolidation of memory. *Neuron, 62*(6), 781–787. doi:10.1016/j.neuron.2009.05.013

Nakazawa, K. K., Quirk, M. C. M., Chitwood, R. A. R., Watanabe, M. M., Yeckel, M. F. M., Sun, L. D. L., et al. (2002). Requirement for hippocampal CA3 NMDA receptors in associative memory recall. *Science, 297*(5579), 211–218. doi:10.1126/science.1071795

Nakazawa, K., McHugh, T. J., Wilson, M. A., & Tonegawa, S. (2004). NMDA receptors, place cells and hippocampal spatial memory. *Nature Reviews Neuroscience, 5*(5), 361–372. doi:10.1038/nrn1385

Neves, G., Cooke, S. F., & Bliss, T. V. P. (2008). Synaptic plasticity, memory and the hippocampus: a neural network approach to causality. *Nature Reviews Neuroscience, 9*(1), 65–75. doi:10.1038/nrn2303

Nicoll, R. A., & Roche, K. W. (2013). Long-term potentiation: Peeling the onion. *Neuropharmacology, 74*, 18–22. doi:10.1016/j.neuropharm.2013.02.010

Nicoll, R. A., & Schmitz, D. (2005). Synaptic plasticity at hippocampal mossy fibre synapses. *Nature Reviews Neuroscience, 6*(11), 863–876. doi:10.1038/nrn1786

Niswender, C. M., & Conn, P. J. (2010). Metabotropic glutamate receptors: physiology, pharmacology, and disease. *Annual Review of Pharmacology and Toxicology, 50*, 295–322. doi:10.1146/annurev.pharmtox.011008.145533

Novák, P., & Zahradník, I. (2005). Computer-aided formation of the whole-cell patch-clamp recording configuration. *General physiology and biophysics*, *24*(3), 337–348.

O'Keefe, J. (1992). Hippocampus, theta, and spatial memory. *Current Opinion in*

Neurobiology, *3*(6), 917–924. doi:10.1016/0959-4388(93)90163-S

Ohm, T. G. (2007). The dentate gyrus in Alzheimer's disease. *Progress in brain research*, *163*, 723–740. doi:10.1016/S0079-6123(07)63039-8

Palop, J. J., Chin, J., Roberson, E. D., Wang, J., Thwin, M. T., Bien-Ly, N., et al. (2007). Aberrant excitatory neuronal activity and compensatory remodeling of inhibitory hippocampal circuits in mouse models of Alzheimer's disease. *Neuron*, *55*(5), 697–711. doi:10.1016/j.neuron.2007.07.025

Paoletti, P., & Neyton, J. (2007). NMDA receptor subunits: function and pharmacology. *Current Opinion in Pharmacology*, *7*(1), 39–47. doi:10.1016/j.coph.2006.08.011

Paoletti, P., Bellone, C., & Zhou, Q. (2013). NMDA receptor subunit diversity: impact on receptor properties, synaptic plasticity and disease. *Nature Reviews Neuroscience*, *14*(6), 383–400. doi:10.1038/nrn3504

Papouin, T., Ladépêche, L., Ruel, J., Sacchi, S., Labasque, M., Hanini, M., et al. (2012). Synaptic and extrasynaptic NMDA receptors are gated by different endogenous coagonists. *Cell*, *150*(3), 633–646. doi:10.1016/j.cell.2012.06.029

Papp, G., Witter, M. P., & Treves, A. (2007). The CA3 network as a memory store for spatial representations. *Learning & memory (Cold Spring Harbor, N.Y.)*, *14*(11), 732–744. doi:10.1101/lm.687407

Park, J. H., Widi, G. A., Gimbel, D. A., Harel, N. Y., Lee, D. H. S., & Strittmatter, S. M. (2006). Subcutaneous Nogo receptor removes brain amyloid-beta and improves spatial memory in Alzheimer's transgenic mice. *Journal of Neuroscience*, *26*(51), 13279–13286. doi:10.1523/JNEUROSCI.4504-06.2006

Pastalkova, E., Serrano, P., Pinkhasova, D., Wallace, E., Fenton, A. A., & Sacktor, T. C. (2006). Storage of spatial information by the maintenance mechanism of LTP. *Science*, *313*(5790), 1141–1144. doi:10.1126/science.1128657

Paxinos, G., & Franklin, K. B. J. (2008). *The Mouse Brain in Stereotaxic Coordinates*. Academic Press.

Pelkey, K. A., Topolnik, L., Lacaille, J.-C., & McBain, C. J. (2006). Compartmentalized Ca(2+) channel regulation at divergent mossy-fiber release sites underlies target cell-dependent plasticity. *Neuron*, *52*(3), 497–510. doi:10.1016/j.neuron.2006.08.032

Pereda, A. E. (2014). Electrical synapses and their functional interactions with chemical synapses. *Nature Publishing Group*, *15*(4), 250–263. doi:10.1038/nrn3708

Perez-Cruz, C., Nolte, M. W., van Gaalen, M. M., Rustay, N. R., Termont, A., Tanghe, A., et al. (2011). Reduced Spine Density in Specific Regions of CA1 Pyramidal Neurons in Two Transgenic Mouse Models of Alzheimer's Disease. *Journal of Neuroscience*, *31*(10), 3926–3934. doi:10.1523/JNEUROSCI.6142-10.2011

Petersen, R. C. (2004). Mild cognitive impairment as a diagnostic entity. *Journal of internal medicine*, *256*(3), 183–194. doi:10.1111/j.1365-2796.2004.01388.x

Phillips, R. G., & LeDoux, J. E. (1992). Differential contribution of amygdala and hippocampus to cued and contextual fear conditioning. *Behavioral Neuroscience*, *106*(2), 274–285.

Piers, T. M., Kim, D. H., Kim, B. C., Regan, P., Whitcomb, D. J., & Cho, K. (2012). Translational Concepts of mGluR5 in Synaptic Diseases of the Brain. *Frontiers in*

pharmacology, *3*, 199. doi:10.3389/fphar.2012.00199

Pinheiro, P. S., & Mulle, C. (2008). Presynaptic glutamate receptors: physiological functions and mechanisms of action. *Nature Reviews Neuroscience, 9*(6), 423–436. doi:10.1038/nrn2379

Pinheiro, P. S., Lanore, F., Veran, J., Artinian, J., Blanchet, C., Crepel, V., et al. (2013). Selective Block of Postsynaptic Kainate Receptors Reveals Their Function at Hippocampal Mossy Fiber Synapses. *Cerebral cortex (New York, N.Y. : 1991), 23*(2), 323–331. doi:10.1093/cercor/bhs022

Pinheiro, P. S., Perrais, D., Coussen, F., Barhanin, J., Bettler, B., Mann, J. R., et al. (2007). GluR7 is an essential subunit of presynaptic kainate autoreceptors at hippocampal mossy fiber synapses. *PNAS, 104*(29), 12181–12186. doi:10.1073/pnas.0608891104

Poirier, J. (1994). Apolipoprotein E in animal models of CNS injury and in Alzheimer's disease. *Trends in Neurosciences, 17*(12), 525–530.

Puzzo, D., Lee, L., Palmeri, A., Calabrese, G., & Arancio, O. (2014). Behavioral assays with mouse models of Alzheimer's disease: practical considerations and guidelines. *Biochemical pharmacology, 88*(4), 450–467. doi:10.1016/j.bcp.2014.01.011

Pyapali, G. K., Sík, A., Penttonen, M., Buzsáki, G., & Turner, D. A. (1998). Dendritic properties of hippocampal CA1 pyramidal neurons in the rat: intracellular staining in vivo and in vitro. *The Journal of Comparative Neurology, 391*(3), 335–352.

Raber, J., Huang, Y., & Ashford, J. W. (2004). ApoE genotype accounts for the vast majority of AD risk and AD pathology. *Neurobiology of Aging, 25*(5), 641–650. doi:10.1016/j.neurobiolaging.2003.12.023

Rajji, T., Chapman, D., Eichenbaum, H., & Greene, R. (2006). The role of CA3 hippocampal NMDA receptors in paired associate learning. *Journal of Neuroscience, 26*(3), 908–915. doi:10.1523/JNEUROSCI.4194-05.2006

Ramamoorthi, K., Fropf, R., Belfort, G. M., Fitzmaurice, H. L., McKinney, R. M., Neve, R. L., et al. (2011). Npas4 regulates a transcriptional program in CA3 required for contextual memory formation. *Science, 334*(6063), 1669–1675. doi:10.1126/science.1208049

Rebola, N., Canas, P. M., Oliveira, C. R., & Cunha, R. A. (2005). Different synaptic and subsynaptic localization of adenosine A2A receptors in the hippocampus and striatum of the rat. *NSC, 132*(4), 893–903. doi:10.1016/j.neuroscience.2005.01.014

Rebola, N., Carta, M., Lanore, F., Blanchet, C., & Mulle, C. (2011). NMDA receptor-dependent metaplasticity at hippocampal mossy fiber synapses. *Nature Neuroscience, 14*(6), 691–693. doi:10.1038/nn.2809

Rebola, N., Luján, R., Cunha, R. A., & Mulle, C. (2008). Adenosine A2A receptors are essential for long-term potentiation of NMDA-EPSCs at hippocampal mossy fiber synapses. *Neuron, 57*(1), 121–134. doi:10.1016/j.neuron.2007.11.023

Rebola, N., Pinheiro, P. C., Oliveira, C. R., Malva, J. O., & Cunha, R. A. (2003). Subcellular localization of adenosine A(1) receptors in nerve terminals and synapses of the rat hippocampus. *Brain Research, 987*(1), 49–58. doi:10.1016/S0006-8993(03)03247-5

Rebola, N., Srikumar, B. N., & Mulle, C. (2010). Activity-dependent synaptic plasticity of

NMDA receptors. *The Journal of Physiology*, *588*(Pt 1), 93–99. doi:10.1113/jphysiol.2009.179382

Regehr, W. G. (2012). Short-term presynaptic plasticity. *Cold Spring Harbor Perspectives in Biology*, *4*(7), a005702. doi:10.1101/cshperspect.a005702

Regehr, W. G., & Tank, D. W. (1991). The maintenance of LTP at hippocampal mossy fiber synapses is independent of sustained presynaptic calcium. *Neuron*, *7*(3), 451–459.

Regehr, W. G., Delaney, K. R., & Tank, D. W. (1994). The role of presynaptic calcium in short-term enhancement at the hippocampal mossy fiber synapse. *The Journal of neuroscience : the official journal of the Society for Neuroscience*, *14*(2), 523–537.

Reid, C. A., Dixon, D. B., Takahashi, M., Bliss, T. V. P., & Fine, A. (2004). Optical quantal analysis indicates that long-term potentiation at single hippocampal mossy fiber synapses is expressed through increased release probability, recruitment of new release sites, and activation of silent synapses. *Journal of Neuroscience*, *24*(14), 3618–3626. doi:10.1523/JNEUROSCI.3567-03.2004

Renner, M., Lacor, P. N., Velasco, P. T., Xu, J., Contractor, A., Klein, W. L., & Triller, A. (2010). Deleterious Effects of Amyloid β Oligomers Acting as an Extracellular Scaffold for mGluR5. *Neuron*, *66*(5), 739–754. doi:10.1016/j.neuron.2010.04.029

Rizzoli, S. O., & Betz, W. J. (2005). Synaptic vesicle pools. *Nature Reviews Neuroscience*, *6*(1), 57–69. doi:10.1038/nrn1583

Roberson, E. D., Halabisky, B., Yoo, J. W., Yao, J., Chin, J., Yan, F., et al. (2011). Amyloid-β/Fyn-induced synaptic, network, and cognitive impairments depend on tau levels in multiple mouse models of Alzheimer's disease. *Journal of Neuroscience*, *31*(2), 700–711. doi:10.1523/JNEUROSCI.4152-10.2011

Rollenhagen, A., & Lübke, J. H. R. (2010). The mossy fiber bouton: the "common" or the "unique" synapse? *Frontiers in Synaptic Neuroscience*, *2*, 2. doi:10.3389/fnsyn.2010.00002

Rollenhagen, A., Sätzler, K., Rodriguez, E. P., Jonas, P., Frotscher, M., & Lübke, J. H. R. (2007). Structural determinants of transmission at large hippocampal mossy fiber synapses. *Journal of Neuroscience*, *27*(39), 10434–10444. doi:10.1523/JNEUROSCI.1946-07.2007

Rolls, E. T., & Treves, A. (1994). Neural networks in the brain involved in memory and recall. *Progress in brain research*, *102*, 335–341. doi:10.1016/S0079-6123(08)60550-6

Rosenzweig, E. S., & Barnes, C. A. (2003). Impact of aging on hippocampal function: plasticity, network dynamics, and cognition. *Progress in Neurobiology*, *69*(3), 143–179. doi:10.1016/S0301-0082(02)00126-0

Rönicke, R., Mikhaylova, M., Rönicke, S., Meinhardt, J., Schröder, U. H., Fändrich, M., et al. (2011). Early neuronal dysfunction by amyloid β oligomers depends on activation of NR2B-containing NMDA receptors. *Neurobiology of Aging*, *32*(12), 2219–2228. doi:10.1016/j.neurobiolaging.2010.01.011

Ruediger, S., Vittori, C., Bednarek, E., Genoud, C., Strata, P., Sacchetti, B., & Caroni, P. (2011). Learning-related feedforward inhibitory connectivity growth required for

memory precision. *Nature*, *473*(7348), 514–518. doi:10.1038/nature09946

Ruiz, A., Fabian-Fine, R., Scott, R., Walker, M. C., Rusakov, D. A., & Kullmann, D. M. (2003). GABAA receptors at hippocampal mossy fibers. *Neuron*, *39*(6), 961–973.

Sachidhanandam, S., Blanchet, C., Jeantet, Y., Cho, Y. H., & Mulle, C. (2009). Kainate receptors act as conditional amplifiers of spike transmission at hippocampal mossy fiber synapses. *Journal of Neuroscience*, *29*(15), 5000–5008. doi:10.1523/JNEUROSCI.5807-08.2009

Saganich, M. J., Schroeder, B. E., Galvan, V., Bredesen, D. E., Koo, E. H., & Heinemann, S. F. (2006). Deficits in synaptic transmission and learning in amyloid precursor protein (APP) transgenic mice require C-terminal cleavage of APP. *Journal of Neuroscience*, *26*(52), 13428–13436. doi:10.1523/JNEUROSCI.4180-06.2006

Salin, P. A., Scanziani, M., Malenka, R. C., & Nicoll, R. A. (1996). Distinct short-term plasticity at two excitatory synapses in the hippocampus. *PNAS*, *93*(23), 13304–13309.

Sanacora, G., Zarate, C. A., Krystal, J. H., & Manji, H. K. (2008). Targeting the glutamatergic system to develop novel, improved therapeutics for mood disorders. *Nature Reviews Drug Discovery*, *7*(5), 426–437. doi:10.1038/nrd2462

Sandi, C., Davies, H. A., Cordero, M. I., Rodriguez, J. J., Popov, V. I., & Stewart, M. G. (2003). Rapid reversal of stress induced loss of synapses in CA3 of rat hippocampus following water maze training. *The European journal of neuroscience*, *17*(11), 2447–2456. doi:10.1046/j.1460-9568.2003.02675.x

Sandler, R., & Smith, A. D. (1991). Coexistence of GABA and glutamate in mossy fiber terminals of the primate hippocampus: an ultrastructural study. *The Journal of Comparative Neurology*, *303*(2), 177–192. doi:10.1002/cne.903030202

Scanziani, M., Capogna, M., Gähwiler, B. H., & Thompson, S. M. (1992). Presynaptic inhibition of miniature excitatory synaptic currents by baclofen and adenosine in the hippocampus. *Neuron*, *9*(5), 919–927.

Scanziani, M., Salin, P. A., Vogt, K. E., Malenka, R. C., & Nicoll, R. A. (1997). Use-dependent increases in glutamate concentration activate presynaptic metabotropic glutamate receptors. *Nature*, *385*(6617), 630–634. doi:10.1038/385630a0

Schmitz, D., Mellor, J., & Nicoll, R. A. (2001). Presynaptic kainate receptor mediation of frequency facilitation at hippocampal mossy fiber synapses. *Science*, *291*(5510), 1972–1976. doi:10.1126/science.1057105

Schmitz, D., Mellor, J., Breustedt, J., & Nicoll, R. A. (2003). Presynaptic kainate receptors impart an associative property to hippocampal mossy fiber long-term potentiation. *Nature Neuroscience*, *6*(10), 1058–1063. doi:10.1038/nn1116

Schneggenburger, R., & Neher, E. (2005). Presynaptic calcium and control of vesicle fusion. *Current Opinion in Neurobiology*, *15*(3), 266–274. doi:10.1016/j.conb.2005.05.006

Scholz, K. P., & Miller, R. J. (1992). Inhibition of quantal transmitter release in the absence of calcium influx by a G protein-linked adenosine receptor at hippocampal synapses. *Neuron*, *8*(6), 1139–1150.

Schweizer, F. E., & Ryan, T. A. (2006). The synaptic vesicle: cycle of exocytosis and

endocytosis. *Current Opinion in Neurobiology*, *16*(3), 298–304. doi:10.1016/j.conb.2006.05.006

Scott, R., Lalic, T., Kullmann, D. M., Capogna, M., & Rusakov, D. A. (2008). Target-cell specificity of kainate autoreceptor and Ca2+-store-dependent short-term plasticity at hippocampal mossy fiber synapses. *Journal of Neuroscience*, *28*(49), 13139–13149. doi:10.1523/JNEUROSCI.2932-08.2008

SCOVILLE, W. B., & MILNER, B. (1957). Loss of recent memory after bilateral hippocampal lesions. *Journal of neurology, neurosurgery, and psychiatry*, *20*(1), 11–21.

Selkoe, D. J. (1991). The molecular pathology of Alzheimer's disease. *Neuron*, *6*(4), 487–498.

Selkoe, D. J. (2002). Alzheimer's disease is a synaptic failure. *Science*, *298*(5594), 789–791. doi:10.1126/science.1074069

Selkoe, D. J. (2011). Alzheimer's disease. *Cold Spring Harbor Perspectives in Biology*, *3*(7). doi:10.1101/cshperspect.a004457

Selkoe, D., Mandelkow, E., & Holtzman, D. (2012). Deciphering Alzheimer disease. *Cold Spring Harbor perspectives in medicine*, *2*(1), a011460. doi:10.1101/cshperspect.a011460

Shankar, G. M., Bloodgood, B. L., Townsend, M., Walsh, D. M., Selkoe, D. J., & Sabatini, B. L. (2007). Natural oligomers of the Alzheimer amyloid-beta protein induce reversible synapse loss by modulating an NMDA-type glutamate receptor-dependent signaling pathway. *Journal of Neuroscience*, *27*(11), 2866–2875. doi:10.1523/JNEUROSCI.4970-06.2007

Shankar, G. M., Li, S., Mehta, T. H., Garcia-Munoz, A., Shepardson, N. E., Smith, I., et al. (2008). Amyloid-beta protein dimers isolated directly from Alzheimer's brains impair synaptic plasticity and memory. *Nature Medicine*, *14*(8), 837–842. doi:10.1038/nm1782

Sheng, M., Sabatini, B. L., & Sudhof, T. C. (2012). Synapses and Alzheimer's Disease. *Cold Spring Harbor Perspectives in Biology*, *4*(5), a005777–a005777. doi:10.1101/cshperspect.a005777

Shepherd, G. M., & Harris, K. M. (1998). Three-dimensional structure and composition of CA3-->CA1 axons in rat hippocampal slices: implications for presynaptic connectivity and compartmentalization. *The Journal of neuroscience : the official journal of the Society for Neuroscience*, *18*(20), 8300–8310.

Sherrington, R., Rogaev, E. I., Liang, Y., Rogaeva, E. A., Levesque, G., Ikeda, M., et al. (1995). Cloning of a gene bearing missense mutations in early-onset familial Alzheimer's disease. *Nature*, *375*(6534), 754–760. doi:10.1038/375754a0

Sisodia, S. S., & St George-Hyslop, P. H. (2002). gamma-Secretase, Notch, Abeta and Alzheimer's disease: where do the presenilins fit in? *Nature Reviews Neuroscience*, *3*(4), 281–290. doi:10.1038/nrn785

Sloviter, R. S., Dichter, M. A., Rachinsky, T. L., Dean, E., Goodman, J. H., Sollas, A. L., & Martin, D. L. (1996). Basal expression and induction of glutamate decarboxylase and GABA in excitatory granule cells of the rat and monkey hippocampal dentate gyrus. *The Journal of Comparative Neurology*, *373*(4), 593–618.

doi:10.1002/(SICI)1096-9861(19960930)373:4<593::AID-CNE8>3.0.CO;2-X

Smart, T. G., & Paoletti, P. (2012). Synaptic neurotransmitter-gated receptors. *Cold Spring Harbor Perspectives in Biology*, *4*(3). doi:10.1101/cshperspect.a009662

Snyder, E. M., Philpot, B. D., Huber, K. M., Dong, X., Fallon, J. R., & Bear, M. F. (2001). Internalization of ionotropic glutamate receptors in response to mGluR activation. *Nature Neuroscience*, *4*(11), 1079–1085. doi:10.1038/nn746

Spires, T. L., & Hyman, B. T. (2005). Transgenic models of Alzheimer's disease: learning from animals. *NeuroRx : the journal of the American Society for Experimental NeuroTherapeutics*, *2*(3), 423–437. doi:10.1602/neurorx.2.3.423

Spires-Jones, T. L., Meyer-Luehmann, M., Osetek, J. D., Jones, P. B., Stern, E. A., Bacskai, B. J., & Hyman, B. T. (2007). Impaired spine stability underlies plaque-related spine loss in an Alzheimer's disease mouse model. *The American Journal of Pathology*, *171*(4), 1304–1311. doi:10.2353/ajpath.2007.070055

Stewart, M. G., Davies, H. A., Sandi, C., Kraev, I. V., Rogachevsky, V. V., Peddie, C. J., et al. (2005). Stress suppresses and learning induces plasticity in CA3 of rat hippocampus: a three-dimensional ultrastructural study of thorny excrescences and their postsynaptic densities. *NSC*, *131*(1), 43–54. doi:10.1016/j.neuroscience.2004.10.031

Straub, C., & Tomita, S. (2012). The regulation of glutamate receptor trafficking and function by TARPs and other transmembrane auxiliary subunits. *Current Opinion in Neurobiology*, *22*(3), 488–495. doi:10.1016/j.conb.2011.09.005

Sutton, M. A., & Schuman, E. M. (2006). Dendritic protein synthesis, synaptic plasticity, and memory. *Cell*, *127*(1), 49–58. doi:10.1016/j.cell.2006.09.014

Südhof, T. C., & Rothman, J. E. (2009). Membrane fusion: grappling with SNARE and SM proteins. *Science*, *323*(5913), 474–477. doi:10.1126/science.1161748

Talantova, M., Sanz-Blasco, S., Zhang, X., Xia, P., Akhtar, M. W., Okamoto, S.-I., et al. (2013). Aβ induces astrocytic glutamate release, extrasynaptic NMDA receptor activation, and synaptic loss. *Proceedings of the National Academy of Sciences*, *110*(27), E2518–27. doi:10.1073/pnas.1306832110

Tamamaki, N., & Nojyo, Y. (1990). Disposition of the slab-like modules formed by axon branches originating from single CA1 pyramidal neurons in the rat hippocampus. *The Journal of Comparative Neurology*, *291*(4), 509–519. doi:10.1002/cne.902910403

Tanzi, R. E. (2005). The synaptic Abeta hypothesis of Alzheimer disease. *Nature Neuroscience*, *8*(8), 977–979. doi:10.1038/nn0805-977

Tebano, M. T., Martire, A., Rebola, N., Pepponi, R., Domenici, M. R., Gro, M. C., et al. (2005). Adenosine A2A receptors and metabotropic glutamate 5 receptors are co-localized and functionally interact in the hippocampus: a possible key mechanism in the modulation of N-methyl-D-aspartate effects. *Journal of Neurochemistry*, *95*(4), 1188–1200. doi:10.1111/j.1471-4159.2005.03455.x

Terry, R. D., Masliah, E., Salmon, D. P., Butters, N., DeTeresa, R., Hill, R., et al. (1991). Physical basis of cognitive alterations in Alzheimer's disease: synapse loss is the major correlate of cognitive impairment. *Annals of Neurology*, *30*(4), 572–580. doi:10.1002/ana.410300410

Toth, K., Suares, G., Lawrence, J. J., Philips-Tansey, E., & McBain, C. J. (2000). Differential mechanisms of transmission at three types of mossy fiber synapse. *Journal of Neuroscience*, *20*(22), 8279–8289.

Townsend, M., Shankar, G. M., Mehta, T., Walsh, D. M., & Selkoe, D. J. (2006). Effects of secreted oligomers of amyloid beta-protein on hippocampal synaptic plasticity: a potent role for trimers. *The Journal of Physiology*, *572*(Pt 2), 477–492. doi:10.1113/jphysiol.2005.103754

Traynelis, S. F., Wollmuth, L. P., McBain, C. J., Menniti, F. S., Vance, K. M., Ogden, K. K., et al. (2010). Glutamate receptor ion channels: structure, regulation, and function. *Pharmacological reviews*, *62*(3), 405–496. doi:10.1124/pr.109.002451

Treves, A., & Rolls, E. T. (1994). Computational analysis of the role of the hippocampus in memory. *Hippocampus*, *4*(3), 374–391. doi:10.1002/hipo.450040319

Trinchese, F., Liu, S., Battaglia, F., Walter, S., Mathews, P. M., & Arancio, O. (2004). Progressive age-related development of Alzheimer-like pathology in APP/PS1 mice. *Annals of Neurology*, *55*(6), 801–814. doi:10.1002/ana.20101

Turrigiano, G. G., & Nelson, S. B. (2004). Homeostatic plasticity in the developing nervous system. *Nature Reviews Neuroscience*, *5*(2), 97–107. doi:10.1038/nrn1327

Tønnesen, J., Katona, G., Rózsa, B., & Nägerl, U. V. (2014). Spine neck plasticity regulates compartmentalization of synapses. *Nature Neuroscience*, *17*(5), 678–685. doi:10.1038/nn.3682

Tønnesen, J., Nadrigny, F., Willig, K. I., Wedlich-Söldner, R., & Nägerl, U. V. (2011). Two-color STED microscopy of living synapses using a single laser-beam pair. *Biophysical journal*, *101*(10), 2545–2552. doi:10.1016/j.bpj.2011.10.011

Um, J. W., Kaufman, A. C., Kostylev, M., Heiss, J. K., Stagi, M., Takahashi, H., et al. (2013). Metabotropic glutamate receptor 5 is a coreceptor for Alzheimer aβ oligomer bound to cellular prion protein. *Neuron*, *79*(5), 887–902. doi:10.1016/j.neuron.2013.06.036

Urban, N. T., Willig, K. I., Hell, S. W., & Nägerl, U. V. (2011). STED nanoscopy of actin dynamics in synapses deep inside living brain slices. *Biophysical journal*, *101*(5), 1277–1284. doi:10.1016/j.bpj.2011.07.027

Vassar, R., Bennett, B. D., Babu-Khan, S., Kahn, S., Mendiaz, E. A., Denis, P., et al. (1999). Beta-secretase cleavage of Alzheimer's amyloid precursor protein by the transmembrane aspartic protease BACE. *Science*, *286*(5440), 735–741.

Vergnano, A. M., Rebola, N., Savtchenko, L. P., Pinheiro, P. S., Casado, M., Kieffer, B. L., et al. (2014). Zinc dynamics and action at excitatory synapses. *Neuron*, *82*(5), 1101–1114. doi:10.1016/j.neuron.2014.04.034

Vogt, K. E., & Nicoll, R. A. (1999). Glutamate and gamma-aminobutyric acid mediate a heterosynaptic depression at mossy fiber synapses in the hippocampus. *PNAS*, *96*(3), 1118–1122.

Vyleta, N. P., & Jonas, P. (2014). Loose coupling between Ca2+ channels and release sensors at a plastic hippocampal synapse. *Science*, *343*(6171), 665–670. doi:10.1126/science.1244811

Walsh, D. M., Klyubin, I., Fadeeva, J. V., Cullen, W. K., Anwyl, R., Wolfe, M. S., et al. (2002). Naturally secreted oligomers of amyloid beta protein potently inhibit hippocampal long-term potentiation in vivo. *Nature*, *416*(6880), 535–539. doi:10.1038/416535a

Wang, H. Y., Lee, D. H., D'Andrea, M. R., Peterson, P. A., Shank, R. P., & Reitz, A. B. (2000). beta-Amyloid(1-42) binds to alpha7 nicotinic acetylcholine receptor with high affinity. Implications for Alzheimer's disease pathology. *Journal of Biological Chemistry*, *275*(8), 5626–5632.

Wang, H.-W., Pasternak, J. F., Kuo, H., Ristic, H., Lambert, M. P., Chromy, B., et al. (2002). Soluble oligomers of beta amyloid (1-42) inhibit long-term potentiation but not long-term depression in rat dentate gyrus. *Brain Research*, *924*(2), 133–140.

Wang, J. H., Ma, Y. Y., & van den Buuse, M. (2006). Improved spatial recognition memory in mice lacking adenosine A2A receptors. *Experimental Neurology*, *199*(2), 438–445. doi:10.1016/j.expneurol.2006.01.005

Wang, Q., Rowan, M. J., & Anwyl, R. (2004). Beta-amyloid-mediated inhibition of NMDA receptor-dependent long-term potentiation induction involves activation of microglia and stimulation of inducible nitric oxide synthase and superoxide. *Journal of Neuroscience*, *24*(27), 6049–6056. doi:10.1523/JNEUROSCI.0233-04.2004

Webster, S. J., Bachstetter, A. D., Nelson, P. T., Schmitt, F. A., & Van Eldik, L. J. (2014). Using mice to model Alzheimer's dementia: an overview of the clinical disease and the preclinical behavioral changes in 10 mouse models. *Frontiers in genetics*, *5*, 88. doi:10.3389/fgene.2014.00088

Wei, W., Nguyen, L. N., Kessels, H. W., Hagiwara, H., Sisodia, S., & Malinow, R. (2010). Amyloid beta from axons and dendrites reduces local spine number and plasticity. *Nature Neuroscience*, *13*(2), 190–196. doi:10.1038/nn.2476

Weisskopf, M. G., & Nicoll, R. A. (1995). Presynaptic changes during mossy fibre LTP revealed by NMDA receptor-mediated synaptic responses. *Nature*, *376*(6537), 256–259. doi:10.1038/376256a0

Weisskopf, M. G., Castillo, P. E., Zalutsky, R. A., & Nicoll, R. A. (1994). Mediation of hippocampal mossy fiber long-term potentiation by cyclic AMP. *Science*, *265*(5180), 1878–1882.

Whitlock, J. R., Heynen, A. J., Shuler, M. G., & Bear, M. F. (2006). Learning induces long-term potentiation in the hippocampus. *Science*, *313*(5790), 1093–1097. doi:10.1126/science.1128134

Wickersham, I. R., Finke, S., Conzelmann, K.-K., & Callaway, E. M. (2007). Retrograde neuronal tracing with a deletion-mutant rabies virus. *Nature Methods*, *4*(1), 47–49. doi:10.1038/nmeth999

Wilke, S. A., Raam, T., Antonios, J. K., Bushong, E. A., Koo, E. H., Ellisman, M. H., & Ghosh, A. (2014). Specific disruption of hippocampal mossy fiber synapses in a mouse model of familial Alzheimer's disease. *PLoS ONE*, *9*(1), e84349. doi:10.1371/journal.pone.0084349

Wintzer, M. E., Boehringer, R., Polygalov, D., & McHugh, T. J. (2014). The hippocampal CA2 ensemble is sensitive to contextual change. *Journal of Neuroscience*, *34*(8), 3056–3066. doi:10.1523/JNEUROSCI.2563-13.2014

Witton, J., Brown, J. T., Jones, M. W., & Randall, A. D. (2010). Altered synaptic plasticity in the mossy fibre pathway of transgenic mice expressing mutant amyloid precursor protein. *Molecular Brain*, *3*, 32. doi:10.1186/1756-6606-3-32

Wu, L. G., & Saggau, P. (1994). Adenosine inhibits evoked synaptic transmission primarily by reducing presynaptic calcium influx in area CA1 of hippocampus. *Neuron*, *12*(5), 1139–1148.

Wu, Z., Guo, Z., Gearing, M., & Chen, G. (2014). Tonic inhibition in dentate gyrus impairs long-term potentiation and memory in an Alzhiemer's disease model. *Nature Communications*, *5*, 4159. doi:10.1038/ncomms5159

Wyeth, M. S., Pelkey, K. A., Petralia, R. S., Salter, M. W., McInnes, R. R., & McBain, C. J. (2014). Neto auxiliary protein interactions regulate kainate and NMDA receptor subunit localization at mossy fiber-CA3 pyramidal cell synapses. *Journal of Neuroscience*, *34*(2), 622–628. doi:10.1523/JNEUROSCI.3098-13.2014

Yassa, M. A., Stark, S. M., Bakker, A., Albert, M. S., Gallagher, M., & Stark, C. E. L. (2010). High-resolution structural and functional MRI of hippocampal CA3 and dentate gyrus in patients with amnestic Mild Cognitive Impairment. *NeuroImage*, *51*(3), 1242–1252. doi:10.1016/j.neuroimage.2010.03.040

Yokoi, M., Kobayashi, K., Manabe, T., Takahashi, T., Sakaguchi, I., Katsuura, G., et al. (1996). Impairment of hippocampal mossy fiber LTD in mice lacking mGluR2. *Science*, *273*(5275), 645–647.

Yoshiike, Y., Kimura, T., Yamashita, S., Furudate, H., Mizoroki, T., Murayama, M., & Takashima, A. (2008). GABA(A) receptor-mediated acceleration of aging-associated memory decline in APP/PS1 mice and its pharmacological treatment by picrotoxin. *PLoS ONE*, *3*(8), e3029. doi:10.1371/journal.pone.0003029

Zalutsky, R. A., & Nicoll, R. A. (1990). Comparison of two forms of long-term potentiation in single hippocampal neurons. *Science*, *248*(4963), 1619–1624.

Zezula, J., & Freissmuth, M. (2008). The A(2A)-adenosine receptor: a GPCR with unique features? *British Journal of Pharmacology*, *153 Suppl 1*, S184–90. doi:10.1038/sj.bjp.0707674

Zhang, F., Gradinaru, V., Adamantidis, A. R., Durand, R., Airan, R. D., de Lecea, L., & Deisseroth, K. (2010). Optogenetic interrogation of neural circuits: technology for probing mammalian brain structures. *Nature Protocols*, *5*(3), 439–456. doi:10.1038/nprot.2009.226

Chapter 6

ANNEXES
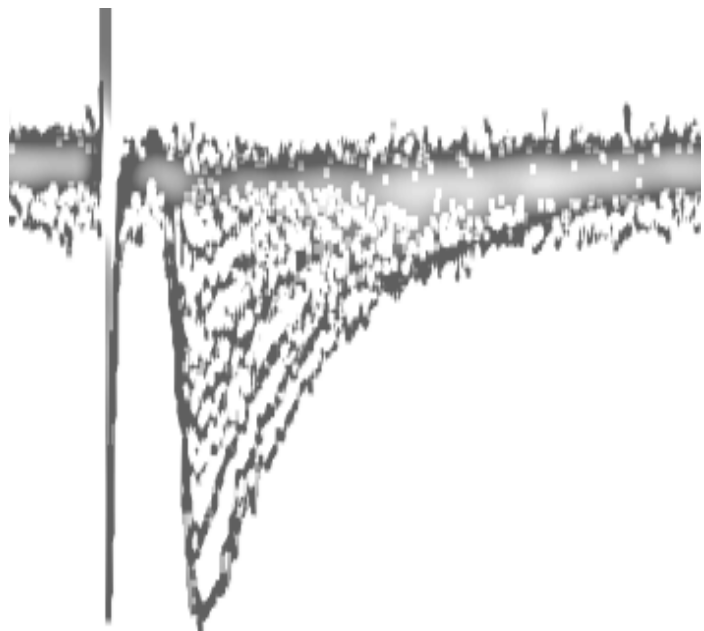
Membrane Lipids Tune Synaptic Transmission by Direct Modulation of Presynaptic Potassium Channels

Mario Carta,[1,4] Frederic Lanore,[1,4] Nelson Rebola,[1,4] Zsolt Szabo,[1] Silvia Viana Da Silva,[1] Joana Lourenço,[1] Agathe Verraes,[3] André Nadler,[2] Carsten Schultz,[2] Christophe Blanchet,[1] and Christophe Mulle[1,*]

[1]University of Bordeaux, Interdisciplinary Institute for Neuroscience, CNRS UMR 5297, 33000 Bordeaux, France
[2]EMBL Heidelberg, Meyerhofstraße 1, 69117 Heidelberg, Germany
[3]Institut Jacques Monod, UMR 7592, CNRS and INSERM ERL U950, University Paris Diderot, Sorbonne Paris Cité, 75013 Paris, France
[4]These authors contributed equally to this work
*Correspondence: christophe.mulle@u-bordeaux.fr
http://dx.doi.org/10.1016/j.neuron.2013.12.028

SUMMARY

Voltage-gated potassium (Kv) channels are involved in action potential (AP) repolarization in excitable cells. Exogenous application of membrane-derived lipids, such as arachidonic acid (AA), regulates the gating of Kv channels. Whether membrane-derived lipids released under physiological conditions have an impact on neuronal coding through this mechanism is unknown. We show that AA released in an activity-dependent manner from postsynaptic hippocampal CA3 pyramidal cells acts as retrograde messenger, inducing a robust facilitation of mossy fiber (Mf) synaptic transmission over several minutes. AA acts by broadening presynaptic APs through the direct modulation of Kv channels. This form of short-term plasticity can be triggered when postsynaptic cell fires with physiologically relevant patterns and sets the threshold for the induction of the presynaptic form of long-term potentiation (LTP) at hippocampal Mf synapses. Hence, direct modulation of presynaptic Kv channels by activity-dependent release of lipids serves as a physiological mechanism for tuning synaptic transmission.

INTRODUCTION

Synaptic transmission mainly flows anterogradely from the action-potential-dependent release of neurotransmitters to the activation of specific postsynaptic membrane receptors. Many neurons can also modulate the strength of their synaptic inputs through the release of retrograde messengers (Regehr et al., 2009). Retrograde messengers, including membrane-derived lipids, gases, peptides, growth factors, or conventional neurotransmitters, can be released from postsynaptic neurons in response to activity and diffuse to presynaptic terminals where they interact with specific targets in order to regulate neurotransmitter release (Regehr et al., 2009). In the CNS, most of the reported lipid-mediated retrograde modulation of synaptic transmission involves endocannabinoids and cannabinoid type 1 receptors (CB$_1$Rs) (Wilson and Nicoll, 2002), which are present in both GABAergic and glutamatergic neurons (Herkenham et al., 1990; Kawamura et al., 2006; Marsicano and Lutz, 2006). Postsynaptic calcium rise leads to the production of endogenous lipids (2-AG and anandamide), which diffuse into the presynaptic terminal and activate CB$_1$Rs, leading to the inhibition of neurotransmitter release (Kano et al., 2009; Marsicano and Lutz, 2006). Other membrane receptors activated by lipids, such as transient receptor potential cation channel subfamily V member 1 (TRPV1) and lysophosphatidic acid receptor 2 receptors, have also been reported to modulate synaptic transmission (Gibson et al., 2008; Trimbuch et al., 2009).

Apart from their action through specific membrane receptors, membrane-derived lipids are also known to modulate ion channel function by direct interaction with the ion channel (Boland and Drzewiecki, 2008). Lipids are known to modulate voltage-dependent calcium channels (Roberts-Crowley et al., 2009), potassium channels (Oliver et al., 2004), glycine receptors (Lozovaya et al., 2005), and GABA$_A$ receptors (Sigel et al., 2011). Membrane-derived lipids may also represent the primary activating ligands of TRP channels (Hardie, 2007; Kukkonen, 2011) or two-pore domain potassium channels (Besana et al., 2005). However, contrasting with the large number of reports on direct modulation of ion channels by membrane-derived lipids, the physiological conditions under which this mechanism is recruited remains elusive.

To address this question, we focused on hippocampal mossy fiber (Mf) CA3 synapses. The efficacy of Mf-CA3 synaptic transmission is tightly controlled by presynaptic Kv channels, and Mf-CA3 presynaptic terminals are amenable to patch-clamp recordings (Geiger and Jonas, 2000). We have identified a retrograde signaling mechanism which results in robust short-term potentiation of synaptic transmission in physiological conditions of activity of hippocampal circuits. This potentiation is mediated by the activation of phospholipase A2 and the release of arachidonic acid (AA) and is not dependent on any known membrane lipid receptor. Using patch-clamp recordings from
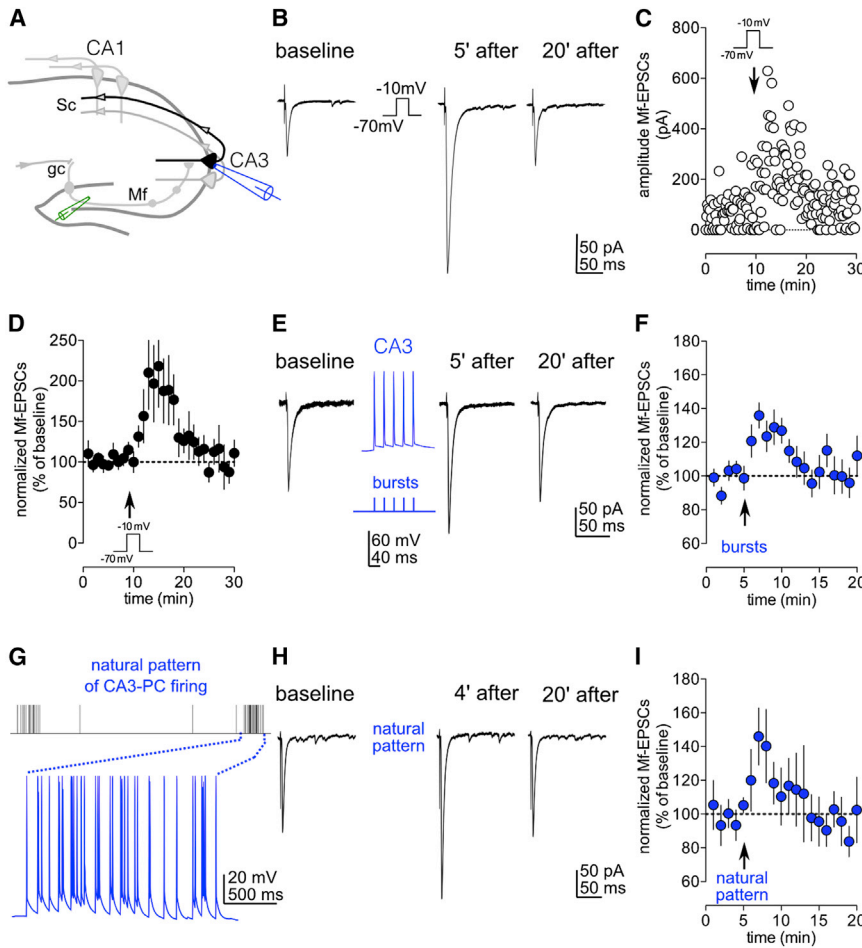
Figure 1. Postsynaptic Depolarization or Postsynaptic Action Potential Firing Induces Potentiation at Mf-CA3 Synaptic Transmission

(A) Illustration of a hippocampal slice with recording (blue, in a CA3 pyramidal cell) and stimulating electrodes (green, inside the dentate gyrus).

(B) Sample traces (average of 30 sweeps) of Mf-EPSCs before and 5′ or 20′ after the depolarization step (from −70 to −10 mV).

(C) Time course of amplitudes of individual Mf-EPSCs recorded in the same cell as in (B).

(D) Summary time course of normalized Mf-EPSCs for experiments illustrated in (B) and (C) (n = 12).

(E) DPE of Mf-EPSCs can be induced by a burst of APs at theta frequency (bursts of five APs delivered at 25 Hz, repeated six times every 140 ms).

(F) Summary time course of normalized Mf-EPSCs for experiments illustrated in (E) (n = 11).

(G) A natural pattern of APs recorded in vivo from a CA3 pyramidal place cell was converted to current steps that were used to evoke APs in the postsynaptic CA3 pyramidal. The APs recorded in a CA3 pyramidal cell in the current clamp mode are shown in blue.

(H) Sample traces of Mf-EPSCs illustrating that DPE can be induced by a natural pattern of APs firing of CA3 pyramidal cells.

(I) Summary time course of normalized Mf-EPSCs for experiments illustrated in (G) (n = 9).

presynaptic boutons and focal AA uncaging, we observed that AA action mainly results in a direct inactivation of presynaptic Kv channels. This leads to the broadening of the presynaptic action potential (AP) and subsequent increase in transmitter release. Our results indicate that modulation of Kv channels by activity-dependent released lipids constitutes a powerful mechanism for tuning synaptic transmission, thus demonstrating the physiological significance of neuronal signaling mechanisms involving direct modulation of voltage-gated ion channels by lipids.

RESULTS

Retrograde Signaling at Mossy Fiber-CA3 Pyramidal Cell Synapses

Depolarization of neuronal membranes results in the calcium-dependent production of membrane-derived lipids, such as endocannabinoids mediating depolarization-induced suppression of inhibition (DSI) (Regehr et al., 2009; Wilson and Nicoll, 2002). We tested whether a similar protocol induced changes in synaptic transmission at Mf-CA3 synapses, which lack presynaptic CB_1Rs (Hofmann et al., 2008; Katona et al., 2006). The application of a depolarization step from −70 to −10 mV for 9 s in CA3 pyramidal cells induced a robust potentiation of

Mf-EPSCs (175% ± 13%, n = 12, p = 0.0005) (Figures 1A–1D), which peaked within 2–3 min and lasted up to 10–15 min. By analogy with DSI, we named this form of plasticity depolarization-induced potentiation of excitation (DPE). DPE varied in its magnitude with the duration of the depolarizing step (Figures S1A and S1B available online). The protocol could be repeated in the same cell (Figure S1C), and DPE magnitude was similar for two Mfs inputs independently stimulated and recorded in the same CA3 pyramidal cell (Figures S1D–S1F). However, DPE was not observed at associational/commissural (A/C) fiber synapses onto CA3 pyramidal cells (Figures S1G and S1H). Because a 9 s depolarizing step may not pertain to a physiological stimulus, we tested whether AP discharge in CA3 pyramidal cells also induced short-term potentiation of Mf-EPSCs. First, we applied a sequence of six bursts of five APs at 25 Hz in CA3 pyramidal cells at the frequency of theta oscillations (Buzsáki, 2005). This mild protocol induced transient potentiation of Mf-EPSCs (129% ± 9%, n = 11, p = 0.0137) (Figures 1E and 1F) to comparable levels as with a 9 s depolarization step with the same K^+-based intracellular solution (145% ± 16%, n = 11, p = 0.39). A similar potentiation could also be observed with bursts of spikes triggered by burst stimulation of Mf-CA3 synapses (eight stimulations at 25 Hz repeated six times at theta frequency; 136% ± 9%, n = 13) (Figures S1J–S1L). The facilitation induced by postsynaptic spikes in this protocol could be separated from the potent and short-lasting posttetanic potentiation
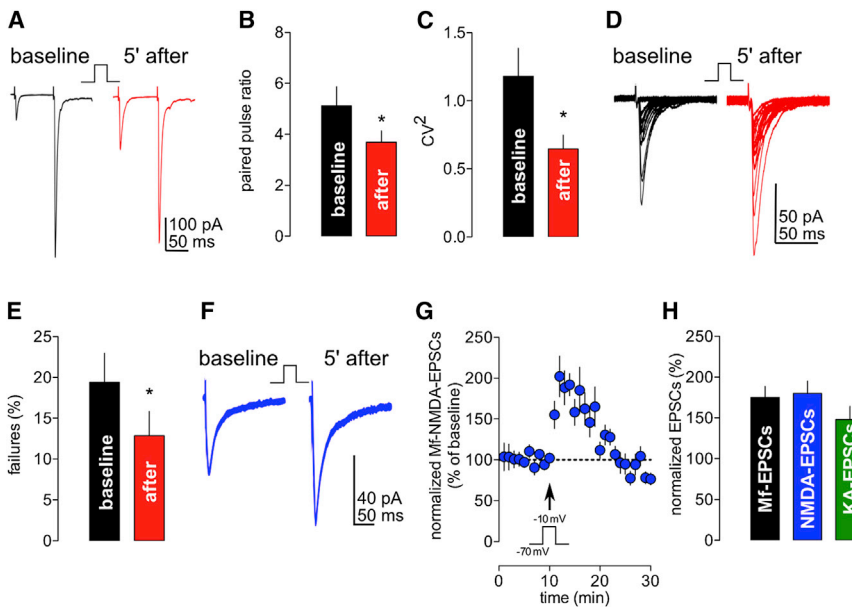
Figure 2. DPE Is Expressed Presynaptically

(A) Sample traces of paired pulse responses (100 ms interval) before and after DPE.

(B) Bar graph summarizing the values of PPR before and after DPE (n = 6, *p = 0.03, Wilcoxon match pairs test).

(C) Bar graph summarizing the change in CV^2 before and after DPE (n = 20, *p = 0.0018, Wilcoxon match pairs test). Values are presented as mean ± SEM of n experiments.

(D) Sample traces illustrating the marked reduction of synaptic failures (stimulation without detectable EPSCs) after DPE.

(E) Bar graph summarizing the significant reduction of synaptic failures after DPE (n = 14, *p = 0.021, Wilcoxon match pairs test).

(F) Sample traces of Mf-NMDA-EPSCs (recorded at −70 mV and in 0.3 mM Mg^{2+}) recorded before and after DPE induction.

(G) Summary time course for experiments illustrated in (C) (n = 8).

(H) DPE is similarly observed when recording Mf-EPSCs (essentially AMPA-EPSCs; n = 12) or isolated NMDA or Kainate-EPSCs (n = 8 and n = 6, respectively).

(Nicoll and Schmitz, 2005) with the use of 20 mM 1,2-bis(o-aminophenoxy)ethane-N,N,N',N'-tetraacetic acid (BAPTA) (94% ± 5%, n = 10, p = 0.0043, ctr versus BAPTA) in the patch pipette (see below and Figures S1J–S1L). Finally, we have used a natural pattern of spike discharge to induce DPE. A single sequence of APs (63 spikes over 18 s) recorded from a CA3 place cell in a freely moving rat entering in a place field (Isaac et al., 2009) was replayed into postsynaptic CA3 pyramidal cells with postsynaptic currents injection, and its effect was continuously recorded while evoking Mf-EPSCs at a frequency of 0.1 Hz (Figures 1G and 1H). This natural sequence of spiking activity enhanced the amplitude of Mf-EPSCs for several minutes (131% ± 10%, n = 9, p = 0.0391). These results indicate that physiologically relevant patterns of CA3 pyramidal cells firing can trigger DPE.

Next, we evaluated whether DPE was expressed pre- or postsynaptically. DPE was accompanied with a significant decrease in paired-pulsed facilitation (baseline, 5.1 ± 0.7; DPE, 3.7 ± 0.4; n = 6, p = 0.03), coefficient of variation (CV^2; baseline: 1.2 ± 0.2; DPE: 0.6 ± 0.1, n = 20, p = 0.0018), and failure rate (baseline: 19.4% ± 3.6%; DPE 12.9% ± 3.0%, n = 14, p = 0.021) (Figures 2A–2E), strongly suggesting a presynaptic mechanism. In addition, as expected for a presynaptic increase in glutamate release, isolated NMDA-EPSCs and Kainate-EPSCs were potentiated to similar extents after DPE (NMDA-EPSCs: 180% ± 15%, n = 8; Kainate-EPSCs: 148% ± 16%, n = 6, p = 0.52) (Figures 2F–2H). Finally, no potentiation was observed when replacing Mf simulation with focal UV uncaging of glutamate at the location of Mf-CA3 synapses on proximal dendrites (Figures S2A–S2D). Hence, DPE is induced postsynaptically and expressed presynaptically.

Next, we tested whether DPE, like DSI, was dependent on an increase in postsynaptic Ca^{2+}. Replacing 0.2 mM EGTA with 20 mM BAPTA in the patch pipette solution (EGTA: 179% ± 14%, n = 13; BAPTA: 89% ± 9%, n = 10, p = 0.0012) or blocking

L-type Ca^{2+} channels with nifedipine (10 μM; 87% ± 10%, n = 9, p = 0.0013) abolished DPE (Figures 3A–3C). Furthermore, we investigated the nature of the retrograde messenger involved in DPE. Conventional neurotransmitters that could potentially be released from the somato-dendritic compartment of CA3 pyramidal cells, including glutamate, GABA, or adenosine (Ludwig and Pittman, 2003), did not appear to be involved in DPE (Table S1). In keeping with this observation, the infusion of botulinum toxin C1 (BotoxC1; 0.5 μM) in the intracellular patch solution to block Ca^{2+}-dependent vesicular release from the somato-dendritic compartment of CA3 pyramidal cells did not affect DPE (solvent: 165% ± 23%, n = 5; BotoxC1: 191% ± 20%, n = 8, p = 0.621) (Figures 3D and 3E). In contrast, BotoxC1 was effective in reducing the amplitude of AMPA-EPSCs both at Schaffer collateral (Sc)-CA1 and Mf-CA3 synapses (Figures S3A–S3D; Table S1), most likely by blocking exocytosis (Lüscher et al., 1999). This suggests that DPE relies on a retrograde messenger that is released in a nonvesicular manner, such as gases (i.e., nitric oxide [NO]) or membrane-derived lipids (Regehr et al., 2009). Interestingly, although gases and membrane-derived lipids were shown to be capable of spreading their signal to neighboring neurons (Regehr et al., 2009), we found that DPE was restricted to the Mf afferences of the depolarized cell (DPE: 163% ± 20%; no DPE: 85 ± 4; n = 11) (Figures 3F–3H).

DPE Depends on Membrane-Derived Lipids

Blocking NO synthesis with L-NG-monomethyl arginine citrate or blocking NO-sensitive guanylyl cyclases with 1H-[1,2,4]oxadiazolo[4,3-a]quinoxalin-1-one did not affect DPE (n = 12, p = 0.653) (Figures S3E and S3F; Table S1). To test for an implication of membrane-derived lipids in DPE, we focused our attention on enzymes involved in the Ca^{2+}-dependent synthesis or in the degradation of the most common lipid messengers known, such as the endocannabinoids 2-AG (2-arachidonoylglycerol)
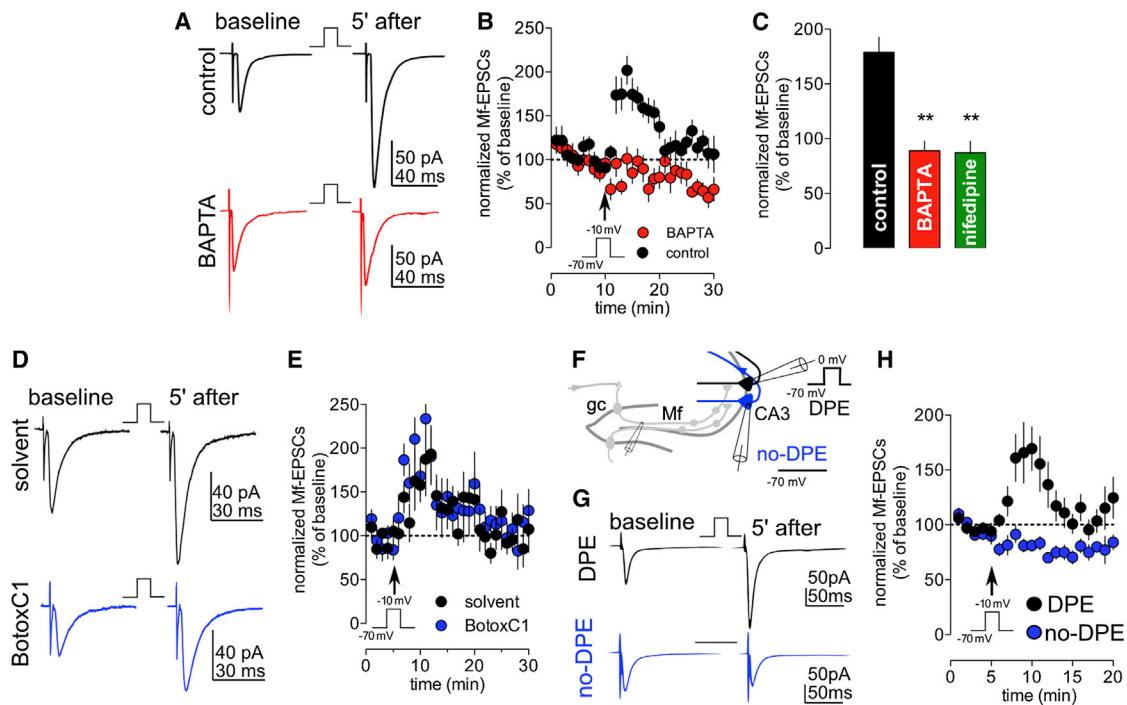
Figure 3. DPE Depends on Postsynaptic Calcium Rise and on a Nonvesicular Release Mechanism

(A–C) Sample traces, summary time course and bar illustrating that DPE is blocked by intracellular perfusion with BAPTA (10–20 mM) or bath application of the VGCC blocker nifedipine (10 μM; BAPTA, n = 10, **p = 0.0012; nifedipine, n = 9, **p = 0.0013, Kruskal-Wallis test).

(D and E) sample traces and summary time course showing that DPE is not blocked by inclusion of BotoxC1 (0.5 μM) in the patch pipette (solvent n = 5; BotoxC1 n = 8).

(F–H) DPE does not spread to neighboring neurons. CA3 pyramidal cells in organotypic slice cultures are highly packed, making this preparation ideal for investigating whether DPE can spread between two neighboring CA3 pyramidal cells.

(F) Two neighboring CA3 pyramidal cells were simultaneously patched, and only one received the depolarizing step.

(G and H) Sample traces and time course illustrating that DPE is confined to the depolarized neuron (n = 11). Values are presented as mean ± SEM of n experiments.

and anandamide (Chevaleyre et al., 2006). DPE was not affected when perturbing the synthesis of 2-AG with the inhibitor of the diacylglycerol lipase, tetrahydrolipstatine (5 μM, n = 9, p = 0.841) (Figures 4A, S4A, and S4F; Table S1) nor when perturbing the degradation of anandamide with the inhibitor of fatty acid amide hydrolase, 3′-(aminocarbonyl)[1,1′-biphenyl]-3-yl)-cyclohexylcarbamate (1 μM, n = 15, p = 0.146) (Figures 4A, S4B, and S4F; Table S1). Furthermore, blocking degradation of 2-AG with a selective inhibitor of monoacylglycerol lipase, JZL 184 (10 μM), did not affect DPE (n = 16, p = 0.417) (Figures 4A, S4C, and S4F; Table S1). These experiments argue against a role for 2-AG or anandamide as retrograde messengers for DPE. In contrast, we found that cytoplasmic phospholipase A2 (cPLA2), a key enzyme responsible for the Ca^{2+}-dependent release of AA from phospholipids (Lambeau and Gelb, 2008) is critically involved in DPE. Indeed, inhibition of cPLA2 with arachidonyl trifluoromethyl ketone (AACOCF3; 10 to 20 μM) fully prevented DPE (ctr: 197% ± 17%, n = 13; AACOCF3: 110% ± 7%, n = 20, p = 0.0001) (Figures 4A–4C). PLA2 inhibition also prevented the enhancement of Mf-EPSCs induced by AP discharge evoked in CA3 pyramidal cells either with the natural firing protocol (ctr: 131% ± 10%, n = 9; AACOCF3: 90% ± 6%, n = 7, p = 0.0079) or through burst stimulation of Mf-CA3 synap-

ses (ctr: 136% ± 9%, n = 13; AACOCF3: 105% ± 8%, n = 12, p = 0.028) (Figure S1L). AA can be further metabolized by cyclooxygenases (COX), for example to prostaglandins, or by lipoxygenases (LOX), to produce downstream products such as hydroxyperoxyeicosatetraenoic acids (HPETEs) or hydroxyeicosatetraenoic acids (HETEs) (Figure 4A). The COX2 inhibitor N-(2-cyclohexyloxy-4-nitrophenyl) methanesulfonamide had no effect on DPE ruling out the participation of its downstream products (data not shown). In contrast, blocking LOX with PD 146176 (10 μM, 12- and 15-LOX inhibitor), baicalein (10 μM, 5- and 12-LOX inhibitor), or nordihydroguaiaretic acid (NDGA; 50 μM), a general LOX inhibitor, significantly reduced DPE (ctr: 191% ± 10%, n = 23; PD 146176: 137% ± 15%, n = 17, p = 0.0014; baicalein: 152% ± 9%, n = 13, p = 0.0297; NDGA: 114% ± 13%, n = 7, p = 0.0059) (Figures 4A, 4D, and S4D–S4F), suggesting the participation of downstream product of AA catabolism by LOX.

To test whether AA can itself increase synaptic transmission, we synthesized caged AA (see the Experimental Procedures). Focal photoactivation of 7-(diethylamino)-coumarin-4-yl-methyl arachidonate (caged AA, 10 μM; a concentration which is well within a physiologically relevant range) (Meves, 2008) onto CA3 pyramidal cell proximal dendrites induced transient potentiation
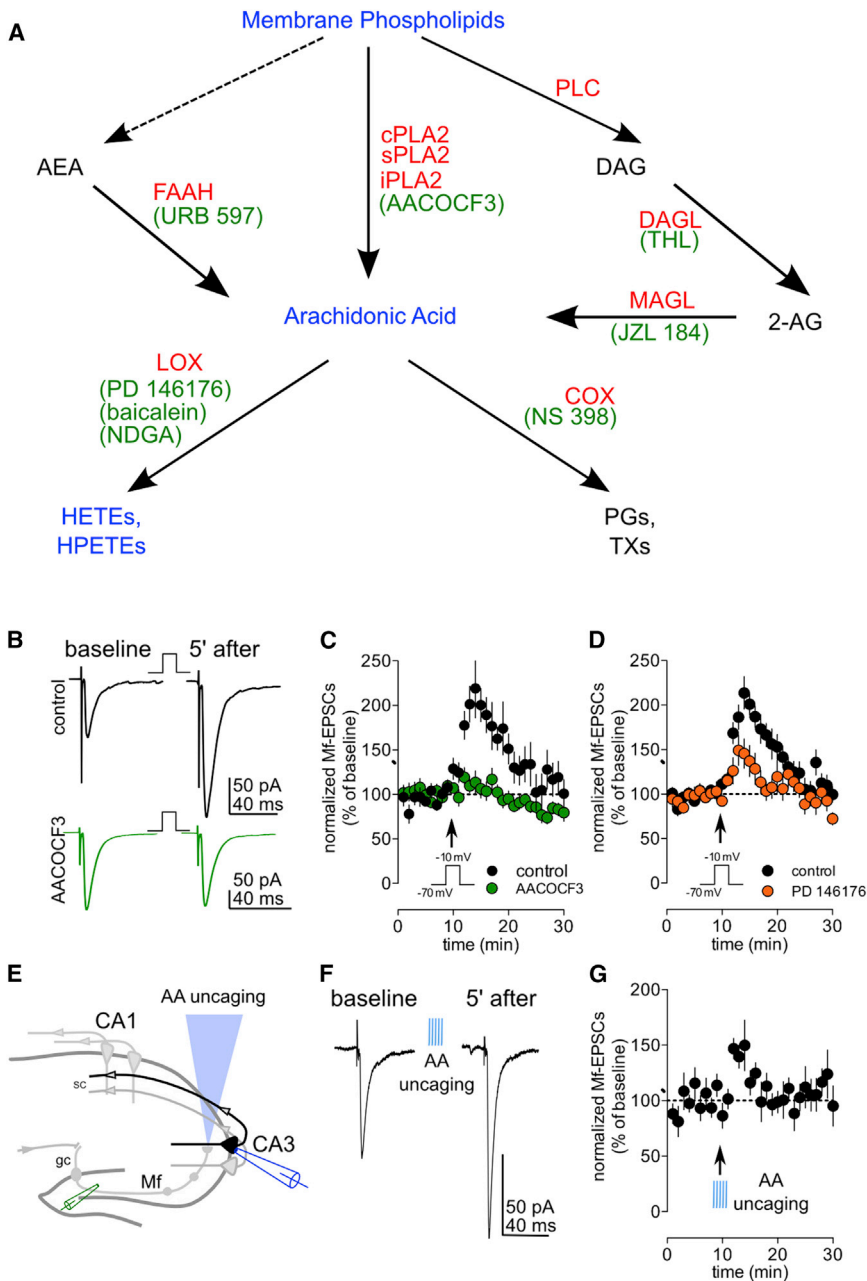
A

Membrane Phospholipids

PLC

cPLA2
sPLA2
iPLA2
(AACOCF3)

AEA   DAG

FAAH
(URB 597)

DAGL
(THL)

Arachidonic Acid

MAGL
(JZL 184)   2-AG

LOX
(PD 146176)
(baicalein)
(NDGA)

COX
(NS 398)

HETEs,
HPETEs   PGs,
TXs

Figure 4. DPE Is Mediated by a Metabolite of cPLA2 and Can Be Mimicked by Exogenous Arachidonic Acid

(A) Signaling cascade for the metabolism of membrane phospholipids with the respective enzymes (red) and corresponding blockers used (green). AEA, anandamide; COX, cyclooxygenase; CYP, cytochrome P450; DAG, DAG lipase; DAGL, DAG lipase; FAAH, fatty acid amide hydrolase; HETE, hydroxyeicosatetraenoic acid; HPETE, hydroperoxyeicosatetraenoic acid; LOX, lipoxygenase; MAGL, MAG lipase; NDGA, nordihydroguaiaretic acid; PG, prostaglandin; cPLA2, cytoplasmic phospholipase A2; PLC, phospholipase C.

(B) Sample traces illustrating the abrogation of DPE by incubating the slice (>30 min) with the PLA2 inhibitor AACOCF3 (10–20 μM).

(C) Summary time course for experiments illustrated in (B) (ctr, n = 13; AACOCF3, n = 20).

(D) DPE was reduced by slice incubation with the LOX inhibitor PD-146176 (10 μM; ctr, n = 23; PD-146176, n = 17).

(E) Caged AA (10 μM) was perfused in the slice for 10–15 min before flashing a UV light in the *stratum lucidum* near the recorded CA3 pyramidal cell.

(F) Sample traces illustrating the transient potentiation of Mf-EPSCs induced by AA uncaging.

(G) Summary graph for experiments illustrated in (F) (n = 7). Values are presented as mean ± SEM of n experiments.

(capsazepine) (Gibson et al., 2008) or GPR55 (cannabidiol) (Ryberg et al., 2007) did not affect DPE (Figures S4I–S4K; Table S1). Protein kinase C (PKC) is another possible target of AA. It has been reported that AA and some of its derivatives can indirectly facilitate PKC activation (Schaechter and Benowitz, 1993). Similar to protein kinase A (PKA), PKC activation facilitates synaptic transmission at Mf-CA3 synapses. However, PKC or PKA activity was not required for DPE (Figures S4L–S4U; Table S1).

AA and some of its derivatives are also known to directly modulate voltage-gated ion channels (Fink et al., 1998). Interestingly, AA induces C-type inactivation of voltage-gated potassium channels (Kv) (Oliver et al., 2004). Cumulative inactivation or pharmacological blockade of presynaptic Kv channels induce a broadening of the AP waveform at Mf bouton (MfB) that results in increased glutamate release (Geiger and Jonas, 2000). To test whether presynaptic Kv channels could be the targets of AA released during DPE, we examined whether blocking Kv channels with low concentrations of 4-aminopyridine (4-AP; 5 or 10 μM) occluded DPE. At these concentrations, 4-AP considerably increased basal synaptic transmission at Mf-CA3 synapses (n = 7 and n = 6 for 4-AP 5 and 10 μM, respectively) (Figures 5A and 5B). Preincubation of the slices with 4-AP significantly

of Mf-EPSCs (145% ± 9%, n = 7, p = 0.0156), confirming that AA can indeed increase transmitter release at Mf-CA3 synapses (Figures 4E–4G).

DPE Occurs via 4-AP-Sensitive Potassium Channels

Next, we sought to identify a putative presynaptic target for AA (or a LOX product of AA). DPE was not affected by pharmacological inhibition of CB_1 or CB_2 receptors by SR141716A and AM 630, respectively (Figures S4G, S4H, and S4K; Table S1), consistent with the finding that DPE does not rely on the production of endocannabinoids. In addition, antagonists against known CNS lipid receptors such as TRPV1
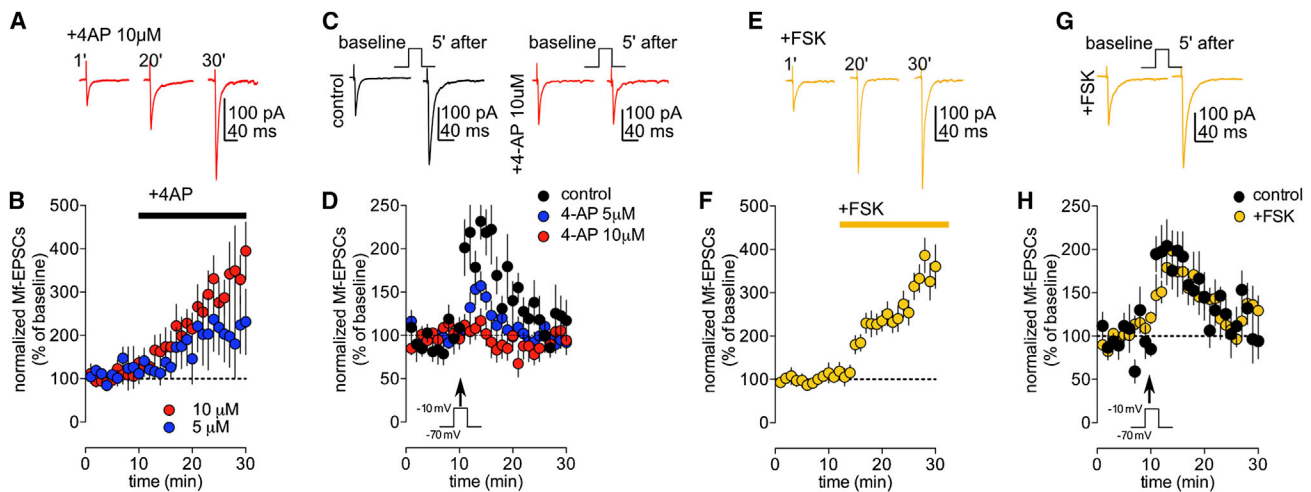
Figure 5. DPE Occurs via 4-AP-Sensitive Potassium Channels

(A and B) Sample traces and time course illustrating the potentiating effect of 5 and 10 μM 4-AP on Mf-EPSCs (average at 25–30 min; 5 μM 4-AP, 207% ± 70%, n = 7; 10 μM 4-AP, 333% ± 34%, n = 6).

(C) Sample traces illustrating occlusion of DPE by preincubation of slices with 4-AP (10 μM).

(D) Summary of the experiments showing occlusion of DPE by 4-AP (ctr, n = 11; 4-AP 5 μM, n = 13; 4-AP 10 μM, n = 9).

(E and F) Potentiation of Mf-EPSCs by forskolin (10 μM; 344% ± 28%, n = 12).

(G and H) Sample traces and summary graph showing that DPE amplitude is not affected when Mf-EPSCs are previously potentiated by forskolin (10–20 μM; ctr, n = 6; forskolin, n = 12). DPE was induced 20–30 min after forskolin application when potentiation of Mf-CA3 synaptic transmission had reached a plateau. Values are presented as mean ± SEM of n experiments.

reduced DPE (ctr: 211% ± 15%, n = 11; 5 μM 4-AP: 145% ± 12%, n = 13, p = 0.0023; 10 μM 4-AP: 114% ± 7%, n = 9, p = 0.0005) (Figures 5C and 5D). The reduction in DPE magnitude did not simply result from a ceiling effect, given that forskolin (10 μM), a known potentiator of Mf-CA3 synapses via the activation of the PKA pathway, increased basal synaptic transmission (n = 12) (Figure 5E and 5F) but did not occlude DPE (ctr: 193% ± 18%, n = 6; forskolin: 193% ± 21%, n = 12, p = 0.4790) (Figures 5G and 5H). Similarly, DPE was not occluded by previously induced presynaptic LTP (Figure S5).

AA Induces the Broadening of Mf-Presynaptic Action Potentials

Thus, we reasoned that AA released from CA3 pyramidal cells during DPE may result in the broadening of MfB APs by the inactivation of 4-AP-sensitive presynaptic Kv channels. To test this hypothesis, we performed patch-clamp recordings from MfBs in organotypic cultures from Thy1-GFP mice (DPE was similarly observed in this preparation) (Figures 3F–3H), which significantly improved identification of MfBs (Figure 6A, S6A, and S6B) (Galimberti et al., 2006). APs triggered by current injection and recorded from MfBs in the current clamp mode displayed previously described property; i.e., marked frequency dependent broadening due to Kv channel inactivation (Figure 6B) (Geiger and Jonas, 2000). Moreover, in agreement with a previous study (Alle et al., 2011), low concentrations of 4-AP (10 μM), which considerably increased glutamate release at Mf synapses, also broadened APs (normalized AP half-width, 4-AP: 182% ± 15%, n = 5, p = 0.0313) (Figures 6C and 6D). We found that focal AA uncaging induced a rapid broadening of the presynaptic AP (normalized AP half-width values, at min 2–3: AA, 122% ± 6%,

n = 6; absolute AP half-width values: AA, baseline 0.55 ± 0.09 ms; after UV, at min 2–3: = 0.69 ± 0.09 ms; n = 6. p = 0.0313) (Figures 6E and 6F), which lasted several minutes. As a control, a similar UV flash given in the absence of the caged compound did not change AP half-width (normalized AP half-width values, at min 2–3: ctr, 99% ± 4%, n = 6; absolute AP half-width values: ctr, baseline = 0.54 ± 0.03 ms; after UV, at min 2–3: = 0.53 ± 0.03 ms, n = 6). Similar results were obtained in acute slices from P28-35 Thy1-GFP mice (Figures S6C and S6D). Thus, our functional and pharmacological data strongly suggest that AA may induce a broadening of APs via the inactivation of Kv channels in the MfB, which then results in an increased release of glutamate.

AA Inhibits Presynaptic Kv Currents

To further confirm that AA indeed modulates presynaptic Kv channels, we tested the effect of AA uncaging on isolated presynaptic Kv currents from MfBs. It has previously been shown that AA significantly reduces Kv currents in oriens-alveus interneurons (OA-I) in the CA1 region (Oliver et al., 2004). First, to validate our assay, we tested AA uncaging on Kv currents recorded from OA-I interneurons in the CA1 area in the cell-attached configuration (Figures S6E–S6G). We found that pharmacologically isolated Kv currents recorded from the soma of OA-I interneurons were potently inhibited by AA uncaging (normalized amplitude, p = 0.0469; normalized area, p = 0.0156) (Figures S6F and S6G). Next, we tested the effect of AA uncaging on pharmacologically isolated Kv currents recorded from MfBs in the cell-attached configuration (Figure 6G). Kv currents recorded from MfBs were inhibited by AA uncaging (normalized amplitude, ctr: 94% ± 4%, n = 7; AA uncaging: 56% ± 9%, n = 7, p = 0.0156; normalized area, ctr: 97% ± 7%, n = 7; AA uncaging: 42% ± 8%,
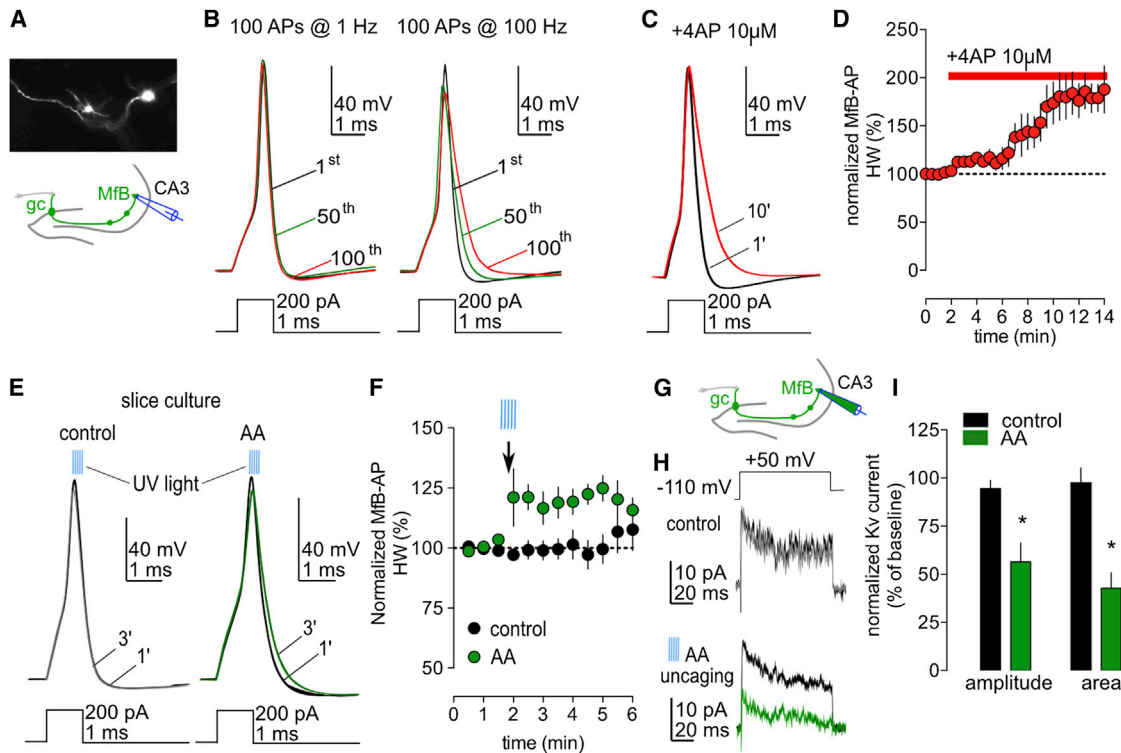
Figure 6. AA Induces Mf-Presynaptic Action Potential Broadening by Inactivation of Presynaptic Kv Channels

(A) Hippocampal organotypic slices were prepared from Thy1-GFP mice to facilitate the visualization of MfBs.

(B) APs evoked by a 1 or 100 Hz train of brief current pulses (200 pA, 1 ms). Black, 1st AP; green, 50th AP; red, 100th AP. Traces were aligned to the onset of the current pulse. Note that AP broadening during repetitive stimulation (1st versus 100th), which is characteristic of MfBs and is mediated by activity-dependent inactivation of presynaptic Kv channels.

(C and D) Sample traces (average of 15–20 sweeps) illustrating that the AP half-width (HW) increases with 4-AP (10 μM; n = 5).

(E) Sample traces (average of three to five sweeps) illustrating that the AP HW increases after AA uncaging. No significant changes were observed in control experiments (UV light applied in the absence of caged AA).

(F) Time course for AA uncaging experiments illustrated in (F) (ctr, n = 6; AA, n = 6). Values are presented as mean ± SEM of n experiments.

(G and H) Sample traces (average of five to six sweeps) illustrating the inhibitory effect of AA uncaging on the amplitude and area of the Kv currents recorded from MfB in the cell-attached configuration. Caged AA (10 μM) was dissolved in the patch pipette solution. A 500 ms prepulse to −110 mV was applied. No change in the currents over time was observed in control experiments (no UV light applied).

(I) Summary graph of the effect of AA uncaging as illustrated in (F) (ctr, n = 7; AA, n = 7; *p = 0.0156, Wilcoxon match pairs test).

n = 7, p = 0.0156) (Figures 6E and 6F). In an attempt to further characterize the mechanism by which AA inhibited Kv currents at MfBs, we have performed outside-out patch-clamp recordings from MfBs in acute slices. We found that AA shifted the voltage dependence of steady-state inactivation of pharmacological isolated Kv currents toward more negative values (Figures S6H and S6I) but did not affect the voltage dependence of activation of Kv currents from the same patches. These results show that Kv channels present at MfBs are highly sensitive to AA. Hence, our data strongly suggest that DPE results from a Ca2+-dependent postsynaptic release of AA (or one of its derivatives) acting on presynaptic Kv channels in order to induce a broadening of APs, which, in turn, results in an increase of glutamate release (Figure 9). We thus report a form of short-term synaptic plasticity in the CNS resulting from the direct modulation of voltage-gated channels by endogenously released lipids.

Next, we aimed to directly investigate whether endogenous AA released from postsynaptic CA3 pyramidal cells could modulate the duration of presynaptic APs in MfBs. We have previously shown that burst stimulation of Mf-CA3 synapses induced the firing of CA3 pyramidal cells, which is sufficient to induce DPE (Figures S1J–S1L). Thus, we have monitored presynaptic AP waveform with patch-clamp recordings while inducing DPE with this protocol. We have triggered bursts of APs by direct current injection in the MfB to induce glutamate release and drive the connected postsynaptic CA3 pyramidal cell to spike and, ultimately, induce DPE (Figure 7). Bursts of action APs in the MfB lead to prolonged broadening of presynaptic APs, consistent with an inactivation of presynaptic Kv channels. This broadening displayed a slow onset similar to the time course of DPE (normalized AP half-width values at min 5–6 [3–4 min after the theta burst]: ctr, 127% ± 8%, n = 11; absolute AP half-width values: ctr, baseline = 0.53 ± 0.03 ms; after theta burst, at min 5–6 = 0.65 ± 0.03 ms, n = 11. p = 0.0049) (Figures 7B–7D). We performed two control experiments in order to verify that presynaptic AP broadening is mediated by postsynaptic AA release in
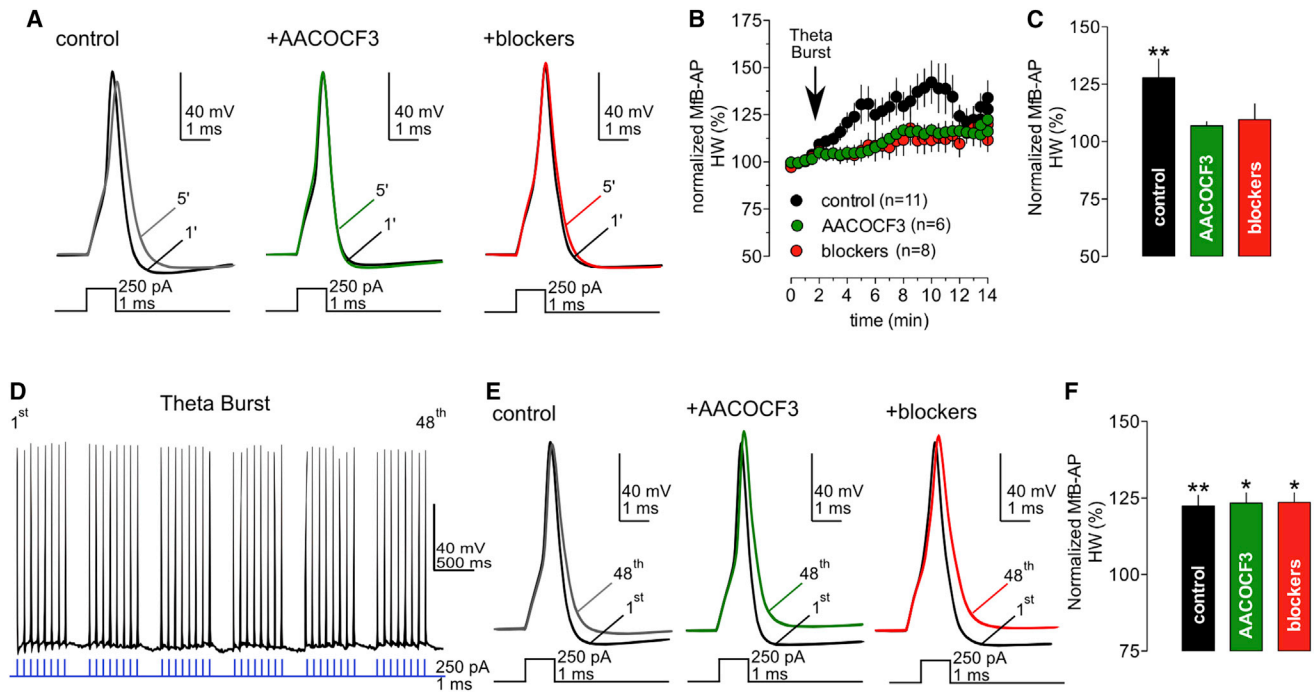
Figure 7. Theta Burst Firing in MfBs Induces AP Broadening, which Depends on PLA2 Activity and Activation of Glutamate Receptors in CA3 Pyramidal Cell

(A) Sample traces (average of three sweeps), illustrating that, in the control condition, the AP half-width is increased 3 min after the burst of APs (delivered at 2 min) in the MfB. No change in the AP duration was observed in the presence of the PLA2 inhibitor (AACOCF3, 20 μM) or a cocktail of glutamate receptor blockers (NBQX, AP5, mGluR1, and mGluR5).

(B) Time course for MfB burst experiments illustrated in (B) (ctr, n = 11; AACOCF3, n = 6; blockers, n = 8). Values are presented as mean ± SEM of n experiments.

(C) Bar graph summarizing the changes in AP half-width at 5–6 min, 3 min after the theta burst in the MfB.

(D) Sample trace illustrating the brief burst of APs triggered by burst injection of currents (eight APs at 25 Hz, repeated six times at theta frequency, 140 ms interval).

(E) Sample traces illustrating that the broadening of the AP (comparing the 1st versus the 48th AP of the burst) does not differ among different experimental conditions.
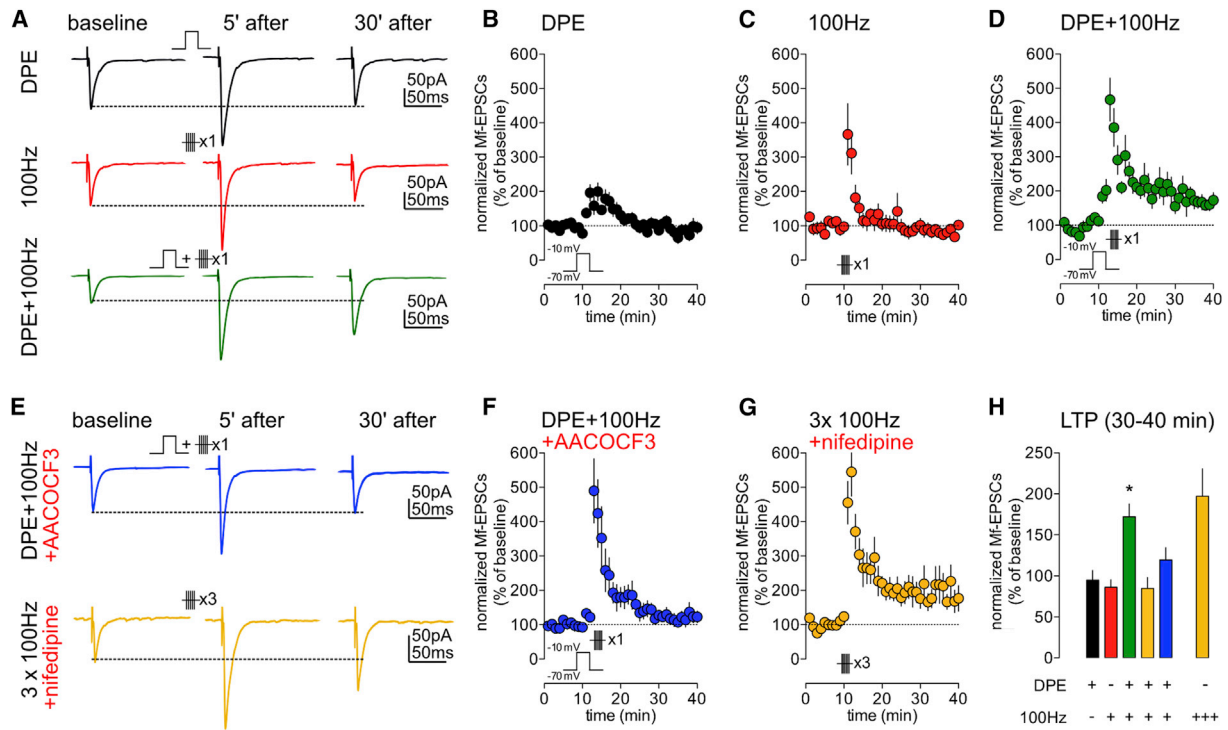
(F) Bar graph summarizing the changes AP HW (1st versus the 48th) during the burst in the MfB (ctr, n = 11; AACOCF3, n = 6; blockers, n = 8). Values are presented as mean ± SEM of n experiments ($^*p = 0.0156$, $^{**}p = 0.002 - 0.0049$, Wilcoxon match pairs test).

these conditions. First, we showed that AP broadening was inhibited by the PLA2 inhibitor AAFCOF3 (normalized AP half-width values at min 5–6 [3–4 min after the theta burst]: AACOCF3, 107% ± 2%, n = 6; absolute AP half-width values: AACOCF3, baseline = 0.47 ± 0.04 ms; after theta burst, at min 5 to 6 = 0.49 ± 0.04 ms, n = 6) (Figures 7B–7D). Second, we showed that the broadening of presynaptic APs requires synaptic activation of glutamate receptors which drive postsynaptic firing. In the presence of a cocktail of ionotropic and metabotropic glutamate receptor antagonists, no broadening of presynaptic APs was observed after burst stimulation (normalized AP half-width values at min 5 to 6 [3 to 4 min after the theta burst]: blockers, 109% ± 7%, n = 8; absolute AP half-width values: blockers, baseline = 0.60 ± 0.03 ms; after theta burst, at min 5 to 6 = 0.61 ± 0.03 ms, n = 8) (Figures 7B–7D). In the absence of burst stimulation, the duration of presynaptic APs over time did not differ between control conditions and during pharmacological treatments (data not shown). These results provide clear evidence that burst stimulation of presynaptic Mf terminals results in prolonged presynaptic AP broadening mediated by lipid

messengers produced via increase in postsynaptic PLA2 activity. Importantly, the pharmacological treatments did not affect the capability of MfBs to undergo short-term use-dependent broadening during a theta burst stimulation per se (normalized AP half-width values 48th versus 1st: ctr, 122% ± 3%, n = 8; AACOCF3, 123% ± 3%, n = 6; blockers, 123% ± 3%, n = 8; absolute AP half-width values: ctr, 1st = 0.59 ± 0.03 ms; 48th = 0.72 ± 0.04 ms, n = 11, p = 0.002; AACOCF3, 1st = 0.46 ± 0.04 ms; 48th = 0.56 ± 0.05 ms, n = 6, p = 0.0156; blockers, 1st = 0.64 ± 0.03 ms; 48th = 0.79 ± 0.05 ms, n = 8, p = 0.0156) (Figures 7E–7G) (Geiger and Jonas, 2000).

DPE Facilitates LTP Induction at Mf-CA3 Synapses
Although there is a strong agreement that Mf-LTP is expressed presynaptically at Mf-CA3 synapses, the participation of the postsynaptic neuron in its induction has been a matter of debate (Mellor and Nicoll, 2001; Nicoll and Schmitz, 2005; Yeckel et al., 1999). Thus, we asked whether DPE could modulate presynaptic Mf-LTP; i.e., whether the transient increase of synaptic transmission induced by DPE could facilitate LTP induction. A single

Figure 8. DPE Lowers the Threshold for Long-Term Potentiation of Mf-EPSCs

(A) Sample traces showing that both DPE and a single HFS train (100 stimuli at 100 Hz) fail to induce long-term potentiation of Mf-EPSCs (Mf-LTP). DPE followed 2 min later by a single HFS train induces Mf-LTP.

(B–D) Summary of the data presented in (A) (100 Hz, n = 6; DPE, n = 9; DPE + 1 HFS, n = 9).

(E) Sample traces illustrating that Mf-LTP observed in (D) is abrogated with AACOCF3 (10 μM). The bottom panel shows that, conversely, presynaptic Mf-LTP can be induced by three HFS even in the presence of nifedipine, indicating that postsynaptic L-type calcium channels are not absolutely required for Mf-LTP.

(F and G) Summary of the experiments presented in (E) (DPE + 1 HFS in the presence of AACOCF3, n = 7; three HFS, n = 5).

(H) Bar graph summarizing the results presented in (B), (C), (D), (F), and (G). Values are presented as mean ± SEM of n experiments (*p = 0.0139, Kruskal-Wallis test).

high-frequency stimulation (HFS) train (100 stimuli at 100 Hz) or the 9 s DPE protocol did not induce any long-lasting potentiation of Mf-EPSCs (35–40 min after the protocol; HFS: 86% ± 9%, n = 6; DPE: 94% ± 11%, n = 9) (Figures 8A–8C and 8H). However, when this single HFS train was applied 2 min after the induction of DPE (at the time in which potentiation is maximal), a long-lasting potentiation of Mf-EPSCs was observed (DPE + 1 HFS: 172% ± 16%, n = 9, p = 0.0139) (Figures 8A, 8D, and 8H). Blocking DPE induction with nifedipine (10 μM) or AACOCF3 (10 to 20 μM) abolished LTP induced by a single train and the 9 s DPE protocol (DPE + 1 HFS: nifedipine, 84% ± 13%, n = 7; AACOCF3, 119% ± 14%, n = 8) (Figures 8E, 8F, and 8H), whereas the conventional presynaptic LTP induced by three HFS trains was not blocked by nifedipine (10 μM; 3 HFS: 215% ± 60%, n = 5) (Figures 8E, 8G, and 8H). Our results confirm numerous studies that have indicated that there is no strict requirement for a rise of Ca^{2+} or depolarization of the postsynaptic CA3 pyramidal cell for inducing presynaptic Mf-LTP (Mellor and Nicoll, 2001). However, we show that a postsynaptic rise of Ca^{2+} in postsynaptic CA3 pyramidal cells, by triggering DPE, facilitates the induction of LTP. Thus, our data shed light on the discrepancies in the literature on the participation of CA3 pyramidal cells in Mf-LTP (Yeckel et al., 1999). The most likely explanation

for a change in threshold for presynaptic LTP with DPE lies in the increased activation of voltage-dependent Ca^{2+} channels (Breustedt et al., 2003; Dietrich et al., 2003) during the tetanus, resulting in higher Ca^{2+} influx and facilitation of the activation of Ca^{2+}-dependent adenylyl cyclases AC1 and AC8 (Figure 9) (Villacres et al., 1998; Wang et al., 2003).

DISCUSSION

Membrane-derived lipids are important signaling molecules used by neurons to modulate synaptic transmission. In the CNS, neuronal depolarization is known to increase the production of lipid messengers, which either act on the neuron where they are produced or diffuse away and modulate presynaptic inputs (Regehr et al., 2009; Wilson and Nicoll, 2002). Almost all presynaptically acting lipid messengers reported so far induce a decrease in neurotransmitter release, mainly by activating CB_1 or TRPV1 receptors (Regehr et al., 2009). Apart from their action through specific receptors, lipids are also known to directly act on voltage-gated ion channels in order to modulate their function (Boland and Drzewiecki, 2008). However, an endogenous mechanism employing such a direct modulation of voltage-gated ion channels by membrane-derived lipids has
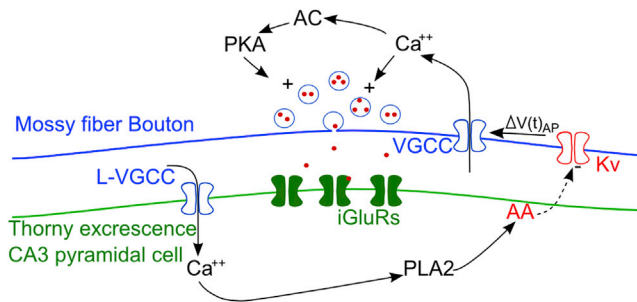
Figure 9. Working Model for the Mechanism of DPE

Depolarization of a CA3 pyramidal cell triggers voltage-dependent Ca^{2+} channels activation. Elevation of intracellular Ca^{2+} concentration activates cPLA2, leading to the release of AA. AA inhibits presynaptic 4-AP-sensitive Kv channels, inducing a broadening of the AP in the presynaptic Mf bouton, and subsequent increased release of glutamate. This retrograde signaling mechanism decreases the threshold for triggering presynaptic LTP of Mf-CA3 synapses.

not yet been reported. Recently, it was shown that 2-AG directly modulates $GABA_A$ receptors, and this modulation has a potential impact on mouse behavior (Sigel et al., 2011), supporting the idea that membrane-derived lipids can, in principle, modulate neuronal signaling not only through membrane receptors but also through direct modulation of ion channels.

Here, we identify a retrograde signaling mechanism by which endogenously released membrane-derived lipids potentiate synaptic transmission through the inhibition of presynaptic Kv channels. Exogenously applied AA appears to regulate synaptic transmission by a variety of mechanisms (Darios et al., 2007; Meves, 2008; Piomelli et al., 1987; Williams et al., 1989), although a role for AA at vertebrate CNS synapses has been challenged (O'Dell et al., 1991). The present study demonstrates that AA (or one of its metabolites) is released in an activity-dependent manner at Mf-CA3 synapses and acts as a retrograde messenger in order to facilitate synaptic transmission. Moreover, we show that 4-AP-sensitive Kv channels represent a target for presynaptic modulation of neurotransmitter release by a lipid-mediated retrograde mechanism.

Mechanisms and Properties of DPE

Here, we propose that DPE results from the Ca^{2+}-dependent release of AA from postsynaptic CA3 pyramidal cells, which then acts as a retrograde messenger in order to broaden presynaptic APs, subsequently potentiating synaptic transmission. Methodologically, lipid uncaging offers the possibility for acute and local manipulation of lipid second messenger concentration (Nadler et al., 2013). This approach allows rapid changes in the concentration of a lipid in a focal neuronal domain in a slice preparation, which is difficult to achieve with bath application of AA. Focal uncaging of AA induced a transient potentiation of Mf-CA3 synapses, a broadening of the presynaptic AP, and an inactivation of Kv channels recorded in patches from MfBs. The AA-induced broadening of the AP was fast in onset and lasted for several minutes, with a time course comparable to the effect of uncaged AA on Mf-EPSCs. The slow decay of AA broadening may be partly due to the off kinetics of AA from Kv

channels and/or to the slow washout of AA. It has been reported that the effects of AA on Kv channels in heterologous expression systems and in the slice preparation could only be reverted after the addition of BSA (Villarroel and Schwarz, 1996). Moreover, as to the duration of DPE itself, the enzymatic machinery involved in the release of AA may, in addition, display slow kinetics. Interestingly, other well-characterized forms of lipid-mediated short term plasticity, namely DSI and DSE, display faster decay kinetics on the order of tens of seconds (Regehr et al., 2009). Whether these differences are due to the enzymatic processes (synthesis and clearance), the nature of the retrograde messenger, or the presynaptic effector is unknown. We show that presynaptic Kv channels sensitive to low concentrations of 4-AP are the likely targets of AA in DPE. Kv channels are known to be highly sensitive to several lipids, especially AA (Meves, 2008). We propose that AA uncaging induces inactivation of Kv channels recorded in patches from MfBs by shifting the voltage dependence of steady-state inactivation toward more negative values. This is well in line with observations of the effects of AA on somatic Kv channels recorded from CA1 pyramidal cells (Angelova and Müller, 2006; 2009).

In control conditions, presynaptic APs at Mf-CA3 synapses are short during low-frequency stimulation but are prolonged up to 3-fold during HFS (100 Hz) as a consequence of cumulative Kv channel inactivation (Geiger and Jonas, 2000). High-frequency-mediated AP broadening only requires discharge of presynaptic APs (Geiger and Jonas, 2000) but not the activation of PLA2. In contrast, DPE depends on the depolarization or spiking activity of the postsynaptic neuron but not on the presynaptic AP discharge. In addition, frequency-dependent broadening of presynaptic APs lasts only seconds (Geiger and Jonas, 2000) as opposed to several minutes for DPE. Hence, DPE and the short-lived broadening of APs by HFS represent two different modes of regulation of presynaptic APs with distinct mechanisms and kinetics that may coexist at the same synapse. It may be possible that, at a high frequency of presynaptic APs, AA-mediated inhibition will be less effective given that Kv channels are already inactivated because of their intrinsic gating properties. In all DPE experiments, presynaptic stimulation was kept at 0.1 Hz, where there is no activity-dependent inactivation of presynaptic Kv channels.

AA induces the broadening of presynaptic APs by about 25%. Several previous studies point out that the relationship between presynaptic AP width and synaptic strength is not linear. For instance, at parallel fiber Purkinje cell synapses, a 23% increase in spike width lead to a 25% increase in total calcium and to a doubling of synaptic strength (Sabatini and Regehr, 1997). At Mf-CA3 synapses, a prolongation of the presynaptic AP by 33%, increased the Ca^{2+} charge by 27%, which, in turn, increased the EPSC peak amplitude by 77% (Geiger and Jonas, 2000). Hence, we hypothesize that the AA-induced broadening of the AP leads to enhanced synaptic transmission by increasing the AP-driven Ca^{2+} influx in presynaptic terminals. The changes in Pr after Mf-LTP most likely involve changes in the release machinery (Nicoll and Schmitz, 2005). However, Mf-LTP is not thought to be expressed as a change in AP-driven Ca^{2+} influx (Kamiya et al., 2002). Accordingly, potentiation induced by Mf-LTP did not occlude DPE. Therefore, the

potentiation induced by Mf-LTP and DPE are most likely parallel mechanisms.

Is DPE a Widespread Mechanism?

cPLA2 is expressed in most regions of the brain and predominantly in neurons (Kishimoto et al., 1999), suggesting that DPE and modulation of transmitter release following Ca^{2+}-dependent cPLA2 activation may be a general phenomenon observed at other central synapses. We observed a robust potentiation of synaptic transmission through DPE at Mf-CA3 synapses but not at A/C-CA3 glutamatergic synapses. At least three reasons may explain this difference. First, the extent of DPE and the conditions of induction possibly vary depending on the sensitivity or type of presynaptic Kv channels or other ion channels, the local density of voltage-gated Ca^{2+} channels, or other sources of Ca^{2+}, such as the activity of mGluRs. Second, the particular architecture of Mf synapses, with a large presynaptic terminal enwrapping the complex and large postsynaptic thorny excrescences may also favor production and accumulation of membrane-derived lipid messengers. Third, Mf-CA3 synapses lack presynaptic CB_1Rs, which mediate short-term inhibition of glutamate release at other synapses. An interesting hypothesis would be that, at certain synapses, the inhibition of synaptic transmission through activity-dependent release of endocannabinoids and activation of CB_1Rs counterbalances the potentiation induced by AA-mediated inhibition of presynaptic Kv channels. The balance between CB_1-dependent inhibition and DPE could be fine-tuned by CB_1Rs expression levels at presynaptic sites.

We have directly tested this hypothesis at Sc-CA1 synapses which express DSE (Depolarization-induced Suppression of Excitation), a short-lasting inhibition of Sc-CA1 synaptic transmission dependent on endocannabinoid signaling and activation of CB_1Rs (Ohno-Shosaku et al., 2002). We showed that a DPE-like phenomenon can be observed at Sc-CA1 synapses in conditions where endocannabinoid signaling was abrogated by blocking presynaptic CB_1Rs (Figure S7). This transient potentiation of Sc-CA1 synaptic transmission was blocked by AACOCF3, the cPLA2 antagonist. In fact, it was previously shown that inhibiting CB_1Rs in dorsal raphe neurons not only blocked DSE but unexpectedly elicited a transient potentiation of EPSC amplitude similar in magnitude and timing to DPE (Haj-Dahmane and Shen, 2009). An additional example is given by the analysis of mice deficient for diacylglycerol lipase (DGL-α) which produces 2-arachidonoylglycerol (2-AG) involved in DSE at central synapses (Tanimura et al., 2010). Interestingly, in these mice, the abolition of DSE at parallel fiber to Purkinje cell synapses unravelled a transient potentiation of synaptic transmission with kinetic and amplitude similar to what we are now reporting at Sc-CA1 synapses (Tanimura et al., 2010). Hence, we can conclude that DPE could be more widespread in the brain, and in particular be prevalent at synapses which do not express CB_1Rs.

Physiological Relevance of DPE

DPE is not only induced by a steady-state depolarization of the postsynaptic neuron but also by protocols that pertain to physiological hippocampal activity. Indeed, DPE can be triggered by a sequence of a few short bursts of postsynaptic APs repeated at the frequency of theta oscillations, which are thought to facilitate the formation of maps and episodic/semantic memories (Buzsáki, 2005). Moreover, this transient potentiation is observed with a natural sequence of AP firing reproducing the spiking activity of a CA3 place cell of a rat exploring its environment (Isaac et al., 2009). Hence, DPE, which is expressed as a change in presynaptic properties, can be induced by the sole spiking activity of postsynaptic CA3 pyramidal cells but does not directly require synaptic activity. Nonetheless, bursts of spikes triggered by synaptic inputs (i.e., Mf-CA3 inputs) are also efficient in triggering DPE. However, in this case, DPE coexists with purely presynaptic forms of short-term facilitation that display in generally shorter time courses (Nicoll and Schmitz, 2005). Although DPE induction does not depend on presynaptic AP firing, we do not exclude that it could be modulated by incoming synaptic activity leading, for instance, to the activation of postsynaptic mGluRs and Ca^{2+} release from internal stores.

As a direct consequence of the fact that DPE can be induced by postsynaptic spiking activity, it will affect all Mf-CA3 synapses in a single CA3 pyramidal cell as opposed to other forms of short-term plasticity that are synapse specific. Concomitant to the fact that DPE does not spread to neighboring CA3 pyramidal cells, this process favors the emergence of an active CA3 pyramidal within the local network. By transiently facilitating synaptic transmission, DPE primes presynaptic long-term plasticity at all Mf synaptic inputs to a single CA3 pyramidal cell. This will most likely occur after a period of high spiking activity, such as when an animal explores its environment (Buzsáki, 2005). The priming event represented by DPE most likely enhances the capacity of local CA3 circuits to rapidly encode a novel context by facilitating long-term synaptic plasticity between dentate gyrus and CA3 pyramidal cells. Hence, the control of voltage-gated ion channels by activity-dependent release of membrane-derived lipids provides a mechanism for the dynamic regulation of neural circuits.

EXPERIMENTAL PROCEDURES

All the animal were used according to the guidelines of the University of Bordeaux/CNRS Animal Care and Use Committee.

Electrophysiology

Parasagittal hippocampal slices (320 μm) were obtained from 18- to 25-day-old C57Bl/6 mice. Slices were transferred to a recording chamber in which they were continuously superfused with an oxygenated extracellular medium (95% O_2 and 5% CO_2) containing 125 mM NaCl, 2.5 mM KCl, 2.3 mM $CaCl_2$, 1.3 mM $MgCl_2$, 1.25 mM NaH_2PO_4, 26 mM $NaHCO_3$, and 20 mM glucose (pH 7.4). Whole-cell recordings were made at ~32°C from CA3 pyramidal cells under infrared differential interference contrast imaging with borosilicate glass capillaries, which had resistances between 4–8 MΩ. For voltage-clamp recordings from CA3 pyramidal cells, the patch electrodes were filled with a solution containing 140 mM $CsCH_3SO_3$, 2 mM $MgCl_2$, 4 mM NaCl, 5 mM phospho-creatine, 2 mM Na_2ATP, 0.2 mM EGTA, 10 mM HEPES, and 0.33 mM GTP (pH 7.3) adjusted with CsOH. DPE was still observed when $CsCH_3SO_3$ was replaced by CsCl or KCl or by the larger cation ($NMDG^+$). DPE was not induced when QX314 (5 mM) was added to the intracellular solution (data not shown): QX314, largely used as Na^+ channel blocker, also blocks voltage-gated calcium channels (VGCC) and interferes with intracellular signaling (Talbot and Sayer, 1996). For current clamp recordings of CA3 pyramidal cells, the intracellular solution contained 140 mM KCH_3SO_3,

10 mM HEPES, 0.2 mM EGTA, 4 mM MgATP, 0.3 mM GTP, and 15 mM phosphocreatine (pH adjusted to 7.3 with KOH). No liquid-junction potential correction was used. Bicuculline (10 μM) was present in the superfusate of all experiments. A patch pipette (open tip resistance ~5 MΩ [about 1 μm tip diameter]) was placed in the dentate gyrus to stimulate Mfs or in the *stratum radiatum* of the CA3 area to stimulate A/C fibers. Mf synaptic currents were identified according to the following criteria: robust low-frequency facilitation, low release probability at 0.1 Hz, rapid rise times of individual EPSCs (~1 ms), and EPSC decays free of secondary peaks that may indicate the presence of polysynaptic contamination. Details for the electrophysiological procedures, including patch-clamp recordings of presynaptic boutons, are provided in the Supplemental Information.

Caged AA Synthesis and Uncaging

Caged AA was synthesized by esterification of AA with diethylamino-4-methylenhydroxycoumarin in the presence of carbodiimide and dimethylamino pyridine in 59% yield after purification by liquid chromatography (for synthetic details, see below). The hydroxycoumarin was prepared according to published procedures (Hagen et al., 2003; Meves, 2008).

A fresh aliquot of caged AA was used for each experiment and was dissolved in extracellular medium. The slices were perfused with extracellular medium containing caged AA for at least 10–15 min before starting the experiments in order to ensure homogenous penetration of the caged compound in the slice. During the application of caged AA, a total amount of 10 ml of extracellular solution containing the caged compound was continuously recirculated and oxygenated. AA was locally uncaged in the *stratum lucidum* of the patched CA3 pyramidal cell or the patched MfB by an UV flash photolysis (Xenon flash lamp, Rapp OptoElectronic). For cell-attached recordings, 10 μM caged AA was dissolved directly in the patch-pipette solution. Synthetic details are provided in the Supplemental Information.

Statistics

Values are presented as mean ± SEM of n experiments. For statistical analysis, nonparametric test were used. A Mann-Whitney test was used for two groups' comparison, and Kruskal-Wallis test followed by a Dunn's multiple comparison test for comparison between more than two groups. Within-cell comparisons were made with Wilcoxon match pairs test in raw nonnormalized values between baseline values and after values obtained after applying the desired protocol. Statistical differences were considered as significant at $p < 0.05$. Statistical analysis was performed with GraphPad Prism software.

All drugs were obtained from Tocris Cookson, Sigma-Aldrich, or Ascent Scientific. BotoxC1 was produced as in Vaidyanathan et al. (1999). The effects of pharmacological manipulations were always compared to interleaved control experiments.

SUPPLEMENTAL INFORMATION

Supplemental Information contains Supplemental Experimental Procedures, seven figures, and one table and can be found with this article online at http://dx.doi.org/10.1016/j.neuron.2013.12.028.

AUTHOR CONTRIBUTIONS

M.C., F.L., and N.R. designed, performed and analyzed the experiments. S.Z., J.L., S.V.D.S., and C.B. helped with some experiments, analysis, and discussion. A.V. produced BotoxC1. A.N. and C.S. synthesized caged lipids. C.M. supervised and guided the project and wrote the manuscript along with M.C., F.L., and N.R. All authors discussed the results and commented on the manuscript.

REFERENCES

Alle, H., Kubota, H., and Geiger, J.R. (2011). Sparse but highly efficient Kv3 outpace BKCa channels in action potential repolarization at hippocampal mossy fiber boutons. J. Neurosci. *31*, 8001–8012.

Angelova, P., and Müller, W. (2006). Oxidative modulation of the transient potassium current IA by intracellular arachidonic acid in rat CA1 pyramidal neurons. Eur. J. Neurosci. *23*, 2375–2384.

Angelova, P.R., and Müller, W.S. (2009). Arachidonic acid potently inhibits both postsynaptic-type Kv4.2 and presynaptic-type Kv1.4 IA potassium channels. Eur. J. Neurosci. *29*, 1943–1950.

Besana, A., Robinson, R.B., and Feinmark, S.J. (2005). Lipids and two-pore domain K+ channels in excitable cells. Prostaglandins Other Lipid Mediat. *77*, 103–110.

Boland, L.M., and Drzewiecki, M.M. (2008). Polyunsaturated fatty acid modulation of voltage-gated ion channels. Cell Biochem. Biophys. *52*, 59–84.

Breustedt, J., Vogt, K.E., Miller, R.J., Nicoll, R.A., and Schmitz, D. (2003). Alpha1E-containing Ca2+ channels are involved in synaptic plasticity. Proc. Natl. Acad. Sci. USA *100*, 12450–12455.

Buzsáki, G. (2005). Theta rhythm of navigation: link between path integration and landmark navigation, episodic and semantic memory. Hippocampus *15*, 827–840.

Chevaleyre, V., Takahashi, K.A., and Castillo, P.E. (2006). Endocannabinoid-mediated synaptic plasticity in the CNS. Annu. Rev. Neurosci. *29*, 37–76.

Darios, F.E.D.E.R., Connell, E., and Davletov, B. (2007). Phospholipases and fatty acid signalling in exocytosis. J. Physiol. *585*, 699–704.

Dietrich, D., Kirschstein, T., Kukley, M., Pereverzev, A., von der Brelie, C., Schneider, T., and Beck, H. (2003). Functional specialization of presynaptic Cav2.3 Ca2+ channels. Neuron *39*, 483–496.

Fink, M., Lesage, F., Duprat, F., Heurteaux, C., Reyes, R., Fosset, M., and Lazdunski, M. (1998). A neuronal two P domain K+ channel stimulated by arachidonic acid and polyunsaturated fatty acids. EMBO J. *17*, 3297–3308.

Galimberti, I., Gogolla, N., Alberi, S., Santos, A.F., Muller, D., and Caroni, P. (2006). Long-term rearrangements of hippocampal mossy fiber terminal connectivity in the adult regulated by experience. Neuron *50*, 749–763.

Geiger, J.R.P., and Jonas, P. (2000). Dynamic control of presynaptic Ca(2+) inflow by fast-inactivating K(+) channels in hippocampal mossy fiber boutons. Neuron *28*, 927–939.

Gibson, H.E., Edwards, J.G., Page, R.S., Van Hook, M.J., and Kauer, J.A. (2008). TRPV1 channels mediate long-term depression at synapses on hippocampal interneurons. Neuron *57*, 746–759.

Hagen, V., Frings, S., Wiesner, B., Helm, S., Kaupp, U.B., and Bendig, J. (2003). [7-(Dialkylamino)coumarin-4-yl]methyl-Caged Compounds as Ultrafast and Effective Long-Wavelength Phototriggers of 8-Bromo-Substituted Cyclic Nucleotides. ChemBioChem *4*, 434–442.

Haj-Dahmane, S., and Shen, R.-Y. (2009). Endocannabinoids suppress excitatory synaptic transmission to dorsal raphe serotonin neurons through the activation of presynaptic CB1 receptors. J. Pharmacol. Exp. Ther. *331*, 186–196.

Hardie, R.C. (2007). TRP channels and lipids: from Drosophila to mammalian physiology. J. Physiol. *578*, 9–24.

Herkenham, M., Lynn, A.B., Little, M.D., Johnson, M.R., Melvin, L.S., de Costa, B.R., and Rice, K.C. (1990). Cannabinoid receptor localization in brain. Proc. Natl. Acad. Sci. USA *87*, 1932–1936.

Hofmann, M.E., Nahir, B., and Frazier, C.J. (2008). Excitatory afferents to CA3 pyramidal cells display differential sensitivity to CB1 dependent inhibition of synaptic transmission. Neuropharmacology 55, 1140–1146.

Isaac, J.T.R., Buchanan, K.A., Muller, R.U., and Mellor, J.R. (2009). Hippocampal place cell firing patterns can induce long-term synaptic plasticity in vitro. J. Neurosci. 29, 6840–6850.

Kamiya, H., Umeda, K., Ozawa, S., and Manabe, T. (2002). Presynaptic Ca2+ entry is unchanged during hippocampal mossy fiber long-term potentiation. J. Neurosci. 22, 10524–10528.

Kano, M., Ohno-Shosaku, T., Hashimotodani, Y., Uchigashima, M., and Watanabe, M. (2009). Endocannabinoid-mediated control of synaptic transmission. Physiol. Rev. 89, 309–380.

Katona, I., Urbán, G.M., Wallace, M., Ledent, C., Jung, K.M., Piomelli, D., Mackie, K., and Freund, T.F. (2006). Molecular composition of the endocannabinoid system at glutamatergic synapses. J. Neurosci. 26, 5628–5637.

Kawamura, Y., Fukaya, M., Maejima, T., Yoshida, T., Miura, E., Watanabe, M., Ohno-Shosaku, T., and Kano, M. (2006). The CB1 cannabinoid receptor is the major cannabinoid receptor at excitatory presynaptic sites in the hippocampus and cerebellum. J. Neurosci. 26, 2991–3001.

Kishimoto, K., Matsumura, K., Kataoka, Y., Morii, H., and Watanabe, Y. (1999). Localization of cytosolic phospholipase A2 messenger RNA mainly in neurons in the rat brain. Neuroscience 92, 1061–1077.

Kukkonen, J.P. (2011). A ménage à trois made in heaven: G-protein-coupled receptors, lipids and TRP channels. Cell Calcium 50, 9–26.

Lambeau, G., and Gelb, M.H. (2008). Biochemistry and physiology of mammalian secreted phospholipases A2. Annu. Rev. Biochem. 77, 495–520.

Lozovaya, N., Yatsenko, N., Beketov, A., Tsintsadze, T., and Burnashev, N. (2005). Glycine receptors in CNS neurons as a target for nonretrograde action of cannabinoids. J. Neurosci. 25, 7499–7506.

Ludwig, M., and Pittman, Q.J. (2003). Talking back: dendritic neurotransmitter release. Trends Neurosci. 26, 255–261.

Lüscher, C., Xia, H., Beattie, E.C., Carroll, R.C., von Zastrow, M., Malenka, R.C., and Nicoll, R.A. (1999). Role of AMPA receptor cycling in synaptic transmission and plasticity. Neuron 24, 649–658.

Marsicano, G., and Lutz, B. (2006). Neuromodulatory functions of the endocannabinoid system. J. Endocrinol. Invest. Suppl. 29, 27–46.

Mellor, J.R., and Nicoll, R.A. (2001). Hippocampal mossy fiber LTP is independent of postsynaptic calcium. Nat. Neurosci. 4, 125–126.

Meves, H. (2008). Arachidonic acid and ion channels: an update. Br. J. Pharmacol. 155, 4–16.

Nadler, A., Reither, G., Feng, S., Stein, F., Reither, S., Müller, R., and Schultz, C. (2013). The fatty acid composition of diacylglycerols determines local signaling patterns. Angew. Chem. Int. Ed. Engl. 52, 6330–6334.

Nicoll, R.A., and Schmitz, D. (2005). Synaptic plasticity at hippocampal mossy fibre synapses. Nat. Rev. Neurosci. 6, 863–876.

O'Dell, T.J., Hawkins, R.D., Kandel, E.R., and Arancio, O. (1991). Tests of the roles of two diffusible substances in long-term potentiation: evidence for nitric oxide as a possible early retrograde messenger. Proc. Natl. Acad. Sci. USA 88, 11285–11289.

Ohno-Shosaku, T., Tsubokawa, H., Mizushima, I., Yoneda, N., Zimmer, A., and Kano, M. (2002). Presynaptic cannabinoid sensitivity is a major determinant of depolarization-induced retrograde suppression at hippocampal synapses. J. Neurosci. 22, 3864–3872.

Oliver, D., Lien, C.-C., Soom, M., Baukrowitz, T., Jonas, P., and Fakler, B. (2004). Functional conversion between A-type and delayed rectifier K+ channels by membrane lipids. Science 304, 265–270.

Piomelli, D., Volterra, A., Dale, N., Siegelbaum, S.A., Kandel, E.R., Schwartz, J.H., and Belardetti, F. (1987). Lipoxygenase metabolites of arachidonic acid as second messengers for presynaptic inhibition of Aplysia sensory cells. Nature 328, 38–43.

Regehr, W.G., Carey, M.R., and Best, A.R. (2009). Activity-dependent regulation of synapses by retrograde messengers. Neuron 63, 154–170.

Roberts-Crowley, M.L., Mitra-Ganguli, T., Liu, L., and Rittenhouse, A.R. (2009). Regulation of voltage-gated Ca2+ channels by lipids. Cell Calcium 45, 589–601.

Ryberg, E., Larsson, N., Sjögren, S., Hjorth, S., Hermansson, N.-O., Leonova, J., Elebring, T., Nilsson, K., Drmota, T., and Greasley, P.J. (2007). The orphan receptor GPR55 is a novel cannabinoid receptor. Br. J. Pharmacol. 152, 1092–1101.

Sabatini, B.L., and Regehr, W.G. (1997). Control of neurotransmitter release by presynaptic waveform at the granule cell to Purkinje cell synapse. J. Neurosci. 17, 3425–3435.

Schaechter, J.D., and Benowitz, L.I. (1993). Activation of protein kinase C by arachidonic acid selectively enhances the phosphorylation of GAP-43 in nerve terminal membranes. J. Neurosci. 13, 4361–4371.

Sigel, E., Baur, R., Rácz, I., Marazzi, J., Smart, T.G., Zimmer, A., and Gertsch, J. (2011). The major central endocannabinoid directly acts at GABA(A) receptors. Proc. Natl. Acad. Sci. USA 108, 18150–18155.

Talbot, M.J., and Sayer, R.J. (1996). Intracellular QX-314 inhibits calcium currents in hippocampal CA1 pyramidal neurons. J. Neurophysiol. 76, 2120–2124.

Tanimura, A., Yamazaki, M., Hashimotodani, Y., Uchigashima, M., Kawata, S., Abe, M., Kita, Y., Hashimoto, K., Shimizu, T., Watanabe, M., et al. (2010). The endocannabinoid 2-arachidonoylglycerol produced by diacylglycerol lipase alpha mediates retrograde suppression of synaptic transmission. Neuron 65, 320–327.

Trimbuch, T., Beed, P., Vogt, J., Schuchmann, S., Maier, N., Kintscher, M., Breustedt, J., Schuelke, M., Streu, N., Kieselmann, O., et al. (2009). Synaptic PRG-1 modulates excitatory transmission via lipid phosphate-mediated signaling. Cell 138, 1222–1235.

Vaidyanathan, V.V., Yoshino, K., Jahnz, M., Dörries, C., Bade, S., Nauenburg, S., Niemann, H., and Binz, T. (1999). Proteolysis of SNAP-25 isoforms by botulinum neurotoxin types A, C, and E: domains and amino acid residues controlling the formation of enzyme-substrate complexes and cleavage. J. Neurochem. 72, 327–337.

Villacres, E.C., Wong, S.T., Chavkin, C., and Storm, D.R. (1998). Type I adenylyl cyclase mutant mice have impaired mossy fiber long-term potentiation. J. Neurosci. 18, 3186–3194.

Villarroel, A., and Schwarz, T.L. (1996). Inhibition of the Kv4 (Shal) family of transient K+ currents by arachidonic acid. J. Neurosci. 16, 2522–2532.

Wang, H., Pineda, V.V., Chan, G.C.K., Wong, S.T., Muglia, L.J., and Storm, D.R. (2003). Type 8 adenylyl cyclase is targeted to excitatory synapses and required for mossy fiber long-term potentiation. J. Neurosci. 23, 9710–9718.

Williams, J.H., Errington, M.L., Lynch, M.A., and Bliss, T.V.P. (1989). Arachidonic acid induces a long-term activity-dependent enhancement of synaptic transmission in the hippocampus. Nature 341, 739–742.

Wilson, R.I., and Nicoll, R.A. (2002). Endocannabinoid signaling in the brain. Science 296, 678–682.

Yeckel, M.F., Kapur, A., and Johnston, D. (1999). Multiple forms of LTP in hippocampal CA3 neurons use a common postsynaptic mechanism. Nat. Neurosci. 2, 625–633.

ORIGINAL ARTICLE

An anterograde rabies virus vector for high-resolution large-scale reconstruction of 3D neuron morphology

Matthias Georg Haberl · Silvia Viana da Silva · Jason M. Guest · Melanie Ginger · Alexander Ghanem · Christophe Mulle · Marcel Oberlaender · Karl-Klaus Conzelmann · Andreas Frick

Abstract Glycoprotein-deleted rabies virus (RABV ΔG) is a powerful tool for the analysis of neural circuits. Here, we demonstrate the utility of an anterograde RABV ΔG variant for novel neuroanatomical approaches involving either bulk or sparse neuronal populations. This technology exploits the unique features of RABV ΔG vectors, namely autonomous, rapid high-level expression of transgenes, and limited cytotoxicity. Our vector permits the unambiguous long-range and fine-scale tracing of the entire axonal arbor of individual neurons throughout the brain. Notably, this level of labeling can be achieved following infection with a single viral particle. The vector is effective over a range of ages (>14 months) aiding the studies of neurodegenerative disorders or aging, and infects numerous cell types in all brain regions tested. Lastly, it can also be readily combined with retrograde RABV ΔG variants. Together with other modern technologies, this tool provides new possibilities for the investigation of the anatomy and physiology of neural circuits.

Keywords Neuronal morphology · Connectivity · Sparse labeling · Circuit reconstruction · Neuron-type classification · Alzheimer's disease

Introduction

The reconstruction of neuronal circuits is central to many questions in neuroscience. Indeed, knowledge of the fine-scale morphology of neurons provides not only insight into the identity and function of individual neurons, but also into the function of neural circuits (Douglas and Martin 2004; Lichtman and Denk 2011; Oberlaender et al. 2012a;

M. G. Haberl and S. Viana da Silva contributed equally to this work.

M. G. Haberl · M. Ginger · A. Frick (✉)
Physiopathologie de la plasticité neuronale, INSERM,
Neurocentre Magendie, U862, Bordeaux, France
e-mail: andreas.frick@inserm.fr

M. G. Haberl · M. Ginger · A. Frick
Physiopathologie de la plasticité neuronale, Univ. Bordeaux,
Neurocentre Magendie, U862, Bordeaux, France

M. G. Haberl
Institute of NeuroInformatics, University of Zurich, Zurich,
Switzerland

S. Viana da Silva · M. Ginger · C. Mulle
Interdisciplinary Institute for Neuroscience, CNRS, UMR 5297,
Bordeaux, France

S. Viana da Silva · M. Ginger · C. Mulle
Interdisciplinary Institute for Neuroscience, Univ. Bordeaux,
UMR 5297, Bordeaux, France

S. Viana da Silva
PDBEB CNC, University of Coimbra, Coimbra, Portugal

J. M. Guest · M. Oberlaender
Digital Neuroanatomy, Max Planck Florida Institute for
Neuroscience, Jupiter, FL, USA

A. Ghanem · K.-K. Conzelmann
Max-von-Pettenkofer Institute and Gene Center of the Ludwig-
Maximilians-University Munich, Munich, Germany

M. Oberlaender
Computational Neuroanatomy Group, Max Planck Institute for
Biological Cybernetics, Tuebingen, Germany

M. Oberlaender
Bernstein Center for Computational Neuroscience, Tuebingen,
Germany

Parekh and Ascoli 2013; Svoboda 2011). Successful neuronal reconstruction depends on a number of key parameters: (1) Neurons must be labeled in a way that permits visualization of all neuronal structures (dendrites, spines, axons, boutons). (2) The full extent of neuronal processes should be efficiently labeled. In particular, this applies to the axons, which extend over large brain volumes (Oberlaender et al. 2011). (3) Labeling would ideally permit visualization by high-resolution light microscopy approaches (such as confocal, two-photon, or super-resolution microscopy). In effect, this means efficient expression of a volume-filling fluorescent marker and a high signal-to-noise ratio for the labeled structure. (4) The ideal labeling method would not only be suited to bulk labeling of populations of neurons, but importantly also provide intense labeling of sparse populations of neurons, or even single neurons. This is, because to date the most successful reconstructions of complete neuronal morphology require sparse or single-cell labeling since the axons of bulk labeled neurons become indistinguishable in the densely packed neuropil unless resolved with electron microscopy (da Costa and Martin 2013; Helmstaedter 2013).

Viral vectors fulfill many of these criteria due to their self-amplifying properties (ensuring a high-level expression of volume-filling markers) (Callaway 2008; van den Pol et al. 2009). In particular, genetically modified rabies virus (RABV) is well suited to this approach due to its highly neurotropic nature, rapid, high-level expression of encoded proteins and relatively low cytotoxicity (Wickersham et al. 2007a; Ginger et al. 2013b). The glycoprotein gene-deleted RABV variant, (RABV ΔG) is an especially useful tool that permits the manipulation of the tropism of the virus through pseudotyping approaches (Mebatsion et al. 1997; Ginger et al. 2013b). This principle has previously been exploited for both retrograde labeling of neurons (Wickersham et al. 2007a; Larsen et al. 2007; Nhan and Callaway 2012) and for labeling inputs into a specific cell population (i.e., mono-trans-synaptic tracing) (Wickersham et al. 2007b; Choi et al. 2010).

Here, we employ a RABV ΔG-based method that allows direct transduction of cell bodies, permitting the tracing and complete 3D reconstruction of dendritic and axonal arbors of sparsely labeled neurons. This method combines the advantages of an anterograde tracer with the brilliant morphological labeling previously described for recombinant RABV ΔG (Wickersham et al. 2007a). This vector fulfills all of the aforementioned criteria for neuronal labeling. Low cytotoxicity, fast and strong expression and intense labeling of even the most distant processes set it apart from 'classical' viral and non-viral anterograde neuroanatomical tracing approaches. Moreover, the ability to infect a range of cell types over a large age window makes this vector a versatile tool for a large number of experimental situations.

Results

To render RABV ΔG capable of cell body infection, we pseudotyped it with a chimeric envelope protein containing the N-terminal domain of the vesicular stomatitis virus glycoprotein (VSV-G). VSV-G binds to highly ubiquitous receptors (Finkelshtein et al. 2013), thus conferring the ability to transduce a wide range of cell types, a property that has previously been exploited for the production of VSV-G pseudotyped viral vectors such as retro- and lentiviruses (Burns et al. 1993). We replaced the membrane anchor and C-terminal cytoplasmic sequence of the authentic VSV-G with that of the RABV-G protein (^{RtmC}) to support selective incorporation of the protein into the RABV ΔG envelope (Fig. 1a). We have generated vectors expressing either a membrane-targeted form of tdTomato labeling the neuronal membrane for subsequent surface reconstruction (Fig. 1c, lower panels; Fig. 3c), or cytoplasmic fluorescent proteins (eGFP and mCherry) (all other figures). The resulting vector [RABV ΔG (VSV G^{RtmC})] consistently transduced cells at the site of injection (Figs. 1, 2, 3, 4, 5, 6).

Important criteria determining the suitability of a viral vector for neuronal tracing are the time course for expression, the intensity of expression, and the morphological detail provided by the labeling. Thus, we compared RABV ΔG (VSV G^{RtmC}) with two commonly used anterograde viral tracers, namely lentivirus, and adeno-associated virus (AAV). We quantified fluorescence intensity and the signal-to-noise ratio for eGFP expressing neurons following injection of these vectors into the hippocampal dentate gyrus (DG) region (Fig. 1b). Fluorescence intensity and signal-to-noise ratio measured at the cell bodies of transduced neurons were significantly higher for RABV ΔG compared to both other vectors (one-way Anova followed by Tukey multiple-comparison; $p < 0.001$). Importantly, these superior labeling qualities were achieved (with no sign of cytotoxicity) at much shorter time scales of infection (6 days post infection for RABV ΔG (VSV G^{RtmC}) versus 12 and 22 days for lentivirus and AAV, respectively). Moreover, dendrites, spines, axons, boutons, as well as filopodia were readily distinguished within RABV ΔG (VSV G^{RtmC}) infected neurons, aiding their visualization and reconstruction (Fig. 1c). Notably, the labeled neurons presented here are DG granule cells, neurons that are difficult to infect using the native RABV (reviewed in Ohara et al. 2009).

We noted that the transduction with RABV ΔG (VSV-G^{RtmC}) occurred in a purely anterograde manner (i.e., infection of cell bodies and subsequent labeling of axons and dendrites). To exclude the possibility that RABV ΔG (VSV-G^{RtmC}) is transported in a retrograde or trans-synaptic manner, we performed injections into the whisker-
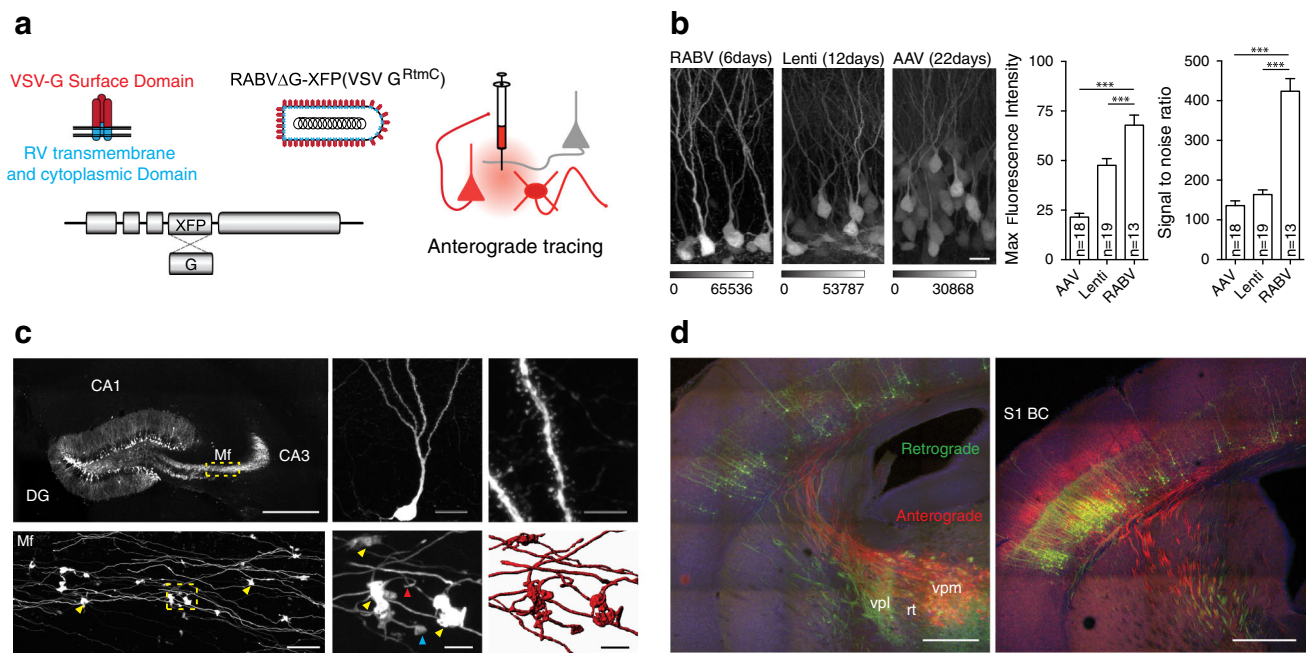
Fig. 1 Novel rabies virus variant for anterograde tracing of neuronal morphology. **a** RABV ΔG expressing a fluorescent protein (XFP: eGFP, mCherry or myr-TdTom) was pseudotyped with a chimeric surface protein containing the transmembrane and cytoplasmic domain of the native RABV glycoprotein (RtmC) and surface domain of the G protein of VSV Indiana virus. **b** Comparison of fluorescence intensity and signal-to-noise ratio of cells infected with RABV ΔG (VSV G^{RtmC}) (RABV), VSV G-pseudotyped lentivirus (LV) and adeno-associated virus (AAV). Data are mean ± SEM ***$p < 0.001$ (one-way ANOVA test). **c** RABV ΔG(VSV G^{RtmC}) infection of the hippocampal dentate gyrus (DG) region resulted in intense labeling of granule cells revealing their fine morphological details including the dendritic tree (*upper middle*), spines (*upper right*), mossy fibers (Mf), and mossy fiber boutons (MfBs, *yellow arrowheads*). This permits semi-automated volume reconstruction (*lower middle* and *lower right panel*) of MfBs with their adjacent filopodia (e.g., *red arrowhead*) and satellites (e.g., *blue arrowhead*). *Scale bars* 500 μm, *upper left* 25 μm, *lower left* 15 μm, *upper middle* 5 μm, *upper right*, *lower middle* and *right*. **d** Reciprocal thalamo-cortical and cortico-thalamical projections in S1 BC and VPm following co-injection of retrograde (*green*) and anterograde (*red*) RABV ΔG. *Scale bars* 500 μm

related barrel cortex (BC) and visually inspected regions known to connect to this structure. While neurons were infected locally at the site of injection, no labeled cell bodies were found in any of the following regions: thalamic ventral posterior medial (VPm) division and posterior medial (POm) division, other areas of the primary somatosensory cortex (S1), secondary somatosensory cortex (S2), primary motor cortex (M1), and contralateral S1 (not shown). In fact, we saw no infected cell outside the local injection site in S1. This property of RABV ΔG (VSV-G^{RtmC}) permits its combined use with a retrogradely transducing RABV ΔG variant (Wickersham et al. 2007a) to unambiguously trace projections both to-, and from-, a given region. An example for this type of experiment is shown for the labeling of reciprocal projections between the VPm division of mouse thalamus and the primary somatosensory barrel cortex (S1-BC; Fig. 1d). Importantly, we found a complete absence of retrograde infection in all injections using RABV ΔG (VSV-G^{RtmC}).

In the aforementioned examples, we demonstrate the utility of this vector for the transduction of populations of neurons. However, as stated previously, reconstruction of the complete structure of a neuron, including its complex and wide-reaching axonal arbors, requires methods for sparse- or single-neuron labeling. This is often achieved by intracellular filling with biocytin (or its analogs), as most viral-based tracers are completely unsuited to this task. RABV, however, is somewhat unique due to its ability to amplify sufficiently from a single infectious particle (reviewed in Callaway 2008) to confer robust, high intensity labeling to all morphological aspects of an infected cell. Although this property is known from the wild-type CVS strain of RABV (Callaway 2008), it has not been demonstrated for glycoprotein-deleted pseudotyped variants of the SAD B19 strain. To examine the ability of our anterograde RABV ΔG vector to confer the sparse labeling necessary for single neuron reconstruction, we injected 5–10 viral particles into the thalamic POm division of a 16-week-old mouse. Within the investigated thalamic volume of ∼400 μm × 400 μm × 400 μm, only seven cells were labeled (Fig. 2a), including three excitatory projecting neurons, one inhibitory interneuron and three astrocytes (Fig. 2a, b). However, all cells were intensely labeled throughout the extent of their processes.
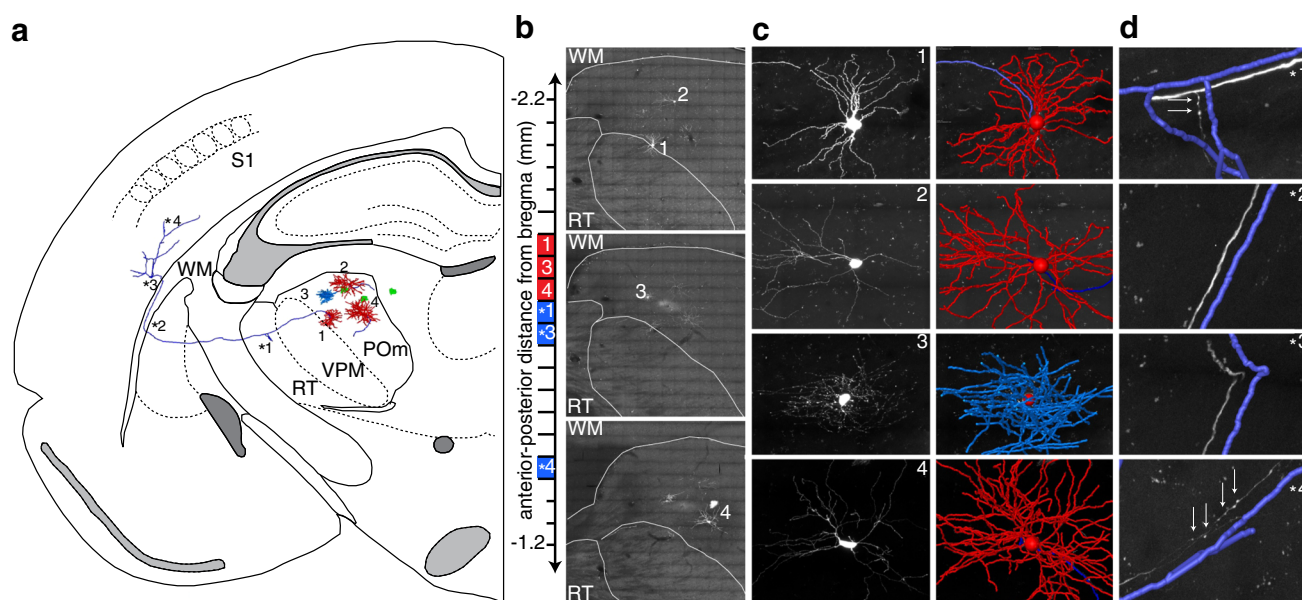
Fig. 2 3D reconstruction of thalamic neurons sparsely labeled with RABV ΔG (VSV-G^RtmC). **a** Three excitatory neurons, one inhibitory interneuron (soma/dendrites: *red*, axon: *blue*) and three astrocytes (*green*) were reconstructed within the imaged volume in thalamus and cortex. **b** Cells were reconstructed from 12 consecutive 50-μm-thick brain sections (*long dashes* of the anterior–posterior axis). Maximum projection images of three sections containing the neuronal somata are shown (*red* within the anterior–posterior axis). **c** *Left* zoom of panel **b**. *Right* Semi-automated reconstructions of the neuronal skeletons are superimposed. In case of the interneuron in *panel 3*, only the soma and axonal arbor are shown. Please note: Reconstructed branches that are not visible in the projection image, such as the gap in the axon in *panel 1*, were traced in adjacent brain sections. **d** One axon was traced into cortex. Maximum projections superimposed with semi-automated reconstructions are shown from exemplary parts of the axon (*blue* within the anterior–posterior axis, *panel* **b**). It branched first within RT (*1*), where individual boutons (at *arrow locations*, not reconstructed) indicated potential synapse locations; traversed through the WM (*2*, *3*), where the axon was perfectly visible; and entered the vibrissal cortex, where labeling quality did not decrease with distance from the soma (i.e., individual boutons were still clearly visible). *Scale bars* 1 mm (**a**) 50 μm (**b**, **c**) and 10 μm (**d**)

Using high-resolution, large-scale confocal microscopy and automated image processing routines (Oberlaender et al. 2007), we reconstructed the somata, dendrites and axons of the four RABV-infected neurons within 12 consecutive 50-μm-thick brain sections (Fig. 2). The high labeling quality in terms of fluorescent intensity, signal-to-noise ratio, and homogeneity across cells (Fig. 2c) including their entire axonal arbor (Fig. 2d) enabled the automated tracing of all morphological fine-structures within the imaged volume. To demonstrate this, we reconstructed the complete 3D morphology of all dendrites, the complete axon of the interneuron, and the initial parts of the axons from the three projecting neurons. Furthermore, we traced and reconstructed one long-range axon. In this case, the neuron projected to the nucleus reticularis (RT) and continued to traverse the white matter tract before entering the vibrissal cortex (S1). This type of axon trajectory has been reported previously for POm neurons (Deschenes et al. 1998). The axon showed no obvious decrease in labeling quality with distance from the soma, allowing identification of individual boutons within thalamus and cortex (Fig. 2d). These results clearly demonstrate the ability of our anterograde RABV ΔG tracer to amplify its genome sufficiently, following infection of a cell by a single particle, to enable tracing of long-ranging axons. As a result of this analysis, we found that the initial axonal segments of the traced neurons were less unidirectional than those described using other methods (Deschenes et al. 1998), possibly indicating that POm projects more diversely to regions other than S1.

To better characterize the efficacy/versatility of our vector, we performed injections into a variety of brain areas and over a range of ages. RABV ΔG (VSV G^RtmC) transduced cells in all mouse brain areas tested, i.e., somatosensory cortex, thalamus, hippocampal dentate gyrus, substantia nigra and cerebellum (Figs. 1c, d, 2b, 3, 4). RABV ΔG (VSV-G^RtmC) was capable of transducing excitatory and inhibitory neurons, as well as glial cells, as illustrated in Figs. 2, 4 and 6. For example, in the cerebellum, we found that the virus efficiently transduced inhibitory stellate cells, basket cells and Purkinje cells, as well as the excitatory granule cells. Notably, this vector mediated efficient and intense cell labeling in mice of all ages tested (1–15 months), permitting its use for the neuroanatomical study of neurodegenerative disorders (AD) or aging, as demonstrated in Fig. 5.

Fig. 3 Efficiency of transduction of targeted brain areas. RABV ΔG XFP (VSV-G^RtmC) transduced cells in all brain structures examined. Confocal microscope images of fluorescently labeled neurons following stereotaxic injection into **a** substantia nigra, **b** anterior amygdaloid, dorsal region, and **c** layers 5 and 6 of the somatosensory cortex. *Scale bars left panels* 1 mm, *right panels* 50 μm
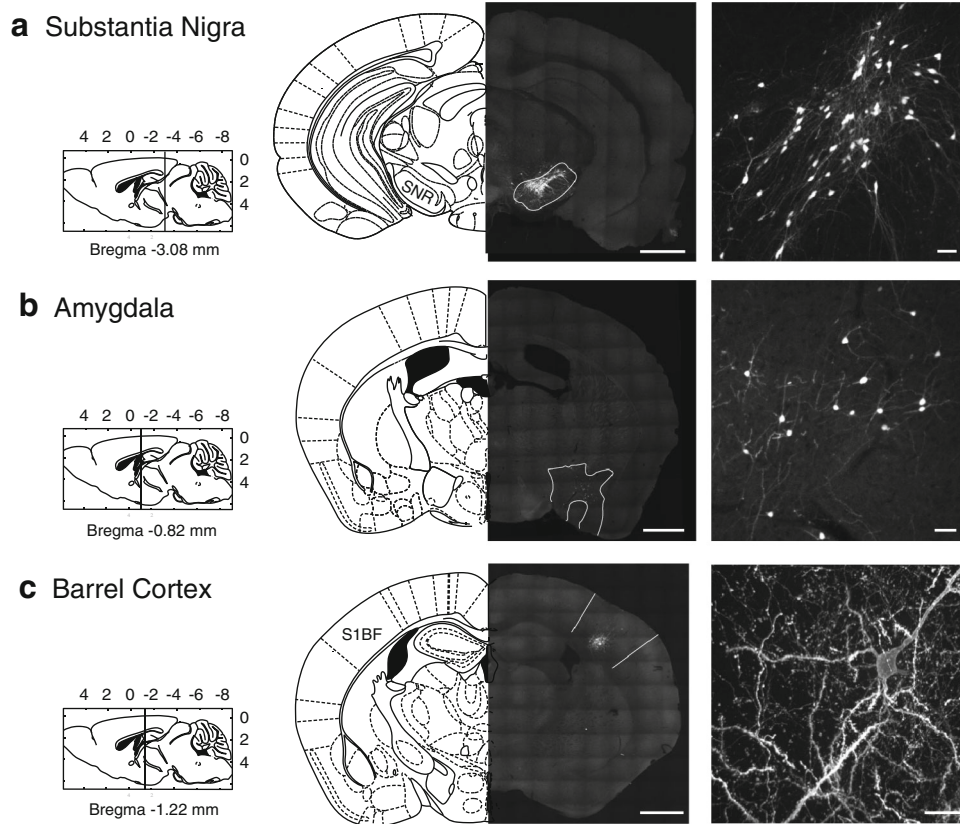
To investigate its tropism in the neocortex in greater detail, we performed injections into layer 5 of S1-BC (Fig. 6), where the composition of cell types has been previously well characterized (i.e., ∼70 % neurons vs. ∼30 % glial cells (Tsai et al. 2009; Meyer et al. 2011)). We found that ∼71 % of the labeled cells in layer 5 were neurons (and thus 29 % were glial cells). Interestingly, only 0.4 % of infected neurons were inhibitory interneurons in contrast to the ∼80 % excitatory versus ∼20 % inhibitory neurons previously reported for layer 5 of the barrel cortex (Meyer et al. 2011). This suggests a strong bias for the transduction of excitatory neurons, as previously reported for VSV-G pseudotyped lentiviral vectors (Nathanson et al. 2009). To further characterize the types of infected glial cells, we used markers for astrocytes [S100β, (Zuo et al. 2004)] and microglia [Iba1, (Schafer et al. 2012)]. We found that ∼15 % of infected cells fell into the former category (Fig. 6g–i), while virtually no microglia were labeled (data not shown). We would like to point out, however, that glial cells form a non-homogeneous group of differing origins and several markers co-exist in the various types (Cahoy et al. 2008). Our finding is therefore only the first step in characterizing the infection of various glial cell types by RABV ΔG (VSV G^RtmC). Nonetheless, our data provide evidence for the ability of pseudotyped RABV ΔG variants to infect glial cells and thus extends the range of cell types that may be amenable to manipulation with RABV ΔG.

Discussion

Here, we demonstrate the utility of RABV ΔG (VSV-G^RtmC) for neuroanatomical studies involving not only bulk populations of neurons, but also sparse or individual neurons. Our vector is exclusively anterograde, permits rapid high intensity labeling, without cytotoxic side effects and can be used over a sufficiently extended time window to permit physiological experiments. In addition, it can transduce a range of cell types/brain areas in both young and aged animals. These qualities are unequaled by any other type of viral tracer, and in addition render it useful for the study of aging or neurodegenerative disorders (Fig. 5) where age/toxicity might be a factor limiting labeling success.

We show that RABV ΔG (VSV-G^RtmC) is able to amplify sufficiently from single-particle infection of a host cell to confer the high intensity labeling necessary for automated detection of morphological features (without prior amplification of the signal) (Fig. 2). Most other viral vectors such as lentivirus and AAV do not provide sufficient labeling intensity for reconstruction upon sparse
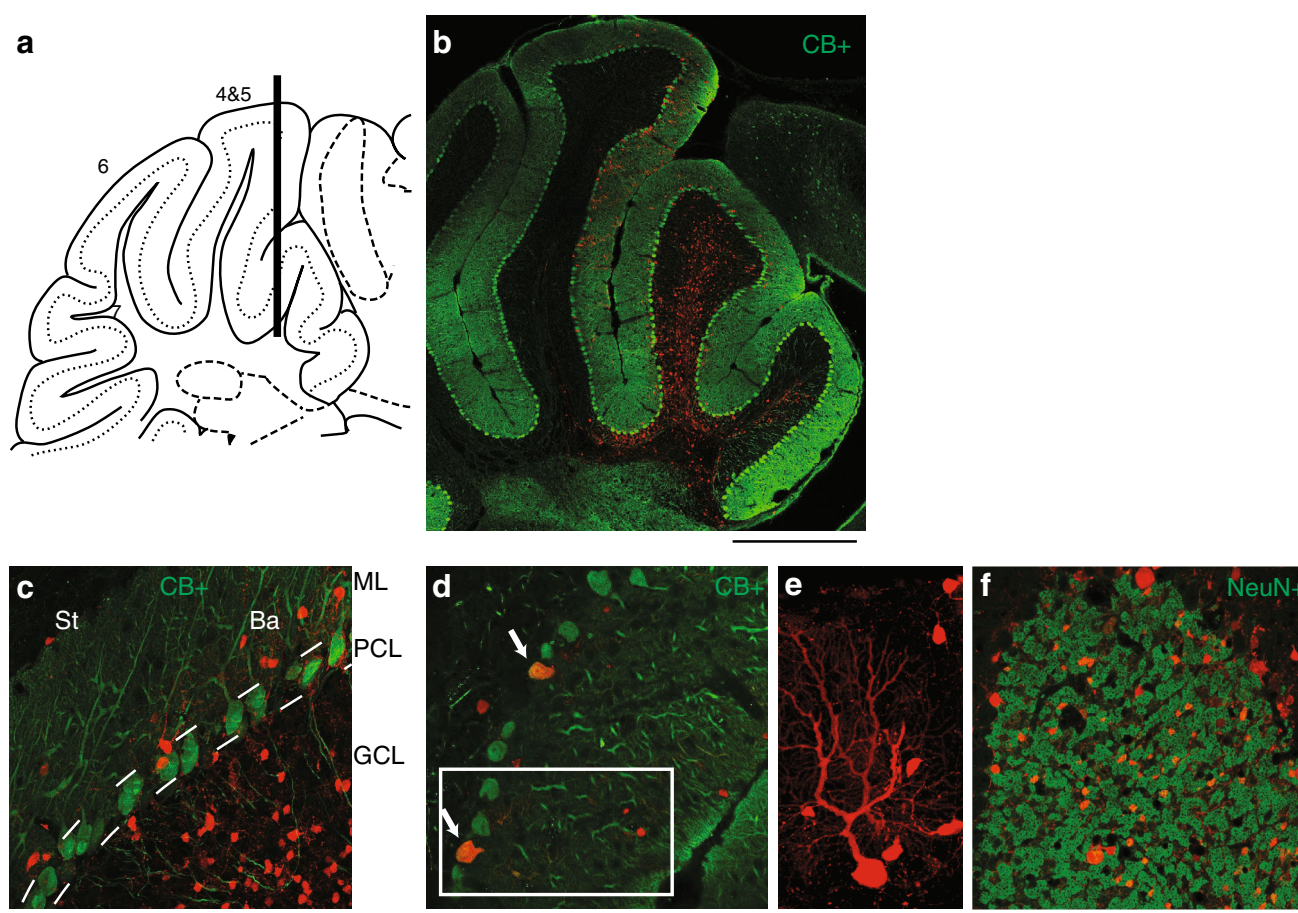
Fig. 4 Transduction in the cerebellum. A multiple-step injection at different depths was applied to investigate the transduction efficacy of RABV ΔG (VSV-G^{RtmC}) in the cerebellar cortex. **a** Injection scheme, black bar illustrates the virus injections into different depths along the needle track. **b** Injection overview of RABV ΔG (VSV-G^{RtmC}) infected cells (*red*) overlaid with calbindin- (CB+) positive cells (*green*). **b**, **c** Transduced cells were found in the molecular layer (ML), the Purkinje cell layer (PCL) and at high abundance in the granule cell layer (GCL). **c** In the molecular layer both of the inhibitory types, stellate cells (St) and basket cells (Ba) were efficiently transduced. Within the Purkinje cell layer (PCL), the calbindin (CB+) immunoreactivity (**d**) and the distinct branching pattern of the dendritic trees (**e**) confirmed the transduction of Purkinje cells. **f** Numerous labeled cells were found in the granule cell layer, where ∼80 % of the transduced cells co-labeled for NeuN indicating that the abundant granule cells are transduced efficiently. *Scale bars* 500 μm (**b**) 25 μm (**c**, **d**, **f**) and 10 μm (**e**)

infection. Indeed, only Sindbis virus (Ghosh et al. 2011) has been reported to amplify sufficiently from a single particle to allow the visualization of long-ranging axonal structures from individual neurons in 3-week-old animals. However, extreme cytotoxicity and reduced efficacy in adult animals (Chen et al. 2000) hamper the practical use of Sindbis virus for the purpose of quantitative morphological tracing.

Our vector may be regarded as a viable alternative to classical single cell labeling approaches, such as those based on biocytin delivery via patch pipettes. The latter are limited by low success rates for recovering complete axonal morphologies [e.g., ∼60 % (Oberlaender et al. 2012b)] and require histological post-processing to stain the biocytin-labeled structures. Moreover, reduced penetrability of axon bundles such as the white matter limits the success of tracing

long-range axons using biocytin-labeling (where post-processing with immunological agents is required). RABV ΔG (VSV-G^{RtmC}), on the other hand, is not affected by any of these issues (Fig. 2). In addition to the aforementioned qualities, the large size of RABV ΔG (VSV-G^{RtmC}) particles limits diffusion, allowing very targeted infection of a spatially restricted brain volume. We propose that co-injection of RABV ΔG (VSV-G^{RtmC}) variants expressing different fluorescent markers, together with large-scale reconstruction of single-cell morphology, could aid the classification of neuron types within a specific brain region or nucleus.

Recently, a glycoprotein-deleted form of another closely related rhabdovirus, the vesicular-stomatitis-virus (rVSV), has also been used as a single-cycle (i.e., non-trans-synaptic) anterograde tracer (van den Pol et al. 2009). Despite strong morphological labeling following fluorescent marker
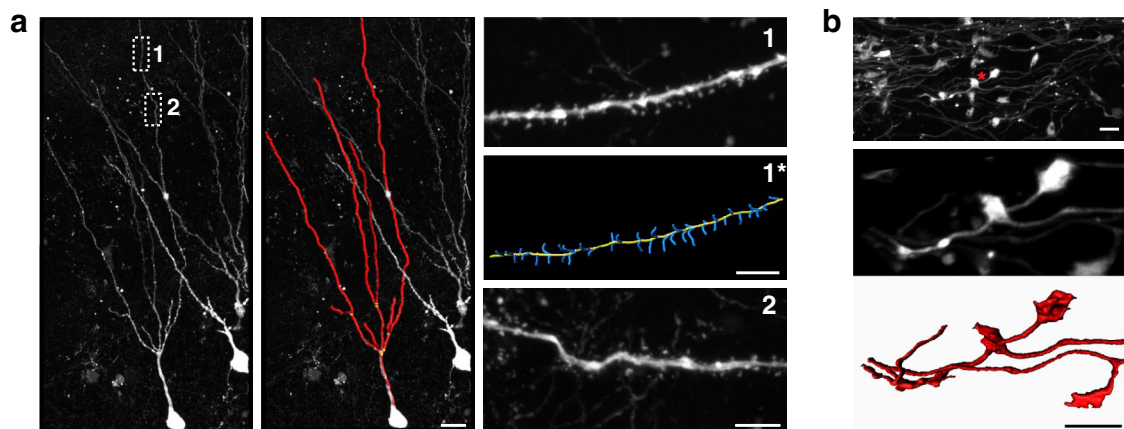
Fig. 5 Labeling and surface reconstruction in aged animals. RABV ΔG-mCherry(VSV-G^{RtmC}) infection of hippocampal dentate gyrus neurons in a 15-month-old APP/PS1 mouse—a mouse model for Alzheimer's disease—enables the fine-detailed reconstruction of dendrites and spines (**a**), as well as of axonal boutons (**b**). **a** Strong labeling facilitated automated reconstruction of the dendritic tree (*left* and *middle panel*; scale: 15 μm) and of dendritic spines (*right panels 1* and *1**; scale 5 μm) of a dentate gyrus cell using Imaris (Bitplane, Zurich, Switzerland). This labeling also revealed anatomical abnormalities like tortuous dendrites, which have previously been described as an effect of aging in humans [*right panel 2* (Tsamis et al. 2010]. **b** Similar to the dendrites/spines, the axons of granule cells (mossy fibers) and their boutons in the CA3 area of the hippocampus were strongly labeled (*upper* and *middle panel*). Automated surface reconstruction (Imaris) of an isolated mossy fiber bouton showing its fine morphological details (*lower panel*). *Scale bars* 5 μm

expression, the use of this virus is limited due to severe, fast-onset cytotoxic effects that cause shut-down of the host cell transcription and nuclear export (Faul et al. 2009). This cytotoxicity strongly restricts the time window for many anatomical/physiological studies to ∼1 day post infection, even for attenuated variants of rVSV ΔG (Beier et al. 2011).

The presumed amphotropic qualities of the chimeric VSV-G envelope protein likely enable transduction of a wider range of species and cell types than those presented here. Of note, a similar VSV-G pseudotyped RABV ΔG vector has recently been described (Gomme et al. 2010). This vector was also shown to be anterograde (Wickersham et al. 2013), although it may have a slightly different tropism due to differences in the transmembrane domain of the glycoprotein-packaging construct. Our findings, together with the latter study, suggest novel applications for RABV ΔG in addition to its use as a retrograde (Wickersham et al. 2007a) or mono-trans-synaptic tracer (Wickersham et al. 2007b). For example, RABV ΔG (VSV-G^{RtmC}) may be used to define a spatially confined starter cell population for mono-trans-synaptic tracing. It may also be employed as a tool to manipulate/monitor neural circuit activity following the expression of, for example, calcium/voltage indicators or photo-activatable channels (Osakada et al. 2011). In addition, it can be readily combined with retrogradely transducing RABV variants. Unlike other previously reported combinations of anterograde and retrograde agents, the present approach enables the exploitation of two vectors with the same diffusion characteristics, high quality of labeling and short time course for expression as shown in Fig. 1d. Lastly, this tool together with other technologies, e.g., permitting dendritic or synaptic protein profiling (Ginger et al. 2013a; Micheva et al. 2010) or gross-scale reconstruction approaches (as described here), could greatly aid the classification of cell-type identity. In conclusion, the combination of different RABV variants with optical, physiological and computational approaches, offers a wide range of possibilities for the investigation of the structure–function relationship of neuronal circuits.

Methods

Engineering of the hybrid glycoprotein

The chimeric VSV/SAD G (VSV G^{RtmC}) cDNA was constructed to encode the ectodomain (aa 1–454) of VSV Indiana G (kindly provided by Dr. John K. Rose) fused to the entire transmembrane and cytoplasmic domain (amino acids 450–524) (Mebatsion et al. 1995) of RABV SAD G. This construct differs from the packaging construct employed by Wickersham et al. (2013), which contained the surface- and trans-membrane domain of the VSV glycoprotein and cytoplasmic domain of the RABV glycoprotein.

Virus production

The production of G-gene deficient RABV SAD ΔG-eGFP and SAD ΔG-mCherry was described previously (Wickersham et al. 2007a). SAD ΔG myr-TdTom was constructed in the same way to encode a protein in which two
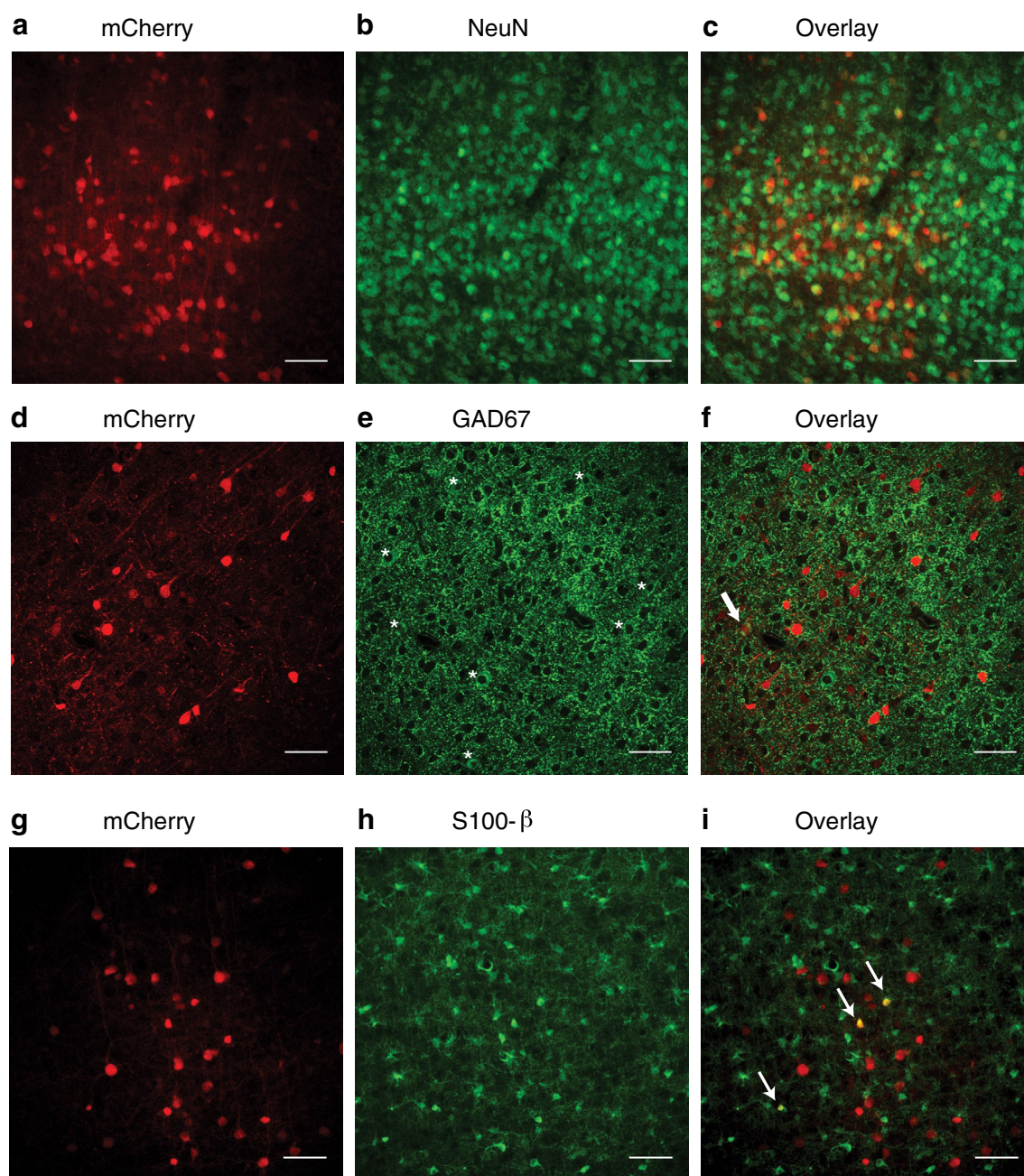
Fig. 6 Tropism of RABV ΔG (VSV-G^{RtmC}) in CNS. Determination of cell-type identity of RABV ΔG (VSV-G^{RtmC}) infected mCherry expressing cells in layer 5 of the barrel cortex (representative images in **a**, **d** and **g**) in 50-μm-thick sections using immunohistochemistry against NeuN (total neuron marker; **b**), GAD67 (marker of inhibitory interneurons; **e**) and S-100β (marker of astrocytes, **h**). Overlay of mCherry and cell-specific marker (**c**, **f** and **i**). Images are either max projections (**a–c**, **g–i**) derived from selected planes of a multi-plane image stack or a single plane (**d–f**) obtained from laser scanning confocal microscopy. *Stars* in panel **e** indicate GAD67 positive cells. A single mCherry-/GAD67 positive neuron is indicated by an *arrow* in (**f**). *Arrows* in panel **i** indicate mCherry-/S-100β positive cells. *Scale bars* 50 μm

tandem copies of a myristoylation signal are fused to tdTomato for membrane targeting (Trichas et al. 2008).

Stocks of VSV G^{RtmC}-pseudotyped rabies viruses [hereafter referred to as RABV ΔG XFP (VSV G^{RtmC})] were prepared essentially as described in (Rancz et al. 2011), with the exception that BSR T7/5 cells (Buchholz et al. 1999) were used instead of BHK-21 cells and pCAGGS VSV/SAD G was used as the transcomplementing plasmid. Cells were replated 24 h after infection with the initial starter stock and the supernatant media discarded and replaced with new media. VSV G^{RtmC}-pseudotyped virus was harvested 3 days post

infection. Titers of the different variants of pseudotyped rabies virus were in the range of 2×10^6–5×10^7 infectious particles/ml, estimated by serial dilution and infection of the BHK-21 cell line.

Stereotaxic injections

All experimental procedures were performed in accordance with French law and the European Directive covering the use of experimental animals (2010/63/EU) and approved by the Ethics Committee of Bordeaux (approval # 5012024-A). Stereotaxic injections were performed as previously described (Cetin et al. 2006) in C57Bl/6 J mice (aged 1–15 months) or in 15-month-old APP/PS1 mice [a mouse model for Alzheimer's disease (Reiserer et al. 2007)]. In brief, viral vectors were injected into the brains of isoflurane anesthetized and head-fixed mice using a 10-µl glass syringe fitted with a 35-gauge needle or a pulled glass pipette. Volume and speed of the injections were controlled using a WPI Ultra Micro Pump. The stereotaxic coordinates were as follows: (1) Thalamic ventral posteromedial (VPm) nucleus: anterior/posterior (A/P) −1.70 mm, lateral (L) 1.60 mm, dorso/ventral (D/V) 3.20 mm; (2) thalamic posteromedial (POm) nucleus: A/P −1.80 mm, L 1.25 mm, D/V 2.75 mm; (3) hippocampal dentate gyrus (DG): A/P −1.90 mm, L 1.20 mm, D/V 1.90 mm; (4) layer 5 (L5) of primary somatosensory barrel cortex (BC): A/P −0.94 mm, L 3.00 mm, D/V 0.80 mm; (5) cerebellum: A/P −5.68 mm, L 0.68 mm, D/V 1.70–0 mm (6) amygdala: A/P −0.82 mm, L 2.45 mm, D/V 4.75 mm; (7) substantia nigra: A/P −3.00 mm, L 1.56 mm, D/V 4.1 mm. A/P and L coordinates are given with respect to the bregma, D/V coordinates with respect to the brain surface. Injection volumes were 200–600 nl for RABV ΔG XFP (VSV G^{RtmC}), 400 nl for AAV (diluted 1/50) and 600 nl for lentivirus. Sparse labeling was achieved by diluting anterograde rabies virus to titers of $\sim 2 \times 10^4$ infectious particles/ml and injection of 250 nl, which resulted in injection of 5–10 infectious particles.

Mouse perfusion and brain sectioning

Mice were deeply anesthetized with a lethal dose of sodium pentobarbital and then transcardially perfused with 30 ml normal Ringer's solution (135 mM NaCl, 5.4 mM KCl, 1 mM CaCl$_2$, 1.8 mM MgCl$_2$, 5 mM HEPES, pH 7.4) followed by 100 ml of a 4 % PFA solution (prepared in 1× phosphate buffered saline (PBS, pH 7.4). Fixed brains were dissected and postfixed in 4 % PFA solution for either 24 h, or 6 h in the case where immunohistology was performed. Free-floating slices (50 µm) were cut using a vibratome (Leica).

Immunohistological determination of the cellular tropism of RABVΔG(VSV-G^{RtmC})

Cell types were identified using antibodies against NeuN (dilution: 1:500; Millipore, clone A60, MAB377) to mark neurons, the 67 kDa isoform of glutamate decarboxylase GAD67 (1:1,500 dilution; Millipore, clone 1G10.2, MAB5406) to label GABAergic neurons (Meyer et al. 2011), S100β (1:1,500; Sigma S2532) to mark astrocytes (Zuo et al. 2004), or against Iba1 (1:500; Wako Cat. #019-19741) to mark microglia (Schafer et al. 2012). NeuN and S100β were detected using Alexa488-conjugated goat anti-mouse H + L (Life technologies), and GAD67 was detected using Alexa647-conjugated goat anti-mouse (subtype IgG2A) (Life technologies).

Immunohistochemical protocols were adapted from Meyer et al. (2011). In brief, free-floating slices were blocked with MOM blocking reagent (Vector Labs) (1 h) in the presence of 0.5 % triton X-100, then for 30 min in 3 % BSA, 4 % NGS, 0.5 % triton in 1× PBS. Slices were incubated 40 h with the primary antibody in 3 % BSA, 2 % NGS in 1× PBS at 4 °C, washed two times with 0.1 M PB then two times with 0.1 M PB + 1 % NGS. Slices were then incubated 2 h at RT with the secondary antibody (1:500) in the presence of 0.3 % triton X-100, washed five times with 0.1 M PB, counter-stained with TO-PRO-3 to label nuclei (1:5,000; Life Technologies), and mounted in prolong gold mounting media. The number of RABV ΔG (VSV G^{RtmC}) transduced cells expressing cell-type specific markers was quantified by manually counting the immunohistochemically stained cells in confocal images stacks.

High-resolution microscopy, tracing and quantification

For reconstruction of thalamic neurons, images were acquired using a prototype confocal laser scanning system (based on LAS AF SP5, Leica Microsystems), equipped with a glycerol immersion objective (HCX PL APO 63x, 1.2 N.A.), a tandem scanning system (Resonance Scanner), spectral detectors with hybrid technology (GaAsP photocathode), and mosaic scanning software [Matrix Screener (beta-version), provided by Frank Sieckmann, Leica Microsystems]. Mosaic image stacks of volumes up to 2 mm × 2 mm × 0.05 mm (in thalamus) and 0.6 × 0.6 × 0.05 mm (in cortex) were acquired at a resolution of 0.094 µm × 0.094 µm × 0.5 µm per voxel (2.5× digital zoom, 8× line average, 8 kHz scanning speed, $\sim 20 \times 20$ and $\sim 6 \times 6$ fields of view in thalamus and cortex, respectively) for each of 12 consecutive 50-µm-thick brain sections. 3D reconstructions were performed using previously described automated tracing algorithms (Oberlaender et al. 2007). Automated tracings were proof-edited (Dercksen et al. 2012) and semi-automatically aligned

across brain sections (Dercksen et al. 2009) using Amira Visualization Software (Visage Imaging).

All remaining images were acquired using either a commercial confocal microscope (Leica SP5) or a commercial spinning disk system (Leica SP2). Hippocampal mossy fiber boutons were reconstructed from image stacks using the Imaris surface tool (Bitplane, Zurich, Switzerland). To compare the fluorescence intensities and signal-to-noise ratios of RABV ΔG (VSV G^{RtmC}), lentivirus-(LV), and adeno-associated virus (AAV) infected brain sections were imaged with identical microscopy settings. Image stacks were acquired at 16 bit-depth at a resolution of 141.47 nm × 141.47 nm × 125.89 nm per voxel (63× magnification, 1.7× digital zoom, 1024 × 1024 pixel per image, 3× line average, 700 Hz scanning speed). Cellular somata were detected automatically in these 3D image stacks using Imaris, and the maximum fluorescence intensity of the somata was quantified as arbitrary unit (0–65536 levels of grey) from 16 bit images. Background levels were calculated for each image stack as the average mean intensity value of several larger distributed areas devoid of any cellular processes (i.e., signal). For illustration purposes, the intensity levels of all three images in Fig. 1b were enhanced to the same extent. Cell counts for immunological cell-type characterizations were performed manually with the use of Amira Visualization Software (Visage Imaging) on confocal image stacks.

Fluorescence intensity comparison

Fluorescence intensities were compared using brains of mice injected at 4 months of age with either lentivirus (MND-eGFP-WPRE, a kind gift of Dr. N. Abrous), AAV 2/9 CAG eGFP-WPRE (Penn Vector Core), or RABV ΔG-eGFP(VSV G^{RtmC}). Injected animals were killed at 6 days post infection (RABV ΔG), 12 days post infection (lentivirus), or 22 days post infection (AAV). eGFP-labeled cells were imaged and analyzed as described above.

Statistics

Significance was evaluated using one-way ANOVA followed by a post hoc Tukey test for multiple comparisons using GraphPad Prism 6 software (San Diego, CA). *** $p < 0.001$. Data are represented as mean ± SEM.

References

Beier KT, Saunders A, Oldenburg IA, Miyamichi K, Akhtar N, Luo L, Whelan SP, Sabatini B, Cepko CL (2011) Anterograde or retrograde transsynaptic labeling of CNS neurons with vesicular stomatitis virus vectors. Proc Natl Acad Sci USA 108(37): 15414–15419

Buchholz UJ, Finke S, Conzelmann KK (1999) Generation of bovine respiratory syncytial virus (BRSV) from cDNA: BRSV NS2 is not essential for virus replication in tissue culture, and the human RSV leader region acts as a functional BRSV genome promoter. J Virol 73(1):251–259

Burns JC, Friedmann T, Driever W, Burrascano M, Yee JK (1993) Vesicular stomatitis virus G glycoprotein pseudotyped retroviral vectors: concentration to very high titer and efficient gene transfer into mammalian and nonmammalian cells. Proc Natl Acad Sci USA 90(17):8033–8037

Cahoy JD, Emery B, Kaushal A, Foo LC, Zamanian JL, Christopherson KS, Xing Y, Lubischer JL, Krieg PA, Krupenko SA, Thompson WJ, Barres BA (2008) A transcriptome database for astrocytes, neurons, and oligodendrocytes: a new resource for understanding brain development and function. J Neurosci 28(1):264–278

Callaway EM (2008) Transneuronal circuit tracing with neurotropic viruses. Curr Opin Neurobiol 18(6):617–623

Cetin A, Komai S, Eliava M, Seeburg PH, Osten P (2006) Stereotaxic gene delivery in the rodent brain. Nat Protoc 1(6):3166–3173

Chen BE, Lendvai B, Nimchinsky EA, Burbach B, Fox K, Svoboda K (2000) Imaging high-resolution structure of GFP-expressing neurons in neocortex in vivo. Learn Mem 7(6):433–441

Choi J, Young JA, Callaway EM (2010) Selective viral vector transduction of ErbB4 expressing cortical interneurons in vivo with a viral receptor-ligand bridge protein. Proc Natl Acad Sci USA 107(38):16703–16708

da Costa NM, Martin KA (2013) Sparse reconstruction of brain circuits: or, how to survive without a microscopic connectome. Neuroimage 80:27–36

Dercksen VJ, Weber B, Guenther D, Oberlaender M, Prohaska S, Hege HC (2009) Automatic Alignment of Stacks of Filament Data. IEEE Int Symp on Biomedical Imaging: From Nano to Macro (ISBI) 971-974

Dercksen VJ, Oberlaender M, Sakmann B, Hege HC (2012) Interactive visualization: a key prerequisite for reconstruction

of anatomically realistic neural networks. Proceedings of the 2009 Workshop on Visualization in medicine and life sciences (VMLS 09)

Deschenes M, Veinante P, Zhang ZW (1998) The organization of corticothalamic projections: reciprocity versus parity. Brain Res Brain Res Rev 28(3):286–308

Douglas RJ, Martin KA (2004) Neuronal circuits of the neocortex. Annu Rev Neurosci 27:419–451

Faul EJ, Lyles DS, Schnell MJ (2009) Interferon response and viral evasion by members of the family rhabdoviridae. Viruses 1(3):832–851

Finkelshtein D, Werman A, Novick D, Barak S, Rubinstein M (2013) LDL receptor and its family members serve as the cellular receptors for vesicular stomatitis virus. Proc Natl Acad Sci USA 110(18):7306–7311

Ghosh S, Larson SD, Hefzi H, Marnoy Z, Cutforth T, Dokka K, Baldwin KK (2011) Sensory maps in the olfactory cortex defined by long-range viral tracing of single neurons. Nature 472(7342): 217–220

Ginger M, Broser P, Frick A (2013a) Three-dimensional tracking and analysis of ion channel signals across dendritic arbors. Front Neural Circuits 7:61

Ginger M, Haberl M, Conzelmann KK, Schwarz MK, Frick A (2013b) Revealing the secrets of neuronal circuits with recombinant rabies virus technology. Front Neural Circuits 7:2

Gomme EA, Faul EJ, Flomenberg P, McGettigan JP, Schnell MJ (2010) Characterization of a single-cycle rabies virus-based vaccine vector. J Virol 84(6):2820–2831

Helmstaedter M (2013) Cellular-resolution connectomics: challenges of dense neural circuit reconstruction. Nat Methods 10(6): 501–507

Larsen DD, Wickersham IR, Callaway EM (2007) Retrograde tracing with recombinant rabies virus reveals correlations between projection targets and dendritic architecture in layer 5 of mouse barrel cortex. Front Neural Circuits 1:5

Lichtman JW, Denk W (2011) The big and the small: challenges of imaging the brain's circuits. Science 334(6056):618–623

Mebatsion T, Schnell MJ, Conzelmann KK (1995) Mokola virus glycoprotein and chimeric proteins can replace rabies virus glycoprotein in the rescue of infectious defective rabies virus particles. J Virol 69(3):1444–1451

Mebatsion T, Finke S, Weiland F, Conzelmann KK (1997) A CXCR4/CD4 pseudotype rhabdovirus that selectively infects HIV-1 envelope protein-expressing cells. Cell 90(5):841–847

Meyer HS, Schwarz D, Wimmer VC, Schmitt AC, Kerr JN, Sakmann B, Helmstaedter M (2011) Inhibitory interneurons in a cortical column form hot zones of inhibition in layers 2 and 5A. Proc Natl Acad Sci USA 108(40):16807–16812

Micheva KD, Busse B, Weiler NC, O'Rourke N, Smith SJ (2010) Single-synapse analysis of a diverse synapse population: proteomic imaging methods and markers. Neuron 68(4):639–653

Nathanson JL, Yanagawa Y, Obata K, Callaway EM (2009) Preferential labeling of inhibitory and excitatory cortical neurons by endogenous tropism of adeno-associated virus and lentivirus vectors. Neuroscience 161(2):441–450

Nhan HL, Callaway EM (2012) Morphology of superior colliculus- and middle temporal area-projecting neurons in primate primary visual cortex. J Comp Neurol 520(1):52–80

Oberlaender M, Bruno RM, Sakmann B, Broser PJ (2007) Transmitted light brightfield mosaic microscopy for three-dimensional tracing of single neuron morphology. J Biomed Opt 12(6): 064029

Oberlaender M, Boudewijns ZS, Kleele T, Mansvelder HD, Sakmann B, de Kock CP (2011) Three-dimensional axon morphologies of individual layer 5 neurons indicate cell type-specific intracortical

pathways for whisker motion and touch. Proc Natl Acad Sci USA 108(10):4188–4193

Oberlaender M, de Kock CP, Bruno RM, Ramirez A, Meyer HS, Dercksen VJ, Helmstaedter M, Sakmann B (2012a) Cell type-specific three-dimensional structure of thalamocortical circuits in a column of rat vibrissal cortex. Cereb Cortex 22(10):2375–2391

Oberlaender M, Ramirez A, Bruno RM (2012b) Sensory experience restructures thalamocortical axons during adulthood. Neuron 74(4):648–655

Ohara S, Inoue K, Witter MP, Iijima T (2009) Untangling neural networks with dual retrograde transsynaptic viral infection. Front Neurosci 3(3):344–349

Osakada F, Mori T, Cetin AH, Marshel JH, Virgen B, Callaway EM (2011) New rabies virus variants for monitoring and manipulating activity and gene expression in defined neural circuits. Neuron 71(4):617–631

Parekh R, Ascoli GA (2013) Neuronal morphology goes digital: a research hub for cellular and system neuroscience. Neuron 77(6):1017–1038

Rancz EA, Franks KM, Schwarz MK, Pichler B, Schaefer AT, Margrie TW (2011) Transfection via whole-cell recording in vivo: bridging single-cell physiology, genetics and connectomics. Nat Neurosci 14(4):527–532

Reiserer RS, Harrison FE, Syverud DC, McDonald MP (2007) Impaired spatial learning in the APPSwe + PSEN1DeltaE9 bigenic mouse model of Alzheimer's disease. Genes Brain Behav 6(1):54–65

Schafer DP, Lehrman EK, Kautzman AG, Koyama R, Mardinly AR, Yamasaki R, Ransohoff RM, Greenberg ME, Barres BA, Stevens B (2012) Microglia sculpt postnatal neural circuits in an activity and complement-dependent manner. Neuron 74(4):691–705

Svoboda K (2011) The past, present, and future of single neuron reconstruction. Neuroinformatics 9(2–3):97–98

Trichas G, Begbie J, Srinivas S (2008) Use of the viral 2A peptide for bicistronic expression in transgenic mice. BMC Biol 6:40

Tsai PS, Kaufhold JP, Blinder P, Friedman B, Drew PJ, Karten HJ, Lyden PD, Kleinfeld D (2009) Correlations of neuronal and microvascular densities in murine cortex revealed by direct counting and colocalization of nuclei and vessels. J Neurosci 29(46):14553–14570

Tsamis IK, Mytilinaios GD, Njau NS, Fotiou FD, Glaftsi S, Costa V, Baloyannis JS (2010) Properties of CA3 dendritic excrescences in Alzheimer's disease. Curr Alzheimer Res 7(1):84–90

van den Pol AN, Ozduman K, Wollmann G, Ho WS, Simon I, Yao Y, Rose JK, Ghosh P (2009) Viral strategies for studying the brain, including a replication-restricted self-amplifying delta-G vesicular stomatis virus that rapidly expresses transgenes in brain and can generate a multicolor golgi-like expression. J Comp Neurol 516(6):456–481

Wickersham IR, Finke S, Conzelmann KK, Callaway EM (2007a) Retrograde neuronal tracing with a deletion-mutant rabies virus. Nat Methods 4(1):47–49

Wickersham IR, Lyon DC, Barnard RJ, Mori T, Finke S, Conzelmann KK, Young JA, Callaway EM (2007b) Monosynaptic restriction of transsynaptic tracing from single, genetically targeted neurons. Neuron 53(5):639–647

Wickersham IR, Sullivan HA, Seung HS (2013) Axonal and subcellular labelling using modified rabies viral vectors. Nat Commun 4:2332

Zuo Y, Lubischer JL, Kang H, Tian L, Mikesh M, Marks A, Scofield VL, Maika S, Newman C, Krieg P, Thompson WJ (2004) Fluorescent proteins expressed in mouse transgenic lines mark subsets of glia, neurons, macrophages, and dendritic cells for vital examination. J Neurosci 24(49):10999–11009

Research Article

Insulin-like growth factor 2 reverses memory and synaptic deficits in APP transgenic mice

Maria Pascual-Lucas[1], Silvia Viana da Silva[2], Marianna Di Scala[3], Carolina Garcia-Barroso[1], Gloria González-Aseguinolaza[3], Christophe Mulle[2], Cristina M Alberini[4], Mar Cuadrado-Tejedor[1,5] & Ana Garcia-Osta[1,*]

Abstract

Insulin-like growth factor 2 (IGF2) was recently found to play a critical role in memory consolidation in rats and mice, and hippocampal or systemic administration of recombinant IGF2 enhances memory. Here, using a gene therapy-based approach with adeno-associated virus (AAV), we show that IGF2 overexpression in the hippocampus of aged wild-type mice enhances memory and promotes dendritic spine formation. Furthermore, we report that IGF2 expression decreases in the hippocampus of patients with Alzheimer's disease, and this leads us to hypothesize that increased IGF2 levels may be beneficial for treating the disease. Thus, we used the AAV system to deliver IGF2 or IGF1 into the hippocampus of the APP mouse model Tg2576 and demonstrate that IGF2 and insulin-like growth factor 1 (IGF1) rescue behavioural deficits, promote dendritic spine formation and restore normal hippocampal excitatory synaptic transmission. The brains of Tg2576 mice that overexpress IGF2 but not IGF1 also show a significant reduction in amyloid levels. This reduction probably occurs through an interaction with the IGF2 receptor (IGF2R). Hence, IGF2 and, to a lesser extent, IGF1 may be effective treatments for Alzheimer's disease.

Introduction

Alzheimer's disease (AD) is the most common form of dementia in the elderly. There is currently no efficacious treatment for the disease. AD is characterized by β-amyloid (Aβ) accumulation (senile plaques), abnormal phosphorylation and aggregation of the microtubule-associated protein tau, synaptic dysfunction and neuronal death (Selkoe, 2011). Furthermore, several studies show that the accumulation of soluble forms of Aβ correlates with synapse dysfunction and loss (Shankar et al, 2007), which appears to occur relatively early in the disease, prior to cell death. Hence, agents that reverse synapse impairments and Aβ accumulation represent promising therapeutic candidates for the treatment and/or prevention of AD.

Recent studies in rodents have provided evidence of an important role for hippocampal insulin-like growth factor 2 (IGF2) in brain plasticity and learning and memory (Chen et al, 2011; Schmeisser et al, 2012). Moreover, recombinant IGF2 injected into the hippocampus significantly enhances memory retention and persistence (Chen et al, 2011). Systemic treatments with IGF2 significantly enhance hippocampal-cortical-dependent memories, including those known to be impaired in rodent models of AD (Stern et al, 2014). This would suggest that IGF2 is an interesting candidate for the treatment of cognitive impairment in AD. Furthermore, the formation and maturation of synapses in the hippocampus, a mechanism that is impaired in AD (Jacobsen et al, 2006; Smith et al, 2009; Ricobaraza et al, 2012) and depends on IGF2/IGF2R signalling, may underlie the IGF2-dependent memory enhancement effect (Schmeisser et al, 2012).

Unlike IGF2, insulin-like growth factor 1 (IGF1) has previously been researched as a potential treatment for AD. Studies have demonstrated that increasing levels of circulating IGF1 lowers amyloid β (Aβ) levels in the brain (Carro et al, 2002). This effect may be the result of the reduced serum-to-cerebrospinal fluid (CSF) traffic of IGF1 reported in both patients with AD (Johansson et al, 2013) and AD mouse models (Trueba-Saiz et al, 2013). However, other authors have demonstrated that reducing IGF1 receptor signalling protects against Aβ toxicity in different AD models (Cohen et al, 2009; Freude et al, 2009).

Based on current knowledge of the effects of IGF2 on synaptogenesis, brain plasticity and memory, we hypothesized that increasing IGF2 expression in the hippocampus may attenuate the memory

1 Neurosciences Division, Center for Applied Medical Research, CIMA, University of Navarra, Pamplona, Spain
2 Interdisciplinary Institute for Neuroscience, Université of Bordeaux, CNRS UMR 5297, Bordeaux, France
3 Gene Therapy and Hepatology Division, Center for Applied Medical Research, CIMA, University of Navarra, Pamplona, Spain
4 Center for Neural Science, New York University, New York, NY, USA
5 Department of Anatomy, School of Medicine, University of Navarra, Pamplona, Spain
*Corresponding author. Tel: +1 34 948 19 47 00 (2023); Fax: +1 34 948 19 47 15; E-mail: agosta@unav.es

deficits and synaptic dysfunction that occur in AD. We therefore analysed the expression of IGF2 in AD brains and employed an adeno-associated viral (AAV) vector gene-delivery system to express IGF2 in the hippocampus of the transgenic mouse model Tg2576 to test their effect on the behavioural, cellular and synaptic phenotypes typical of AD. The effects were compared to a group of animals injected with AAV expressing IGF1, since no memory enhancement effect has been attributed to this growth factor (Chen *et al*, 2011).

Results

AAV8-mediated expression of IGF2 reverses both memory and dendritic spine density impairments in aged wild-type mice

Since IGF2 has a role in memory processes, we studied whether age-related memory loss may be associated with changes in hippocampal IGF2 levels. By using quantitative Western blot analysis, the effect of age on endogenous IGF2 levels was measured in the hippocampus of 15-month-old versus 7-month-old wild-type (WT) animals. Interestingly, as depicted in Fig 1A, the levels of endogenous IGF2 were significantly reduced with age in mice hippocampi. Next, we analysed whether restoring IGF2 levels could be effective in reversing age-related memory deficits. To achieve this, we studied whether the overexpression of hippocampal IGF2 could enhance memory in aged WT mice compared to the overexpression of IGF1. AAV vectors are widely used for gene transfer into the central nervous system (CNS), since they induce efficient and long-term transduction of non-dividing cells with no toxicity and a low immune reaction (Burger *et al*, 2005; Mandel *et al*, 2006). We chose AAV8 serotype, an efficient serotype that is non-toxic to neurons, to express IGF2 and IGF1 into the hippocampus (Cearley & Wolfe, 2006; Klein *et al*, 2006; Malik *et al*, 2012). AAV vectors encoding green fluorescent protein (GFP), IGF2 or IGF1 were developed as described in the Materials and Methods section and bilaterally injected into the hippocampus of 18-month-old WT mice. Two months later, AAV-GFP mice were euthanized to confirm the

transduction efficiency of the AAV serotype in the hippocampus (Supplementary Fig S1). Long-term neuronal expression of GFP in the cell bodies of pyramidal CA1 neurons in the dorsal hippocampus and the neuropil was detected (Fig 1B). Hippocampal neurons interact extensively with neurons in the entorhinal cortex (EC), a brain area that shows early signs of AD pathology and abundant amyloid plaques (Gomez-Isla *et al*, 1996). The expression of growth factors in the EC could contribute to their therapeutic potential. Interestingly, we found that some neurons in the EC of injected mice expressed GFP, which would indicate that the AAV delivered into the hippocampus infected and transduced cells in the EC. No signal was detected in non-infected mice (Fig 1B).

To verify the viral expression of IGFs in the hippocampus of AAV-IGF-injected mice, PCRs were performed on the IGFs 3 months after the injections and compared to similar PCRs conducted on sham-injected mice. We performed conventional PCR using a 5′ primer designed against the 5′ end of the corresponding IGF cDNA and a 3′ primer aligned to the 3′ UTR-polyadenylation signal sequence of the recombinant IGF, which differs from that of the naturally expressed IGF mRNA (see Materials and Methods). As shown in Fig 1C, AAV-IGF-injected mice had an amplified band that corresponded to the IGF expression in the hippocampus of injected mice (lanes 3 and 4). No band was detected in sham-injected hippocampi (sham, lanes 1 and 2).

Western blot analysis of hippocampal protein extracts obtained from WT mice (sham-injected) or injected with AAV-IGF2 and euthanized 3 months later revealed that hippocampal AAV-IGF2 administration resulted in a marked accumulation of IGF2 compared to sham-injected animals, and this lasted up to 3 months (Fig 1D). Unfortunately, the IGF1 levels could not be determined by Western blot analysis, since no specific and sensitive antibody was available.

The memory capacity of aged AAV-IGF-treated mice was assessed using the fear-conditioning paradigm and the Morris water maze (MWM) test. The effects of AAV-mediated IGF1 and IGF2 expression on fear learning were tested in 20-month-old WT mice (2 months after the AAV injection). Animals were subjected to the milder single CS-US pairing protocol, which made it possible to detect subtler

---

Figure 1. AAV8-mediated expression of IGF2 reverses both memory and dendritic spine density impairments in aged wild-type (WT) mice.

A Quantitative Western blot analysis of hippocampal extracts that reveal a decrease in IGF2 in the hippocampus of aged (15-month-old) WT mice compared to 7-month-old WT animals. Data are expressed as arbitrary units (mean $\pm$ SEM) with respect to the WT 7-month-old mice (unpaired two-tailed Student's *t*-test, $n = 4$, **$P = 0.01$).

B Two months after the intrahippocampal administration of AAV8-GFP, GFP was detected in the pyramidal cells of CA1 and in neurons of the entorhinal cortex (Cx). No signal was detected in sham-injected animals. Scale bar = 10 μm.

C Gel analysis of PCR products obtained with the primers designed to determine the presence of AAV-mediated expression of IGF1 or IGF2 (WT AAV-IGF) in the hippocampus of WT mice. No band was detected in the sham-injected mice (WT sham).

D Western blot analysis of hippocampal extracts that reveal the overexpression of the IGF2 protein in the AAV-IGF2-injected mice compared to the sham-injected animals.

E Contextual freezing responses of aged WT mice 2 months after AAV-IGF2 injection (WT IGF2) showed a significant enhancement of memory retention measured as % freezing compared to the sham-injected mice (WT). In this, and all subsequent figures, results are expressed as mean $\pm$ SEM (Kruskal–Wallis followed by Mann–Whitney *U*-test, $n = 10$–12, **$P = 0.0074$).

F Escape latency to the hidden platform in the Morris water maze test for aged WT, WT IGF1 and WT IGF2 mice. Latency to reach the platform decreased in every group as the training sessions progressed (non-parametric Friedman test, $n = 10$–12, **$P = 0.0029$ WT, *$P = 0.05$ WT IGF1, ***$P = 0.00026$ WT IGF2). No differences were observed among the groups.

G Percentage of time spent searching for the target quadrant in the probe test (on days 4, 7 and 9). On days 4 and 9, WT IGF2 mice showed significant improvement in memory retention, measured as % of time spent in the right quadrant, compared to WT mice (one-way ANOVA followed by Scheffe's *post hoc* test, $n = 10$–12, *$P = 0.043$ day 4, *$P = 0.050$ day 9).

H Representative images of Golgi-impregnated apical dendrites of CA1 hippocampal pyramidal neurons. Scale bar = 10 μm (left panel). Quantification of overall spine density in 20-month-old WT mice (right panel). Spine density significantly increased in WT IGF1 and WT IGF2 mice compared to sham WT mice (Kruskal–Wallis followed by Mann–Whitney *U*-test, $n = 36$ neurons, *$P = 0.025$ WT versus WT IGF1, ***$P = 1.03E\text{-}11$ WT versus WT IGF2. The increase was greater for WT IGF2 mice, where spine density significantly increased compared to WT IGF1 (***$P = 4.70E\text{-}08$).
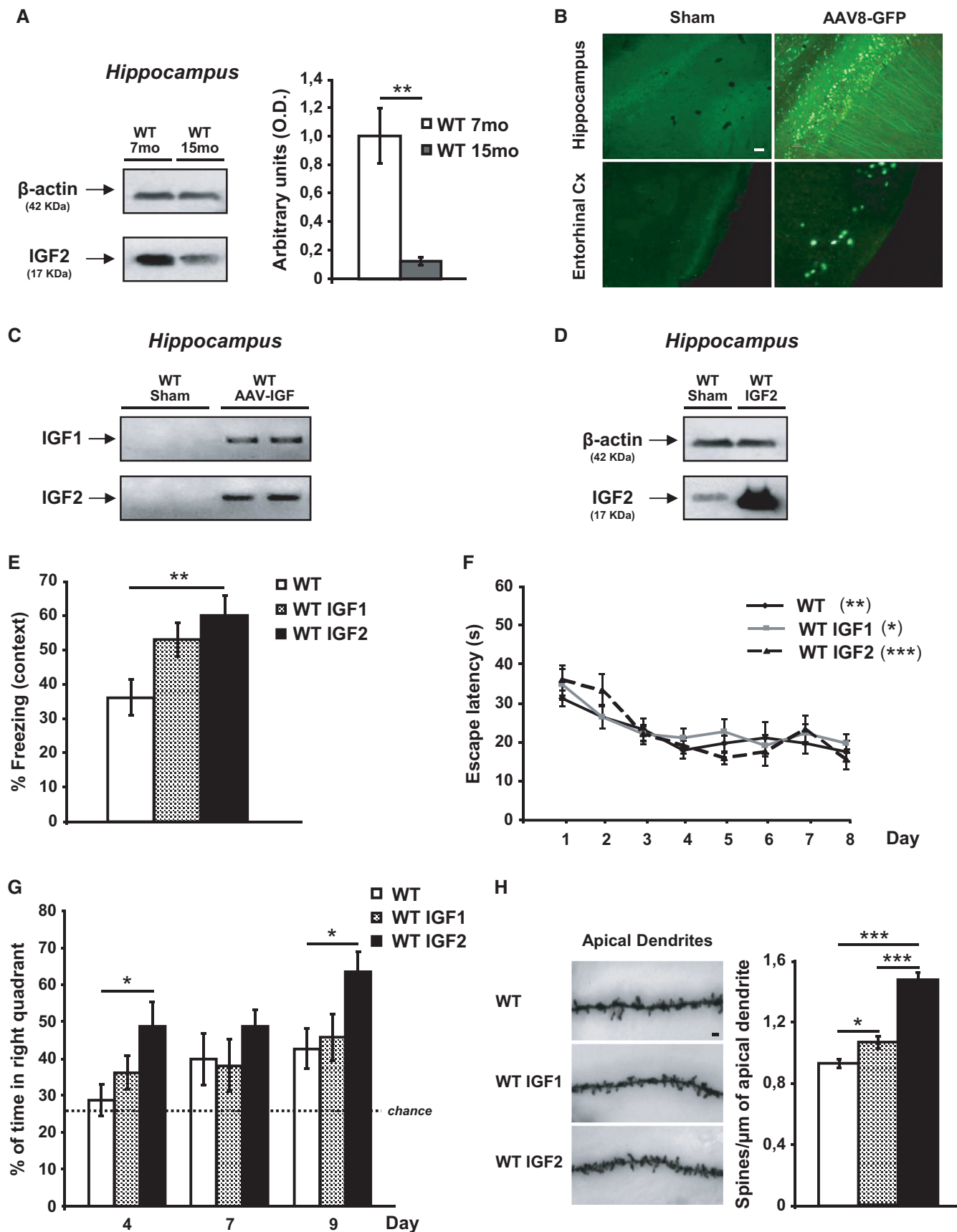
Figure 1.

learning deficits. Freezing responses were significantly enhanced by AAV-IGF2 compared to sham mice. AAV-IGF1-treated mice showed weaker memory enhancement (Fig 1E). These results demonstrate that IGF2 treatment reverses age-related defects in associative learning, which would suggest that synaptic function is enhanced.

The effect of IGF1 and/or IGF2 on MWM learning and spatial memory was also assessed in the mice. No significant differences were observed among the groups during the visible-platform training phase, which would indicate that the animals' ability to perform the task was similar. The groups did not differ in their swim speeds. No significant differences were observed among the groups during the invisible-platform training phase, and the animals were able to find the platform location (Fig 1F). Interestingly, AAV-IGF2-treated mice showed significantly better memory retention in the retention phase on days 4 and 9 when compared to sham mice, whereas AAV-IGF1-treated mice behaved in a similar way to the control group (Fig 1G). Interestingly, when compared to younger animals, AAV-IGF2-treated mice behaved in a similar way to 7-month-old WT animals during the probe test on days 4 and 7 (achieving 50% of time in the right quadrant) and performed even better in the probe test on day 9 (62 versus 50%, see Supplementary Fig S2).

Taken together, these results confirm that IGF2, and not IGF1, reverses age-related memory deficits in hippocampal-dependent learning tasks. The reposition of hippocampal IGF2 (down-regulated during aging, Fig 1D) may underlie this memory enhancement observed in aged mice.

Dendritic spine loss is associated with the normal aging process, so we examined spine density using the Golgi-Cox staining method (Fig 1H) to test whether the IGF2-induced behavioural recovery correlated with structural changes in dendritic spine density. The subregion CA1 was chosen for dendritic spine analysis since it has been shown as critical for contextual learning (Rampon *et al*, 2000). AAV-mediated expression of IGF2 significantly increased the apical dendritic spine density of CA1 pyramidal neurons. In the case of AAV-IGF1-injected mice, an increase in dendritic spine density was also detected, but the effect was significantly lower than in AAV-IGF2-injected mice (Fig 1H). Here, we demonstrate that we developed an experimental memory-enhancing gene-therapy system through which functional IGF can be transferred into the mouse hippocampus with a single injection.

IGF2 expression is reduced in the hippocampus of patients with AD and in Tg2576 mice

Previous studies have reported controversial results concerning the levels of IGF2 mRNA transcripts in the AD hippocampus compared to controls (Stein & Johnson, 2002; Stein *et al*, 2004; Steen *et al*, 2005). Here, we determined the IGF2 protein expression levels using Western blot analysis with an IGF2 antiserum (ab9574, Abcam, Cambridge, UK). We analysed IGF2 levels in human AD brain samples (EC and hippocampus), in Tg2576 mice hippocampi and in hippocampal neuronal cultures of Tg2576 mice or hippocampal neuronal cultures of WT mice treated with conditioned medium (CM) containing high concentrations of Aβ peptide, a procedure that induces a reduction in synaptic density similar to that found in AD (DaRocha-Souto *et al*, 2012).

Quantitative Western blot analyses showed a significant reduction in IGF2 in hippocampal samples from patients with AD ($n = 8$) (Braak stage V-VI) compared to non-AD control subjects ($n = 5$) of

a similar age and sex (Fig 2A). The dramatic decrease in IGF2 expression levels observed in the hippocampus of AD cases was not found in the EC of AD samples ($n = 6$ per group; Fig 2A).

Next, IGF2 levels were determined in hippocampal extracts obtained from 7-month-old Tg2576 mice compared to age-matched WT mice. A significant decrease in IGF2 levels was found in the transgenic animals compared to age-matched WT mice (Fig 2B). Similar results were also found in the hippocampal cultures of Tg2576 mice and in the WT hippocampal neuronal culture treated with Aβ (CM) (Fig 2C) compared to those of WT mice, which would suggest a possible link between hippocampal Aβ accumulation and lower IGF2 concentration.

AAV8-mediated expression of IGF1 and IGF2 in the AD mouse brain

Our results showed that IGF2 expression decreases in the hippocampus of patients with AD and in the Tg2576 mouse model of AD. This led us to hypothesize that IGF2 administration could improve AD symptoms. Thus, we used our AAV-mediated gene-transfer system (AAV-IGF2) as a therapeutic strategy for AD, where the transduction of IGF2 into the brain appears to be necessary.

To determine the temporal profile of AAV-IGF expression in the hippocampus of Tg2576 mice, PCRs using primers for selective detection of the recombinant IGFs but not the endogenous ones (as described above) were carried out 4 and 8 months after the injections and compared to PCRs conducted on sham Tg2576 mice. As shown in Fig 3A, AAV-IGF-injected mice had an amplified band that corresponded to the expression of AAV-IGF in the hippocampus of the injected mice (lanes 3 and 4). No band was detected in the hippocampi of sham-injected Tg2576 mice (sham, lanes 1 and 2).

Hippocampal neurons interact extensively with neurons in the EC and the prefrontal cortex (Braak *et al*, 1996). As also suggested by our viral expression described above (Fig 1A), we tested whether the AAV-IGF tropism for connected brain regions led to IGF expression in the prefrontal cortex (Fig 3A). The expression of growth factors in the other brain areas could contribute to their potential therapeutic effect. We detected PCR product amplification, which corresponded to AAV-IGF expression in the prefrontal cortex of the AAV-IGF-injected mice (lanes 3, 4), whereas no bands were detected in the sham-injected mice (sham: lanes 1 and 2). These results suggest that the AAV injected into the hippocampus also partially reaches and transduces cells in regions other than the hippocampus, such as the prefrontal cortex, and therefore may also elicit a protective effect there.

Furthermore, we performed quantitative real-time PCR using specific primers designed against the corresponding cDNA of the murine IGFs (to detect the recombinant and the endogenous IGFs). As depicted in Fig 3B, AAV-IGF-injected mice showed a robust increase in the expression of the corresponding IGF in the hippocampus (Tg2576 IGF1 and Tg2576 IGF2) compared to sham-injected Tg2576 mice (Tg2576 sham).

The mRNA increase detected by PCR was confirmed in subsequent experiments that detected IGF protein levels. Western blot analysis of hippocampal protein extracts obtained from Tg2576 mice that were sham injected or injected with AAV-IGF2 and euthanized 8 months after the injections revealed that AAV-IGF2 injection produced a significant accumulation of IGF2 compared to sham
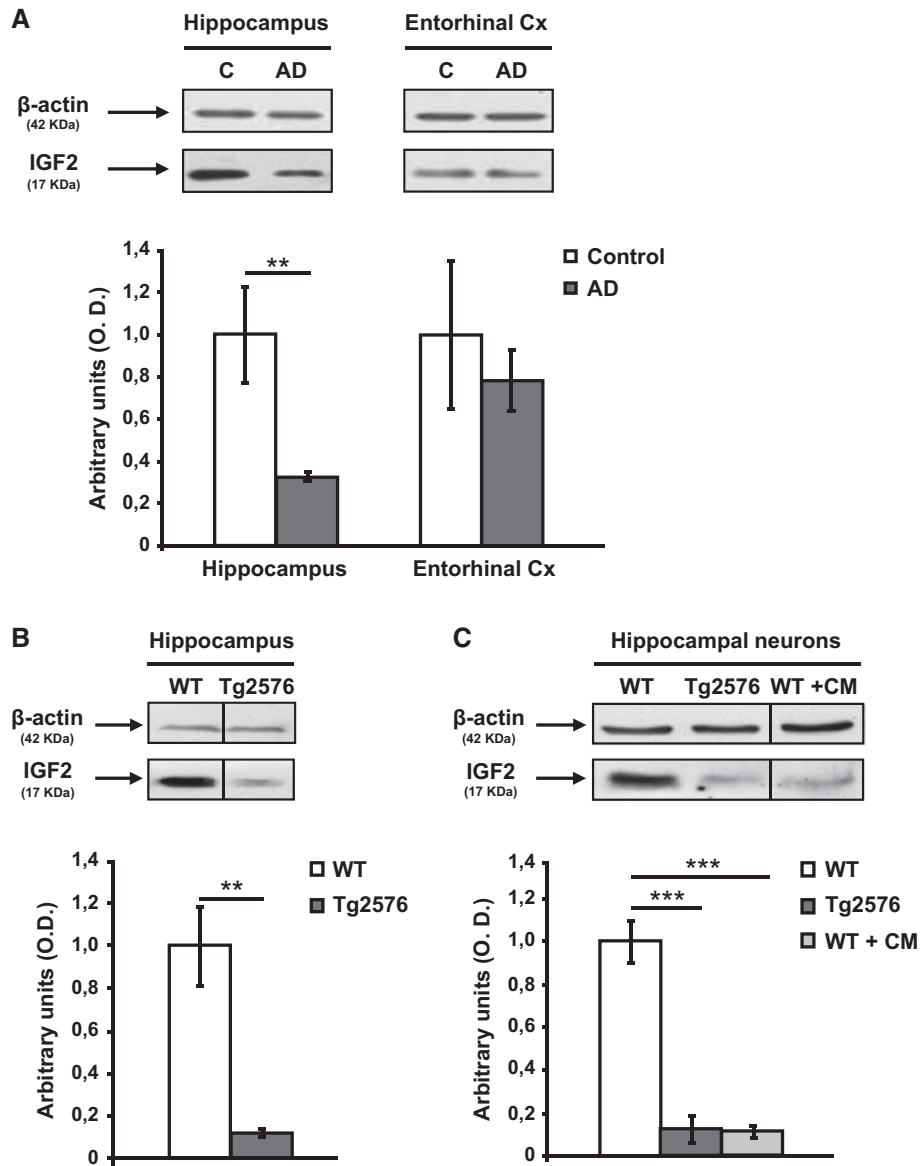
Figure 2. IGF2 protein levels are down-regulated in hippocampal samples of patients with AD and Tg2576 mice, and in Tg2576 neuronal culture.

Quantification of the relative expression of IGF2 protein by Western blot analysis and normalization to β-actin for protein load in:

A   Hippocampal ($n = 8$) and entorhinal cortex (Cx, $n = 6$) from patients with AD compared to corresponding non-demented controls ($n = 5$ and $n = 6$ respectively). In this, and all subsequent figures, data are expressed as arbitrary units (mean ± SEM) with respect to their respective controls (unpaired two-tailed Student's *t*-test, $n = 5–8$, **$P = 0.007$).

B   Seven-month-old Tg2576 mice hippocampus compared to age-matched WT mice (unpaired two-tailed Student's *t*-test, $n = 4$, **$P = 0.010$).

C   Neuronal cultures of Tg2576 mice and neuronal cultures of WT mice exposed to conditioned medium (CM) obtained from Tg2576 primary neurons for 24 h compared to their respective control (one-way ANOVA followed by Scheffe's *post hoc* test, $n = 5–6$, ***$P = 0.0006$ WT versus Tg2576, ***$P = 0.0003$ WT versus WT + CM).

Source data are available online for this figure.

injection, thus demonstrating the long-term expression of the recombinant protein for up to 8 months (Fig 3C).

IGF2 reverses both memory and dendritic spine density impairments in aged Tg2576 mice

The memory capacity of AAV-IGF-treated mice was assessed using two hippocampal-dependent tasks: contextual fear conditioning and the MWM. The effects of AAV-mediated IGF1 and IGF2 expression on contextual fear learning and memory were tested in Tg2576 transgenic mice at two different ages: 16 months old (4 months after the AAV injection) and 20 months old (8 months after the AAV injection). Compared to WT mice, and in line with previous studies (Ricobaraza *et al*, 2012), the Tg2576 mice at both ages exhibited severe disruption in freezing behaviour in the contextual fear-conditioning task conducted 24 h after training (Fig 4A and B).
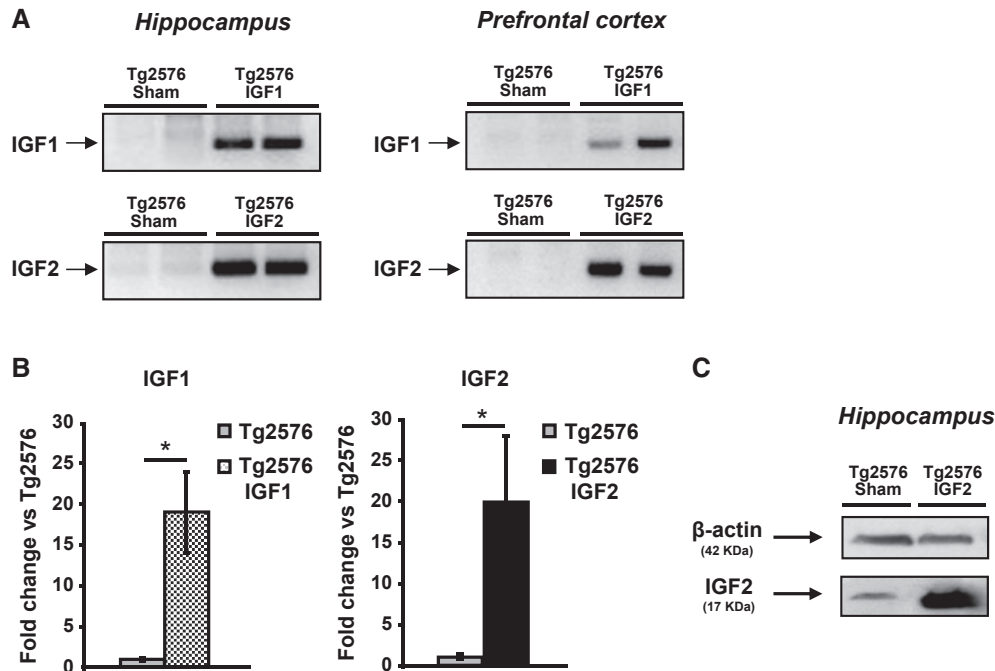
Figure 3. AAV-mediated expression of IGF1 and IGF2 in Tg2576 mouse brain.

A   Gel analysis of PCR products to determine the presence of AAV-mediated IGF1 and IGF2 expression. AAV-IGF-injected Tg2576 mice showed a PCR product corresponding to IGF expression in the hippocampus and the prefrontal cortex. No band was detected in the sham-injected mice (Tg2576 sham).

B   Quantification of the relative expression of IGF transcripts by real-time PCR analysis using primers designed against the corresponding cDNAs of the murine IGFs. AAV-IGF-injected Tg2576 mice showed a robust increase in the corresponding IGF compared to their respective controls (Tg2576 sham). Data are expressed as the fold change (mean ± SEM) with respect to the controls (unpaired two-tailed Student's t-test, n = 5–6, *P = 0.036 Tg2576 IGF1, *P = 0.050 Tg2576 IGF2).

C   Western blot analysis of hippocampal extracts revealing the overexpression of IGF2 protein in the AAV-IGF2-injected mice (Tg2576 IGF2) compared to Tg2576 sham.

Source data are available online for this figure.

However, AAV-IGF2 significantly rescued memory impairment at both 16 months (Fig 4A) and 20 months old (Fig 4B), whereas AAV-IGF1 showed only a significant effect at 16 months of age (Fig 4A).

The effect of IGF1 and IGF2 on MWM learning and spatial memory was only assessed in 20-month-old mice (8 months after the AAV injection), since it has already been established that Tg2576 mice at this age present impairments in both acquisition and retention phases (Westerman et al, 2002). No significant differences were observed among the groups during the visible-platform training phase, which would indicate that the animals' ability to perform the task was similar. Furthermore, the groups did not differ in their swim speeds. The effect of IGF1 and/or IGF2 on spatial learning was assessed according to the variance of intra-group latency (over trials), which was analysed using the non-parametric Friedman test (see Materials and Methods). The analysis showed that, while the mean latency to reach the platform significantly decreased in WT mice and in AAV-IGF2-treated Tg2576 mice as the training sessions progressed, such a change was not observed in AAV-IGF1 or sham Tg2576 mice (Fig 4C). On days 4, 7 and 9, the mice were subjected to a retention probe trial in which the platform was removed. No differences were observed among the groups on the first probe (day 4); however, on days 7 and 9, sham and AAV-IGF1-treated Tg2576 mice showed a significantly poorer performance when compared to WT littermates, whereas AAV-IGF2-treated Tg2576 mice behaved in a similar way to WT littermates (Fig 4D). Taken together, these

results indicate that IGF2 (Fig 4A–D) reverses memory deficits in Tg2576 mice.

Given that impaired synaptic function may underlie memory deficits in AD, and that synapse dysfunction and dendritic spine loss develop in Tg2576 mice (Ricobaraza et al, 2012), we tested whether IGF2-induced behavioural recovery correlates with structural changes in dendritic spine density. To this end, we examined spine density using the Golgi-Cox staining method (Fig 4E). A significant decrease in spine density of apical dendrites of CA1 pyramidal neurons was found in 20-month-old Tg2576 mice compared to WT mice, in line with previous findings (Ricobaraza et al, 2012). Compared to sham mice, AAV-mediated IGF1 or IGF2 expression significantly reversed the deficits in apical dendritic spine density of CA1 pyramidal neurons, with AAV-IGF1 causing the levels to return to control values and AAV-IGF2 causing an increase (Fig 4E).

Both IGF1 and IGF2 rescue hippocampal mEPSCs in Tg2576 mice

Given that both IGF1 and IGF2 expression rescued the dendritic spine density deficit in Tg2576 mice, we tested the effects of IGFs on synaptic transmission of CA1 and CA3 pyramidal cells. AAV-IGFs were bilaterally injected into the hippocampus of 4-month-old Tg2576 mice, and 3 months later, the mEPSCs in whole-cell patch-clamp mode from CA1 and CA3 pyramidal cells were recorded (7-month-old Tg2576 mice). It has been described in literature that at this age, there is already reduction in spine number in the hippo-
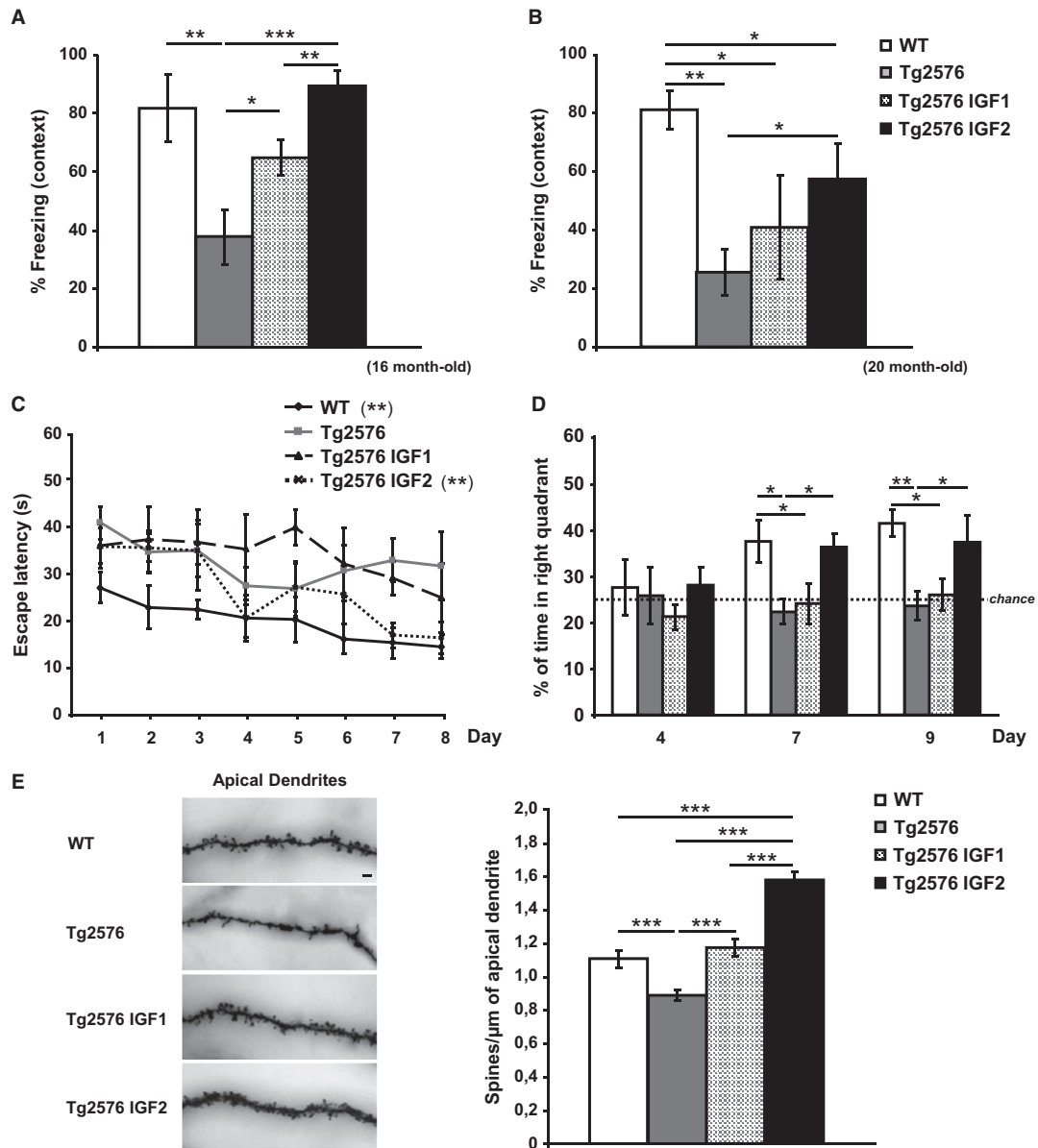
Figure 4. **IGF2 reverses memory deficits and restores spine density in 16- and 20-month-old Tg2576 mice.**

A   Contextual freezing responses of 16-month-old Tg2576 mice were impaired when compared to controls (WT), and significantly improved 4 months after the AAV-IGF1 (Tg2576 IGF1) and AAV-IGF2 (Tg2576 IGF2) injections. In this, and all subsequent figures, the results are expressed as mean ± SEM (Kruskal–Wallis followed by Mann–Whitney U-test, n = 10–12, ** P = 0.008 WT versus Tg2576, * P = 0.041 Tg2576 versus Tg2576 IGF1, *** P = 0.0002 Tg2576 versus Tg2576 IGF2, ** P = 0.0029 Tg2576 IGF1 versus Tg2576 IGF2).

B   Memory impairments in Tg2576 mice progressed with age, and at 20 months, only Tg2576 IGF2 mice showed a significant improvement in memory retention, measured as % contextual freezing, compared to sham-injected Tg2576 mice (Tg2576) (Kruskal–Wallis followed by Mann–Whitney U-test, n = 10–12, ** P = 0.0014 WT versus Tg2576, * P = 0.037 WT versus Tg2576 IGF1, * P = 0.039 WT versus Tg2576 IGF2, * P = 0.050 Tg2576 versus Tg2576 IGF2).

C   Escape latency to the hidden platform in the Morris water maze test for WT, Tg2576, Tg2576 IGF1 and Tg2576 IGF2 mice. Latency to reach the platform decreased in WT and Tg2576 IGF2 mice as the training sessions progressed. No such change was observed in Tg2576 IGF1 or Tg2576 mice (non-parametric Friedman test, n = 10–12, ** P = 0.002 WT, ** P = 0.005 Tg2576 IGF2).

D   Percentage of time spent searching for the target quadrant in the probe test (days 4, 7 and 9). Tg2576 mice performed significantly more poorly than WT mice. AAV-IGF2-injected groups performed similarly to WT mice on days 7 and 9 (one-way ANOVA followed by Scheffe's *post hoc* test, n = 10–12, * P = 0.045 WT versus Tg2576 day 7, * P = 0.05 WT versus Tg2576 IGF1 day 7, * P = 0.049 Tg2576 versus Tg2576 IGF2 day 7, ** P = 0.007 WT versus Tg2576 day 9, * P = 0.044 WT versus Tg2576 IGF1 day 9, * P = 0.035 Tg2576 versus Tg2576 IGF2 day 9).

E   Representative images of Golgi-impregnated apical dendrites of CA1 hippocampal pyramidal neurons. Scale bar = 10 μm (left panel). Quantification of overall spine density in 20-month-old Tg2576 mice (right panel). Significant reduction in spine density was detected in 20-month-old Tg2576 mice compared to WT mice (Kruskal–Wallis followed by Mann–Whitney U-test, n = 27–36 neurons, *** P = 0.0009 WT versus Tg2576). AAV-IGF1 treatment in Tg2576 mice (Tg2576 IGF1) completely reversed spine loss, which returned to littermate control levels (WT) (*** P = 1.67E-05 Tg2576 versus Tg2576 IGF1). AAV-IGF2 treatment (Tg2576 IGF2) increased spine density to above control values (*** P = 6.05E-08 Tg2576 IGF2 versus WT, *** P = 1.94E-12 Tg2576 IGF2 versus Tg2576, *** P = 2.86E-06 Tg2576 IGF2 versus Tg2576 IGF1).

campus (Ricobaraza *et al*, 2012) and decrease in IGF2 levels (Fig 2B). In the presence of bicuculline (10 μM) and TTX (1 mM), mEPSC frequency was assessed by measuring inter-event intervals (IEI). We found that mEPSC frequency was markedly decreased in the pyramidal cells of both CA1 (Fig 5B and C) and CA3 (Supplementary Fig S3B and C) of Tg2576 mice, as indicated by the increase in inter-event intervals (IEI). IGF1 or IGF2 expression fully reversed the deficit in mEPSC frequency. This result is consistent with the spine density recovery observed in AAV-IGF1 and AAV-IGF2 mice (Fig 4E).

The average mEPSC amplitude decreased in the pyramidal cells of both CA1 (Fig 5D and E) and CA3 of Tg2576 mice (Supplementary Fig S3D and E). Although the difference was highly significant, the reduction was only in the order of 20%. This reduction in mEPSC amplitude can be explained by a decrease in the average density of postsynaptic AMPA receptors or alternatively by a change in their biophysical properties. Neither IGF1 nor IGF2 changed the mEPSC amplitude (Fig 5D and E; Supplementary Fig S3D and E).

IGF2 but not IGF1 reduces brain Aβ levels and amyloid plaques in 20-month-old Tg2576 mice

Next, we examined the potential mechanisms involved in IGF-induced spine density and synaptic transmission recovery in the APP model. It is thought that synaptic impairments in AD are triggered by Aβ accumulation resulting from an imbalance between Aβ production and clearance (Hardy & Selkoe, 2002). Thus, amyloid pathology was analysed in the group of 20-month-old Tg2576 mice overexpressing IGF1 or IGF2 and compared to sham Tg2576 mice (8 months after injection). The amyloid burden analysis in the hippocampus was assessed by immunofluorescence using the monoclonal antibody 6E10, which recognizes the amino-terminal region of Aβ, and quantified using the analySIS image system (Gomez-Isla *et al*, 1996; Ribe *et al*, 2005). As depicted in Fig 6A, a high density of amyloid plaques was found in the hippocampus of 20-month-old Tg2576 mice, in line with previous findings (Ribe *et al*, 2005). A marked reduction in the hippocampal amyloid burden was detected in AAV-IGF2 Tg2576 mice, whereas no change was observed in AAV-IGF1 mice compared to sham-injected Tg2576 mice (Fig 6A).

Next, levels of $A\beta_{42}$ and $A\beta_{40}$ were determined by ELISA in the prefrontal cortex and in the parietotemporal cortex, regions that are extensively affected by amyloid burden in Tg2576 mice (Ribe *et al*, 2005). A significant reduction of 26 and 38% in $A\beta_{42}$ levels, and 24 and 50% in $A\beta_{40}$ levels, was observed in the prefrontal and the parietotemporal cortex, respectively, of AAV-IGF2-treated Tg2576 mice compared to sham-injected controls (Fig 6B). No changes were found in AAV-IGF1-treated Tg2576 mice compared to sham-injected Tg2576 mice (Fig 6B). To confirm the effect of AAV-IGF2 on the improvement in amyloid burden in cortical areas, the number of amyloid plaques was also quantified in the EC and motor cortex by immunofluorescence using the monoclonal antibody 6E10. A reduction in amyloid burden was found in AAV-IGF2-treated mice compared to sham-injected mice (Supplementary Fig S4).

Hence, hippocampal IGF2, but not IGF1, rescues amyloid burden typical of AD.

IGF2/IGF2R facilitates Aβ clearance

To begin elucidating the mechanisms by which IGF2 improves amyloid pathology in Tg2576 mice, *in vitro* experiments were carried out. Tg2576 neuronal cultures (DIV 10) were infected with AAV-IGF2, AAV-IGF1 or AAV-luciferase (Luc). After 3 days, the $A\beta_{42}$ levels in the cell media were determined using ELISA. A significant reduction in $A\beta_{42}$ levels (Fig 7A) was observed in the media of primary Tg2576 neurons infected with AAV-IGF2 compared to non-infected neurons (Tg2576 control). There was no significant difference in the $A\beta_{42}$ levels in the media of Tg2576 neurons infected with AAV-IGF1 or AAV-Luc versus the control (Fig 7A).

IGF2 mediates its actions mainly through the IGF2R, but it also binds to the IGF1R with a lower affinity. To determine which receptor (IGF2R or IGF1R) mediates the effect of IGF2 on $A\beta_{42}$ reduction, AAV-IGF2-infected neurons were pre-incubated with a blocking anti-IGF2R antibody (2 ng/μl) or the selective IGF1R antagonist JB1 (500 pg/μl) 24 h before media collection. The extracellular $A\beta_{42}$ reduction was significantly blocked when neurons were exposed to anti-IGF2R antibody. No effect was observed with JB1 (Fig 7B), which would indicate that IGF2R mediates the effect of IGF2 on $A\beta_{42}$ load reduction, while IGF1R does not.

Next, we analysed whether the IGF2R-mediated reduction in $A\beta_{42}$ levels results from an increased clearance of $A\beta_{42}$. To this end, we used CM obtained from Tg2576 neuronal cultures (Tg2576-CM) as a natural source of $A\beta_{42}$ to treat the WT neuronal culture. After 48 h, $A\beta_{42}$ (measured by ELISA) was entirely depleted from the media (Fig 7C, CM), which demonstrates that neurons degrade extracellular $A\beta_{42}$. The degradation was partially blocked when cells were incubated for 48 h with Tg2576-CM containing a collection of proteinase inhibitors (PI) (Fig 7C, CM + PI), which would suggest the involvement of other cell-mediated clearance processes in $A\beta_{42}$ elimination. To determine whether IGF2R is involved in these processes, cells exposed to Tg2576-CM were also incubated with a blocking anti-IGF2R antibody (CM+anti-IGF2R). In these conditions, extracellular $A\beta_{42}$ degradation was also partially blocked. Furthermore, when neurons exposed to Tg2576-CM were incubated with both PI and anti-IGF2R antibody (CM + PI + anti-IGF2R), $A\beta_{42}$ degradation was entirely blocked (Fig 7C). These results confirm that IGF2R plays an important role in $A\beta_{42}$ clearance processes in neurons.

To verify that IGF2R plays a role in the clearance of $A\beta_{42}$, we employed a murine hepatoma cell line (HepA129), which does not express IGF2R (IGF2R-KO). Cells were exposed to Tg2576-CM, and $A\beta_{42}$ levels were analysed using ELISA at different time intervals after incubation (1, 4 and 24 h). As a control, mouse embryonic liver hepatocyte-like cells, BNL.CL.2, which express IGF2R (IGF2R-expressing), were used. Remarkably, after 4 h of incubation, extracellular $A\beta_{42}$ was completely eliminated from the BNL.CL.2 cell media, but not from the HepA129 cell media, where $A\beta_{42}$ was detected even after 24 h (Fig 7D). These results support the hypothesis that IGF2R may act as an $A\beta_{42}$ scavenger.

Discussion

In this study, we used AAV to develop an experimental gene-therapy system for transferring functional IGF2 into the mouse hippocam-
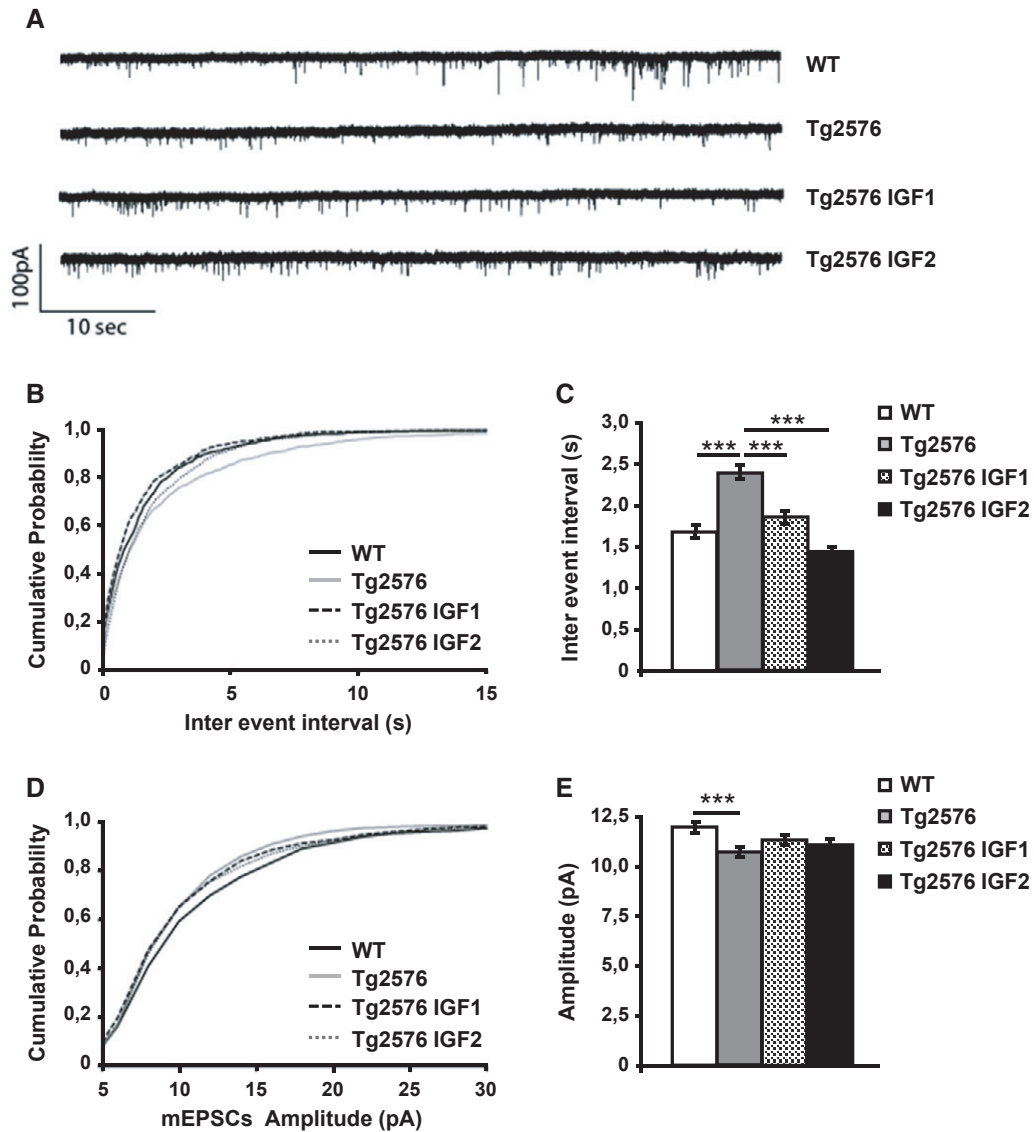
Figure 5. IGF1 and IGF2 treatment restores CA1 synaptic transmission to control levels.

Miniature EPSCs were recorded from CA1 pyramidal cells in 7-month-old animals 4 months after treatment. Cells were held at -70 mV in the presence of bicuculline (10 μM) and TTX (1 μM).

A   Representative traces of spontaneous AMPA EPSCs were isolated from the first 15 min after whole cell configuration.

B   Cumulative probability analysis of the distribution of inter-event intervals between mEPSCs showed a very significant difference between WT and Tg2576 (non-parametric Kolmogorov–Smirnov test, n = 10, P = 0.0002). Treatment with IGF1 and IGF2 rescued the frequency of mEPSCs to values that were no different from those of the control animals (P = 0.0129 Tg2576 versus Tg2576 IGF1, P < 0.0001 Tg2576 versus Tg2576 IGF2).

C   Average mEPSC interval between the first 100 events of 10 cells per treatment (one-way ANOVA followed by Tukey's *post hoc* test, n = 10, ***P < 0.001).

D   Cumulative probability analysis of mEPSC amplitude showed a difference between Tg2576 and WT (non-parametric Kolmogorov–Smirnov test, n = 10, P = 0.0003). The mEPSC amplitude of the treated groups was not rescued to the values of the WT animals (P = 0.3136 Tg2576 versus Tg2576 IGF1, P = 0.4658 Tg2576 versus Tg2576 IGF2).

E   Average amplitude of the first 100 events of 10 cells per treatment (one-way ANOVA followed by Tukey's *post hoc* test, n = 10, ***P < 0.001).

pus for a long time with a single injection. We observed for the first time that the levels of endogenous IGF2 were significantly decreased with age in the mice hippocampi. This observation further supports the potential involvement of IGF2 in age-dependent memory deterioration. Thus, we conducted *in vivo* experiments demonstrating that IGF2 enhances memory and induces synapse formation in the hippocampus of WT rodents. Furthermore, after observing that IGF2 levels decreased in the hippocampus of patients

with AD and in the Tg2576 mouse model, we used AAV to deliver IGF2 and IGF1 into the hippocampus of Tg2576 mice to determine their potential therapeutic efficacy. We demonstrated that AAV-IGF2-injected Tg2576 mice performed significantly better in memory tests, showed increased spine density and excitatory synaptic transmission and presented significantly lower amyloid levels than sham Tg2576 mice. A partial recovery in both memory and synaptic transmission was also observed in AAV-IGF1-injected
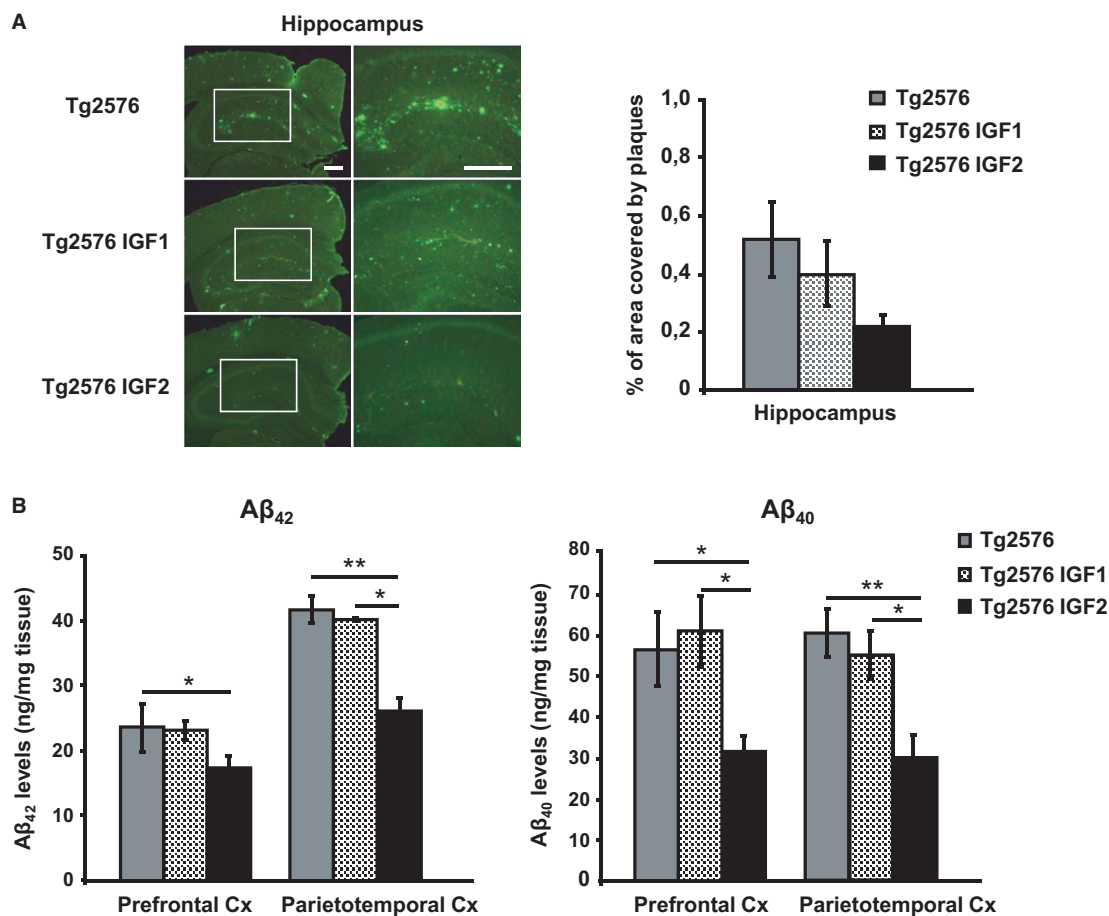
Figure 6. IGF2 reduces amyloid burden in 20-month-old Tg2576 mice.

A Representative hippocampal sections of sham- (Tg2576), AAV-IGF1- (Tg2576 IGF1) and AAV-IGF2- (Tg2576 IGF2) treated Tg2576 mice are shown (left panel). Scale bar = 100 μm. Amyloid burden quantification (right panel). Multiple extracellular deposits stained with 6E10 antiserum were detected in Tg2576 and Tg2576 IGF1 mice. Amyloid burden is reduced in the hippocampus of Tg2576 IGF2 mice ($n = 3$–5); however, no significant differences were found.

B $A\beta_{42}$ and $A\beta_{40}$ concentration determined by ELISA in the prefrontal and parietotemporal cortices (Cx) of Tg2576 mice and Tg2576 IGF1 mice showed similar values. Interestingly, Tg2576 IGF2 mice exhibited a significant reduction in $A\beta_{42}$ (one-way ANOVA followed by Scheffe's *post hoc* test, $n = 7$–8, *$P = 0.050$ Tg2576 versus Tg2576 IGF2 prefrontal Cx, **$P = 0.007$ Tg2576 versus Tg2576 IGF2 parietotemporal Cx, *$P = 0.038$ Tg2576 IGF1 versus Tg2576 IGF2 parietotemporal Cx) and $A\beta_{40}$ (*$P = 0.019$ Tg2576 versus Tg2576 IGF2 prefrontal Cx, *$P = 0.014$ Tg2576 IGF1 versus Tg2576 IGF2 prefrontal Cx, **$P = 0.003$ Tg2576 versus Tg2576 IGF2 parietotemporal Cx, *$P = 0.038$ Tg2576 IGF1 versus Tg2576 IGF2 parietotemporal Cx) cortical levels. Data are the mean ± SEM.

Tg2576 mice. Furthermore, IGF2 was identified for the first time as a regulator of amyloid levels in neuronal population, probably through the IGF2R. These findings suggest that IGF2 has potential therapeutic properties that could be beneficial for the treatment of AD.

IGF2 is mainly produced during foetal development. Although its levels drop in adulthood, they remain higher in the brain than other members of the insulin system. In line with previous findings (Rivera *et al*, 2005), we observed that IGF2 protein levels decline in the hippocampus of the AD brain; this led us to test the hypothesis that IGF2 is a potential treatment for AD in preclinical models. We demonstrated that IGF2 overexpression in the hippocampus of Tg2576 mice after the onset of severe AD improved hippocampal-dependent memory and synaptic deficits in these mice. In addition, when AAV-IGF2 was injected into the hippocampus of aged WT mice, the animals showed an improvement in memory performance. Memory impairments in Tg2576 mice and age-related memory loss

are associated with spine loss in pyramidal CA1 neurons (Ricobaraza *et al*, 2012) and reduced mEPSC frequency in CA1 pyramidal neurons in Tg2576 mice as young as 3 months old (D'Amelio *et al*, 2011). We observed that IGF2-induced cognitive recovery in both the aged and AD model was accompanied by an increase in spine density and the rescue of synaptic functions through an increase in mEPSC frequency in the AD transgenic mouse model. This is consistent with a recent finding that IGF2-IGF2R signalling promotes synapse formation and spine maturation in the mouse brain (Schmeisser *et al*, 2012). These results are also in line with evidence that IGF2 facilitates memory consolidation and long-term hippocampal potentiation in rats (Chen *et al*, 2011). Furthermore, IGF2 may affect neurogenesis (Bracko *et al*, 2012) and, through this mechanism, contribute to hippocampal-dependent spatial learning and memory, which has been linked to neurogenesis (Bracko *et al*, 2012; Ouchi *et al*, 2013). In keeping with this, the hippocampal expression of IGF2 was found to rescue adult neurogenesis and improve spatial
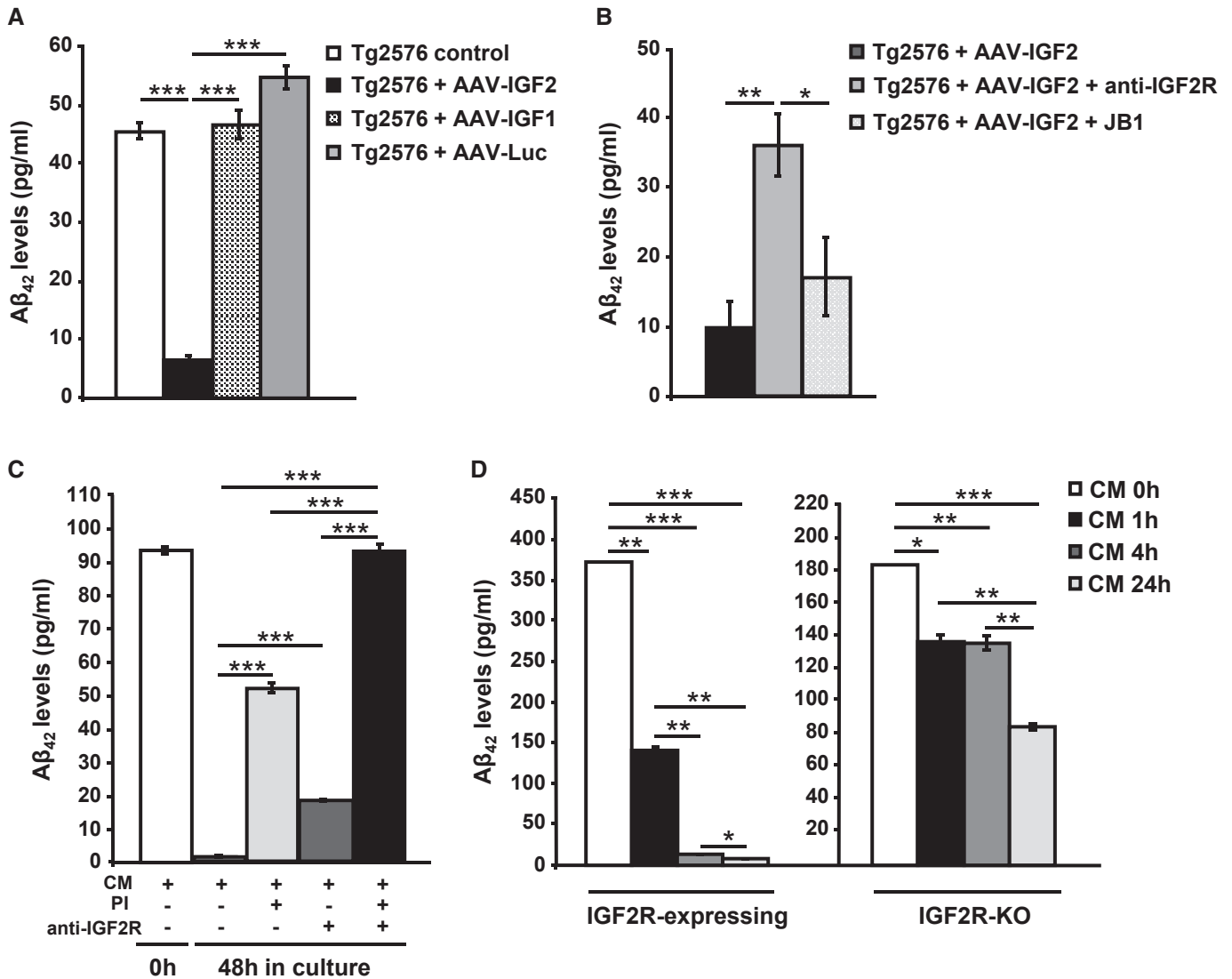
Figure 7. IGF2/IGF2R mediates $A\beta_{42}$ clearance in neurons.

A ELISA analysis to detect $A\beta_{42}$ levels in the media of Tg2576 primary neuronal culture infected with AAV-IGF1, AAV-IGF2 or AAV-Luc. A significant depletion in extracellular $A\beta_{42}$ levels was detected in the media of AAV-IGF2-infected neurons. In this, and all subsequent figures, data (mean ± SEM) are expressed in pg of $A\beta_{42}$/ml of conditioned medium. Bars represent the analysis from three independent experiments (one-way ANOVA followed by Scheffe's *post hoc* test, $n = 3$–4, ***$P = 3.12E$-08 Tg2576 control versus Tg2576 + AAV-IGF2, ***$P = 1.91E$-08 Tg2576 + AAV-IGF2 versus Tg2576 + AAV-IGF1, ***$P = 2.39E$-09 Tg2576 + AAV-IGF2 versus Tg2576 + AAV-Luc).

B ELISA analysis to detect $A\beta_{42}$ levels in the medium from Tg2576 primary neuronal cultures transfected with AAV-IGF2. Pre-incubation with anti-IGF2R antibody partially prevented $A\beta_{42}$ clearance in the media of infected neurons. Bars represent the analysis from three independent experiments (one-way ANOVA followed by Scheffe's *post hoc* test, $n = 3$–4, **$P = 0.009$, *$P = 0.036$).

C ELISA analysis to detect $A\beta_{42}$ levels in media obtained from WT primary neuronal cultures exposed to conditioned medium (CM) from Tg2576 neurons for 48 h. Full depletion in extracellular $A\beta_{42}$ occurred after 48 h; this was prevented by pre-incubation with proteinase inhibitors (PI) and/or anti-IGF2R antibody (one-way ANOVA followed by Scheffe's *post hoc* test, $n = 3$–4, ***$P = 2.65E$-09 CM versus CM + PI, ***$P = 3.56E$-05 CM versus CM + anti-IGF2R, ***$P = 1.26E$-11 CM versus CM + PI + anti-IGF2R, ***$P = 1.57E$-08 CM + PI versus CM + PI + anti-IGF2R, ***$P = 7.80E$-11 CM + anti-IGF2R versus CM + PI + anti-IGF2R).

D Analysis by sandwich ELISA of $A\beta_{42}$ levels at different time intervals (0, 1, 4 and 24 h) in the media of hepatic cell lines (BNL.CL.2 and HepA129; IGF2R-expressing and IGF2-KO, respectively) exposed to conditioned medium from Tg2576 primary neurons (CM). After 4 h of incubation, extracellular $A\beta_{42}$ was completely eliminated from the IGF2R-expressing cell medium (one-way ANOVA followed by Scheffe's *post hoc* test, $n = 3$–4, **$P = 0.002$ CM 0 h versus CM 1 h, ***$P = 1.99E$-05 CM 0 h versus CM 4 h, ***$P = 8.23E$-06 CM 0 h versus CM 24 h, **$P = 0.006$ CM 1 h versus CM 4 h, **$P = 0.006$ CM 1 h versus CM 24 h, *$P = 0.02$ CM 4 h versus CM 24 h), but not from the IGF2R-KO cell medium, where $A\beta_{42}$ was detected even after 24 h (*$P = 0.011$ CM 0 h versus CM 1 h, **$P = 0.009$ CM 0 h versus CM 4 h, ***$P = 0.0001$ CM 0 h versus CM 24 h, **$P = 0.002$ CM 1 h versus CM 24 h, **$P = 0.0014$ CM 4 h versus CM 24 h). Bars represent the analysis from three independent measurements.

working memory deficits in the Dgcr8 (DiGeorge chromosomal region 8) deficient mouse model of schizophrenia (Ouchi *et al*, 2013). Furthermore, an increase in IGF2 contributes to the

improvement in cognitive dysfunction by several pharmacological treatments, such as galantamine, choline or dicholine succinate (Cline *et al*, 2012; Kita *et al*, 2013) (Napoli *et al*, 2008). Hence, our

results contribute to the body of evidence accumulated in recent years that IGF2 plays an important role in learning and memory formation, and demonstrate that by restoring dendritic spine density, IGF2 may significantly promote the recovery of memory impairments.

Hippocampal IGF1 overexpression in Tg2576 mice also resulted in the recovery of hippocampal spine density and restoration of synaptic transmission. However, when memory was assessed in 20-month-old mice, Tg2576 AAV-IGF1-injected mice failed to learn the tasks and were thus found to have significant impairments, whereas Tg2576 AAV-IGF2-injected mice had learning abilities that were similar to those of non-transgenic mice. Hence, despite the fact that IGF1 has some effect, our results suggest that IGF2 is far more effective. This was confirmed for age-related memory loss, since AAV-IGF2-injected mice performed significantly better than the AAV-IGF1-treated group (Fig 1E and F). Furthermore, the results are consistent with the fact that IGF2R is the receptor that mediates the effect of IGF2 on synaptogenesis (Schmeisser *et al*, 2012) and memory formation (Chen *et al*, 2011). In addition, IGF2R exhibits a much lower binding affinity for IGF1 (El-Shewy & Luttrell, 2009). Although a possible role for IGF1 upon activation of IGF1R via Akt signalling cannot be ruled out, further studies are required to shed light on the role of IGF1 on memory function and synapse formation.

Crucially, we showed that IGF2 overexpression in the hippocampus leads to a significant reduction in Aβ content in the brains of Tg2576 mice. However, this effect was not observed in AAV-IGF1-injected mice. These results do not correlate with those of previous studies that demonstrated that the systemic administration of IGF1 promotes Aβ clearance from the brain (Carro *et al*, 2002, 2006). The authors suggest that circulating IGF1 increases Aβ carrier proteins and thus favours Aβ clearance from the brain. It is important to note that hippocampal IGF1 overexpression may trigger a different effect on amyloid pathology than increasing levels of circulating IGF1. In accordance with our data, there is a very recent study that addresses the role of IGF2 in the amelioration of amyloidosis using a different AD mouse model (Mellott *et al*, 2014). Mellott *et al* found a decrease in amyloid deposits in APP/PS1 mice brain after 1 week of intraventricular infusion of human recombinant IGF2. They suggested that an enhance in cholinergic transmission and the synthesis of neuronal growth factors may be the mechanisms involved in IGF2-mediated Aβ clearance (Mellott *et al*, 2014).

In our study, in relation to the mechanism by which IGF2 improves Aβ pathology in Tg2576 mice, the results obtained in the *in vitro* assays suggest that the IGF2R appears to be involved in the protease-independent Aβ clearance mechanisms by neurons. The presence of the antagonistic anti-IGF2R antibody partially blocked Aβ clearance from the media of neuronal cultures expressing IGF2. An upregulation of IGF2R levels was observed in the hippocampus of AAV-IGF2-injected Tg2576 mice (Supplementary Fig S5). IGF2R is known to be involved in protein processing and clearance, primarily through lysosomal degradation, since IGF2R mediates lysosomal enzyme trafficking (El-Shewy & Luttrell, 2009). The extracellular fraction of IGF2R contains 15 homologous domains of 147 amino acids. The IGF2-binding domain has been mapped to domain 11, whereas M6P residues bind domains 3 and 9 (Braulke, 1999). Aβ has recently been shown to precisely bind IGF2R domain 11,

which would suggest that IGF2R may act as an Aβ scavenger (Murakoshi *et al*, 2013). Taken together, these results demonstrate for the first time, to our knowledge, that IGF2/IGF2R is involved in the extracellular Aβ degradation mechanism, and suggest that IGF2R may be involved in the Aβ clearance observed in AAV-IGF2-injected Tg2576 mice.

Thus, IGF2 may represent an effective therapeutic target for the memory, synaptic loss and amyloid accumulation that accompany AD pathology.

Materials and Methods

Viral construction, production and purification

For construction of the recombinant viral genomes AAV-IGF1 and AAV-IGF2, IGF1 (GenBank accession number NM_010512.4) and IGF2 (GenBank accession number NM_001122737.1) cDNAs were amplified using gene specific primers where the 5′-primer contained a *XbaI* restriction site and the 3′-primer contained a *BglII* restriction site, and cDNA obtained from foetal hippocampus brain as template. The PCR products were subsequently cloned into pCR2.1 to obtain pCR2.1-IGF1 and pCR2.1-IGF2. The IGF1/IGF2 fragments were excised with *XbaI* and *BglII* and cloned into dsAAV-EF1α-eGFP (Applied Viromics, Fremont, CA) previously digested with *XbaI* and *BglII* to obtain the plasmids dsAAV-EF1α-IGF1 and dsAAV-EF1α-IGF2. This plasmid carries the AAV8 backbone with an intact 5′ terminal resolution site (trs) without the 3′trs analogous. Thus, the expression of IGF1 and IGF2 is under the transcriptional control of the constitutive and ubiquitous promoter of human elongation factor-1 (GenBank accession number J04617.1).

rAAV8 vectors were produced by polyethylenimine (PEI)-mediated cotransfection in HEK-293 cells as previously described (Paneda *et al*, 2009). For each production, a mixture of plasmids, 20 μg of pro-AAV plasmid and 55 μg pDP8.ape (PlasmidFactory GmbH & Co. KG, Bielefeld Germany), was transfected into 293 cells 15 cm plate using linear PEI 25 kDa (Polysciences, Warrington, PA) and harvested 72 h after transfection, and virus was released from the cells by three rounds of freeze-thawing. Crude lysate from all batches was then treated with Benzonase (50 U/ml crude lysate) for 1 h at 37°C and then kept at −80°C until purification. Purification of crude lysate was performed by iodixanol gradients according to the method of Zolotukhin *et al* (1999). The purified batches were concentrated and diafiltrated by cross-flow filtration (Spectrum Laboratories, Rancho Dominguez, CA) with a molecular mass cut-off of 400 kDa. The batches were then concentrated further by passage through Centricon tubes (YM-100; Millipore, Bedford, MA). After concentration, the viral batches were filtered (pore size, 0.22 mm) and stored at −80°C. Viral titres in terms of genome copies per millilitre were determined by Q-PCR, performed three times in triplicate at three different dilutions.

Animals

A group of aged WT animals was used to test the effect of IGF2 and IGF1 on cognitive function. For this aim, male 18-month-old C57BL/6 mice were used. Animals were housed 4–5 per cage with *ad libitum*

access to food and water and maintained in a temperature-controlled environment on a 12-h dark/light cycle. Next, as a model of AD, we used transgenic mice Tg2576 overexpressing human 695-aa isoform of amyloid precursor protein (hAPP) carrying the Swedish double mutation (APPswe: K670N, M671L) driven by a hamster prion promoter (Hsiao *et al*, 1996). The mice were on an inbred C57BL/6/SJL genetic background. Behavioural and biochemical studies were performed comparing Tg2576 females to age-, sex- and strain-matched transgenic negative littermates (WT).

All procedures were carried out in accordance with the current European and Spanish regulations (86/609/EEC; RD1201/2005). This study was approved by the Ethical Committee of the University of Navarra (no. 137/010).

rAAV administration

Eighteen-month-old male C57BL/6 (12 per group), 12-month-old female Tg2576 (15 per group) or 4-month-old female Tg2576 (6 per group, for electrophysiology measurements) were anesthetized with ketamine/xylazine (80/10 mg/kg, i.p.) and placed in a stereotactic frame. The scalp was shaved and a longitudinal incision was made along the midline of the skull. The dorsal surface of the skull was then exposed, and two burr hole were drilled above the infusion sites. 1.0 μL of virus suspension or saline solution (sham mice) was infused to the CA1 region of the hippocampus (−2.0 mm AP, ±1.7 mm ML, −2.0 mm DV to bregma) according to the Paxinos and Watson mouse brain atlas (1998). A 1-μl Hamilton syringe was used for the infusion (Hamilton Co., Reno, NV). The infusion rate was 0.2 μl/min, and the needle remained in place for 5 min after the infusion for vector absorption. The same procedure was used for the infusion in the other hemisphere. Finally, the site was stitched closed.

Human AD samples and controls

A total of 24 brain samples from the Navarra Health Service / Osasunbidea's Research Biobank were included in the study. The samples were obtained from 15 patients with clinical diagnosis of dementia and 9 elderly normal controls. Patients with AD met criteria proposed by the National Institute on Aging and the Alzheimer's Association workgroups for AD dementia with documented decline (McKhann *et al*, 2011). For all subjects, informed consent had been obtained from relatives before the removal of brain tissue at death and subsequent use of the material for research. This study was carried out in accordance with the Medical Ethics Committee of the University of Navarra. At autopsy, brains were removed and stored at −80°C until processing.

Primary neuronal cultures

Primary neuronal cultures were derived from the hippocampus of embryonic day 16 (E16) Tg2576 or wild-type (WT) mice. Hippocampi were triturated using glass pipettes until neurons were dissociated. Neurons were plated in serum-free neurobasal media with B27 supplement (Invitrogen, Gaithersburg, MD) and 2 mM L-glutamine on poly-L-lysine-treated (0.1 mg/ml; Sigma) 12-well plates. In Tg2576 neuronal cultures, to maintain increased levels of extracellular Aβ, media were not changed. Primary neurons were viable for

> 3–4 weeks under our culturing conditions. Genotyping was performed on cerebellum from the same embryo.

Tg2576 and non-transgenic hippocampal cultures at 21 DIV were collected in a cold lysis buffer with protease inhibitors (0.2 M NaCl, 0.1 M HEPES, 10% glycerol, 0.2 M NaF, 2 mM $Na_4P_2O_7$, 5 mM EDTA, 1 mM EGTA, 2 mM DTT, 0.5 mM PMSF, 1 mM Na_3VO_4), left on ice for 30 min and centrifuged at 14,000 *g* for 20 min at 4°C. The supernatant was aliquoted and stored at −80°C. Total protein concentrations were determined using the BioRad Bradford protein assay (BioRad Laboratories, CA).

For viral transduction of Tg2576 neuronal cultures, neurons were cultured for 10 days in 12-well plates prior to transduction with 1.13×10^8 viral transducing units per well. Blocking anti-IGF2R antibody (1:100, Santa Cruz Biotechnology) or the selective IGF1R antagonist JB1 (500 pg/μl, Cymit Química, Barcelona) was used 24 h before collecting the media to block the IGF2R or IGF1R. The medium was collected 72 h after the virus infection and stored at −80°C until Aβ42 was determined by ELISA.

For Aβ$_{42}$ measurements in WT neurons, hippocampal cultures at 20 DIV were treated with 50% Tg2576 conditioned medium (CM) as a natural source of Aβ$_{42}$, protease inhibitor (PI) cocktail (Complete Protease Inhibitor Cocktail, Roche Diagnostics, Mannheim, Germany) and/or rabbit polyclonal antibody anti-IGF2R (1:100, Santa Cruz Biotechnology). The medium was collected after 48 h and stored at −80°C until Aβ$_{42}$ was determined by ELISA.

Cell line cultures

BNL CL.2 and HepA129 cell lines were obtained as a gift from the Dr. Fortes at CIMA (Dpto of Gene Therapy and Hepatology). Cells were cultured in 12-well plates to 90% confluence at 37°C in an atmosphere of 5% CO_2. BNL CL.2 cells were grown in Dulbecco's modified Eagle's medium (DMEM) supplemented with Glutamax (Gibco, Invitrogen, CA), 100 units/ml penicillin/streptomycin and 10% foetal bovine serum (FBS). HepA129 cells were grown in Roswell Park Memorial Institute (RMPI) 1640 medium supplemented with Glutamax (Gibco, Invitrogen, CA), 100 units/ml penicillin/streptomycin and 10% FBS.

Cells were exposed to Tg2576 conditioned medium for 1, 4 and 24 h, and the medium was collected and stored at −80°C until Aβ$_{42}$ measurements by ELISA.

Contextual fear conditioning

The behavioural procedure involved three phases: habituation, training and testing. During habituation phase, mice were habituated to the conditioning box (context) for 5 min with no stimuli presented. Twenty-four hours later (training phase), mice were placed in the training chamber and allowed to explore for 2 min, and afterwards, a footshock (0.3 mA) unconditioned stimulus was administered (2 s) and 30 s after mice were returned to their home cage. A stronger paradigm of training (2 CS-US pairings, separated by a 10-s resting interval) was used for the group of transgenic mice.

Mice were returned to the conditioning chamber 24 h after training and allowed to explore the context for 3 min, during which freezing behaviour was recorded (contextual long-term memory). Freezing scores were expressed as percentages. The conditioning

procedure was carried out in a StartFear system (Panlab S.L., Barcelona, Spain) that allows recording and analysis of the signal generated by the animal movement through a high-sensitivity Weight Transducer system. The analogical signal is transmitted to the FREEZING and STARTLE software modulated through the load cell unit for recording purposes and posterior analysis in terms of activity/immobility.

Morris water maze

To evaluate the working and spatial memory function in response to AAV-IGF1/IGF2 injection, the Morris water maze test was performed, as previously described (Ricobaraza et al, 2009). Mice underwent visible-platform training for three consecutive days (eight trials per day) using a platform raised above the surface of the water. No visible cues were present during this phase. The visible-platform phase was followed by hidden-platform training (visible cues present) during which mice were trained to locate a platform submerged 1 cm beneath the water surface for 8 consecutive days (four trials per day). In both visible- and hidden-platform versions, mice were placed pseudo-randomly in selected locations. Each trial was terminated when the mouse reached the platform or after 60 s, whichever came first. After each hidden-platform trial, mice remained on the platform for 20 s. Twenty hours after the 12th, 24th and 32nd trials, all mice were subjected to a probe trial in which they swam for 60 s in the pool with no platform. All trials were monitored by a camera above the centre of the pool connected to a SMART-LD program (Panlab S.L., Barcelona, Spain) for subsequent analysis of escape latencies (time required to reach the platform), swimming speed, path length and percentage time spent in each quadrant of the pool during probe trials. All experimental procedures were performed blind to groups.

RNA extraction and PCR

Total RNA from hippocampus and prefrontal cortex of mice was isolated using Trizol reagent (Sigma-Aldrich, St Louis, MO). The RNA was treated with DNase at 37°C for 30 min and reverse-transcribed into cDNA. To detect the expression of viral IGFs, conventional PCR was performed with oligonucleotide primers specific to viral IGFs; thus, the 5′ primer was designed against the 5′ end of the corresponding IGF cDNA and a 3′ primer aligned to the 3′ UTR, poly-adenylation signal sequence of the recombinant IGF, which is common for both viral IGF2 (forward: 5′-GCTTGCCAAA GAGCT CAAAG-3′; reverse: 5′-ACTCGAGGTCGAGGCCAGA-3′), and viral IGF1 (forward: 5-CCCCACTGAAGCCTACAAAA-3′; reverse: 5′-ACTCGAGGTCGAGGCCAGA-3′). The PCR product was analysed on a 1% agarose gel containing SYBR Safe DNA gel stain (Invitrogen, Carlsbad, CA) under ultraviolet light.

For the quantification of IGFs expression, quantitative real-time PCR assays were performed in triplicate using Power SYBR Green PCR Master Mix (Applied Biosystems, Warrington, UK), and specific primers to mouse IGF2 (forward: 5′-CGCTTCAGTTTGTCTGTTCG-3′; reverse: 5′-GGAAGTACGGCCTGAGAGGTA-3′), mouse IGF1 (forward: 5′-GGACCGAGGGGCTTTTACTTC-3′; reverse: 5′-AGTCTTGG GCATGTCAGTGTGG-3′) and β-actin (forward: 5′-CCTGACAGACTA CCTCATGAAG-3′; reverse: 5′-CCATCTCTTGCTCGAAGTCTAG-3′) was used as internal control. Real-time PCR was done using an ABI

Prism 7300 sequence detector (Applied Biosystems, Foster City, CA), and data were analysed with Sequence Detection software v. 3.0. (Applied Biosystems).

Immunofluorescence

Under xylazine/ketamine anaesthesia, 20-month-old Tg2576 mice from each group (n = 4) were transcardially perfused with saline and 4% paraformaldehyde in phosphate buffer (PB). After perfusion, the brain was removed, post-fixed for 1 h at 4°C in the same fixative solution and cryoprotected overnight at 4°C in 30% sucrose in PB. Coronal microtome sections (30 μm thick) containing the hippocampal formation were collected and processed for immunostaining. Brain sections were incubated in 70% formic acid for 10 min to expose the epitope prior to incubation with blocking solution (PBS containing 0.5% Triton X-100, 0.1% BSA and 2% normal goat serum) for 2 h at room temperature. Sections were then incubated for 24 h at 4°C with mouse monoclonal 6E10 (against amino acids 1–17 of Aβ peptide, 1:200, Covance) diluted in blocking solution. After washing with PBS, the brain sections were incubated with the secondary antibody (1:200, Alexa Fluor 488 goat anti-mouse highly cross-absorbed Molecular Probes, Eugene, Oregon) for 2 h at room temperature in the dark. Fluorescence signals were analysed on a confocal microscope (LSM 510 Meta, Carl Zeiss, Germany) using a Plan-neofluar 40×/1.3 oil DIC objective. Sections were evaluated in Z-series (0.4 mm steps) using LSM 510 Meta software.

Amyloid deposition was quantified using Aβ immunostaining (monoclonal anti- Aβ 6E10) and the AnalySIS Image System (Ribe et al, 2005). Video images were captured of each region of interest on 30-μm sections, and a threshold of optical density was obtained that discriminated staining from background. Manual editing eliminated artefacts. The amyloid burden, defined as the total percentage of area covered by amyloid deposits over three sections, was calculated for hippocampus.

Protein extracts

Brain samples were homogenized in a cold lysis buffer with protease inhibitors (0.2 M NaCl, 0.1 M HEPES, 10% glycerol, 0.2 M NaF, 2 mM $Na_4P_2O_7$, 5 mM EDTA, 1 mM EGTA, 2 mM DTT, 0.5 mM PMSF, 1 mM Na_3VO_4), left on ice for 30 min and centrifuged at 14,000 g for 20 min at 4°C. To analyse IGF2 expression in mice, hippocampi were homogenized in a buffer containing 0.32 M sucrose, 5 mM HEPES pH 7.4, 1 mM MgCl2, 1 mM EDTA, 1 mM NaHCO3, 0.1 mM PMSF and protease inhibitors. The supernatant was aliquoted and stored at −80°C. Total protein concentrations were determined using the BioRad Bradford protein assay (BioRad Laboratories, CA).

Western blot analysis

Protein samples were mixed with 6× Laemmli sample buffer, resolved onto SDS-polyacrylamide gels and transferred to nitrocellulose membranes. The membranes were blocked with 5% milk in TBS followed by overnight incubation with the following primary antibodies diluted in 2.5% milk in TBS: rabbit polyclonal anti-IGF2 (1:500, Abcam) and anti-β-actin (1:100,000 Sigma-Aldrich, St. Louis,

USA). Following two washes in TBS/Tween-20 and one in TBS alone, the immunolabelled protein bands were detected with an HRP-conjugated anti-rabbit (1:5,000, Santa Cruz) or anti-mouse (1:5,000, Santa Cruz) antibody. Finally, antibody binding was visualized by enhanced chemiluminescence system (ECL; GE Healthcare Bioscience) and autoradiographic exposure to Hyperfilm™ECL (GE Healthcare Bioscience). Quantity One™ software v.4.6.3 (Bio-Rad) was used for protein quantification.

Dendritic spine measurements

A modified Golgi-Cox method was used (Glaser and Van der Loos, 1981). Briefly, brains were removed from the skull and placed in Golgi-Cox solution (1% potassium dichromate, 1% mercury chloride, 0.8% potassium chromate) for 3 weeks. Brains were then washed in water and 90% ethanol, and 200-μm-thick slices were cut on a vibratome and soaked in 16% ammonia solution for 1 h. After fixation in 1% sodium thiosulphate solution, slices were dehydrated and mounted with DPX. Slides were coded before quantitative analysis, and the code was broken only after the analysis was completed. To be selected for morphometric analysis, Golgi-impregnated pyramidal cells had to be located within the CA1 and have consistent impregnation throughout untruncated dendrites. CA1 dendrites were classified into primary and secondary dendrites: dendrites directly originating from cell soma were classified as primary dendrites, and those originating from primary dendrites were classified as secondary. Each selected neuron was captured in a Nikon Eclipse E600 light microscope, and images were recorded at a resolution of 1,000–1,500 dots per inch (dpi) using a digital camera (Nikon DXM 1200F). Data for the statistical analyses were obtained from 100× pictures of a random sample of apical secondary dendrites taken between 100 and 200 μm apart from the soma, where spine density is relatively uniform in CA1 pyramidal neurons (Megias *et al*, 2001). For each mouse ($n = 3$–4 per group), 9 neurons (three dendritic segments were measured per neuron, at least 30 μm long) were analysed.

Slice preparation and electrophysiology

Seven to 8-month-old mice (3–4 months after the AAV injection) were anesthetized with ketamine (80 mg/kg, i.p.) and xylazine (10 mg/kg i.p.) and intracardially perfused in an ice-cold oxygenated cutting solution (200 mM of sucrose, 20 mM glucose, 0.4 mM $CaCl_2$, 8 mM $MgCl_2$, 2 mM KCl, 1.3 mM NaH_2PO_4, 26 mM $NaHCO_3$, 3 mM pyruvate and 2 mM of kynurenic acid (pH 7.3). Brain was quickly dissected, and slices of 350 μm were made with a Leica vibratome and then kept in oxygenated artificial CSF [125 mM NaCl, 2.5 mM KCl, 2.5 mM $CaCl_2$, 1.3 mM $MgSO_4$, 1.25 mM NaH_2PO_4, 26 mM $NaHCO_3$ and 20 mM glucose (pH 7.4)] at 33°C for 30 min in the presence of kynurenic acid (2 mM) and left to rest for 30 min at room temperature without kynurenic acid. Slices were used within a maximum of 6 h after cutting.

Brain slices were transferred to a recording chamber, in which they were continuously superfused with oxygenated (95% O_2 and 5% CO_2) artificial CSF. The patch pipettes were filled with a solution caesium methanesulfonate-based solution (140 mM $CsMeSO_3$, 2 mM $MgCl_2$, 4 mM NaCl, 0.2 mM EGTA, 5 mM P-creatine, 3 mM $ATPNa_2$, 0.3 mM GTP, 10 mM HEPES). Bicuculline (10 μM) and TTX (1 μM) were present in the superfusate of all experiments. Cells were clamped at −70 mV, and mEPSCs were recorded for 15 min in both CA1 and CA3 pyramidal cells. The access resistance of the cells was < 20 MΩ, and recordings were discarded from analysis if the resistance changed by > 20% over the course of the experiment. Recordings were made using an EPC 10.0 amplifier (HEKA Elektronik) and were filtered at 0.5–1 kHz, digitized at 1–5 kHz.

The amplitude and the time interval between events were measured, and the values of the first 100 events and intervals of every cell were plotted using a threshold of 6 pA. For each condition, 10 cells were recorded, from 3 to 5 animals.

Determination of Aβ levels

Cortical $A\beta_{42}$ and $A\beta_{40}$ levels were measured by using a sensitive sandwich ELISA kit (Invitrogen, Camarillo, CA). Cortical tissue was weighed and homogenized in 8× mass of cold-ice guanidine buffer (5M guanidine HCl/50 mM Tris HCl pH 8.0). The homogenates were mixed for 4 h at room temperature and were diluted 1:50 in Dulbecco's phosphate-buffered saline containing 5% BSA and 0.03% Tween-20 (DPBS-BSAT) supplemented with protease inhibitor cocktail (Complete Protease Inhibitor Cocktail, Roche Diagnostics, Mannheim, Germany) followed by centrifugation at 16,000 *g* for 20 min at 4°C. The supernatant was diluted and loaded onto ELISA plates in duplicate. For $A\beta_{42}$ measurement from conditioned medium, it was directly diluted and loaded onto ELISA plates in duplicate. The assays were performed according to the manufacturer's instructions, and Aβ standards were prepared in a buffer with the same composition as the samples.

Data and statistical analyses

The results were processed for statistical analysis using SPSS package for Windows, version 15.0 (SPSS, Chicago, IL, USA). Unless otherwise indicated, results are presented as mean ± standard error of the mean (SEM). Normal distribution of data was checked by the Shapiro–Wilk test. Unpaired two-tailed Student's *t*-test was used in case two groups were compared. Normally distributed variables for more than two groups were analysed using one-way ANOVA followed by Scheffe's *post hoc* test. Non-normally distributed were analysed using Kruskal–Wallis test. In the invisible-platform phase of Morris water maze, Friedman's test was performed to determine the intra-group comparisons over trials. Electrophysiological data (cumulative distribution of the peak amplitude and intervals of mEPSCs) were analysed using Kolmogorov–Smirnov (KS) test.

The paper explained

Problem

Alzheimer's disease (AD) is the most common cause of dementia in the elderly and with no proven effective treatment currently. Agents that reverse synapse impairments and Aβ accumulation represent promising therapeutic candidates for the treatment. An important role for hippocampal IGF2 in brain plasticity and learning and memory has been reported, and therefore, it may represent a new therapeutic candidate for AD treatment.

Results

We report that the endogenous levels of IGF2 decrease in the hippocampus with aging and in pathological conditions related to AD. Thus, we employed an adeno-associated viral (AAV) vector system to deliver IGF2 in the hippocampus of the transgenic mouse model Tg2576 to test its effect on the behavioural, cellular and synaptic phenotypes typical of AD. We demonstrated that the overexpression of hippocampal IGF2 restores memory and synaptic transmission deficits related to AD. We also demonstrated that IGF2 facilitates Aβ degradation in Tg2576 mice brain, which may be mediated by IGF2R.

Impact

Our results strongly suggest that increasing IGF2 in brain has a therapeutic effect in AD pathogenesis. This is in accordance with other studies that identify IGF2 as a natural memory boost, an alternative to purely pharmacological agents. However, in one side, IGF2 is related to cancer because it favours cell growth. Since IGF2 and IGF2R are known to be imprinted, it would be interesting to know whether the epigenetic changes triggered during learning can also induce IGF2 expression. Besides the gene therapy used in this study, it would be helpful to discover the mechanism by which neurons can increase IGF2 production in the brain in AD conditions.

Author contributions

AGO and MCT conceived the general framework of this study and designed experiments. MPL performed most of the experiments. MDS and GGA contributed to viral construction. SVS and CM designed and performed electrophysiology experiments. CGB contributed to behavioural experiments. AGO, MCT and MPL discussed the results. AGO, MCT, CMA and MPL wrote the manuscript. All authors have read the manuscript and provided the input.

Conflict of interest

The authors declare that they have no conflict of interest.

References

Braak H, Braak E, Yilmazer D, Bohl J (1996) Functional anatomy of human hippocampal formation and related structures. *J Child Neurol* 11: 265–275

Bracko O, Singer T, Aigner S, Knobloch M, Winner B, Ray J, Clemenson GD Jr, Suh H, Couillard-Despres S, Aigner L *et al* (2012) Gene expression profiling of neural stem cells and their neuronal progeny reveals IGF2 as a regulator of adult hippocampal neurogenesis. *J Neurosci* 32: 3376–3387

Braulke T (1999) Type-2 IGF receptor: a multi-ligand binding protein. *Horm Metab Res* 31: 242–246

Burger C, Nash K, Mandel RJ (2005) Recombinant adeno-associated viral vectors in the nervous system. *Hum Gene Ther* 16: 781–791

Carro E, Trejo JL, Gomez-Isla T, LeRoith D, Torres-Aleman I (2002) Serum insulin-like growth factor I regulates brain amyloid-beta levels. *Nat Med* 8: 1390–1397

Carro E, Trejo JL, Gerber A, Loetscher H, Torrado J, Metzger F, Torres-Aleman I (2006) Therapeutic actions of insulin-like growth factor I on APP/PS2 mice with severe brain amyloidosis. *Neurobiol Aging* 27: 1250–1257

Cearley CN, Wolfe JH (2006) Transduction characteristics of adeno-associated virus vectors expressing cap serotypes 7, 8, 9, and Rh10 in the mouse brain. *Mol Ther* 13: 528–537

Chen DY, Stern SA, Garcia-Osta A, Saunier-Rebori B, Pollonini G, Bambah-Mukku D, Blitzer RD, Alberini CM (2011) A critical role for IGF-II in memory consolidation and enhancement. *Nature* 469: 491–497

Cline BH, Steinbusch HW, Malin D, Revishchin AV, Pavlova GV, Cespuglio R, Strekalova T (2012) The neuronal insulin sensitizer dicholine succinate reduces stress-induced depressive traits and memory deficit: possible role of insulin-like growth factor 2. *BMC Neurosci* 13: 110

Cohen E, Paulsson JF, Blinder P, Burstyn-Cohen T, Du D, Estepa G, Adame A, Pham HM, Holzenberger M, Kelly JW *et al* (2009) Reduced IGF-1 signaling delays age-associated proteotoxicity in mice. *Cell* 139: 1157–1169

D'Amelio M, Cavallucci V, Middei S, Marchetti C, Pacioni S, Ferri A, Diamantini A, De Zio D, Carrara P, Battistini L *et al* (2011) Caspase-3 triggers early synaptic dysfunction in a mouse model of Alzheimer's disease. *Nat Neurosci* 14: 69–76

DaRocha-Souto B, Coma M, Perez-Nievas BG, Scotton TC, Siao M, Sanchez-Ferrer P, Hashimoto T, Fan Z, Hudry E, Barroeta I *et al* (2012) Activation of glycogen synthase kinase-3 beta mediates beta-amyloid induced neuritic damage in Alzheimer's disease. *Neurobiol Dis* 45: 425–437

El-Shewy HM, Luttrell LM (2009) Insulin-like growth factor-2/mannose-6 phosphate receptors. *Vitam Horm* 80: 667–697

Freude S, Hettich MM, Schumann C, Stohr O, Koch L, Kohler C, Udelhoven M, Leeser U, Muller M, Kubota N *et al* (2009) Neuronal IGF-1 resistance reduces Abeta accumulation and protects against premature death in a model of Alzheimer's disease. *Faseb J* 23: 3315–3324

Glaser EM, Van der Loos H (1981) Analysis of thick brain sections by obverse-reverse computer microscopy: application of a new, high clarity Golgi-Nissl stain. *J Neurosci Methods* 4: 117–125

Gomez-Isla T, Price JL, McKeel DW Jr, Morris JC, Growdon JH, Hyman BT (1996) Profound loss of layer II entorhinal cortex neurons occurs in very mild Alzheimer's disease. *J Neurosci* 16: 4491–4500

Hardy J, Selkoe DJ (2002) The amyloid hypothesis of Alzheimer's disease: progress and problems on the road to therapeutics. *Science* 297: 353–356

Hsiao K, Chapman P, Nilsen S, Eckman C, Harigaya Y, Younkin S, Yang F, Cole G (1996) Correlative memory deficits, Abeta elevation, and amyloid plaques in transgenic mice. *Science* 274: 99–102

Jacobsen JS, Wu CC, Redwine JM, Comery TA, Arias R, Bowlby M, Martone R, Morrison JH, Pangalos MN, Reinhart PH *et al* (2006) Early-onset behavioral and synaptic deficits in a mouse model of Alzheimer's disease. *Proc Natl Acad Sci USA* 103: 5161–5166

Johansson P, Aberg D, Johansson JO, Mattsson N, Hansson O, Ahren B, Isgaard J, Aberg ND, Blennow K, Zetterberg H *et al* (2013) Serum but not cerebrospinal fluid levels of insulin-like growth factor-I (IGF-I) and IGF-binding protein-3 (IGFBP-3) are increased in Alzheimer's disease. *Psychoneuroendocrinology* 38: 1729–1737

Kita Y, Ago Y, Takano E, Fukada A, Takuma K, Matsuda T (2013) Galantamine increases hippocampal insulin-like growth factor 2 expression via alpha7 nicotinic acetylcholine receptors in mice. *Psychopharmacology* 225: 543–551

Klein RL, Dayton RD, Leidenheimer NJ, Jansen K, Golde TE, Zweig RM (2006) Efficient neuronal gene transfer with AAV8 leads to neurotoxic levels of tau or green fluorescent proteins. *Mol Ther* 13: 517–527

Malik SZ, Maronski MA, Dichter MA, Watson DJ (2012) The use of specific AAV serotypes to stably transduce primary CNS neuron cultures. *Methods Mol Biol* 846: 305–319

Mandel RJ, Manfredsson FP, Foust KD, Rising A, Reimsnider S, Nash K, Burger C (2006) Recombinant adeno-associated viral vectors as therapeutic agents to treat neurological disorders. *Mol Ther* 13: 463–483

McKhann GM, Knopman DS, Chertkow H, Hyman BT, Jack CR Jr, Kawas CH, Klunk WE, Koroshetz WJ, Manly JJ, Mayeux R *et al* (2011) The diagnosis of dementia due to Alzheimer's disease: recommendations from the National Institute on Aging-Alzheimer's Association workgroups on diagnostic guidelines for Alzheimer's disease. *Alzheimers Dement* 7: 263–269

Megias M, Emri Z, Freund TF, Gulyas AI (2001) Total number and distribution of inhibitory and excitatory synapses on hippocampal CA1 pyramidal cells. *Neuroscience* 102: 527–540

Mellott TJ, Pender SM, Burke RM, Langley EA, Blusztajn JK (2014) IGF2 ameliorates amyloidosis, increases cholinergic marker expression and raises BMP9 and neurotrophin levels in the hippocampus of the APPswePS1dE9 Alzheimer's disease model mice. *PLoS ONE*, 9: e94287

Murakoshi Y, Takahashi T, Mihara H (2013) Modification of a small beta-barrel protein, to give pseudo-amyloid structures, inhibits amyloid beta-peptide aggregation. *Chemistry* 19: 4525–4531

Napoli I, Blusztajn JK, Mellott TJ (2008) Prenatal choline supplementation in rats increases the expression of IGF2 and its receptor IGF2R and enhances IGF2-induced acetylcholine release in hippocampus and frontal cortex. *Brain Res* 1237: 124–135

Ouchi Y, Banno Y, Shimizu Y, Ando S, Hasegawa H, Adachi K, Iwamoto T (2013) Reduced adult hippocampal neurogenesis and working memory deficits in the Dgcr8-deficient mouse model of 22q11.2 deletion-associated schizophrenia can be rescued by IGF2. *J Neurosci* 33: 9408–9419

Paneda A, Vanrell L, Mauleon I, Crettaz JS, Berraondo P, Timmermans EJ, Beattie SG, Twisk J, van Deventer S, Prieto J *et al* (2009) Effect of adeno-associated virus serotype and genomic structure on liver transduction and biodistribution in mice of both genders. *Hum Gene Ther* 20: 908–917

Rampon C, Tang YP, Goodhouse J, Shimizu E, Kyin M, Tsien JZ (2000) Enrichment induces structural changes and recovery from nonspatial memory deficits in CA1 NMDAR1-knockout mice. *Nat Neurosci* 3: 238–244

Ribe EM, Perez M, Puig B, Gich I, Lim F, Cuadrado M, Sesma T, Catena S, Sanchez B, Nieto M *et al* (2005) Accelerated amyloid deposition, neurofibrillary degeneration and neuronal loss in double mutant APP/tau transgenic mice. *Neurobiol Dis* 20: 814–822

Ricobaraza A, Cuadrado-Tejedor M, Perez-Mediavilla A, Frechilla D, Del Rio J, Garcia-Osta A (2009) Phenylbutyrate ameliorates cognitive deficit and reduces tau pathology in an Alzheimer's disease mouse model. *Neuropsychopharmacology* 34: 1721–1732

Ricobaraza A, Cuadrado-Tejedor M, Marco S, Perez-Otano I, Garcia-Osta A (2012) Phenylbutyrate rescues dendritic spine loss associated with memory deficits in a mouse model of Alzheimer disease. *Hippocampus* 22: 1040–1050

Rivera EJ, Goldin A, Fulmer N, Tavares R, Wands JR, de la Monte SM (2005) Insulin and insulin-like growth factor expression and function deteriorate with progression of Alzheimer's disease: link to brain reductions in acetylcholine. *J Alzheimers Dis* 8: 247–268

Schmeisser MJ, Baumann B, Johannsen S, Vindedal GF, Jensen V, Hvalby OC, Sprengel R, Seither J, Maqbool A, Magnutzki A *et al* (2012) IkappaB kinase/nuclear factor kappaB-dependent insulin-like growth factor 2 (Igf2) expression regulates synapse formation and spine maturation via Igf2 receptor signaling. *J Neurosci* 32: 5688–5703

Selkoe DJ (2011) Alzheimer's disease. *Cold Spring Harb Perspect Biol* 3: a00457

Shankar GM, Bloodgood BL, Townsend M, Walsh DM, Selkoe DJ, Sabatini BL (2007) Natural oligomers of the Alzheimer amyloid-beta protein induce reversible synapse loss by modulating an NMDA-type glutamate receptor-dependent signaling pathway. *J Neurosci* 27: 2866–2875

Smith DL, Pozueta J, Gong B, Arancio O, Shelanski M (2009) Reversal of long-term dendritic spine alterations in Alzheimer disease models. *Proc Natl Acad Sci USA* 106: 16877–16882

Steen E, Terry BM, Rivera EJ, Cannon JL, Neely TR, Tavares R, Xu XJ, Wands JR, de la Monte SM (2005) Impaired insulin and insulin-like growth factor expression and signaling mechanisms in Alzheimer's disease–is this type 3 diabetes? *J Alzheimers Dis* 7: 63–80

Stein TD, Johnson JA (2002) Lack of neurodegeneration in transgenic mice overexpressing mutant amyloid precursor protein is associated with increased levels of transthyretin and the activation of cell survival pathways. *J Neurosci* 22: 7380–7388

Stein TD, Anders NJ, DeCarli C, Chan SL, Mattson MP, Johnson JA (2004) Neutralization of transthyretin reverses the neuroprotective effects of secreted amyloid precursor protein (APP) in APPSW mice resulting in tau phosphorylation and loss of hippocampal neurons: support for the amyloid hypothesis. *J Neurosci* 24: 7707–7717

Stern SA, Kohtz AS, Pollonini G, Alberini CM (2014) Enhancement of memories by systemic administration of insulin-like growth factor II. *Neuropsychopharmacology* 39: 2179–2190

Trueba-Saiz A, Cavada C, Fernandez AM, Leon T, Gonzalez DA, Fortea Ormaechea J, Lleo A, Del Ser T, Nunez A, Torres-Aleman I (2013) Loss of serum IGF-I input to the brain as an early biomarker of disease onset in Alzheimer mice. *Transl Psychiatry* 3: e330

Westerman MA, Cooper-Blacketer D, Mariash A, Kotilinek L, Kawarabayashi T, Younkin LH, Carlson GA, Younkin SG, Ashe KH (2002) The relationship between Abeta and memory in the Tg2576 mouse model of Alzheimer's disease. *J Neurosci* 22: 1858–1867

Zolotukhin S, Byrne BJ, Mason E, Zolotukhin I, Potter M, Chesnut K, Summerford C, Samulski RJ, Muzyczka N (1999) Recombinant adeno-associated virus purification using novel methods improves infectious titer and yield. *Gene Ther* 6: 973–985